



Australian Combustion Symposium 2019

PROCEEDINGS

The University of Adelaide
4–6 December 2019

SPONSORED BY



Proceedings of the 2019 Australian Combustion Symposium
4–6 December 2019, The University of Adelaide

Editors

Paul Medwell
Zeyad Alwahabi
Michael Evans
Shaun Chan
Alfonso Chinnici
Zhao Tian
Bassam Dally

<http://anz-combustioninstitute.org/ACS2019/>

Reproduction of all or part of this document, including storing in electronic form, is permitted, provided it is fully referenced.

Each contribution included has been subject to a peer-review process by at least two independent expert referees of each full-length paper. The reviewers provided written feedback on the paper and the authors revised their manuscripts to address the comments. The revised manuscript of each paper was then considered by the Editors before acceptance for inclusion into the proceedings. Authors were given the option of publishing only the abstract of their submission.

The copyright of the individual contributions contained in this volume is retained and owned by the authors of the papers. Neither The Combustion Institute Australia & New Zealand Section nor the Editors possess the copyright of the individual papers.

The Combustion Institute Australia & New Zealand Section and the Editors of the volume assume no responsibility for the accuracy, completeness or usefulness of the information provided in these proceedings. No responsibility is assumed by the publisher or editors for any use or operation of any methods, products, instructions or ideas contained in the material presented.

Proceedings of the Australian Combustion Symposium: ISSN 1839-8162 (Online)

FOREWARD

Adelaide is going to take centre stage in combustion research over the next few months. It is fitting that it hosts the 2019 Australian Combustion Symposium as a preamble to hosting the global event of the 38th International Combustion Symposium in July 2020.

The combustion community in Australia and overseas is well positioned to respond to global challenges in energy supplies and continues to address issues of the gradual decarbonisation of the sector. This is evident from the broad scope of topics that are addressed at the 2019 Australian Combustion Symposium which is held at the University of Adelaide. A recent emphasis in many of the papers to be presented at this conference is on cleaner fuels and fuel blends, as well on understanding and controlling pollutants formation with a focus on particles.

The conference program also brings together an outstanding team of invited speakers. The “Bilger Lecture” will be presented by Professor Epaminondas Mastorakos, from the University of Cambridge addressing “Recent developments in turbulent combustion modelling and laser-based experiments and their relevance to practical systems”. Professor Mara de Joannon, from CNR, Italy will presented a plenary talk in the “Stability of MILD Combustion in temperature tailored reactors - A perspective on thermal conversion of energy carriers”, while Professor Bogdan Z. Dlugogorski, from Charles Darwin University will address the topic of “Flammability of Hydrogen Sulfide (H₂S) and Carbon Disulfide (CS₂)”.

The contribution of young scientists and research students is an essential part of these conferences. Therefore, a novel feature was introduced in this conference as a series of invited “Technical Talks” by Early Career Combustion Scientists who are on track to become future leaders of combustion research. Their talks address a broad range of interesting and highly relevant topics. For research students, and to assist with their travel costs to the conference, fifteen grants were awarded by the Australia and New Zealand Section of the Combustion Institute.

As Chairman of the ANZ-Section and on behalf of all our membership and delegates, I would like to thank the local organizing committee in Adelaide for their tireless work and dedication in making the 2019 Australian Combustion Symposium an outstanding success. Our thanks go to: A/Profs Paul Medwell and Zeyad Alwahabi, Dr Michael Evans, Drs Shaun Chan, Zhao Tian and Alfonso Chinnici, and Prof. Bassam Dally.

We hope you enjoy this conference and we look forward to seeing you at the upcoming 38th International Combustion Symposium which will also be held in Adelaide.

Assaad Masri
25 November 2019

PREFACE

The 2019 Australian Combustion Symposium was held 4–6 December 2019 at The University of Adelaide. We were delighted that Prof. Epaminondas Mastorakos delivered the Bilger Lecture, and esteemed plenary speakers were Prof. Mara de Joannon and Prof. Bogdan Dlugogorski. Another eight invited speakers also featured in the programme to deliver technical talks.

The biennial meeting is Australia's preeminent conference in the field of combustion, and builds on a long-standing series of events, including Sydney (2017), Melbourne (2015) and Perth (2013). The conference will be a precursor to the prestigious *38th International Symposium on Combustion*, which will also be in Adelaide. Both meetings are held under the auspices of the Australia and New Zealand section of the Combustion Institute.

The programme featured 54 presentations, which were selected based on the scientific review of a four-page research paper (eight pages for invited speakers) by two technical experts. Authors were given the option of publishing the full paper or only the abstract.

The meeting would not have been possible without the support of the following sponsors and exhibitors. We gratefully acknowledge the contributions of...

SPONSORS

- The University of Adelaide
- Mission Innovation
- The University of New South Wales, Sydney
- Coherent Scientific
- Kenelec Scientific
- Lastek
- NewSpec
- Scitech

EXHIBITORS

- InnoLas Laser
- IR Sweep
- Scitek
- Testo

Local organising committee:

Paul Medwell (chair)
Zeyad Alwahabi (co-chair)
Michael Evans (secretary)
Shaun Chan (lead technical reviewer)
Alfonso Chinnici
Zhao Tian
Bassam Dally



SPONSORS

The following companies had a booth at the conference and their financial support contributed to the success of the conference...



pco.

on the cutting edge

pco.edge family

now with advanced sCMOS

image sensor

small form factor

100 fps @ full resolution



CAMERA **LinkHS**

1.1 GByte/s image data bandwidth
Best data reliability with Forward Error Correction
Long distance of 300 meters with multimode fiber

CAMERA **LinkHS**

Long distance of 300 meters with multimode fiber
Best data reliability with Forward Error Correction
1.1 GByte/s image data bandwidth

intensified sCMOS

the new intensified pco.dicam C1 with 16 bit dynamic range

intensified sCMOS technology
2048 x 2048 pixel

exposure time **3 ns**
with 25 mm intensifier

104 fps
@ full resolution



enhanced extinction ratio gating

Scitech
imaging specialists

T: 1300 SCITECH
sales@scitech.com.au
www.scitech.com.au

with CAMERA **LinkHS** interface

pco-imaging.com



NewSpec

Excellence deserves the best support



Lasers & Light Sources

CW, tunable, pulsed & ultrafast lasers. Solid-state, fiber and dye lasers. High-energy, High-repetition rate systems. Incoherent light sources, Laser diodes and controllers



Electron Microscopy & Atomic Force Microscopy

FESEM, SEM, TEM, FIB, sample preparation. AFMs.



Motion & Vibration Control

Optical tables, breadboards, & workstations. Manual & automated linear, rotation & tilt stages. Hexapods, multi-axis stages, actuators & motion controllers.



Spectroscopy & Imaging Systems

High-performance CCD, ICCD, EMCCD, eMCCD, InGaAs, and back-illuminated sCMOS cameras. Spectrographs & complete spectroscopy systems.



XRF, LIBS & OES

Laboratory & in-field based instruments for materials analysis. Handheld XRF/LIBS analysers, benchtop XRF, mobile & desktop OES.



Vacuum Equipment, Control & Accessories

Pressure measurement & control, materials delivery, gas analysis & control. Power & reactive gas generation & vacuum technology & accessories.



Optics & Accessories

UV, VIS, NIR and IR optics. Lens, mirrors, filters, beamsplitters, polarisation optics, diffraction gratings, windows, prisms, fiber optics. Opto-mechanics & Lab supplies.



Optical Surface Profilers & Laser Interferometers

3D Optical Surface Profiling Systems & Laser Interferometer Systems for surface analysis.

330 Glen Osmond Rd
Myrtle Bank SA 5064

T +61 8 8463 1967
F +61 8 8410 8816
sales@newspec.com.au

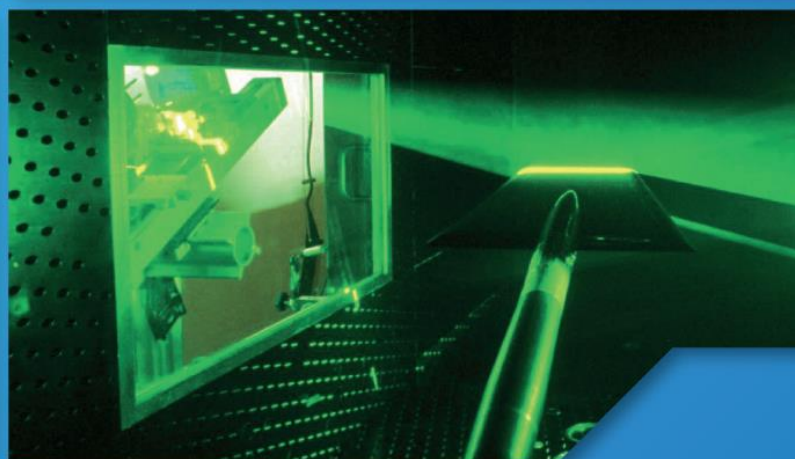
newspec.com.au



Delivering excellence in SPM and Profilometry through Partnership

High Performance Nd:YAG, Tuneable and Fibre Lasers

Nanosecond Nd:YAG lasers
Dye lasers & solid state OPOs
Fibre lasers and amplifiers



Merion MW DPSS Laser

Repetition rates to 200Hz
Quick and easy access to
1064, 532, 355 and 266nm
Automated phase
matching of harmonics



(08) 8150 5200
sales@coherent.com.au
www.coherent.com.au

Coherent
SCIENTIFIC

Established in 1962, Kenelec Scientific is one of Australia's leading scientific and environmental technology companies. Based in Melbourne, with distributors located throughout Australia and New Zealand, we are industry leaders in the supply of state-of-the-art hardware, software, and complete measurement systems from TSI Incorporated for fluid mechanics and particle diagnostics researchers.

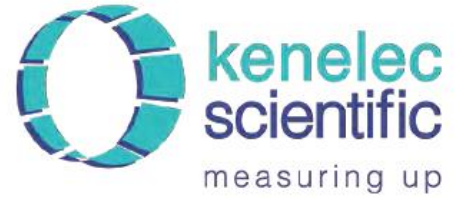
A TSI instrument solution equips fluid mechanics and particle diagnostics researchers with the state-of-the-art hardware, software and complete measurement systems providing diagnostics of fluid flow and particle/droplet sizing in a wide range of applications including: aerodynamics, hydrodynamics, spray diagnostics, multiphase flows, turbulent boundary layer flows, combustion diagnostics and many more.

Additionally, Kenelec Scientific offers services to design a new system, or upgrade an existing system, with the latest technology and combination of measurement techniques:

- **PIV** - Particle Image Velocimetry,
- **LDV** - Laser Doppler Velocimetry
- **PDPA** - Phase Doppler Particle Analysis
- **PLIF** - Planar Laser Induced Fluorescence
- **TA** - Thermal (Hot Wire) Anemometry

Contact our team to discuss the solution that best suits your needs.

We look forward to working with you.



Find out more about our extensive range of **products and services:**

+61 3 9873 1022
sales@kenelec.com.au
www.kenelec.com.au

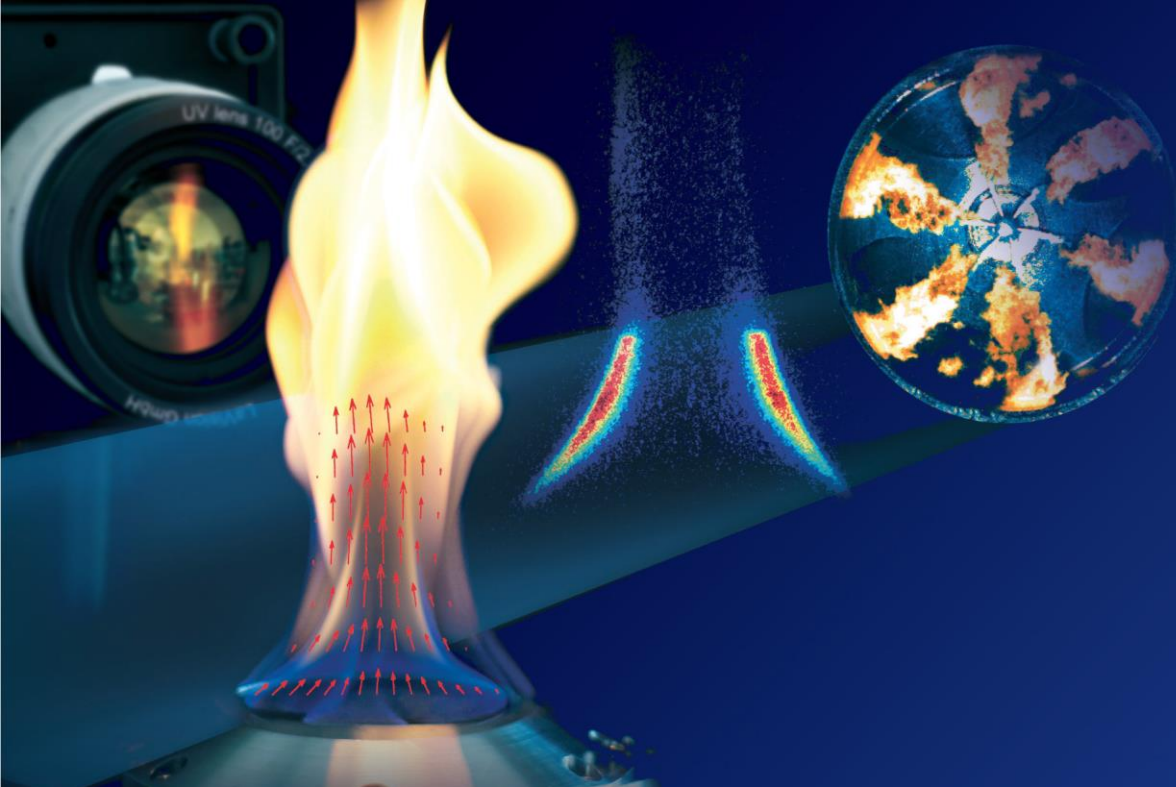
Exclusive Channel Partner of:





LAVISION

FOCUS ON IMAGING



Innovative Imaging Systems

Fuel LIF Imaging, Air-Fuel Mixing

Flame Front Visualization

Flame Structure and Stability

Soot Concentration

Flame and Soot Temperature

LaVision GmbH

Anna-Vandenhoeck-Ring 19
D-37081 Göttingen / Germany
Tel. +49 551 9004 0
Email: sales@lvision.com
www.lvision.com

Lastek
Photonics Technology Solutions 

University of Adelaide - Thebarton Campus
10 Reid St, Thebarton, South Australia 5031
Toll Free Australia: 1800 882 215
Toll Free New Zealand: 0800 441 005
email: sales@lastek.com.au
www.lastek.com.au

QE Pro

High Performance Spectrometer



 **Ocean
Insight**

Lastek
Photonics Technology Solutions 

EXHIBITORS

The following companies had a booth at the conference...





INNOVATIVE LASERS FOR SCIENCE AND INDUSTRY



EVO

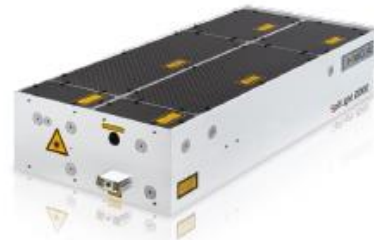
Diode Pumped Lasers:

- * Up to 100 W, 1 Joule
- * Frequency: 1–1000 Hz
- * 24/7 Industrial Applications

SpitLight

Flash Lamp pumped Lasers:

- * Up to 2.5 J
- * Frequency: 1–100 Hz
- * Compact High-Energy Lasers



OPO

NIR-UV emission

- * Wavelength: 210–2500 nm
- * Integrated Pump Laser
- * Shot-to-shot wavelength tuning

pico & MAGNA

Sub-Nanosecond Lasers:

- * Pulse-Width down to 500 ps
- * Amplified up to 2 J
- * Active Q-switch, low Jitter





testo 340 and testo 350 Emission analyser



testo 300 Flue gas analyser

Chat with Testo
@ the Australian
Combustion
Symposium

testo combustion range

Innovation you just have to see, touch and try out.

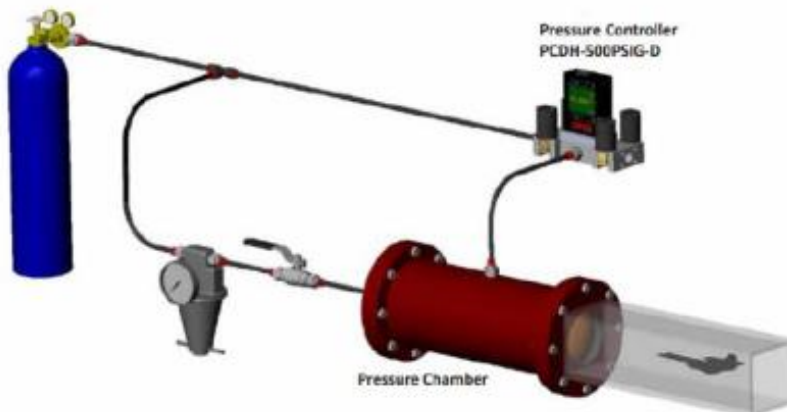
Australian Combustion Symposium 2019

Scitek's focus is on providing honest instrument selection advice, combined with benchmark service. Our key staff members are experts with many years' experience and extensive training. Every technical team member undergoes annual overseas training in our factories or at scientific events.

Scitek has extensive experience with mass flow control technology on all levels and Alicat products to support your science. One of Alicat's key industries is in Aerospace and Defense applications, where accuracy, repeatability—and perhaps most of all—reliability are critical requirements. Advanced pressure controllers, mass flow meters and mass flow controllers have made Alicat part of aerospace development, testing and experiments from the cockpit, through the payload, all the way to the thrusters.

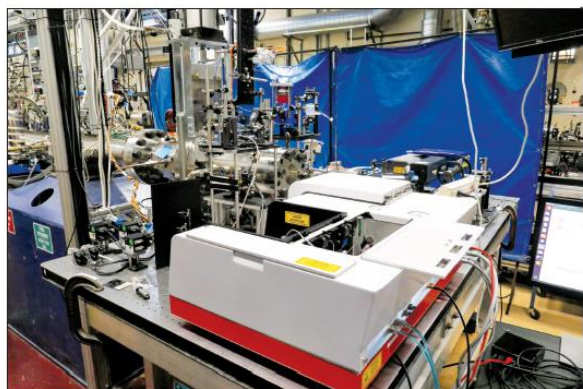
Their aerospace and defense customers in labs, academia and industrial settings work on life support, aerodynamics design, thrust control, cooling systems and systems testing. Read below for information on:

- Leak testing valves for capsule engines
- Satellite attitude control with pressure control
- Liquid cooling suit and engine systems
- Gas mixing exotic atmospheres
- Accurate totalizing and dosing for buoyancy
- Simulating breathing



Bringing Quantum Cascade Laser Spectroscopy to Combustion Diagnostics

Why new methods for combustion diagnostics?



Experimental setup with the IRis-F1 at the shock tube (Hanson Group Lab, Stanford University)

Absorption spectroscopy is an important tool for combustion diagnostics. And yet, combustion processes are also a challenging environment for most spectrometers, demanding specifications that traditional instruments often cannot meet.

Speed. The typical timescales involved in combustion processes range from microseconds to - at most - a few milliseconds. Studying a process that happens so fast requires an equally fast measurement method.

Single-shot measurements. By their very nature, combustion diagnostics involve processes which are hard to repeat: even when running two nominally identical shocks down a shock tube, the temperature and pressure produced will be slightly different. This means experiment data has to be collected in a single repetition.

Broad spectral coverage. Most combustion measurements aim to measure several species at the same time - both, narrowband and broadband absorbers. Being able to observe multiple spectral features is often a key requirement.

Optical power. Dealing with combustion necessarily entails managing large thermal emissions, and that requires very large optical power. This makes it possible to transmit through a shock tube and distinguish the instrument's laser light from the background thermal radiation.

Advantages of dual-comb spectroscopy

Frequency comb laser sources based on quantum cascade lasers (QCLs) manage to fulfill the aforementioned requirements. By relying on fundamentally different principles than other types of spectrometers, this technology provides real advantages over both FTIR and single wavelength laser-based mid-infrared spectrometers.

The minimum time required for measuring a complete spectrum is less than one microsecond, a feature made possible by an innovative technology called multi-heterodyne detection. The broadband lasers emit several hundred colors at the same time, covering tens of wavenumbers. All the emitted wavelengths are detected simultaneously within microseconds.

In addition, frequency comb laser sources can offer brightness levels that are orders of magnitude higher than standard FTIR spectrometers. Because of this, dual-comb spectroscopy provides a unique combination of brightness, optical bandwidth, and speed.



Setup of the combustion kinetics measurement at Prof. Farooq's Lab (KAUST)

The IRis-F1: a fast, high-resolution spectrometer



IRsweep's IRis-F1: the first commercial turnkey quantum cascade laser frequency combs spectrometer

IRsweep's goal is to bring high-performance mid-infrared spectroscopy to field applications - including combustion diagnostics.

The IRis-F1 spectrometer exploits the superior sensing performance of mid-infrared frequency combs. It offers an unmatched combination of fast detection, high brightness and broad spectral coverage.

Its suitability to combustion diagnostics has been thoroughly proven on several occasions, through our collaboration with experts of the field such as Professor Hanson's Group at Stanford University and Professor Farooq's at KAUST in Saudi Arabia.

It has been shown that the concentration of multiple species can be tracked during the evolution of a single shock with a duration of just one microsecond. The unique sensing capabilities provided by the IRis-F1 open the door to many new possibilities in the field of combustion process diagnostics.

LIST OF PAPERS

Bilger Lecture

Recent developments in turbulent combustion modelling and laser-based experiments and their relevance to practical systems <i>Epaminondas Mastorakos</i>	1
---	---

Plenary Contributions

Stability of MILD Combustion in temperature tailored reactors: A perspective on thermal conversion of energy carriers <i>Mara de Joannon</i>	2
Flammability of Hydrogen Sulfide (H ₂ S) and Carbon Disulfide (CS ₂) – Review of Present Insights into Reaction Mechanisms <i>Bogdan Dlugogorski</i>	3

Invited Technical Contributions

Recent Progress in the Control and Understanding of Turbulent Spray Formation <i>Agisilaos Kourmatzis</i>	11
Supersonic Ethylene Combustion – Revamping the Cavity <i>Anand Veeraragavan</i>	19
A Physical Understanding of how Multiple Mapping Conditioning Works <i>Andrew Wandel</i>	20
What is important for accurate soot predictions? <i>Heinz Pitsch</i>	28
Sound sources in premixed flames <i>Mohsen Talei</i>	29
Industrial Gas Turbine Combustor Design: Exhaust CO Emissions <i>Robert Gordon</i>	37
Combustion strategies for multi-fuel capable compression ignition engines <i>Sanghoon Kook</i>	45
The Dynamics of Supersonic Turbulent Combustion <i>Vincent Wheatley</i>	53

Contributed Full Papers

- Soot particle structure variation associated with in-cylinder gas pressure/temperature in a small-bore diesel engine
Lingzhe Rao, Yilong Zhang, Sanghoon Kook..... 61
- In-cylinder and exhaust soot morphology in an optical spark ignition direct injection (SIDI) petrol engine
Dongchan Kim, Sanghoon Kook 65
- Fuel reactivity effects on premixed combustion in a diesel engine
Yilong Zhang, Siyuan Meng, Harsh Goyal, Sanghoon Kook, Chol-Bum Kweon, Kenneth Kim..... 69
- One-Step Chemical Kinetic Scheme for Propane in High Temperature Applications
Raoul Mazumdar, Hideaki Ogawa, Adrian Pudsey, Mathew Bricalli 73
- Comparative study of spray characteristics of high alcohol-diesel blends
Sattar Algayyim, Andrew Wandel..... 77
- Flame image velocimetry for in-flame flow field analysis in an optically accessible diesel engine
Jinxin Yang, Lingzhe Rao, Yilong Zhang, Charitha de Silva, Sanghoon Kook..... 81
- Image selection method for combustion analysis in an optical diesel engine
Siyuan Meng, Yilong Zhang, Sanghoon Kook..... 85
- Effect of intake air e-boosting on external EGR-diluted diesel combustion
Xinyu Liu, Sanghoon Kook..... 89
- Initial Characterisation of a hybrid air-blast and electrostatic atomizer for spray combustion
Tushar Ahmed, Agisilaos Kourmatzis, Assaad Masri..... 93
- Measurement of wave speeds at the liquid-air interface of an air-blast atomized biodiesel spray
Aaron Gutteridge, Gajendra Singh, Agisilaos Kourmatzis, Assaad Masri 97
- Comparison of real-time NO_x emission measurements from two heavy-duty diesel engines
G M Hasan Shahariar, Thuy Chu-Van, Timothy Bodisco, Mojibul Sajjad, Kabir Adewale Suara, Zoran Ristovski, Richard Brown..... 101
- A Parametric Study on Fluidisation Characteristics and Product Yields in Bubbling Fluidised Bed Reactor
Joshua Clissold, Salman Jalalifar, Fatemah Salehi, Rouzbeh Abbassi..... 105

LES/PDF Modelling of Turbulent Premixed Flames in the Flamelet Regime Using an MMC – Shadow Position Mixing Model <i>Yashar Shoraka, Sebastian Galindo-Lopez, Matthew Cleary, Assaad Masri, Alexander Klimenko</i>	109
Numerical Analysis of Point Source Fire on Fire-Wind Enhancement <i>Esmaeel Eftekharian, Fatemah Salehi, Yaping He, Kenny Kwok</i>	113
Joint OH-CH PLIF imaging in highly-sheared turbulent premixed propane flames <i>Mohammed Kanj, Matthew Dunn, Mrinal Juddoo, Scott Steinmetz, Guoqing Wang, Assaad Masri</i>	117
Ignition Waves in Compartment Fire Flashover <i>Vasily Novozhilov</i>	121
Grid Sensitivity Study for Air Blast Atomisation Using an LES-PDF form of ELSA Model <i>Fakhar Abbas, Giovanni Tretola, Matthew Cleary, Salvador Navarro-Martinez, Assaad Masri</i>	125
Particle-intense MMC-LES simulations of mixed-mode turbulent piloted jet flame <i>Saeed Aldawsari, Sebastian Galindo-Lopez, Matthew Cleary, Assaad Masri</i>	129
CFD modelling of DC arc plasma system for application in cleaner chemical production <i>Jyothikrishna Perambadur, Alexander Klimenko, Pradeep Shukla, Victor Rudolph</i>	133
Numerical study of the flame structure and swirling motion of small-scale fire whirls <i>Xiang Fang, Anthony Yuen, Guan Yeoh, Sherman Cheung</i>	137
Effect of inlet manifold water injection on diesel engine performance and emissions <i>Sujit Kafle, Andrew Wandel, Saddam Al-Lwayzy</i>	141
Contributed Papers — Abstract only	
Numerical Investigation of Tandem Cavity Configurations with Supersonic Ethylene Combustion <i>Sarah Mecklem, Will Landsberg, Anand Veeraragavan</i>	145
Algebraic Flame Surface Density Model Development using Gene-Expression Programming <i>Man-Ching Ma, Mohsen Talei, Richard Sandberg</i>	146
Some Recent Results on Hydrogen Oxidation in a Flow Reactor <i>Zhewen Lu, Yi Yang, Joshua Lacey, Michael Brear</i>	147

An Update on the Rate Constant of $H + O_2 (+M) \rightarrow HO_2 (+M)$, $M = N_2$ using $H_2/O_2/NO_x$ Reaction in a Flow Reactor <i>Zhewen Lu, Yi Yang, Joshua Lacey, Michael Brear</i>	148
Fast Pyrolysis of Lignin at Low Temperatures: An In-depth Understanding of the Char Structural Changes <i>Yee Wen Chua, Yun Yu, Hongwei Wu</i>	149
Investigation of flammability factor in CNG jets using LES <i>Mohammad Reza Yosri, Joshua Lacey, Mohsen Talei, Robert Gordon, Michael Brear</i>	150
Chemistry reduction of hydrogen-methane mixtures with a focus on the laminar flame speed <i>Jen Zen Ho, Mohsen Talei, Robert Gordon, Michael Brear</i>	151
Sound generation by turbulent premixed flames with reduced chemistry <i>Davy Brouzet, Mohsen Talei, Michael Brear</i>	152
Preliminary Observations of Turbulent Flames in a Confined and Pressurised Jet in Hot and Vitiated Coflow Burner <i>Michael Evans, Paul Medwell, Shaun Chan</i>	153
Multiple injections of iso-octane and n-heptane: Part I <i>Sensen Xing, Guanxiong Zhai, Aleš Srna, Haijun Mo, Paul Medwell, Sanghoon Kook, Guan Yeoh, Shaun Chan</i>	154
Multiple injections of iso-octane and n-heptane: Part II <i>Haijun Mo, Sensen Xing, Guanxiong Zhai, Aleš Srna, Paul Medwell, Sanghoon Kook, Guan Yeoh, Shaun Chan</i>	155
High-order accurate hybrid LES/PDF simulations of an experimental H_2/N_2 lifted jet flame <i>Harshad Ranadive, Armin Wehrfritz, Evatt Hawkes</i>	156
A-priori evaluation of low-dimensional manifold combustion models under diesel engine conditions <i>Deepak Dalakoti, Armin Wehrfritz, Bruno Savard, Evatt Hawkes</i>	157
PLIF Imaging of a Low Emission Reverse-Cross Flow Combustor <i>Shreshtha Kumar Gupta, Santanu Pramanik, Vaibhav Kumar Arghode, R. V. Ravikrishna, Robert Gordon</i>	158
Experimental and numerical study of ammonia oxidation and pyrolysis in a Jet Stirred Flow Reactor. Evaluation of wall surface reactions effects <i>Pino Sabia, Maria Virginia Manna, Raffaele Ragucci, Mara de Joannon</i>	159
Classification of MILD and autoignitive ethylene flames diluted with N_2 , O_2 and CO_2 <i>Jordan Kildare, Michael Evans, Alfonso Chinnici, Paul Medwell</i>	160

Numerical Modelling of Mild Combustion at Elevated Pressures <i>Douglas Proud, Michael Evans, Paul Medwell</i>	161
Influence of steam dilution on flame structure and soot formation of hot, diluted ethylene flames <i>Alfonso Chinnici, Michael Evans</i>	162
Hybrid solar-combustion processes of renewable fuels <i>Alfonso Chinnici, Gus Nathan, Bassam Dally</i>	163
Experimental Investigation of Soot Evolution in Turbulent Non-premixed Bluff-body Ethylene/Nitrogen Flames <i>Amir Rowhani, Zhiwei Sun, Paul Medwell, Gus Nathan, Bassam Dally</i>	164
An Experimental Study of Laminar Flame Speed of Partially Dissociated NH ₃ and Air Mixtures <i>Harry Lesmana, Mingming Zhu, Zhezi Zhang, Jian Gao, Junzhi Wu, Dongke Zhang</i>	165
Computational Fluid Dynamics Modelling of Rotating Detonation Engines <i>Ian Shaw, Michael Evans, Rey Chin, Paul Medwell</i>	166

Recent developments in turbulent combustion modelling and laser-based experiments and their relevance to practical systems

Epaminondas Mastorakos

University of Cambridge

em257@eng.cam.ac.uk

ABSTRACT

The prediction, at the design stage, of pollutants emitted from combustion devices such as reciprocating engines and gas turbines, would be advantageous from the perspective of allowing innovation and savings in development costs. However, designers are at present limited by the lack of fundamental knowledge and accurate enough simulations tools. The explosive growth of high-repetition rate imaging and of computing power that allows Large-Eddy Simulation for realistic devices the last few years has changed drastically both experiments and numerical research in this field, and in particular has offered validation of theoretical models in ways that were not available before. The time-resolved behaviour of the flame is discussed through its relevance to thermoacoustics, a very important phenomenon for gas turbine combustors, and to lean blow-out, which is of vital importance for operability of low-NO_x concepts. The need for simultaneous multi-scalar imaging is emphasized. The limitations and strengths of present modelling approaches are also discussed from the perspective of usefulness to industry and the future use of CFD for combustors.

Stability of MILD Combustion in temperature tailored reactors: A perspective on thermal conversion of energy carriers

**M. de Joannon¹, P. Sabia¹, G. Sorrentino², P. Bozza¹, G. Ceriello², V. Manna^{1,2},
G. Ariemma¹, A. Cavaliere², R. Ragucci¹**

¹Istituto di Ricerche sulla Combustione - C.N.R., Napoli – Italy

² Università degli Studi di Napoli, Federico II, Napoli-Italy
dejoannon@irc.cnr.it

ABSTRACT

MILD combustion processes and systems are among the few advanced combustion technologies which intrinsically satisfy the general criteria of sustainability, fuel flexibility and readiness level required to face the energy issue. Because of inlet/local high diluted and preheated conditions in which the fuel conversion occurs, the process evolves through peculiar distributed spontaneous ignition based on local igni-diffusive structures, very different from the ones occurring in premixed and diffusion flames. Igni-diffusion will be described and discussed in relation to elementary configurations and different possible initial conditions highlighting its unique characteristics. By means of the stabilization of MILD combustion process for a wide palette of energy carriers, from standard carbon based fuels, to biogas, alcohols, ammonia and mixtures surrogating wastes it will be proved the possibility to tailor the operational temperature in a wide range of values provided that the attainment of the cross-over temperature of high temperature radical branching is locally achieved. This outstanding feature turns the concept of “combustion process” into those of “thermochemical conversion process” where the output conditions can be easily tuned based on end-use needs.

Flammability of Hydrogen Sulfide (H₂S) and Carbon Disulfide (CS₂) – Review of Present Insights into Reaction Mechanisms

Bogdan Z. Dlugogorski^{1,*}, Zhe Zeng², Ibukun Oluwoye², Mohammednoor Altarawneh³

¹ Charles Darwin University, Office of Deputy Vice-Chancellor and Vice-President, Research & Innovation, Darwin, NT 0909, Australia

² Murdoch University, College of Science, Health, Engineering and Education (SHEE), WA 6150, Australia

³ United Arab Emirates University, Department of Chemical and Petroleum Engineering, Al-Ain 15551, United Arab Emirates

Abstract

Reduced sulfur species persist as important industrial raw materials and as essential impurities in most fossil fuels. They also display extreme flammability, triggering serious fire emergencies in industries, even as highly diluted mixtures in chemical and petrochemical storage, transportation and laboratories. This contribution reviews the flammability and oxidation mechanism of reduced sulfur species (especially, ¹H₂S and ¹CS₂), explaining their fire hazard from molecular considerations. (To avoid confusion, we explicitly state the spin multiplicity as a superscript number in front of each species.) The flammability of H₂S and CS₂ is characterised by their extremely low ignition temperature and flash point. By examining the key elementary reactions in their oxidation mechanisms, we highlight the occurrence of intersystem-crossing (ISC) processes, which significantly reduce the activation energy for the chain initiation and chain branching steps, leading to the ignition of H₂S and CS₂ at lower temperature. ISC represents the transition between two electronic states with different spin multiplicities at the same energy level, resulting in the crossing-over between triplet and singlet reaction pathways. The oxidation of reduced sulfur species transits into the singlet (excited state) reaction pathway through the ISC seams, offering alternative corridors with much lower activation barriers. In comparison, the oxidation of hydrocarbons proceeds along the conventional triplet (ground state) reaction pathways that typically entail significantly higher activation barriers. For H₂S oxidation, we highlight the occurrence of ISC in ¹H₂S + ³O₂, ²SH + ²SH, ³S + ³O₂, and ³SO + ³O₂ reactions. Similarly, the CS₂ oxidation relies on the ISC process for ¹CS₂ + ³O₂ and ¹CS + ³O₂. These occurrences of ISC reactions highlight the reduced sulfur species as a group of a very flammable character.

Keywords: Flammability, Reduced Sulfur Species, Intersystem Crossing (ISC), Reaction Mechanisms

1. Introduction

Sulfur stands as an essential impurity in fossil fuels, biofuels and municipal wastes [1, 2]. Constituting up to 5 wt % in unprocessed fossil fuels [3], sulfur gives rise to industrial problems on a large scale, most notably relating to environment protection and fire safety. The fire hazard issue originates from the flammable nature of the reduced sulfur species, which are usually present as raw industrial material and impurities in fuels. Almost half of the global reserves of natural gas contains H₂S [4], typically in concentrations of more than 100 ppm [5], earning a moniker of sour gas for these deposits. The presence of ¹H₂S, even when highly diluted, triggers serious industrial fire (and toxicity) hazards in petroleum piping and oil tanks [6].

Apart from ¹H₂S, other less-known reduced sulfur species – carbon disulfide (¹CS₂) and carbonyl sulfide (¹COS) – are also produced during combustion, or thermal pyrolysis of fuels [6]. As an excellent non-polar solvent, ¹CS₂ has found numerous applications in both laboratory and industry. However, ¹CS₂ displays extreme flammability [7] and high explosion propensity [8], which has led to several fire accidents in industrial facilities [9], laboratories [10] and chemical warehouses [11]. As an impurity in natural gas, ¹CS₂ also lowers the ignition point of methane, resulting in increased fire hazard in application of fossil fuels [12, 13].

Table 1 compares the flash points and the auto-ignition temperatures of ¹H₂S and ¹CS₂ with other flammable

chemicals. The flash point of ¹H₂S resides at -82 °C, below those of ¹CS₂, methanol and gasoline. Moreover, its auto-ignition temperature falls much below that of ¹H₂ (232 °C versus 500 °C). This indicates that, insertion of sulfur atom into the ¹H₂ molecule significantly raises its hazardous nature. With respect to ¹CS₂, its flash point matches that of gasoline at -43 °C, while its auto-ignition temperature exceeds that of white phosphorous, but only by 56 °C. Compared to the hydrocarbon species, reduced sulfur compounds induce significant fire hazards of fossil fuels.

Table 1: Comparison of flammability properties of H₂S and CS₂ with other highly-flammable species.

Fuel type	Flash point (°C)	Auto-ignition temperature (°C)
White phosphorous (P)	n.a.	34
Hydrogen (H ₂)	n.a.	500
Hydrogen sulfide (H ₂ S)	-82	232
Carbon disulfide (CS ₂)	-43	90
Ethanol (C ₂ H ₅ OH)	17	365
Gasoline	-43	280

As important feedstock in the manufacturing of fibres [14] and fertilisers [15], sulfur-containing species initiated several factory [11, 16] and transportation [17] fires. Fire accidents of flammable chemicals usually involve significant fatalities, and economic and productivity losses. Moreover, these fires induce explosions and contaminate surrounding areas with toxic products of incomplete

combustion. Once released into air through oxidation, sulfur species convert to SO_x , mainly as sulfur dioxide [18, 19]. Beside its well-known role as a potent greenhouse gas, $^1\text{SO}_2$ reacts with $^3\text{O}_2$ and water to be returned to the Earth's surface as acid rain.

This review investigates the fire hazard of $^1\text{H}_2\text{S}$ and $^1\text{CS}_2$ by scrutinising their detailed oxidation mechanism. We carefully examine the reactions ensuing between sulfur species and oxygen from experimental and quantum chemistry perspectives. The underlying focus in this review is to survey chemical phenomena behind high flammability of sulfur-containing species. The review concludes by summarising pertinent knowledge gaps and proposing future research directions to consolidate our current understanding of a rather complex combustion chemistry of sulfur.

2. Hydrogen Sulfide (H_2S)

2.1 Flammability and oxidation mechanism of H_2S

As illustrated in the introduction, H_2S features a low flash point of $-82\text{ }^\circ\text{C}$ and an auto-ignition temperature that resides at $232\text{ }^\circ\text{C}$. Under ambient conditions in mixtures with air, the explosion limit of H_2S extends from 4.3 % to 46 % [20, 21]. The low ignition temperature and the wide range of explosion limits of H_2S clearly identify it as a chemical that exhibits extreme fire-hazard properties. Yet, until present, realistic predictions of this properties have fallen outside capabilities of the kinetic mechanisms of oxidation of H_2S .

Cullis and Mulcahy (1972) conducted the first comprehensive review of the combustion of H_2S [22]. This seminal work surveyed early low-temperature photolysis experiments and flame studies and proposed the consumption channels of H_2S to form a wide array of intermediates, such as ^2SH , ^3SO , $^3\text{SO}_3$, ^3S , $^3\text{S}_2$, ^2OH and $^2\text{HO}_2$, leading to the final products of $^1\text{SO}_2$ and H_2O . However, due to the lack of reliable kinetic parameters for some key reactions and thermochemical data for several species, robust validation of the proposed mechanism remained largely impractical.

A further study by Gargurevich [23] summarised some early work on kinetics of sulfur chemistry and also estimated the rate parameters for some missing steps to resolve the role of H_2S in the Claus process. A subsequent investigation of Hughes et al. [24] discussed the uncertainties underlying the key reaction steps, such as $^3\text{SO} + ^2\text{OH}$ and $^1\text{SO}_2 + ^2\text{H}$. Realising the importance of ^2SH , ^3S and ^3SO radical species in the mechanism, Tsuchiya et al. [25] measured the reaction rates of three critical elementary reactions: $^2\text{SH} + ^3\text{O}_2$, $^3\text{S} + ^3\text{O}_2$ and $^3\text{SO} + ^3\text{O}_2$ in shock-tube experiments within a high-temperature window of 1000 to 1600 K. Cerru et al. [26, 27] developed a reduced combustion mechanism for oxidation of H_2S that extended the radical pool to contain ^2HSS , $^1\text{HSSH}$, ^2HSO and $^2\text{HSO}_2$; here, the word ‘‘reduced’’ means incomplete, as the authors realised that their mechanism may not be complete. However, the authors highlighted the significant

uncertainties germane to reactions involving ^2SH , ^2HSS and $^1\text{HSSH}$, proposing that, an accurate account for the combustion chemistry of $^1\text{H}_2\text{S}$ must consider all reactions corridors that involve these species.

Recent studies of Zhou et al. [28, 29] and Gao et al. [30] have combined experimental work and high-level theoretical calculations to resolve the role of H_2/S_2 system (including ^2SH , ^2HSS and $^1\text{HSSH}$) in H_2S oxidation, in which these authors suggested a reaction process that crosses over between triplet and singlet potential-energy surfaces. The updated mechanism results in a satisfactory agreement with further experimental validation in a vertical tubular flow reactor at 950 – 1150 K under atmospheric pressure [31]. Song et al. further expanded the experiments using a flow reactor operated under high pressure of 30 and 100 bar [32], and interpreted the results based on Zhou's et al. mechanism under ambient pressure [31]. Song' et al. [32] performed their experiments in high-pressure tubular reactor to ensure the plug-flow condition. For this reason, they revised rate parameters for certain reactions ($\text{SH} + \text{O}_2$, $\text{HSO} + \text{O}_2$, $\text{HSS} + \text{O}_2$) to allow the kinetic mechanism, developed to operate under atmospheric conditions, to fit their experimental measurements. The reaction of $^2\text{SH} + ^2\text{SH}$ produces either $^1\text{H}_2\text{S} + ^3\text{S}$ (chain propagation) or $^1\text{HSSH}$ (chain termination) signifying a chief step during the oxidation of $^1\text{H}_2\text{S}$.

Figure 1 summarises the key consumption steps for $^1\text{H}_2\text{S}$ oxidation based on the studies mentioned above. In the next section, we will discuss each step (Reactions R1 – R6) in light of accurate quantum chemistry calculation that introduce the likely occurrence of intersystem crossing to elucidate the experimentally-observed excessive flammability of $^1\text{H}_2\text{S}$.

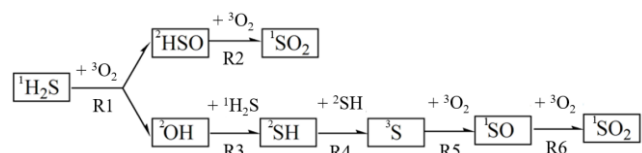
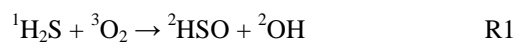


Figure 1. Key oxidation steps that operate in the combustion of $^1\text{H}_2\text{S}$.

2.2 Intersystem crossing for key elementary steps

For the chain initiation step R1 ($^1\text{H}_2\text{S} + ^3\text{O}_2$), Montoya et al. [33] have conducted quantum chemistry calculation at the G2 level of theory [34]. A direct H abstraction by the ground-state O_2 molecule incurs a sizable activation energy of 168.8 kJ/mol at 0 K via the transition structure TSb as Fig. 2 demonstrates. However, the products of this reaction reside approximately at the same energy level as the transition state, suggesting that the reaction proceeds in reverse; i.e., by ^2SH abstracting H from $^2\text{HO}_2$. It is more likely that, the reaction involves an intersystem-crossing process, as described in Reaction R1 and depicted in Fig. 2



By considering the reaction between H₂S and singlet ¹O₂, Montoya et al. [33] found an insertion channel through a spin-forbidden formation of SOOH, i.e., four-member ring as the transition state, yielding ¹HOOSH as an intermediate. This intermediate further dissociates into ²HSO and ²OH, acting as a chain branching step. A crossing point between singlet and triplet reaction pathway allows the initial reactants on the triplet surface to transit onto the singlet reaction pathway. The singlet ¹HOOSH adduct falls into an energy well of 15.8 kJ/mol in comparison to the initial triplet reactants ¹H₂S + ³O₂, and 49 kJ/mol below the separated products of ²HSO and ²OH; i.e., it displays significant stability. While Montoya et al. [33] proposed the ISC process without locating the crossing point, Zhou et al. [31] estimated the ISC barrier as 147 kJ/mol, based on the experimental results from a tubular-flow reactor.

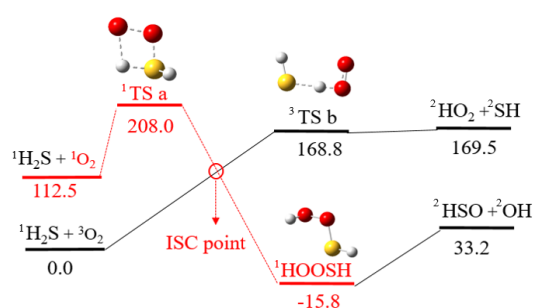
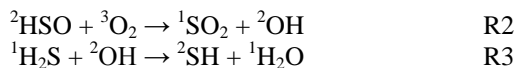


Figure 2. Potential enthalpy surface for ¹H₂S + ³O₂ calculated with G2 method at 0 K by Montoya et al. [33]. All energy values (in kJ/mol) are in reference to the initial reactants of ¹H₂S + ³O₂.

The subsequent consumption process of ²HSO has not been investigated in detail, with no known potential surface in literature. The sole estimation from Zhou et al. [31], for Reaction R2, suggests an activation energy at 27.6 kJ/mol to produce ¹SO₂ and ²OH. Herein, we envisage that a four-centred transition state, i.e., a four-member ring of ¹HOOSO forms to produce ²OH and ²SO₂. The emerging ²OH radical readily extracts one hydrogen atom from H₂S via a trivial activation energy at 4.2 kJ/mol (Reaction R3), as calculated by Ellingson and Truhlar [35].



Tsuchiya et al. [25] performed the direct measurement of the kinetics of the reaction of ²SH + ³O₂ in shock-tube experiments. They fitted the activation energy of 75 kJ/mol in a temperature range from 1400 to 1700 K. The theoretical calculation of Zhou et al. [36] at ground state (triplet pathway) predicted the formation of ³SO + ²OH and ²HSO + ³O via activation barriers at 81 kJ/mol and 89 kJ/mol at 0 K, respectively. However, an activation barrier of 75 - 89 kJ/mol is still remarkable for a chain-branching process, leading us to consider other pathways to propagate the radicals.

Theoretical calculation conducted by Zhou et al. [28, 29] with consideration of ISC offers a new channel for SH

conversion. As depicted in Fig. 3, the triplet reaction pathway displays an activation barrier at 23.7 kJ/mol at 0 K, much lower than that of Reactions R4a and R4b. ²SH abstracts H from another ²SH to produce ¹H₂S and ³S atom. An alternative path is provided through the singlet pathway. Direct combination of two SH radicals produces singlet ¹HSSH that converts to singlet ¹H₂SS by H migration between the S atoms. Subsequent fission of S-S bond and intersystem crossing from singlet to triplet surface result in ¹H₂S and ³S in ground state as final products. A further experimental study by Gao et al. [30] confirms that, the ISC channel dominates the reaction pathway under low temperature (< 800 K) with an estimated activation energy at 3 kJ/mol, while the triplet pathway governs the reaction above 1000 K. This channel plays an important role in chain propagation to produce a S atom, via a significantly low activation barrier.

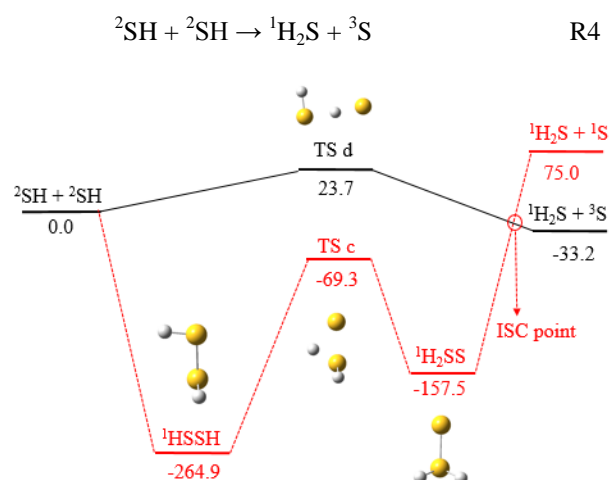
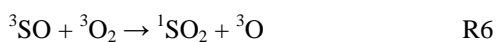


Figure 3. Potential energy surface for ²SH + ²SH at 0 K calculated by Zhou et al. [29]. All energy values are in reference to initial reactants ²SH + ²SH, in kJ/mol.

Further interaction between ³S and ³O₂ generates ³SO and ³O. This channel exhibits a substantial influence on the H₂S oxidation to produce SO₂. Lu et al. [37] reported results from combined experimental measurements and theoretical calculations. Profiles of product species reveal that, the S + ³O₂ reaction demonstrates different temperature dependence for low ($T < 1000$ K, $E_a < 3$ kJ/mol) and high ($T > 1000$ K, $E_a > 30$ kJ/mol) temperature range. The behaviour of the ³S + ³O₂ reaction is similar to that of the SH + SH reaction discussed above. Computational work of the same researchers, performed at the G2M level of theory, has also explored other possible reaction pathways. Lu et al. [37] calculated the potential surfaces for S + O₂ reactions separately on singlet and triplet surfaces, without pointing out the crossing-over between the two reaction surfaces (ISC). The reaction, proceeding on a singlet surface, represents the only channel that can account for the low-temperature oxidation. At temperatures higher than 1200 K, the triplet pathway dominates the overall ³S + ³O₂ reaction (Reaction R5).



Tsuchiya et al. [25] observed similar behaviour for the reaction of $^3\text{SO} + ^3\text{O}_2$ (Reaction R6), concluding that, the activation energy of this corridor resides 34.0 kJ/mol above the separated reactants within a temperature range of 1130 – 1640 K. However, for lower temperatures of 250 – 585 K, the activation energy corresponds to 19.0 kJ/mol, as reported by Garland [38]. This significant discrepancy may also originate from an ISC phenomenon operating in the low temperature window of Reaction R6. No theoretical calculation has been conducted for $^3\text{SO} + ^3\text{O}_2$ and we found no potential energy surface for Reaction R6 in literature.



The inclusion of ISC processes leads to significant lowering of the activation energy for key elementary reactions that proceed in the oxidation of H_2S . The updated mechanism (that includes the ISC pathway) results in a satisfactory agreement with experimental measurements obtained from a vertical tubular flow reactor operated below 1150 K under atmospheric pressure [31]. To summarise, the low activation barriers for reactions between H_2S and O_2 , caused by the unusual ISC process, results in the remarkable flammability of H_2S . As we pointed out above, the plausible occurrence of the ISC process in $\text{HSO} + \text{O}_2$, $\text{SH} + \text{O}_2$ and $\text{SO} + \text{O}_2$ reactions warrants further investigations.

3. Carbon Disulfide (CS_2)

3.1 Flammability and oxidation mechanism of CS_2

Myerson and Taylor [39] extensively studied the ignition of $^1\text{CS}_2$ - $^3\text{O}_2$ mixtures as an extremely flammable chemical, as a representative case for branched-chain reactions. They demonstrated that, a mixture containing as little as 0.03 % (by mol) CS_2 in oxygen ignites at 80 °C and 0.05 bar, resulting in sustained appearance of cool flames. Once ignited, a cool flame propagates through the mixture at 55 °C, with the temperature rise in the flame of less than 15 °C. The most important oxidation products comprise ^1CO , $^1\text{SO}_2$, $^1\text{CO}_2$, ^1CS and ^3SO , as well as ^1COS . Intermediates such as ^3SO , ^3S and ^3O appear much more reactive than ^1COS and ^1CS [40], as inferred from low concentration of ^3SO , ^3S and ^3O in the reacting system.

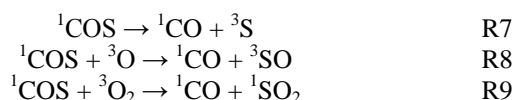
Hanst and Myerson [41] were the first researchers who studied the kinetics of the explosive combustion of CS_2 . They applied the absorption spectroscopy to follow the variations in the concentrations of radical and molecular species during the explosion of $^1\text{CS}_2$. The $^1\text{CS}_2$ - $^3\text{O}_2$ mixture, initially heated to between 190 °C and 300 °C, exploded spontaneously. Strong and continuous absorptions confirmed the formation of ^3SO and ^1CS with the appearance of $^1\text{SO}_2$ in the early stages of the explosions [42]. Spectroscopic techniques also served to investigate explosions of CS_2 initiated by shock waves [43] and flash photolysis [44]. In both cases, $^1\text{CS}_2$ oxidised mainly to ^3SO , $^1\text{SO}_2$ and ^1CO . However, experimental measurements on slow and explosive combustion of $^1\text{CS}_2$ have not contributed much insight into mechanisms governing its

oxidation, as researchers only reported the final products at particular low-temperature ranges.

Along the same line of enquiry, Azatyan et al. [45] studied a low pressure flame of $^1\text{CS}_2$ to probe the high-temperature combustion mechanism, with the electron spin resonance (ESR) technique to detect ^1O , ^1CS and ^3SO as intermediates. By analysing the relationship between ^3O and ^3SO in experiments, the authors proposed the formation of ^1COS as a major conversion channel between O and SO with the reaction: $^1\text{COS} + ^3\text{O} \rightarrow ^1\text{CO} + ^3\text{SO}$. To confirm the occurrence of this reaction, the authors added small amounts of ^1COS to the $^1\text{CS}_2$ flames, in a temperature interval of 350 °C to 600 °C. They reported a lower accumulation of ^3O and an increased yield of ^3SO , validating the profound influence of ^1COS on the oxidation of $^1\text{CS}_2$.

Homman et al. [46] deployed the isothermal flow reactor to study the combustion of $^1\text{CS}_2$ in an excess of $^3\text{O}_2$ at 927 °C and 0.4 bar. They confirmed the presence of ^1COS in the oxidation process of $^1\text{CS}_2$. In order to describe their experimentally-observed profiles of product species, they constructed a reduced kinetic model that included ^1COS as an intermediate, concluding that the reaction of $^1\text{CS}_2 + ^3\text{O} \rightarrow ^1\text{COS} + ^3\text{S}$ affords the production of ^1COS .

Glarborg and Marshall [47] have recently proposed a detailed oxidation mechanism of ^1COS based on evaluation of experimental measurements from literature, and then studied its predictions with kinetic modelling. For the consumption of ^1COS , the authors considered three pathways:



For thermal decomposition process ($^1\text{COS} \rightarrow ^1\text{CO} + ^3\text{S}$), a high activation energy at 260 kJ/mol, fitted from their experimental measurement over a high temperature window of 1900 – 3230 K [47], makes the process too slow to account for the conversion of COS . The ^1COS interaction with atomic oxygen (R8: $^1\text{COS} + ^3\text{O} \rightarrow ^1\text{CO} + ^3\text{SO}$) presents the major consumption channel for COS . The authors fitted the rate parameters based on the experimental measurements of Homman et al. [46] around 1270 K, indicating an activation energy at 21.8 kJ/mol. The dominant products are $^1\text{CO} + ^3\text{SO}$, while $^1\text{CO}_2 + ^3\text{S}$ could form at higher temperature. In the absence of atomic O for the chain initiation, the activation energy for the reaction between COS and O_2 , R9 ($^1\text{COS} + ^3\text{O}_2 \rightarrow ^1\text{CO} + ^1\text{SO}_2$) amounts to 134.4 kJ/mol.

Furthermore, to evaluate their mechanism, Glarborg and Marshall [47] have compared prediction of their model on oxidation of ^1COS with analogous experimental measurements obtained from studies involving batch, flow reactors [46] and shock tubes [48]. Although the proposed mechanism of oxidation of ^1COS captured well the experimental profiles measured by Homman et al. [46] of

major species quantitated at the outlet of a tubular flow reactor, the reaction onset required a slight correction. Chiang et al. recognised the sensitivity of the overall mechanism to the reaction of $^1\text{COS} + ^3\text{O}$ and proposed the appearance the intersystem crossing from triplet to singlet surface [49].

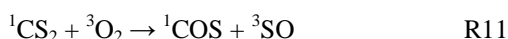
Howgate and Barr [50] attempted to construct the first detailed kinetic model for $^1\text{CS}_2$ oxidation to represent the $^1\text{CS}_2$ - $^3\text{O}_2$ flame. The authors included a direct interaction between $^1\text{CS}_2$ and $^3\text{O}_2$ to produce ^1CS and $^1\text{SO}_2$ to account for the chain initiation with an activation energy at 179.5 kJ/mol. Further investigation by Hardy and Gardiner [51] adopted this chain initiation step in the oxidation mechanism and achieved satisfactory agreement with their experimental measurement for the ignition delay time of CS_2 in shock-tube experiments. The subsequent studies of Saito et al. [52] and Murakami et al. [53], involving shock-tube experiments, led to the estimation of the activation energy of the reaction $^1\text{CS}_2 + ^3\text{O}_2$ as 134.5 kJ/mol and 130.0 kJ/mol, respectively.



Recently, Glarborg et al. [54] formulated a kinetic model for oxidation of $^1\text{CS}_2$, applying quantum-chemical calculations to determine the rate constants for the key reactions of $^1\text{CS}_2/^1\text{CS} + ^3\text{O}_2$. The present authors have also updated the mechanism of oxidation of $^1\text{CS}_2$ with the results of ISC calculations to explain the flammability of $^1\text{CS}_2$ [55, 56]. Figure 4 outlines the key consumption channels for $^1\text{CS}_2$ oxidation based on the studies mentioned above. In the next section, we will discuss each step (Reactions R8 – R13) based on results from quantum-chemical computations and will introduce the intersystem crossing to explain the flammability of $^1\text{CS}_2$.

3.2 Intersystem crossing for key elementary steps

For the reaction of $^1\text{CS}_2 + ^3\text{O}_2$, Glarborg et al. [54] investigated the corridors on both the triplet and singlet surfaces, and concluded the products to comprise ^1COS and ^3SO instead of formation of ^1CS and $^1\text{SO}_2$.



As depicted in Fig. 5, the triplet pathway of $^1\text{CS}_2 + ^3\text{O}_2$ climbs to form the $^3\text{CS}_2\text{O}_2$ adduct, which then dissociates into ^1COS and ^3SO via a barrier of 223 kJ/mol. However, the singlet oxidation offers an alternative pathway that operates via a significantly lower activation barrier. Compared to the triplet $^3\text{CS}_2\text{O}_2$ structure that features a strong O-O bond, the singlet SOOCS adduct forms via the dissociative addition of oxygen atoms at C and S atom requiring a profoundly reduced barrier. By locating the cross-over between the energy surfaces of triplet and singlet corridors, we have estimated the crossing point to reside 145 kJ/mol above the separated reactants of $^1\text{CS}_2$ and $^3\text{O}_2$ and the triplet surface, which coincides with the

experimentally interpreted values from the shock-tube experiments (130.0 – 179.5 kJ/mol) [51-53].

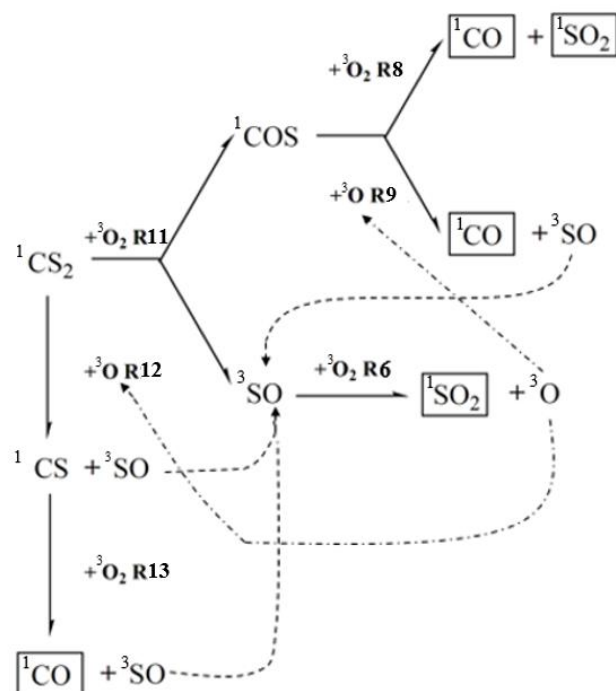


Figure 4. Oxidation pathways of $^1\text{CS}_2$ with formation of ^1COS . The initiation step constitutes $^1\text{CS}_2 + ^3\text{O}_2$ while the final products amount to ^1CO and $^1\text{SO}_2$.

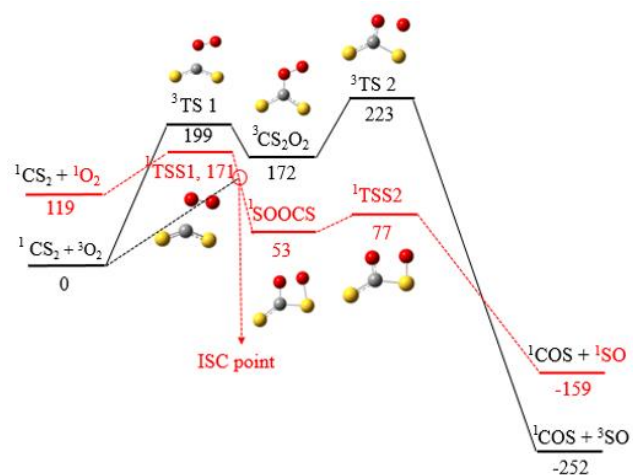
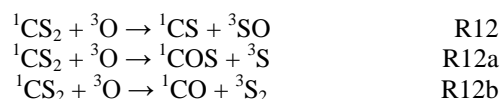


Figure 5. Potential energy surface for $^1\text{CS}_2 + ^3\text{O}_2$ calculated by Glarborg et al. [57]. All energy values are in reference to initial reactants $^1\text{CS}_2 + ^3\text{O}_2$, in kJ/mol.

With the formation of ^3SO through Reaction R11, its contact with $^3\text{O}_2$ (Reaction R6) gives ^3O as the most important chain carrier. The subsequent reaction between $^1\text{CS}_2$ and ^3O proceeds through three reaction passageways, resulting in products of $^1\text{CS} + ^3\text{SO}$, $^1\text{COS} + ^3\text{S}$ and $^1\text{CO} + ^3\text{S}_2$.



An experimental study using a fast flow reactor concluded that, the formation of ${}^1\text{CS} + {}^3\text{SO}$ dominates the overall process, with only small generation of ${}^1\text{COS} + {}^3\text{S}$ and ${}^1\text{CO} + {}^3\text{S}_2$ [58]. However, theoretical calculations on the triplet surface support just the formation of ${}^1\text{CS} + {}^3\text{SO}$, with a small activation energy at 4.2 kJ/mol. To produce ${}^1\text{COS} + {}^3\text{S}$ or ${}^1\text{CO} + {}^3\text{S}_2$, the reactions must overcome higher barriers of 41.3 kJ/mol and 33.2 kJ/mol, respectively, as shown in Fig. 6 [58]. Thus, both reactions should be negligible when contrasted with the formation of ${}^1\text{CS} + {}^3\text{SO}$ [59]. Here, we would like to suggest possible singlet reaction pathways to account for the formation of ${}^1\text{COS} + {}^3\text{S}$ and ${}^1\text{CO} + {}^3\text{S}_2$ [60], as detected in experiments.

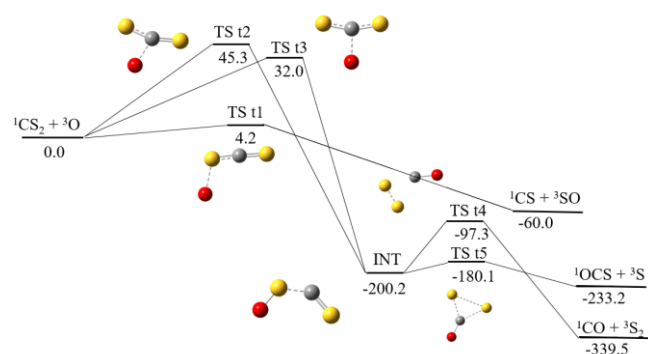


Figure 6. Potential energy surface calculated in this work for ${}^1\text{CS}_2 + {}^3\text{O}$ reaction [58]. Relative enthalpies are in kJ/mol at 298.15 K.

As calculated by Glarborg et al. [54], ${}^3\text{O}_2$ consumes ${}^1\text{CS}$ with an activation energy of 117.5 kJ/mol on the triplet surface. From their shock-tube experiments, Murakami et al. reported the activation energy of R10 as 51.0 ± 61.7 kJ/mol [53]. Bearing in mind a significant uncertainty in experiments and high activation barrier incurred by the triplet corridors, we consider the occurrence of ISC for R13:



Figure 7 illustrates our calculated reaction rate constant for Reaction R13 [55] along with the available experimental measurements from literature. The calculated activation barrier in case of the triplet oxygen corresponds to 110.0 kJ/mol, which compares well with the analogous value reported by Glarborg et al. [57] of 117.5 kJ/mol. The addition of singlet ${}^1\text{O}_2$ onto ${}^1\text{CS}$ leads to the formation of the ${}^1\text{OCSO}$ adduct, which resides 129 kJ/mol below the separated reactants of ${}^1\text{CS}$ and ${}^1\text{O}_2$. Climbing through a trivial barrier of 29 kJ/mol, the ${}^1\text{OCSO}$ adduct dissociates to ${}^1\text{CO}$ and ${}^1\text{SO}$.

From their shockwave-tube experiments, Murakami et al. reported the activation energy, albeit within a large error bound, for the reaction of ${}^1\text{CS}$ and ${}^3\text{O}_2$ of 51.0 ± 61.7 kJ/mol [61]. Abián et al. increased this value to 79.2 kJ/mol in order to improve comparison between experimental and modelled concentration of product species [62]. All these values fall significantly below those of the conventional triplet pathway calculated in our

previous work (110 kJ/mol) [55]. In light of these experimental measurements and empirical fitting of rate constants, we conclude that, the reaction ${}^1\text{CS} + {}^3\text{O}_2$ proceeds through intersystem crossing with an estimated crossing point located 82 kJ/mol above the separated reactants of ${}^1\text{CS}$ and ${}^3\text{O}_2$.

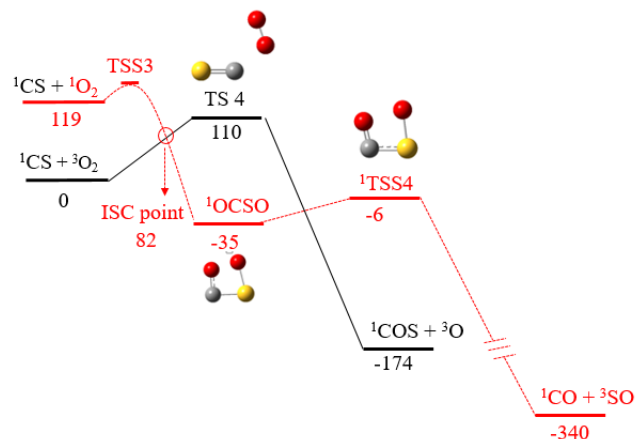


Figure 6. Potential energy surface calculated in this work for ${}^1\text{CS} + {}^3\text{O}_2$ reaction [55]. Relative enthalpies are in kJ/mol at 298.15 K.

In general, the mechanism proposed by Glarborg et al. [54] produces predictions that concur well with experimental results pertinent to ignition delays and explosion limits of CS_2 . However, the mechanism tends to over-predict the concentration of species under low temperature conditions, especially with respect to measurements from flow reactors [62] and shock tubes [53]. Our recent work has introduced ISC pathways to the key elementary reactions ${}^1\text{CS} + {}^3\text{O}_2$, ${}^1\text{CS}_2 + {}^3\text{O}_2$, ${}^1\text{S} + {}^3\text{O}_2$ and ${}^1\text{SO} + {}^3\text{O}_2$ and reduced the ignition temperature by 260 K to achieve very good agreement with the experimental results as demonstrated in Fig. 8 [55].

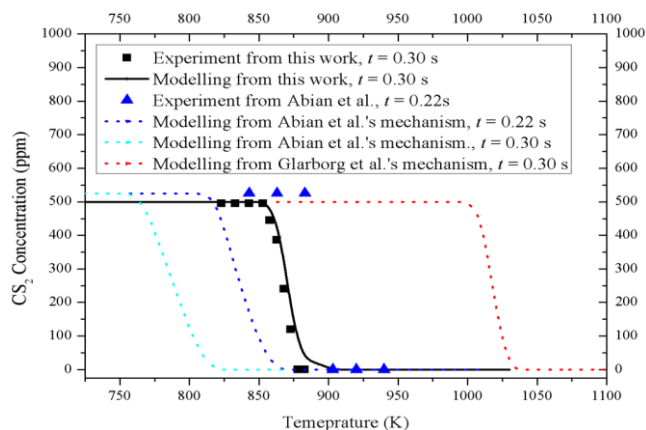


Figure 7. Comparison between our experimental results (■) for CS_2 consumption with the corresponding laboratory measurements of Abián et al. [62] (▲) and modelling profile based on mechanism of Abián et al. [62], Glarborg et al. [54] and our updated mechanism [55].

To link the oxidation mechanisms presented herein with the fire-hazard behaviour of sulfur species, Table 2 compares the laminar burning velocity of ${}^1\text{H}_2\text{S}$ and ${}^1\text{CS}_2$ with those of

$^1\text{CH}_4$, $^1\text{C}_2\text{H}_2$, $^1\text{C}_2\text{H}_4$, $^1\text{C}_2\text{H}_6$ and $^1\text{H}_2$. Even as H_2 displays an extreme fire hazard, the burning velocity of $^1\text{CS}_2$ exceeds that of H_2 . Please note that, we have modelled the laminar burning velocity of CS_2 and H_2S with mechanisms available in references [32, 56] and transport data estimated by the Reaction Mechanism Generator (RMG) [63]. We have also demonstrated that, the oxidation of $^1\text{H}_2\text{S}$ and $^1\text{CS}_2$ incurs low activation energies that mark their chain initiation steps. This explains the extraordinary fire hazard of the reduced sulfur species.

Table 2. Comparison of flat flame speed among $^1\text{CH}_4$, $^1\text{C}_2\text{H}_2$, $^1\text{C}_2\text{H}_4$, $^1\text{C}_2\text{H}_6$, $^1\text{H}_2$, $^1\text{H}_2\text{S}$ and $^1\text{CS}_2$ under ambient pressure, along with the activation energy of the initiation step for each species.

Fuel type	E_a (kJ/mol)	S_L (cm/s)	Source
CH_4	238	40	[72]
C_2H_2	312	136	[73]
C_2H_4	241	67	[74]
C_2H_6	214	41	[75]
H_2	182	210	[76]
H_2S	147	272	modelling
CS_2	135	244	modelling

4. The occurrence of intersystem crossing (ISC) process in sulfur species

Intersystem crossing processes usually occur when vibrational levels of the two excited states overlap, as the transition entails little or no energy gained or lost in this situation. As the orbital coupling in such molecules are substantial and a change in spin is thus more favourable, intersystem crossing arises most commonly in heavy-atom molecules. Compared to traditional C/H/O/N combustion systems, the reduced sulfur species involving heavy atom (S) exhibit higher propensity for the ISC between different electronic states. Especially, for reactions between sulfur species and oxygen, such as the above-discussed $^1\text{H}_2\text{S} + ^3\text{O}_2$, $^1\text{CS}_2 + ^3\text{O}_2$, $^3\text{S} + ^3\text{O}_2$, $^3\text{SO} + ^3\text{O}_2$ and $^1\text{CS} + ^3\text{O}_2$, the ISC processes dominate in the low to medium temperature range (< 800 K). Oxygen and sulfur belong to the same group in periodic table, i.e., they share similar distribution of the outermost electrons. Oxygen atoms carry six electrons located in $2s^2 2p^4$ orbitals while sulfur atoms comprise six electrons located in $3s^2 3p^4$ orbitals. In the p orbitals, two of the four electrons have to be paired, while the last two could be unpaired to assume the triplet state or be paired to give a higher-energy singlet state. The similarities between S and O atom assist in the conversion of triplet into singlet adducts when they couple with each other in reactions, i.e., intersystem crossing process (ISC) as discussed in sulfur oxidations [55].

5. Conclusions

This contribution has reviewed the presently known insights into the reaction that occur in the oxidation of $^1\text{H}_2\text{S}$ and $^1\text{CS}_2$ and may involve intersystem crossing (ISC),

explaining the extreme flammability behaviour of these species. Throughout this article, we have illustrated low activation barriers for several key elementary reactions, most notably, chain initiation ($^1\text{H}_2\text{S} + ^3\text{O}_2$ and $^1\text{CS}_2 + ^3\text{O}_2$) and chain propagation ($^2\text{SH} + ^2\text{SH}$, $^3\text{S} + ^3\text{O}_2$, $^3\text{SO} + ^3\text{O}_2$ and $^1\text{CS} + ^3\text{O}_2$). However, studies that report safety properties and combustion mechanisms of reduced sulfur species are rather limited. Sophisticated experimental techniques, such as MBMS and synchrotron VUV photon ionisation MS could be applied to identify the electronic state of captured species in the combustion medium of the target reduced sulfur species. Theoretically, more detailed calculations need to be carried out to map out potential energy surfaces (PES) for singlet and triplet reactions networks. Characterisation of overlapping the two PESs using multi-reference characters methods may enable to locate the crossing points accurately.

6. Acknowledgments

This study was funded by the Australian Research Council and supported by grants of computing time from the National Computational Infrastructure (NCI), Canberra, Australia and the Pawsey Supercomputing Centre, Perth, Australia. Z. Zeng thanks Shell Global Solution for the award of research grant.

7. References

- [1] A. Williams, J. Jones, L. Ma, M. Pourkashanian, Pollutants from the combustion of solid biomass fuels, *Progress in Energy and Combustion Science* 38 (2012) 113-137.
- [2] G. Huffman, S. Mitra, F. Huggins, N. Shah, S. Vaidya, F. Lu, Quantitative analysis of all major forms of sulfur in coal by X-ray absorption fine structure spectroscopy, *Energy & Fuels* 5 (1991) 574-581.
- [3] C.-L. Chou, Sulfur in coals: A review of geochemistry and origins, *International Journal of Coal Geology* 100 (2012) 1-13.
- [4] D. Huo, The Global Sour Gas Problem. <https://sej.stanford.edu/global-sour-gas-problem> (accessed 20 Sep 2019).
- [5] G. Hammer, T. Lübcke, R. Kettner, M.R. Pillarella, H. Recknagel, A. Commichau, H.J. Neumann, B. Paczynska-Lahme, Natural gas, Ullmann's Encyclopedia of Industrial Chemistry, (2000).
- [6] L. Chen, S. Bhattacharya, Sulfur emission from Victorian brown coal under pyrolysis, oxy-fuel combustion and gasification conditions, *Environmental Science & Technology* 47 (2013) 1729-1734.
- [7] Material Safety Data Sheet, Carbon Disulfide,, in: Cogee Chemicals (Ed.).
- [8] F. Taylor, A. Myerson. First limit induction time studies of $\text{CS}_2 - \text{O}_2$ explosions. In. Symposium (International) on Combustion; 1958: Elsevier. p. 72-79.
- [9] Five Injured at Sulfur Storage Mound Fire in Port Manatee, Florida. <https://dustsafetyscience.com/five-injured-at-sulfur-storage-mound-fire-in-port-manatee-florida/> (accessed 25/08/2019).
- [10] G.M. Bodner, Lecture demonstration accidents from which we can learn, *Journal of Chemical Education* 62 (1985) 1105.
- [11] S. Chittora, A.K. Dwivedi, Recent trends in safety management system in carbon disulfide plant: a review, *Journal of Industrial Pollution Control*, 29 (1970) 219-222.
- [12] Z. Zeng, B.Z. Dlugogorski, I. Oluwoye, M. Altarawneh, Co-oxidation of methane (CH_4) and carbon disulfide (CS_2), *Proceedings of the Combustion Institute* 37 (2019) 677-685.
- [13] Z. Zeng, M. Altarawneh, I. Oluwoye, P. Glarborg, B.Z. Dlugogorski, Inhibition and Promotion of Pyrolysis by Hydrogen Sulfide (H_2S) and Sulfanyl Radical (SH), *The Journal of Physical Chemistry A* 120 (2016) 8941-8948.
- [14] P.W. Sherwood, Raw materials for man-made fibers, *Industrial & Engineering Chemistry* 55 (1963) 37-42.

- [15] F. Zhao, M. Hawkesford, S. McGrath, Sulphur assimilation and effects on yield and quality of wheat, *Journal of Cereal Science* 30 (1999) 1-17.
- [16] A. Potenza, This blue sulfur hellfire in Wyoming is mesmerizing — and toxic. <https://www.theverge.com/2017/7/10/15947592/sulfur-mound-fire-video-worland-wyoming> (accessed 25/08/2019).
- [17] M.P. Praveen, Safety takes a back seat in transportation of chemicals. <https://www.thehindu.com/news/cities/Kochi/Safety-takes-a-back-seat-in-transportation-of-chemicals/article16091178.ece> (accessed 23 Oct 2019)
- [18] C. Vovelle, *Pollutants from combustion: formation and impact on atmospheric chemistry*, Springer Science & Business Media 2013.
- [19] Z. Zeng, M. Altarawneh, B.Z. Dlugogorski, Atmospheric oxidation of carbon disulfide (CS₂), *Chemical Physics Letters* 669 (2017) 43-48.
- [20] P. Gray, M.E. Sherrington, Explosive oxidation of hydrogen sulphide: self-heating, chain-branching and chain-thermal contributions to spontaneous ignition, *Journal of the Chemical Society, Faraday Transactions 1: Physical Chemistry in Condensed Phases* 70 (1974) 2338-2350.
- [21] R. Pahl, K. Holtappels, Explosions Limits of H₂S/CO₂/Air and H₂S/N₂/Air, *Chemical Engineering & Technology: Industrial Chemistry- Plant Equipment- Process Engineering- Biotechnology* 28 (2005) 746-749.
- [22] C. Cullis, M. Mulcahy, The kinetics of combustion of gaseous sulphur compounds, *Combustion and Flame* 18 (1972) 225-292.
- [23] I.A. Gargurevich, Hydrogen sulfide combustion: Relevant issues under Claus furnace conditions, *Industrial & Engineering Chemistry Research* 44 (2005) 7706-7729.
- [24] K. Hughes, M. Blitz, M. Pilling, S. Robertson, A master equation model for the determination of rate coefficients in the H + SO₂ system, *Proceedings of the Combustion Institute* 29 (2002) 2431-2437.
- [25] K. Tsuchiya, K. Kamiya, H. Matsui, Studies on the oxidation mechanism of H₂S based on direct examination of the key reactions, *International Journal of Chemical Kinetics* 29 (1997) 57-66.
- [26] F. Cerru, A. Kronenburg, R. Lindstedt, Systematically reduced chemical mechanisms for sulfur oxidation and pyrolysis, *Combustion and Flame* 146 (2006) 437-455.
- [27] F. Cerru, A. Kronenburg, R. Lindstedt. A comparison of detailed and reduced chemical mechanism for sulphur oxidation. In: *Proceeding of the European Combustion Meeting*; 2005. p. 1227.
- [28] C. Zhou, K. Sendt, B.S. Haynes, Theoretical study of reactions in the multiple well H₂/S₂ system, *The Journal of Physical Chemistry A* 113 (2009) 8299-8306.
- [29] C. Zhou, K. Sendt, B.S. Haynes, Theoretical study of hydrogen abstraction and sulfur insertion in the reaction H₂S + S, *The Journal of Physical Chemistry A* 112 (2008) 3239-3247.
- [30] Y. Gao, C. Zhou, K. Sendt, B.S. Haynes, P. Marshall, Kinetic and modeling studies of the reaction S+H₂S, *Proceedings of the Combustion Institute*, 33 (2011) 459-465.
- [31] C.R. Zhou, K. Sendt, B.S. Haynes, Experimental and kinetic modelling study of H₂S oxidation, *Proceedings of the Combustion Institute* 34 (2013) 625-632.
- [32] Y. Song, H. Hashemi, J.M. Christensen, C. Zou, B.S. Haynes, P. Marshall, P. Glarborg, An exploratory flow reactor study of H₂S oxidation at 30–100 bar, *International Journal of Chemical Kinetics* 49 (2017) 37-52.
- [33] A. Montoya, K. Sendt, B.S. Haynes, Gas-phase interaction of H₂S with O₂: a kinetic and quantum chemistry study of the potential energy surface, *The Journal of Physical Chemistry A* 109 (2005) 1057-1062.
- [34] L.A. Curtiss, K. Raghavachari, G.W. Trucks, J.A. Pople, Gaussian- 2 theory for molecular energies of first- and second- row compounds, *The Journal of Chemical Physics* 94 (1991) 7221-7230.
- [35] B.A. Ellingson, D.G. Truhlar, Explanation of the unusual temperature dependence of the atmospherically important OH + H₂S → H₂O + HS reaction and prediction of the rate constant at combustion temperatures, *Journal of the American Chemical Society* 129 (2007) 12765-12771.
- [36] C. Zhou, K. Sendt, B.S. Haynes, Computational study of the reaction SH+ O₂, *The Journal of Physical Chemistry A* 113 (2009) 2975-2981.
- [37] C.-W. Lu, Y.-J. Wu, Y.-P. Lee, R. Zhu, M. Lin, Experimental and theoretical investigations of rate coefficients of the reaction S (³P) + O₂ in the temperature range 298–878 K, *The Journal of Chemical Physics* 121 (2004) 8271-8278.
- [38] C.M. Vagelopoulos, F.N. Egolopoulos. Direct experimental determination of laminar flame speeds. In: *Symposium (International) on Combustion*; 1998: Elsevier. p. 513-519.
- [39] A.L. Myerson, F.R. Taylor, The ignition limits of 1-3 mixtures of carbon disulfide and oxygen, *Journal of the American Chemical Society* 75 (1953) 4348-4350.
- [40] J. Hardy, W. Gardiner Jr. Shock tube study of carbon disulfide oxidation. In: *Symposium (International) on Combustion*; 1977: Elsevier. p. 985-995.
- [41] P.L. Hanst, A.L. Myerson, Absorption spectroscopy of explosions, *Review of Scientific Instruments* 25 (1954) 469-470.
- [42] A.L. Myerson, F.R. Taylor, P.L. Hanst, Ultraviolet absorption spectra and the chemical mechanism of CS₂-O₂ explosions, *The Journal of Chemical Physics* 26 (1957) 1309-1320.
- [43] D. Sheen, Shock- tube study of the oxidation of carbon disulfide, *The Journal of Chemical Physics* 52 (1970) 648-655.
- [44] J. McGarvey, W. McGrath, Kinetic spectroscopy in the vacuum ultraviolet region I. The dissociation energy of SO and the combustion of hydrogen sulphide, carbon disulphide and carbonyl sulphide, *Proceedings of the Royal Society of London. Series A. Mathematical and Physical Sciences*, 278 (1964) 490-504.
- [45] V. Azatyan, U. Gershenson, E. Sarkissyan, G. Sachyan, A. Nalbandyan. Investigation of low-pressure flames of a number of compounds containing sulfur by the ESR method. In: *Symposium (International) on Combustion*; 1969: Elsevier. p. 989-994.
- [46] G.K. K.H. Homan, H. Wagner, Carbon disulfide oxidation 3: the isothermal oxidation of carbon disulfide, *Berichte der Bunsen-Gesellschaft für Physikalische Chemie* 74 (1970) 74-49.
- [47] P. Glarborg, P. Marshall, Oxidation of reduced sulfur species: carbonyl sulfide, *International Journal of Chemical Kinetics* 45 (2013) 429-439.
- [48] A. Lifshitz, M. Frenklach, P. Schechner, H. Carroll, Shock initiated ignition in COS/O₂/Ar mixtures, *International Journal of Chemical Kinetics* 7 (1975) 753-773.
- [49] H.-C. Chiang, N.-S. Wang, S. Tsuchiya, H.-T. Chen, Y.-P. Lee, M. Lin, Reaction Dynamics of O (¹D, ³P) + OCS Studied with Time-Resolved Fourier Transform Infrared Spectroscopy and Quantum Chemical Calculations, *The Journal of Physical Chemistry A* 113 (2009) 13260-13272.
- [50] D.W. Howgate, T.A.B. Jr., Dynamics of the CS₂-O₂ flame, *The Journal of Chemical Physics* 59 (1973) 2815-2829.
- [51] J. Hardy, W.C. Gardiner, Shock tube study of carbon disulfide oxidation, *Symposium (International) on Combustion* 16 (1977) 985-995.
- [52] K. Saito, Y. Ueda, R. Ito, T. Kakumoto, A. Imamura, Measurements of the bimolecular rate constants for S + O₂ → SO + O and CS₂ + O₂ → CS + SO₂ at high temperatures, *International Journal of Chemical Kinetics*, 18 (1986) 871-884.
- [53] Y. Murakami, M. Kosugi, K. Susa, T. Kobayashi, N. Fujii, Kinetics and Mechanism for the Oxidation of CS₂ and COS at High Temperature, *Bulletin of the Chemical Society of Japan* 74 (2001) 1233-1240.
- [54] P. Glarborg, B. Halaburt, P. Marshall, A. Guillory, J.r. Troe, M. Thellefsen, K. Christensen, Oxidation of reduced sulfur species: carbon disulfide, *The Journal of Physical Chemistry A* 118 (2014) 6798-6809.
- [55] Z. Zeng, B. Z. Dlugogorski, M. Altarawneh, Flammability of CS₂ and other reduced sulfur species, *Fire Safety Journal* 91 (2017) 226-234.
- [56] Z. Zeng, B. Z. Dlugogorski, I. Oluwoye, M. Altarawneh, Combustion chemistry of carbon disulphide (CS₂), *Combustion and Flame* 210 (2019) 413-425.
- [57] P. Glarborg, B. Halaburt, P. Marshall, A. Guillory, J. Troe, M. Thellefsen, K. Christensen, Oxidation of Reduced Sulfur Species: Carbon Disulfide, *The Journal of Physical Chemistry A* 118 (2014) 6798-6809.
- [58] I.R. Slagle, J.R. Gilbert, D. Gutman, Kinetics of the reaction between oxygen atoms and carbon disulfide, *The Journal of Chemical Physics* 61 (1974) 704-709.
- [59] V. Saheb, Quantum chemical and theoretical kinetics study of the O (³P) + CS₂ reaction, *The Journal of Physical Chemistry A* 115 (2011) 4263-4269.
- [60] R.D. Froese, J.D. Goddard, The COS₂ potential energy surface: Aspects of the lowest singlet and triplet potential energy surfaces for the reaction of oxygen atoms with carbon disulfide, *The Journal of Chemical Physics* 98 (1993) 5566-5578.
- [61] Y. Murakami, M. Kosugi, K. Susa, T. Kobayashi, N. Fujii, Kinetics and mechanism for the oxidation of CS₂ and COS at high temperature, *Bulletin of the Chemical Society of Japan* 74 (2001) 1233-1240.
- [62] M. Abián, M. Cebrián, Á. Millera, R. Bilbao, M.U. Alzueta, CS₂ and COS conversion under different combustion conditions, *Combustion and Flame* 162 (2015) 2119-2127.
- [63] C.W. Gao, J.W. Allen, W.H. Green, R.H. West, Reaction Mechanism Generator: Automatic construction of chemical kinetic mechanisms, *Computer Physics Communications* 203 (2016) 212-225.

Recent Progress in the Control and Understanding of Turbulent Spray Formation

Agisilaos Kourmatzis

School of Aerospace, Mechanical and Mechatronic Engineering,
The University of Sydney, NSW 2006, Australia

Abstract

The mechanisms that drive the formation of a spray suitable for combustion are generally well understood on a global level. Despite this, it remains a formidable challenge to be able to accurately predict the full cascade of processes that occur from initial instability formation on the liquid-air interface, to subsequent atomization, dispersion, and evaporation. In this article, some recent work in spray atomization and combustion will be reviewed, highlighting key insights within the context of the broader literature on primary and secondary atomization. The article will firstly provide a succinct summary of recent progress made in the measurement and interpretation of near-field spray dynamics, followed by developments in our understanding of atomization modes. A summary of recent spray burner designs will follow with the objective of highlighting a range of experiments whereby processes of atomization, evaporation, and downstream combustion can all be reliably measured within a single platform.

Keywords: Atomization, Spray Combustion, Turbulent Sprays

1. Introduction

There is consensus that in a simple atomization problem, where a liquid jet is injected into a gas, instabilities lead to the formation of liquid fragments and subsequently droplets [1], with turbulence influencing this process. This simple view becomes increasingly obscured as modifications are made to spraying devices such that twin-fluid mixing can also be induced inside the nozzle, leading for instance to cavitation, or aeration of the liquid jet prior to its ejection from the nozzle. Mechanisms such as effervescent atomization [2] or blurry injection [3] are some of the ways of achieving this, and have proven potential to significantly reduce droplet size with less energy requirements. Regardless of the mode of atomization and its complexity in the near-field, there will initially be a defined liquid-air interface which subsequently becomes increasingly perturbed until it forms into fragments and droplets, leading to thousands of interfaces, which in the near-field of a spray, are highly contorted with a topological evolution that is challenging to predict. This becomes even more complicated for the case of supercritical conditions or flash-evaporating sprays, however these remain beyond the scope of this paper.

Historically, the transition from liquid jet to droplets has been categorized under an initial “primary atomization” process, which transitions to a subsequent “secondary atomization”, with qualitative observations being used to delineate between different regimes [4] in order to aid predictive modeling and analytical understanding. Categorizing atomization in terms of “primary” and “secondary” atomization is a convenience, and while our understanding in this area has improved substantially over the last ~20 years, it is still challenging to predict when all atomization processes are complete for a particular spray. The prediction of even the simplest quantity such as break-up length remains challenging, and this, along with the prediction of the final droplet size of a spray, are two

critical factors that would partly dictate the initiation of a flame, whether through an auto-ignition or forced ignition process [5, 6].

It is understood that instabilities control the formation of many sprays. In laminar sprays, the well-known Rayleigh instability dictates droplet formation, and in situations with shear, the Kelvin-Helmholtz instability becomes dominant [1, 7, 8]. Significant acceleration of liquid fragments at high Weber numbers can see a Rayleigh-Taylor instability become relevant [1]. In effervescent atomization, “bubble explosions” were quoted to be the attributing factor to atomization. However, there is now evidence [9] suggesting that these sprays form due to longitudinal instabilities that cause repeated collisions. Even in electrostatic atomization, it is a Rayleigh instability, modified by Coloumbic repulsion that leads to droplet formation [10]. Therefore, the formation of initial perturbations cannot be ignored. However, the relative competition between various modes of instability, and how they contribute to atomization, remain very poorly understood. It is only in the last few years that we have even begun to resolve how turbulence influences these processes [11], and this has largely been due to developments in experimental methods as well as DNS.

Understanding the processes that govern spray formation is only one part of the picture. Complementing this area is an ability to develop spray injectors that can advantageously make use of certain types of instabilities such that downstream processes can be controlled. Control over the structure of liquid fragments in the near field can affect downstream temperature profiles [12, 13] and, potentially, reaction zone structure growth [14]. Hybridization of atomization modes offers an avenue which would provide designers with more degrees of freedom to control the formation of a spray, and hence influence downstream combustion. This is generally an area which has received very little attention. As an example, the use of longitudinal

instabilities from effervescent atomization in tandem with shear induced instabilities has been proven to improve mixing processes [9] and dampen otherwise persisting downstream instabilities which would have undesirable effects on combustion. Likewise, combination of electrostatic atomization with traditional air-blast atomization has also been recently demonstrated, and given the known effects of electric charge on soot formation [15] this particular method of hybridization may offer an ability to control both atomization and combustion processes in a unique way.

In this brief paper, drawing on research from the University of Sydney Combustion Group, and within the above context, the aim is to provide some insights into i) recent progress made in the imaging and analysis of near-field spray dynamics and instabilities, ii) the implications of turbulence on our description of atomization mechanisms, iii) recent research into the hybridization of atomization modes, and iv) the implications of the near-field of the spray on downstream combustion processes.

2. Near-field spray imaging

There have been a number of recent reviews on developments in experimental techniques for sprays with one standing out in particular [16]. Many of these techniques focus on analyzing the developed spray region downstream of where atomization has been completed, and where combustion starts to take place. This is a region of the spray which is generally occupied by spherical droplets. Traditional techniques such as phase Doppler anemometry (PDA), LIF/Mie, diffraction sizing, rainbow techniques, laser extinction, and other similar methods have been widely used here and reviewed elsewhere [16]. The primary measurement output from these techniques is a statistical droplet size measurement, the precise definition of which will depend on the measurement technique. For instance, laser diffraction usually provides some measure of cumulative volume diameter (e.g. $D_{V,50}$) whereas in LIF/Mie, a measure of Sauter mean diameter (D_{32}) is provided, and it is therefore important for the user to fully understand the differences in diameter measurement provided by different techniques. This can be a common source of error when comparing numerical to experimental data. Another example is comparison of diameter measurements from phase Doppler anemometry (PDA) which provides a point statistic from a time average, and backlight imaging which provides a spatial statistic. Corrections for instance must be made to directly compare diameter measurements from these two methods [17].

The focus of this section will only be on very recent experimental developments on the analysis of atomization of sprays in the near-field. Importantly, here we focus on spray formation where individual liquid fragments such as ligaments and the liquid jet can all be easily identified. For this to be possible, optical densities must be less than $\sim 1-2$, and therefore we are not in a “dense” spray regime. Dense spray imaging techniques, as relevant to high pressure injectors for instance, are not discussed here, however offer significant details on near-field spray core structure which

cannot be provided through more standard methods. The reader is directed to the excellent review of Linne [18] for further information on this.

2.1 High Speed Near-Field Imaging method

The technique which enables direct measurement of atomization processes (not applicable to highly dense sprays) is straight forward so that much of the recent development of this method has been in the image processing methodologies as opposed to the hardware. High speed backlight imaging involves the use of a high-speed camera coupled with a long distance microscope lens. The illumination source needs to be strong enough so as to provide enough light over a $\sim 3 \times 3 \text{mm}$ window and at repetition rates of up to 10-20kHz.

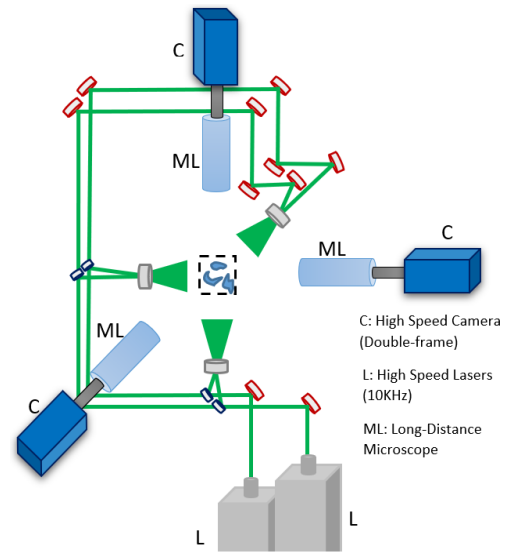


Figure 1: Layout of three-camera high speed backlight illumination

Work using this technique published in [19-21] has used Edgewave lasers (ranging from 15W to 100W) with the beam guided through a series of diffusing optics to illuminate the measurement volume. The QM100 microscope lens used enables a spatial resolution typically from $2 \mu\text{m}$ to $4 \mu\text{m}$ depending on the configuration, with a depth of field that can also vary but is typically $\sim 30 \mu\text{m}$.

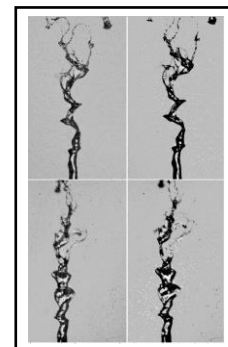


Figure 2: Sample four-frame image of an atomizing liquid jet using the multi-angle illumination method with liquid jet Reynolds number $Re_l=910$, aerodynamic Weber number $We=80$, and mass flux ratio $m=0.01$.

Figure 1 shows one possible configuration of the imaging system with three cameras and two lasers, which would enable three-dimensional measurement of the liquid morphology whilst simultaneously providing a method of tracking fragments in time (as in particle tracking velocimetry (PTV)). This is possible by splitting the original two beams into 3 pairs of beams (using a series of 50/50 and 70/30 splitters), with the two beams in each pair being separated in time by 5-30 μ s.

A sample image using this technique from two cameras and two lenses, operated in “PTV mode” (separation in time (\sim 5 μ s) from left to right and separation in space (90deg) from bottom to top) is shown in Fig. 2. This figure demonstrates the initial formation of instabilities on a liquid jet, as well as its subsequent atomization into fragments. A challenging aspect of this imaging method is correctly identifying the interface between the liquid and the air. Kashdan et al [17, 22] presented a method based on a gradient threshold in order to identify the location of “halos” around individual droplets which was only validated on spherical objects. In [14], a binarization technique is presented, validated against PDA for spherical droplets, which employs a background threshold as a function of the droplet number density. The latter technique is used in all of the multi-angle imaging methods presented by the University of Sydney group and ensures a threshold which minimizes the statistical error of droplets merging together whilst in parallel minimizing the statistical error of truncating the outer periphery of a droplet. This truncation can occur if a droplet is exceedingly de-focused which results in a gradient of intensity across the face of the droplet or fragment that cannot be accurately accounted for using a single binarization threshold. Multi-threshold binarization methods were attempted however resulted in minimal improvements. Despite the limitations of high speed backlight imaging, errors in volume for larger non-spherical fragments (typical of ligaments) were estimated to be of the order of \sim 11% [19], and compared to PDA measurements of SMD, the error was consistently less than 10% [14].

Work by Pham et al. [20] demonstrated that the backlight method using two cameras is also able to accurately measure the local volume flow-rate of a liquid spray containing a high proportion of non-spherical liquid fragments for Weber numbers less than \sim 20 (where a method such as PDA would result in a high rejection rate). This was achieved using an image processing methodology which fits multiple ellipses around individual non-spherical fragments and tracks them through the field of view. This has most recently been extended further by our group to a more robust method, operating on the principle of image discretization, which is proving to be functional over a much wider range of Weber numbers (MCS 2019 submission by Singh et al.).

Despite there being robust image processing methods that can provide quantities of fragment volumes, velocities, and various shape metrics in the near-field of sprays, there is still a significant lapse in data from simultaneous measurements of gas and liquid phase. Significant progress has recently been made in this area using holography and

by combining PIV with backlight imaging [23, 24] to identify vortex formation behind individual droplets, providing further insights into how gas phase dynamics change with break-up regime for a canonical single droplet atomization experiment. However, there remains a significant amount of work to be done to fully ascertain the accuracy of these measurements for a range of conditions.

2.1.1 Measurement of Local Non-Dimensional Numbers

Pham et al. [21] used the multi-angle illumination technique to sub-range an image by droplet size, such that small droplets could be used as tracers of the gas phase. While the Stokes numbers of the droplets were still greater than 1, there was still a capability of estimate a slip velocity such that a local Weber number could be approximated. To the best of the author’s knowledge, this was the first time that such local measurements were obtained in atomizing turbulent sprays.

A motivation of the study was to understand how the local Weber number varies according to global conditions. Shinjo and Umemura [25] identified that the local Weber number approaches a value of order \sim 1 when ligaments begin to break. This followed from original work from Umemura and Osaka [26] which specifically identified a square root local Weber number \sim 0.8 in the transition from an unstable wave to an atomizing droplet (jetting to dripping). This local Weber number definition makes use of the local slip velocity at the scale of the droplet, and uses the half radius of the fragment as an appropriate length-scale. The experiments of Pham et al. [21] enabled direct measurement of this quantity for a completely different spray to that examined by Shinjo and Umemura. It demonstrated that the value of $\sqrt{\text{We}}$ \sim 0.8 is a quantity that was approached regardless of the Weber number, and this is shown in Figure 3. Interestingly, this same local Weber number was identified in a separate study from an electrified spray under laminar conditions [27].

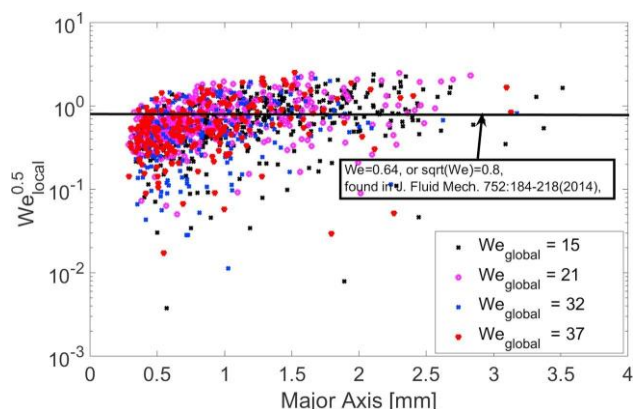


Figure 3: Square root of local Weber number vs. major axis of fragment (regardless) of shape, from a Weber number of 15 to 37. Figure reproduced from [21].

Results from four different studies [21, 25-27] suggest that there is a degree of universality in how a ligament breaks up into a droplet at the local scale. One is tempted to draw an analogy to turbulence, where local isotropy is accepted as an assumption regardless of the Reynolds number,

however the physical mechanisms here are of course different. Nevertheless, direct imaging of liquid atomization and tracking of small droplets or particles to enable simultaneous gas phase measurements, can clearly provide us with unique insights which have not been possible until recently.

An ability to accurately measure gas (the true carrier phase) and liquid phase simultaneously, remains a key limitation. This is a particular problem in the context of interpreting instability formation on liquid jets, while it also forms a substantial gap in our ability to compare models to experimental data. In the opinion of this author, this type of measurement, is the next key step in our ability to fully understand what drives the formation of droplets.

2.2 Near-field atomization: What to look at?

A key motivation for analyzing the near-field of sprays is to provide quantitative data on parts of the spray which have been historically difficult to probe. Not only does this assist in the development of numerical models, but it is also critical towards improving our understanding of the physical mechanisms that lead to droplet formation. With the introduction of techniques that can finally measure these regions of the spray, the challenge becomes one of knowing what to analyze, and whether or not it is of importance.

Initial work conducted by the Combustion Research group focused on quantifying non-spherical fragments through definition of some consistent shape identifying metrics, and this was originally done through identifying objects on the basis of their nominal average size and aspect ratio, after fitting them with an ellipse [14]. This categorization is schematically shown in Figure 4. This approach was adopted to enable computation of statistics of ligament size or fragment area and perimeter, with a sample of such a result shown in Figure 5.

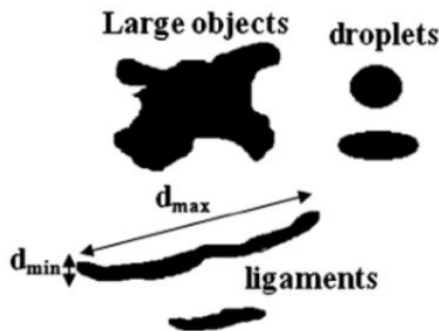


Figure 4: Categorization of near-field spray by shape of fragments observed, using aspect ratio as a key metric. Figure reproduced from [14].

Figure 5 shows the characteristic size (D_{ch} =average of major and minor axis of ellipse for droplets and other objects, D_{ch} =major axis of ellipse for ligaments) for a typical air assisted atomization case. Of particular interest is the shape in the distribution that arises, where the droplet size distribution clearly abides by the expected log-normal distribution (which has been confirmed through subsequent work). However the distribution of unbroken volumes for

instance (larger, unbroken fragments), does not abide by a distribution shape which is as consistently defined. The data provides a useful bank of information to study the potential relationships between the formation of irregular structures and the formation of droplets. As will be discussed in a later section of this paper, that information is also important towards describing downstream combustion behaviour both in a piloted spray burner and in an auto-ignition burner.

The ability to directly measure the distributions of differently shaped objects is of particular use towards PDF modeling approaches and reveals insights into the shape of distributions of different fragments which lead to the following question: can the droplet size distribution be related to the distribution of ligaments or to the distribution of other fragments in the spray?

Essentially the question to ask is, “where does the droplet size distribution come from”, the title of a recent paper published by Canu et al. [28]. In that contribution, an Eulerian-Lagrangian-Spray-Atomization (ELSA) framework was extended by incorporating information on the curvature of liquid fragments in the near field. This was proven useful in demonstrating that probability distributions of fragment curvature can be used to identify spray transitions, and also revealed a log-normal distribution of curvature, i.e. a similar shape as with the droplet size distribution.

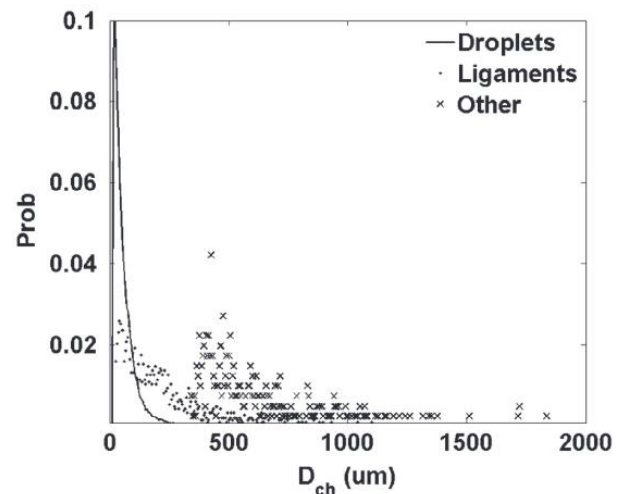


Figure 5: Sample probability distribution of characteristic size of droplets, ligaments and other fragments for case ET1 from [14]. Figure reproduced from [14].

Experimental measurements can aid in providing time-resolved and direct measurement of curvature not only on the liquid jet but also potentially on the fragments that issue from the liquid jet as a function of time. Perhaps one of the only studies published to date which focused on the analysis of distributions of ligaments but also insightfully on the distributions of wavelengths on a liquid jet is that of Marmottant and Villermaux [7]. In the study it was confirmed that ligament dynamics give rise to a droplet size distribution that can be accurately related to the corrugation of waves on the liquid jet itself. Extending such analysis over a wider non-dimensional space and in highly turbulent flows, has not been conducted. The original work by Marmottant and Villermaux was extended by Varga et al

[29] to analyse the influence of Rayleigh-Taylor instabilities and while our understanding on how ligaments and droplets form in these complex sprays has clearly progressed, there remains a paucity of experimental data providing rigorous quantitative statistics on the full cascade from liquid jet instability formation, to fragment formation and finally to the droplet size distribution.

2.3 Implications of Turbulence

Recent work by our group has also focused on direct measurement of wave formation on liquid jets with Figure 6 demonstrating one example of how the distribution of waves from a surface can match the distribution of ligament size. This type of data can provide insights into what causes ligaments to form and this work is part of an ongoing study in the group examining the key relationships between instability growth and fragment statistics over a very wide non-dimensional space.

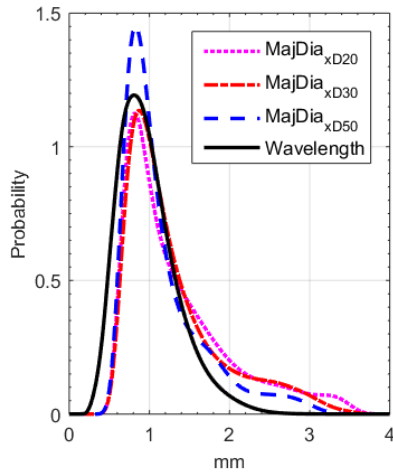


Figure 6: Probability Distribution of primary instability wavelength and ligament major axis from a coaxial airblast atomizer with $We=39$, $Re_l=4180$, $m=0.22$.

There is no disputing that instabilities are one of the causes of ligament formation and subsequent droplet formation. However the influence of turbulence on this phenomenon is relatively poorly understood. There have been some recent insights into the role of instabilities when there is turbulence in the gas phase, and given its practical relevance, some key results are presented here.

In a practical scenario, where the gas phase is turbulent, is it possible to accurately interpret the role of instabilities on a liquid jet or fragment? One way of approaching this problem is to simply assume that every droplet that forms in the spray is a result of a particular instability that formed earlier upstream on a liquid fragment. The problem is identifying the type of instability that the droplet would form from, and of course many droplets can break up due to other mechanisms such as collisions. In [11], it was demonstrated that at high turbulence intensities in the gas phase, where the Weber number is high, it is reasonable to assume that every droplet forms due to a Rayleigh Taylor instability. This was originally suggested by Varga et al [29] for the case of a standard coaxial airblast atomizer. The wavelength of the Rayleigh Taylor instability (λ_{RT}) is estimated as in [29] through equation (1) where σ is the

surface tension, a is an acceleration of liquid fragments, and ρ is density.

$$\lambda_{RT}(t) = 2\pi \left(\frac{3\sigma_l}{\rho_l a(t)} \right)^{1/2} \quad (1)$$

$a(t)$ is given by equation (2):

$$a(t) = \frac{10\rho_g (u_g(t)(1 + (\rho_g/\rho_l)^{1/2}) - U_l)^2}{\rho_l \lambda_l} \quad (2)$$

In [11], the primary instability (λ_l) was measured from the images for the lowest turbulence intensity only. The reader should note that the primary instability wavelength was measured from a number of representative snapshots, and was not a statistical measurement. However, the instantaneous gas phase velocity u_g was measured using laser Doppler anemometry, such that an approximate reconstruction of the probability distribution of Rayleigh-Taylor wavelengths was made possible as shown in Figure 7. For a high turbulence intensity case (T.I.=28%) it was found that the experimental data of droplet size measured using PDA was remarkably close to the estimated wavelength distribution after scaling through a single constant. Unfortunately, as good as this approximation was at high turbulence intensities, it completely broke down at lower turbulence intensities, where a mean wavelength estimate was possible, but not the full distribution. Analysis of the influence of the spectral broadness of the turbulent flow was not conducted however and could provide further insight.

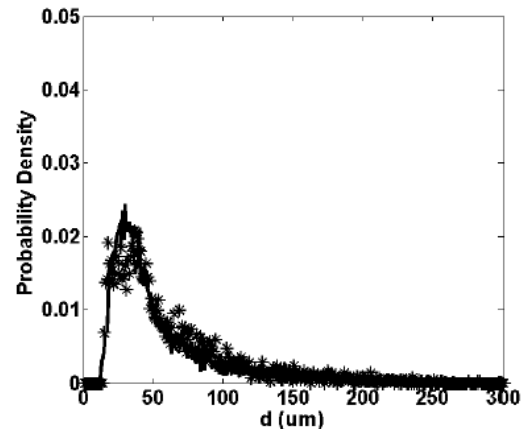


Figure 7: Droplet size distribution (markers) and distribution of Rayleigh-Taylor wavelength (theoretically reconstructed with experimental velocity data) for the air assisted atomizer of [11] with a mean gas phase velocity of 31m/s, liquid jet diameter of 210um and turbulent intensity of 28%. Figure originally appears as subfigure in [11].

Approaching a predictive capability to estimate a full droplet size distribution using information from the near-field, as shown above for the specific condition measured, would be a truly significant leap forward in the modeling of sprays. Unfortunately, this has yet to be achieved for a wide range of conditions, which results in the necessity of empirical scalings. While this is not necessarily a handicap,

it does require the constant provision of experimental data for every different atomizer configuration, which is time consuming and expensive.

Knowledge of which instabilities compete to form droplets is not only of fundamental interest, but can also guide the design of injectors, and progress is currently being made in this area through our group (see ACS 2019 submission by Gutteridge et al.). While instability formation is key towards understanding droplet generation, what is just as important is an ability to control the instabilities and subsequent droplet sizes. Constant use of simple twin-fluid atomizers like coaxial air-blast atomizers, or simple single orifice high pressure injectors, offer very little ability to do this effectively.

3. Hybrid Atomization Mechanisms

The use of more than one atomization mode to contribute to the formation of a spray offers a degree of control which is not afforded by standard injectors. In this section, due to space limitations, only two possibilities for hybrid atomization will be presented. The first is a conventional coaxial air-blast atomization mechanism in tandem with effervescent atomization [9], and the second is conventional coaxial air-blast atomization in tandem with electrostatic atomization.

Hybridizing atomizers in this way not only has practical benefits in that the formation of the spray can be controlled, but is also interesting from a fundamental standpoint. For instance, in electrostatic atomization, Coulombic repulsion is a key force that contributes to atomization [10, 30], and this is a body force term that acts throughout the jet. However, once a droplet forms, the predominant action of the Coulomb force will be a radial repulsion of liquid. In contrast, in air-blast atomization, shear forces contribute to the disintegration of the liquid jet from the surface inwards, rather than throughout the liquid column. In contrast to both of the above, effervescent atomization results in longitudinal instabilities which lead to collisions of bubbles that can result in the radial expulsion of liquid, or results in a bubble explosion that drives spherical expulsion of liquid, which is unique, and a function of the gas-to-liquid ratio.

Hybridizing atomization modes therefore results in the introduction of a number of competing forces, and practically offers more degrees of freedom to alter downstream spray behaviour through controlling the relative importance of different modes of instability or atomization mechanisms.

3.1 Effervescent-Airblast Atomization

Effervescent atomization has been reviewed elsewhere [2] and remains an active area of development given how efficient the method is at generating a spray with much less air than a typical airblast atomizer. The technique does not need small orifice diameters in order to result in small droplets, and can also operate effectively at low pressures. One of the known modes that drive effervescent atomization is the repeated expulsion of liquid “bubbles”, which is a result of an intermittent void fraction in the liquid jet. While this results in a very efficient atomization

process through the development of longitudinal instabilities and bubble bursting events, it is inherently erratic [9].

A hybrid effervescent-airblast atomizer is shown in Figure 8. The addition of a shear flow around the central core in this instance offers an ability to maintain the advantage of effervescent atomization (highly efficient mist generation through longitudinal collisions and bubble bursting events) whilst employing an airblast mode to improve mixing. Results published in [9] demonstrated that the addition of an air-blast component, while influencing droplet size at low effervescent aeration levels, did not do so at higher levels, but still maintained a significant influence on the degree of dispersion and mixing.

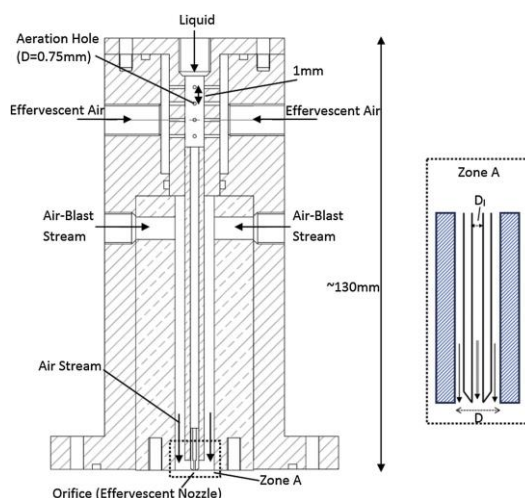


Figure 8: Schematic of the hybrid air-blast and effervescent atomizer. Figure reproduced from [9].

3.2 Electrostatic-Air-blast

Electrostatic atomization is a mode that has received considerable attention in the form of an “electrospray” [15, 31] which relates to the electrostatically manipulated atomization of conducting liquids. With liquids that have a high electrical resistivity (higher than $\sim 5 \times 10^8 \Omega\text{m}$, such as Diesel, Mineral Turpentine, or Kerosene), the spray formation process becomes markedly different, and falls into the regime of “charge injection atomization” [30]. In these cases, a higher electrical field is imposed to the liquid through two electrodes that are a few hundreds of micrometers apart, but electrical charge is also able to reside in the liquid for some time, making it able to influence the flow-field and vice versa. Instabilities in electrostatic atomization are somewhat understood though not over a wide non-dimensional space. Rayleigh instabilities tend to generate the droplets initially, and then Coloumbic fission can fragment droplets into smaller ones over time [10, 27]. A unique feature of this atomization mechanism is that it can also result in a highly bimodal droplet size distribution, with small droplets preferentially concentrating around the periphery of the spray core due to their ability to rapidly migrate radially outward (because of a high charge per unit volume). Electrostatic atomization on its own has limitations due to the necessity for very high charge levels and also the requirement for very small orifice

diameters to maintain a high charge to volume ratio. Hybridizing this mode therefore becomes attractive, and a simple starting point is through the addition of a coaxial air flow.

Such hybridization may provide insights into how this type of atomizer can be used to control the droplet size distribution shape (due to the ability of the charge to generate bimodality in the distribution) but also break-up length, through independent variation of an applied voltage. Figure 9 shows a schematic of a hybrid airblast/electrostatic atomizer which is currently being developed by our group (see ACS 2019 submission by Ahmed et al). This system houses a long high voltage needle electrode shrouded within a fuel injecting tube, which is contained within a co-flowing stream of air. The final orifice is electrically grounded, and the system is designed to enable a degree of control between the electrode and the orifice in order to control the electric field in the inter-electrode gap. Images of the influence of charge at different Weber numbers (not shown here) demonstrate that there is a highly charged mist that forms around the central core, which would be consistent with previous observations in high pressure charged sprays [32]. This means that there will be a charge distribution across the spray, which clearly not only influences atomization but is also likely to significantly influence reaction zone structures. Previous work has demonstrated that the addition of charge onto a single droplet can have a significant influence on the dynamics of soot particles [15], however there is limited data on the interaction between charge and combustion.

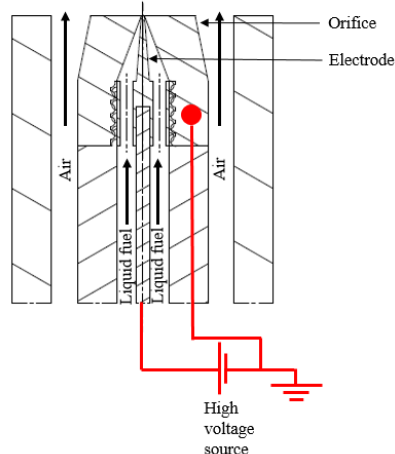


Figure 9: Schematic of the hybrid air-blast and electrostatic atomizer, designed for either a piloted or auto-ignition spray burner.

4. From Atomization to Spray Combustion

Spray combustion, whether initiated through an auto-ignition or forced ignition process will not generally interact with atomizing liquid. The processes of atomization and heat release are spatially separated and also occur over different time-scales.

However, the quality of atomization will be a strong contributor towards identifying whether a flame can be stabilized, given that it will dictate at what location

downstream, sufficient vapour and mixing will form for combustion to occur. The presence of a denser liquid core will also directly influence entrainment processes [12] and reaction zone structures [14]. In order for predictive models to be able to accurately reproduce the full cascade of processes that occur in a spray flame, it is necessary to focus experimental efforts on benchmark burners that can provide full measurements of liquid fraction at the exit plane, while also droplet dynamics measurements downstream, in conjunction with measurement of reactive species. Achievement of all of these measurements, remains a formidable challenge. In this brief section, two burners are presented which were designed for the specific purpose of analyzing the full range of processes from atomization to combustion, in a single geometry.

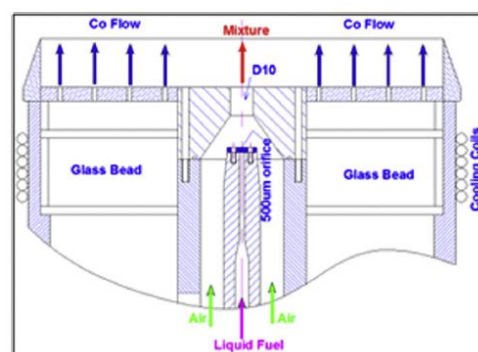


Figure 10: Auto-Ignition Burner with Atomizing Spray at the Exit Plane. Figure reproduced from [14].

The first burner described is a hot co-flow (heat from products of premixed air/H₂) auto-ignition burner shown in Figure 10, which was one of the first platforms which enabled full measurement of atomization processes at the exit plane, in addition to flame stabilization and heat release. A key finding from the study indicated that the change in the size of the most non-spherical fragments at the exit plane trended with the change in lift-off height of the flame [14]. A threshold in the lift-off height was identified where on the lean side it varied with the mass fuel to air ratio as per a dilute auto-igniting spray flame [33], and on the globally rich side, the opposite trend was observed where the lift-off height was now “atomization controlled”. This indicated a flame where downstream behaviour was altered through a change in the near-field spray structure, ultimately due to a control over the vapour mass fraction. This variation and impact of the near-field structure was also evident through broadband chemiluminescence measurements [14] indicating that the rate of intensity increase past the lift-off height was significantly diminished in the flame with the highest proportion of non-spherical non-atomized fragments.

The burner above while insightful, did not offer an ability to control the degree of atomization at the exit plane without changing the global fuel/air ratio, which led to the development of the Sydney University Needle Burner (SYNSBURNTM) [34]. This piloted burner enables translation of a liquid injecting tube within a co-flowing air-blast stream, enabling a certain degree of control over the degree of both atomization and vapour pre-mixing at the exit plane. Full recession of the needle brings the burner

towards a dilute spray configuration (albeit still without a fully developed flow). Stability limits of the flame highlighted substantial differences from a dilute spray burner [35] with only a moderate change in the slope of blow off velocity to mass loading (g/min) as a function of recession. This was an interesting finding which has yet to be fully explained. Temperature measurements were also recently conducted in this spray flame using femtosecond coherent-anti-Stokes-Raman-spectroscopy [12, 13]. Interference from droplets was not identified as a significant concern given both the short time duration of the pulse and small probe volume size. The recent measurement campaign highlighted that the presence of large non-atomized liquid fragments had a direct influence on the entrainment of hot gases from the pilot within the potential core of the jet and showed evidence of ligaments influencing the thermal structure of downstream reaction zones.

5. Concluding Remarks

This brief review has highlighted some recent work focusing on improvements made in the interpretation of near-field images collected in atomizing sprays, whether or not a control of any of the atomization processes is possible, and finally touched on two recent experiments which aim to provide platforms that enable us to study the full cascade of processes from atomization to combustion. Analysis of liquid fragments at the exit plane with analysis of near-field instabilities will provide further insights into the processes that drive atomization over a wide non-dimensional space. Control of downstream spray and combustion behaviour is potentially possible through the provision of atomizer designs that can make use of different modes of atomization, however significant research is still required to understand how multi-modal atomization can control the formation of sprays in both canonical and practical flows.

6. Acknowledgments

I would firstly like to acknowledge Prof. Assaad R. Masri who has been integral in helping me shape my thinking over the years, being a central part of all of the research presented here. Dr. Phuong Pham has also been a key part of developing the multi-angle illumination system, with subsequent contributions by Dr. Albyn Lowe, Gajendra Singh and Aaron Gutteridge. PhD candidate Tushar Ahmed from our group is the current driver of the EHD atomization research mentioned here. The research has been funded by the Australian Research Council, the Qatar Foundation, and the University of Sydney under the DVCR/SOAR program.

7. References

[1] Lasheras JC, Hopfinger EJ. *Annu Rev Fluid Mech.* 2000;32:275-+.

- [2] Sovani SD, Sojka PE, Lefebvre AH. *Prog Energ Combust.* 2001;27(4):483-521.
- [3] Ganan-Calvo AM. *Appl Phys Lett.* 2005;86(21).
- [4] Faeth GM, Hsiang LP, Wu PK. *Int J Multiphas Flow.* 1995;21:99-127.
- [5] Mastorakos E. *P Combust Inst.* 2017;36(2):2367-83.
- [6] Mastorakos E. *Prog Energ Combust.* 2009;35(1):57-97.
- [7] Marmottant PH, Villermaux E. *J Fluid Mech.* 2004;498:73-111.
- [8] Lasheras JC, Villermaux E, Hopfinger EJ. *J Fluid Mech.* 1998;357:351-79.
- [9] Kourmatzis A, Lowe A, Masri AR. *Experimental Thermal and Fluid Science.* 2016;75:66-76.
- [10] Shrimpton JS. *Ieee T Dielect El In.* 2005;12(3):573-8.
- [11] Kourmatzis A, Masri AR. *J Fluid Mech.* 2015;764:95-132.
- [12] Lowe A, Thomas LM, Satija A, Lucht RP, Masri AR. *Combust Flame.* 2019;200:417-32.
- [13] Thomas LM, Lowe A, Satija A, Masri AR, Lucht RP. *Combust Flame.* 2019;200:405-16.
- [14] Kourmatzis A, Pham PX, Masri AR. *Combust Flame.* 2015;162(4):978-96.
- [15] Anderson EK, Koch JA, Kyritsis DC. *Combust Flame.* 2008;154(3):624-9.
- [16] Fansler TD, Parrish SE. *Meas Sci Technol.* 2015;26(1).
- [17] Kashdan JT, Shrimpton JS, Whybrew A. *Part Part Syst Char.* 2004;20(6):387-97.
- [18] Linne M. *Prog Energ Combust.* 2013;39(5):403-40.
- [19] Kourmatzis A, Pham PX, Masri AR. *Meas Sci Technol.* 2017;28(3).
- [20] Pham PX, Kourmatzis A, Masri AR. *Meas Sci Technol.* 2017;28(11).
- [21] Pham PX, Kourmatzis A, Masri AR. *Experimental Thermal and Fluid Science.* 2018;95:44-51.
- [22] Kashdan JT, Shrimpton JS, Whybrew A. *Part Part Syst Char.* 2004;21(1):15-23.
- [23] Flock AK, Guildenbecher DR, Chen J, Sojka PE, Bauer HJ. *Int J Multiphas Flow.* 2012;47:37-49.
- [24] Guildenbecher DR, Gao J, Chen J, Sojka PE. *Int J Multiphas Flow.* 2017;94:107-22.
- [25] Shinjo J, Umemura A. *Int J Multiphas Flow.* 2010;36(7):513-32.
- [26] Umemura A, Osaka J. *J Fluid Mech.* 2014;752:184-218.
- [27] Singh G, Pham PX, Kourmatzis A, Masri AR. *Fuel.* 2019;241:941-53.
- [28] Canu R, Puggelli S, Essadki M, Duret B, Menard T, Massot M, et al. *Int J Multiphas Flow.* 2018;107:230-45.
- [29] Varga CM, Lasheras JC, Hopfinger EJ. *J Fluid Mech.* 2003;497:405-34.
- [30] Yule AJ, Shrimpton JS, Watkins AP, Balachandran W, Hu D. *Fuel.* 1995;74(7):1094-103.
- [31] Kyritsis DC, Roychoudhury S, McEnally CS, Pfeiffer LD, Gomez A. *Experimental Thermal and Fluid Science.* 2004;28(7):763-70.
- [32] Kourmatzis A, Ergene EL, Shrimpton JS, Kyritsis DC, Mashayek F, Huo M. *Exp Fluids.* 2012;53(1):221-35.
- [33] O'Loughlin W, Masri AR. *Combust Flame.* 2011;158(8):1577-90.
- [34] Lowe A, Kourmatzis A, Masri AR. *Combust Flame.* 2017;176:511-20.
- [35] Gounder JD, Kourmatzis A, Masri AR. *Combust Flame.* 2012;159(11):3372-97.

Supersonic Ethylene Combustion - Revamping the Cavity

Will O. Landsberg and Ananthanarayanan Veeraragavan

Centre for Hypersonics, The University of Queensland, QLD, 4067, AUSTRALIA

anandv@uq.edu.au

ABSTRACT

Supersonic combustion of hydrocarbon fuels in high Mach number scramjets remains an ongoing challenge, typically relying on archaic wall-recesses which have remained largely unchanged for decades. This work documents the process of designing for shock tunnel experimentation under semi-direct connect conditions, employing empirical methods, simple numerical tools and complex chemically reacting, computational fluid dynamics to examine varying cavity geometries. An array of axisymmetric diffuser geometries were examined, compressing the tunnel test flow to scramjet combustor entry conditions. Final recommendations for the chosen configurations to be tested within a shock tunnel are hence given.

A Physical Understanding of how Multiple Mapping Conditioning Works

Andrew P. Wandel

School of Mechanical and Electrical Engineering, University of Southern Queensland, Queensland, Australia

Abstract

Multiple Mapping Conditioning (MMC) uses a mathematical reference space to provide an alternative dimension for modelling the turbulent transport that mixes parcels of fluid. Conceptualising this process is challenging when relying on the mathematics of the governing equations. This article presents the physical bases underlying the mathematics. The geometric processes used to create maps of the Earth are used as analogies for how combustion systems are modelled. Direct Numerical Simulations (DNS) are used to visualise how the 3-D turbulent distortions of non-premixed scalar fields can be represented by the 1-D mixture fraction. How the mixture fraction can be mapped to a reference variable is described, concluding with the processes used to apply the different methods of MMC to the modelling of turbulent combustion systems.

Keywords: Multiple Mapping Conditioning, MMC, map projections, Conditional Moment Closure, CMC, Mapping Closure

1. Introduction

Multiple Mapping Conditioning (MMC) [1] is a model for turbulent combustion that aims to address the challenges of accounting for all the effects of turbulence on the mixing of chemical species. These effects are extensive and, in particular, the interaction between chemistry and turbulence in modern combustion systems requires careful modelling [2]. A host of models have therefore been developed [3,4]. The most popular models are naturally those which provide quality results for a number of regimes. Although each proponent of their favourite model thinks highly of it, none has yet been proven to successfully model the full spectrum of regimes. It is expected that there are situations where one model ought to be preferred over the others because it either produces greater accuracy or produces a similar accuracy for lower computational effort. An effort to review all models is not within the scope of this article: the focus of this article is the MMC model.

Recent reviews of MMC developments [5,6] describe the mathematics of the models developed from the original MMC framework [1], and how these models have been validated using various test cases. This article takes a different perspective, by seeking to describe how the MMC model simulates the physical processes of mixing; this is done by analogy with geographical mapping techniques.

While this article focusses on the mixture fraction (for non-premixed combustion), there is no mathematical or physical impediment to substituting references to “mixture fraction” with “reaction progress variable” (for premixed combustion) in this article. Naturally, care must be taken due to the source term for the reaction progress variable.

The purpose of maps is to represent a large system in a useful layout. While the concept of mapping has been explicitly stated in the names of some models, mapping techniques are used in any model that uses as an independent variable a quantity that is not a physical coordinate. In this article, the tree of models that build towards MMC are discussed, with relevant common mapping practices providing an introduction to each model.

2. Mixture Fraction as a Basis

2.1 Scale maps

Figure 1 shows, to scale, a representation of inner Adelaide, including the layout of streets, the Torrens River, rail lines, and parkland. Such a map is useful for navigating the inner parts of Adelaide city by showing the relative spacing between different parts precisely. This is because the area shown is relatively small and flat, enabling a fixed scale for both dimensions.

This map is useful for planning journeys, with the chosen route taking into account such aspects as the distance travelled, the types of road along the route (e.g. freeway), and the number of traffic lights. A modern addition is to overlay real-time traffic information, with sections of road currently experiencing heavy traffic being coloured red, while sections which are free-flowing are coloured green.



Figure 1: Map of City of Adelaide and North Adelaide [7].

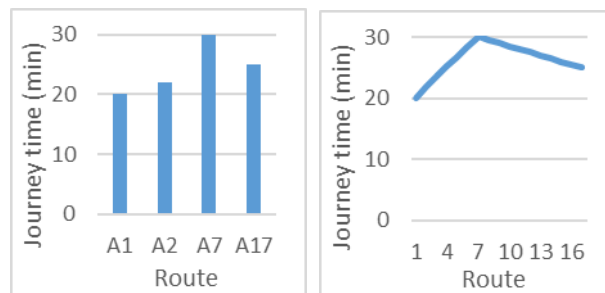


Figure 2: Estimated journey time to a point 20 km north of Adelaide City using various routes. Left: standard bar-chart representation; right: standard representation if route number represents values of a continuous variable.

In planning a journey, an assessment is made of the estimated total time required to reach the destination based on all these criteria. This total time is evaluated by integrating the speed at each point along the route, which is appropriately normalised to calculate the average speed for the journey. If all possible routes are designated unique scalar values, then it is possible to directly compare the average travel times (left image of Figure 2). If the route numbers represent a continuum, then the right image of Figure 2 would be used.

2.2 Scale maps analogy for combustion

This same process is undertaken in turbulent combustion when mixture fraction or reaction progress variable is used as a basis. Points in space that have a common feature—the same value of mixture fraction Z (by analogy, points along a route)—are collected. Then their properties—temperature T , species mass fraction Y (by analogy, the speed)—are integrated (averaged) to produce a single value of the conditional average $\langle Y|Z \rangle$. This process is repeated for all values of mixture fraction (by analogy, all routes).

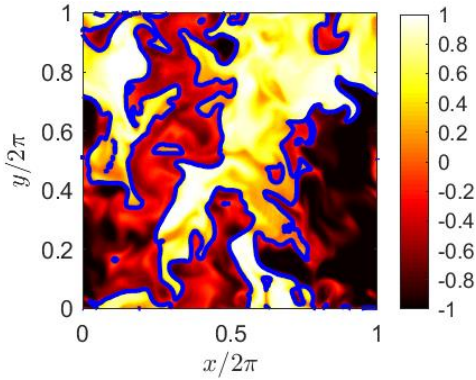


Figure 3: The initial mixture fraction field from DNS [8]. The domain has length 2π in all directions. The blue lines represent $Z = 0$.

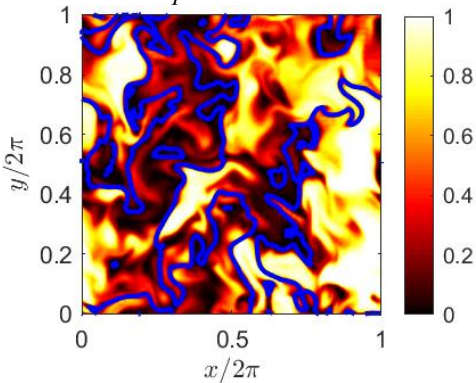


Figure 4: The initial field of scalar Y corresponding to Figure 3 [8]. The blue lines represent $Z = 0$.

As a demonstration of how the physical domain is mapped to the mixture-fraction domain, Figure 3 shows an initial mixture fraction field produced by homogeneous, decaying 128^3 Direct Numerical Simulations (DNS) with an initial Taylor Reynolds number of 57.0 [8]. Figure 4 shows the initial field of scalar $Y = Z^2$, which represents one of the chemical species. When all points with the same mixture fraction are considered (e.g. all points along the blue lines for $Z = 0$), then the values of Y can be averaged, producing

a single point in Figure 5 (the origin in the case of the blue lines in Figure 3). Once this has been repeated for the entire domain of mixture fraction, the familiar representation of the conditional average is obtained (Figure 5). The domain in Figure 4 is representative of a single cell in a simulation, and Figure 5 presents a model for the unresolved sub-grid fluctuations that are present.

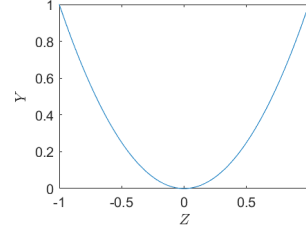


Figure 5: The initial distribution of scalar Y as a function of mixture fraction Z , corresponding to Figure 3 and Figure 4.

2.3 Scale maps analogy for stochastic processes

Some turbulent combustion models are solved by using a stochastic implementation, which means that they use stochastic particles that move through the system. Each particle is a statistical realisation whose motion on average represents the motion of an actual parcel of fluid. With sufficient particles, the statistics of the flow can be reproduced (the statistical error as a function of number of particles is governed by the central limit theorem).

The stochastic particles can be likened to traffic flow through the city, with similar particles (i.e. those with the same starting point and initial conditions—by analogy, the destination) overall following the same route. However, each particle will follow a unique route to reach the final destination (by analogy, cars will divert into side-streets and rejoin the main route after following an appropriate network of streets). Each route has a likelihood of being followed by a particle; this is governed by the overall velocity and the gradients in the domain. Low turbulent intensities result in particles moving coherently (the road is clear); high turbulent intensities cause particles to disperse (delays cause some cars to divert into alternate routes in an effort to find a path with less resistance).

For all such turbulent combustion models, the particles move through scalar space within the sub-grid cell (e.g. from Figure 5, they are transported in the Z -direction or within the Z - Y plane). This motion models how the particles move through physical space, crossing gradients of Z . An advantage of the stochastic method is that only those values that are possible are simulated, reducing the computational load (in Figure 5, stochastic particles are only found along the line, whereas the deterministic method would require calculation at every point within the Z - Y plane). By analogy, in the stochastic method only cars which head along a route that is close to the desired route are simulated; whereas in the deterministic method, routes that head in the wrong direction for most of the journey must be considered.

If a statistically-significant number of particles are realised, then information about the system can be obtained by averaging the results from the particles. This can be from global averages (e.g. the mean temperature in the cell) or

conditional averages (e.g. the mean temperature in the cell, for a particular mixture fraction). This is mathematically the same as the integration process described in Sect. 2.2, except the calculation for each mixture fraction is made by identifying those particles which possess that mixture fraction, then averaging the specified variable for those particles only.

2.4 Benefits of mixture fraction as a basis

Using mixture fraction as a basis was pioneered by Bilger’s Fast Chemistry Limit (FCL) model [9]: in stable flames, the field of a conserved scalar was unaffected by the flame’s presence. Conserved scalars can only change their value by being transported to a region with a different value (there are no source or sink terms in their transport equation). The mixture fraction is conventionally defined to be the fraction of the mass of gas at any point which originated from the fuel stream (prior to mixing). (If there is liquid fuel, then the conventional definition of mixture fraction, just like the reaction progress variable, is not conservative.)

The FCL model exploited this property of conserved scalars being independent of combustion by assuming that the turbulent mixing timescales were significantly larger than the chemical timescales, so that it could be assumed that each point in the domain is at chemical equilibrium. The computations can then be greatly simplified: the chemistry can be pre-calculated and stored in a look-up table, then the chemical and thermodynamic state of any location in the domain is known by referring to the entry in the look-up table for the mixture fraction at that location.

The FCL model was a significant advance in computational speed with reasonable accuracy but is only accurate for large Damköhler numbers. Nonetheless, the use of mixture fraction as an independent variable in non-premixed combustion modelling was appealing, and was used in the Flamelet model by Peters [10,11], and later the Conditional Moment Closure (CMC) by Klimenko [12], then Bilger [13] (see [14]).

Taking the value $Z = 0$ as an example (shown by the blue lines in Figure 4), the FCL model works by accessing the look-up table for $Z = 0$ and applying the value for Y in that look-up table to those locations in the domain with $Z = 0$. In other words, every location covered by a blue line in Figure 4 would have the set value of $Y = 0$.

The Flamelet model is more sophisticated than the FCL model because, at each location, it also accounts for the scalar dissipation rate

$$N_Z = D\nabla Z \cdot \nabla Z, \quad (1)$$

where D is the molecular diffusivity, while simultaneously considering the reaction rate. Since the gradients of mixture fraction at $Z = 0$ vary throughout space, the Flamelet model will produce different values of Y at each of the different points along the blue lines in Figure 4.

The CMC model predicts the average value of the scalar Y dependent on what the value of Z is at that location; this is a conditional mean: $\langle Y|Z \rangle$. Similar to the FCL model, CMC will produce the same value of Y at all points along the blue

lines in Figure 4. However, CMC uses the conditional scalar dissipation $\langle N_Z|Z \rangle$ to provide transport in mixture-fraction space ($\langle Y|Z \rangle$ is changed by the values of $\langle Y|Z \rangle$ at neighbouring values of Z) while simultaneously evaluating the reaction rate. Since diffusion in mixture-fraction space occurs due to the spatial variation of mixture fraction, diffusion in mixture-fraction space models the turbulent diffusion in physical space.

For homogeneous flow (because of the relatively-low Reynolds number in the DNS, the entire domain represented by Figure 3 can be considered to be a single cell for simulations), the CMC equation is:

$$\frac{\partial \langle Y|Z \rangle}{\partial t} = \langle N|Z \rangle \frac{\partial^2 \langle Y|Z \rangle}{\partial Z^2} + \langle W|Z \rangle, \quad (2)$$

where the last term is the change due to chemical reactions.

The Flamelet and CMC models have spawned many variations, enabling them to accurately model more regimes by overcoming some of the model’s deficiencies.

2.5 Challenges of mixture fraction as a basis

2.5.1 Predicting the mixture fraction field

The principal challenge of using mixture fraction as a basis for non-premixed combustion is accurately predicting the mixture fraction field. The purpose of Eq. (2) in a simulation is to provide the mean value of density so that velocity coupling is achieved. Means are calculated using the mixture fraction’s probability density function (pdf) $P_Z(Z)$ as part of a weighting factor in a weighted average:

$$\langle Y \rangle = \int_{-\infty}^{\infty} \langle Y|Z \rangle P_Z(Z) dZ. \quad (3)$$

The pdf combined with Eq. (2) models the spatial distribution of scalars shown in Figure 3 that exists within a simulated cell. The oft-neglected mixture fraction pdf and its oft-forgotten transport equation are crucial for accurate modelling using CMC, and for interpreting results presenting statistics conditioned on mixture fraction. The transport equation for the joint-pdf (jpdf) $P_{\mathbf{Y}}$ of any system of scalars $\mathbf{Y} \in \{Y_1, Y_2, \dots, Y_n\}$ is [15]:

$$\frac{\partial \langle \rho | \mathbf{Y} \rangle P_{\mathbf{Y}}}{\partial t} + \frac{\partial \langle \rho u_j | \mathbf{Y} \rangle P_{\mathbf{Y}}}{\partial x_j} = \sum_{\alpha=1}^n \frac{\partial \rho W_{\alpha} P_{\mathbf{Y}}}{\partial Y_{\alpha}} - \sum_{\alpha=1}^n \sum_{\beta=1}^n \frac{\partial^2 \langle \rho N_{\alpha\beta} | \mathbf{Y} \rangle P_{\mathbf{Y}}}{\partial Y_{\alpha} \partial Y_{\beta}} \quad (4)$$

If the flow is homogeneous, then the convection term (2nd on the lhs) can be neglected; if the scalars are conservative, then the source term (1st on the rhs) can also be neglected. If there is a single (conservative) scalar defined as $\mathbf{Y} \in \{Z\}$ then the pdf transport equation (for CMC) is obtained:

$$\frac{\partial \langle \rho | Z \rangle P_Z}{\partial t} = - \frac{\partial^2 \langle \rho | Z \rangle \langle N_Z | Z \rangle P_Z}{\partial Z^2}. \quad (5)$$

Equation (5) for the mixture fraction pdf must be solved in order to implement CMC. However, the conditional scalar dissipation $\langle N_Z|Z \rangle$ is unknown and there is no transport equation for this quantity. The options are: to model the conditional scalar dissipation and use Eq. (5) to determine P_Z , or model P_Z and use Eq. (5) to determine the conditional scalar dissipation. The latter is normally preferred, using a presumed pdf (either a β -function pdf or a clipped-Gaussian pdf). However, this does not necessarily reproduce the actual distribution of mixture fraction (Figure 6).

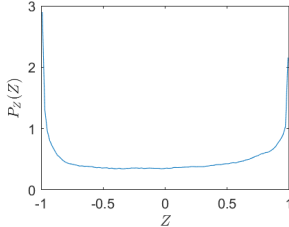


Figure 6: Mixture fraction pdf for Figure 3.

2.5.2 Low Damköhler-number flows

The other challenge for using mixture fraction as a basis is when the Damköhler number is approximately of order one, i.e. when turbulent transport and chemical reactions change the composition at a similar rate. This is principally due to cold mixing of reactants, and is a major cause of extinction. In such flows, the values of Y vary for a fixed value of Z .

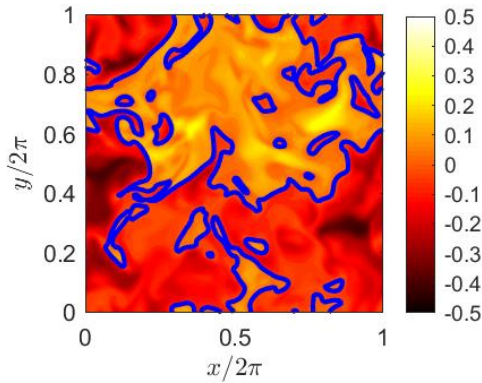


Figure 7: The mixture fraction field from DNS after 2 eddy turnover times [8]. The blue lines represent $Z = 0$.

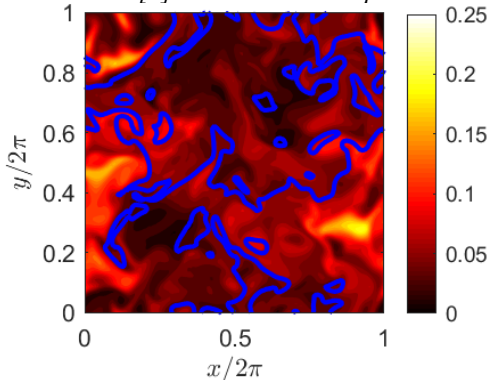


Figure 8: The field of scalar Y corresponding to Figure 7 [8]. The blue lines represent $Z = 0$.

Consider the DNS results after 2 eddy turnover times have elapsed (Figure 7 and Figure 8). Because Y has evolved somewhat independently of Z , it is noticeable that the isolines of $Z = 0$ pass through a variety of values of Y . This

is clearly apparent in Figure 9, where approximately half of the possible range of Y -values are encountered somewhere in the domain where $Z = 0$. At this stage of the decay, the mixture fraction distribution is approximately Gaussian (Figure 10), so there is significant scatter in Y for most of the domain.

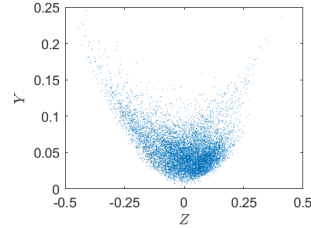


Figure 9: Scatter plot of 10 000 randomly-sampled points from DNS after 2 eddy turnover times [8].

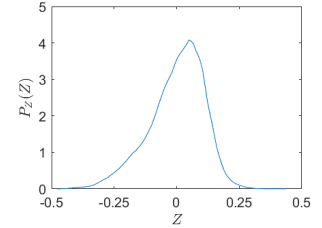


Figure 10: Mixture fraction pdf for Figure 7 [8].

First-order CMC is incapable of accurately modelling this type of flow, so either 2nd-order CMC (where the magnitudes of the fluctuations from the conditional mean are modelled), or doubly-conditioned CMC (where another variable is added to the basis, typically sensible enthalpy or possibly scalar dissipation, so that there are no conditional fluctuations in the multi-dimensional basis space) are required [14]. Studying Figure 9, in 2nd-order CMC the conditional rms (the rms for each value of Z) models the scatter that is present; a challenge for 2nd-order CMC is that any conditional skewness is ignored. In doubly-conditioned CMC, the entire space shown in Figure 9 is the domain for the two basis scalars, with the only contribution to the solution coming from the part of the domain where the scatter is seen (i.e. where the jpdf is non-zero); a challenge for doubly-conditioned CMC is defining the jpdf.

3. Mapping Closure Model

3.1 Mercator projections

In the cylindrical projection method of mapping, lines of latitude and longitude are forced to remain parallel to each other (Figure 11). The globe is contained within a cylinder and locations are projected from the sphere to a point on the curved wall of the cylinder with the same latitude; lines of longitude are parallel to the cylinder's axis. The curved wall is unravelled to produce the map. This method was devised for ease of navigation with a compass: bearings in the (four) cardinal directions are represented truly.

However, cylindrical projections stretch lines of latitude that are closer to the poles, so that a non-uniform scale is applied to the map. Although the distance between two lines of longitude is represented as constant, the actual distance increases with decreasing distance from the equator: the scale diminishes with decreasing distance from the equator. To compensate for this distortion and make the scale in both directions equal at each point, in the Mercator projection the distance between lines of latitude is inversely related to the distance from the nearer pole. (It is also therefore impossible to render the poles themselves.) This representation is commonly used when computers render the entire Earth, so that Antarctica appears to possess almost as much land mass as the rest of the world

combined, when it is 13 million km², compared to Australia and Europe (7.7 and 10.5 million km² respectively).

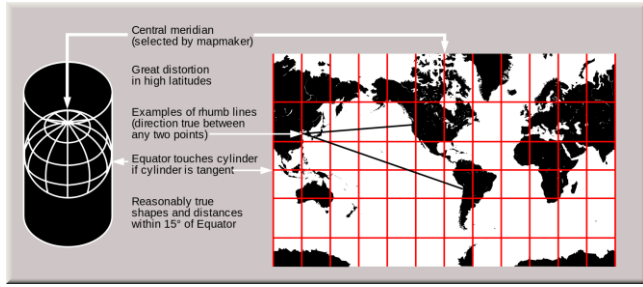


Figure 11: Methodology of Mercator variant of cylindrical projection [16]. Left: the geometry of a cylindrical projection; right: the resultant map.

3.2 Mercator projections analogy for combustion

Cylindrical projections can be represented using a Cartesian coordinate system, with non-linear scales on both axes. For a turbulent combustion system which is doubly-conditioned (such as Figure 9), the cylindrical projection provides a method for rescaling the distribution of values to appear elliptical (which can be modelled by a jointnormal distribution): the non-linear rescaling increases distortion with increasing distance from the centre (mean).

For a single scalar dimension, the rescaling follows the same general procedure of the latitude's distortion in the Mercator projection. If there is significant probability at a bound of mixture fraction, the distortion in the mapping dimension is greatest at each of those bounds, and is least near the centre. This is used in the Mapping Closure model, and in all applications of MMC except generalised MMC.

3.3 Mapping Closure model

A solution to the challenge of modelling the mixture fraction pdf (Sect. 2.5.1) is to use some other quantity as a basis and allow the mixture fraction to change relative to that quantity. The Mapping Closure [17,18] achieves this by introducing a "reference variable" ξ that is associated with the mixture fraction.

The stretching process of the pdf from the real mixture fraction to the mathematical reference variable is visualised in Figure 12. By analogy with the Mercator projection, mixture fraction (the blue line in Figure 12) is the true latitude (as seen from space), while ξ is the mapped result (the outcome of the cylindrical projection) with values stretched apart near the edges to produce the green line (stretching of latitude increases closer to the poles).

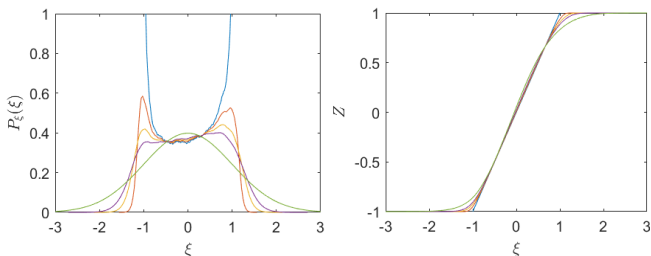


Figure 12: Evolution of mixture fraction (blue line) as it is stretched to a conventional reference variable (green line). Left: pdf; right: mapping function.

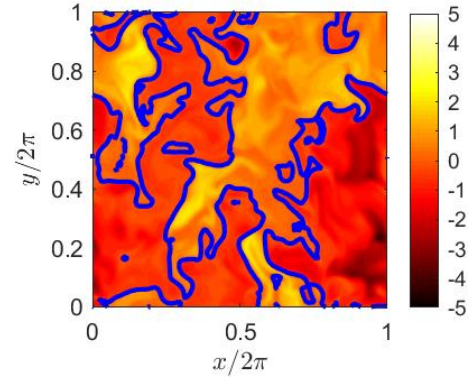


Figure 13: The initial reference variable field corresponding to Figure 3. The blue lines represent $Z = 0$.

In this case, there is some compression of the pdf for $\xi \approx 0$. However, to convert from the bimodal mixture fraction pdf to the unimodal reference variable pdf, a significant amount of stretching is required at the tails. The effect of the stretching on the mapping function is shown in Figure 12, where the gradient slightly increases for $\xi \approx 0$, in line with the compression, while the many points at $Z \approx \pm 1$ are distributed to much larger magnitudes of ξ . The resultant reference variable field (Figure 13) appears to show greater resolution in those regions where its magnitude is large (e.g. the horseshoe near the bottom), but this does not result in a large variation in the evolution of any scalar.

The mathematical relationship between Z and its reference variable comes from how the probability is stretched:

$$P_Z dZ = P_\xi d\xi$$

$$P_Z = \left(\frac{dZ}{d\xi} \right)^{-1} P_\xi \quad (6)$$

i.e. the mixture fraction pdf can be determined using both the reference variable pdf, and the Jacobian between the mixture fraction and its reference variable. The Jacobian in Eq. (6) is only mathematically stable if it is determined using $\langle Z | \xi \rangle$; in homogeneous flows, it can be analytically determined. However, an analytical solution for inhomogeneous flows is not generally available; a numerical approach to solving the derivative was devised [8] and has been used in every MMC model since.

The relationship between any scalar Y and ξ is solved using:

$$\frac{\partial \langle Y | \xi \rangle}{\partial t} = \langle B | \xi \rangle \frac{\partial^2 \langle Y | \xi \rangle}{\partial \xi^2} + \langle W | \xi \rangle$$

$$\langle B | \xi \rangle \equiv \langle N_\xi | \xi \rangle \quad (7)$$

The similarity between Eqs. (7) and (2) provides an opportunity to model the conditional scalar dissipation, effectively closing the 1st-order CMC model:

$$\langle N | Z \rangle = \left(\frac{\partial \langle Z | \xi \rangle}{\partial \xi} \right)^2 \langle B | \xi \rangle. \quad (8)$$

The transport equation for the reference variable pdf can be obtained by simplifying Eq. (4) in the same manner as Eq. (5) because, in non-premixed combustion, ξ is

conventionally associated with Z , so has the same general properties:

$$\frac{\partial \langle \rho | \xi \rangle P_\xi}{\partial t} = - \frac{\partial^2 \langle \rho | \xi \rangle \langle B | \xi \rangle P_\xi}{\partial \xi^2} \quad (9)$$

If P_ξ is chosen to satisfy a Gaussian distribution, then one of the possible solutions (mathematically, there are multiple possible solutions) is:

$$B = \langle B | \xi \rangle. \quad (10)$$

Equation (10) simplifies the solution of Eq. (7), while Eq. (8) [after multiplying through by the first Eq. (6) and integrating] provides a simple relationship to determine B :

$$B = \langle N \rangle \left\langle \left(\frac{\partial \langle Z | \xi \rangle}{\partial \xi} \right)^2 \right\rangle^{-1} \quad (11)$$

The distribution of the scalar Y in reference space is shown in Figure 14, revealing that there are a significant number of points with $Y=1$. These will retain their values initially because the diffusive length scale in reference variable space should never be large, modelling the behaviour that the volume of large regions of unmixed fluid decreases at a finite rate. Despite $\xi \approx 0$ being the most likely, the values of Y in that region should change reasonably rapidly because of the constant value of B . This models the sharp changes in the Y field (Figure 4), which is reflected in the large gradients in the ξ field (Figure 13).

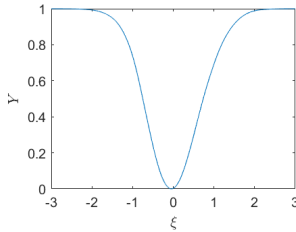


Figure 14: The initial distribution of scalar Y as a function of reference variable, corresponding to Figure 12.

4. Multiple Mapping Conditioning

4.1 Deterministic Multiple Mapping Conditioning

The Mapping Closure was not devised to address the challenges of CMC in modelling the mixture fraction distribution, since the first publication of Mapping Closure predates the first publication of CMC. (Since the invention of CMC was the Ph.D. work of Klimenko, it is possible that the Mapping Closure and CMC are contemporaneous.) A limitation of the Mapping Closure is that it is only applicable to homogeneous flows; deriving MMC to enable the modelling of inhomogeneous flows ensued [1]. The mapping process for deterministic 1st-order MMC is identical to the Mapping Closure model (Sect. 3.3).

Flows with low Damköhler numbers are problematic for deterministic 1st-order MMC, so the same principles used in CMC have been applied to MMC: either multiple referencing variables (akin to doubly-conditioned CMC), or modelling the fluctuations about the conditional mean (probabilistic MMC, akin to 2nd-order CMC).

4.2 Multiply-conditioned MMC

The approach for doubly-conditioned MMC is, in principle, identical to a full Mercator projection (Sect. 3.2), with mixture fraction equivalent to latitude and the other variable (sensible enthalpy or scalar dissipation) equivalent to longitude. However, the rescaling is somewhat more complex, since neither sensible enthalpy nor scalar dissipation is independent of mixture fraction (unlike latitude and longitude), e.g. Figure 5 or Figure 9.

Figure 15 shows a scalar dissipation field, where it is apparent that there are tendrils of high dissipation, with each tendril tending to follow a line of constant mixture fraction (c.f. Figure 7). However, it is also apparent that the scalar dissipation can be very different for the same mixture fraction (Figure 16).

Double-conditioning on mixture fraction and either sensible enthalpy or scalar dissipation means that interactions between points in the modelled space are restricted, so that a point on the blue lines with high dissipation can only interact with other points on the blue lines which also have high dissipation. Such points are physically close together and would naturally interact.

This method has been implemented using mixture fraction with both scalar dissipation (with 1–3 dissipation time scales) [19] and sensible enthalpy [20]. The principal difficulty for the scalar dissipation method is that the scales of dissipation range over many decades, so many dissipation timescales need to be defined, which makes the system unwieldy. The principal challenge for the sensible enthalpy method is that when initial conditions are similar to Figure 5 (as done in standard flamelet initial conditions), there is no natural mechanism for the system to evolve from the initial manifold to produce something akin to Figure 9.

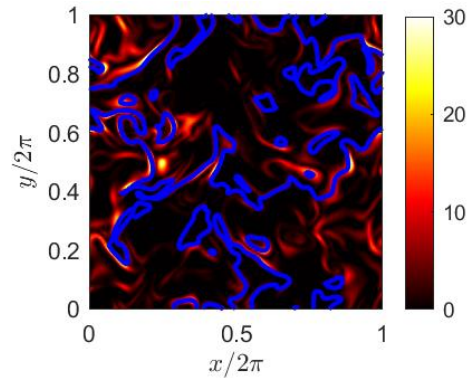


Figure 15: Scalar dissipation rate N_Z corresponding to Figure 7 [8]. The blue lines represent $Z = 0$.

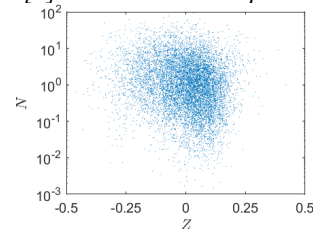


Figure 16: Scatter plot of 10 000 randomly-sampled values of scalar dissipation from DNS after 2 eddy turnover times [8].

Partially-premixed combustion can be modelled by mixture fraction and reaction progress variable as the dimensions of the reference space. This should be more practicable than using sensible enthalpy since the chemical reaction rate can independently generate deviations from an initial field such as Figure 5. While probabilistic MMC has been successful in partial premixtures, any attempt to span the spectrum of mixtures in a single model requires double conditioning.

A challenge for any application of double conditioning is maintaining an appropriate (physical) correlation between the reference variables because mathematically they are independent variables (like latitude and longitude).

4.3 Probabilistic Multiple Mapping Conditioning

Although doubly-conditioned CMC and second-order CMC have both been used widely, the more popular method in MMC is definitively second-order MMC because its unique modelling challenges can be solved more readily. Unlike second-order CMC, the most common method for solving probabilistic MMC is to use stochastic particles (Sect. 2.3). Moving in reference space instead of mixture fraction space does not affect the final outcome, since it is possible to create a field of each scalar in physical space (Figure 13).

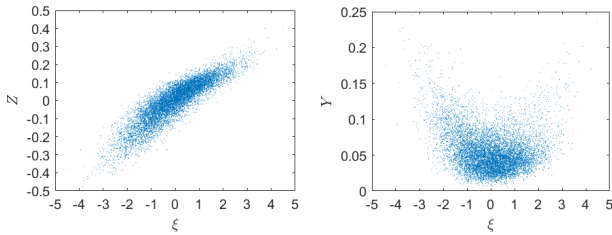


Figure 17: Possible mapping of scalars to reference variable, with the same samples as Figure 9. Left: mixture fraction; right, scalar Y .

A potential mapping of mixture fraction to a reference variable is shown in Figure 17 (simulating the reference variable in DNS is not well-defined, so a representative amount of scatter has been artificially incorporated). This reflects the physical behaviour that two points with the same value of mixture fraction do not necessarily behave the same because of the different gradients of mixture fraction, so the two points probably have different values of reference variable. As a consequence, there appears to be more scatter in the mapping of Y to ξ (Figure 17) than Y to Z (Figure 9). However, because the interactions of Y are governed by the interactions of Z , this is not a challenge to accurate modelling.

In common with pdf turbulent combustion models [15], probabilistic MMC requires a mixing model to close the term for diffusion in scalar space, which is the first term on the rhs in the deterministic formulation of Eq. (7). Invariably, the mixing model is chosen to be the modified Curl’s model [21,22] since this is the model that allows the most freedom in controlling the particle interactions. In particular, conditional fluctuations

$$Z'' = Z - \langle Z | \xi \rangle \quad (12)$$

are values to be controlled, in contrast with conditional MMC, where $Z'' = 0$. This is done in the process of mixing

by ensuring that particles are unable to mix with sufficient intensity to (on average) reach $\langle Z | \xi \rangle$. This process of restricting the rate at which particles relax to $\langle Z | \xi \rangle$ models the real process of turbulent transport whereby parcels of fluid can be carried across large gradients of scalar, but a finite period is required to break apart a parcel of fluid so that all the molecules within the parcel completely interact with the new surroundings.

A key feature of MMC is that only particles with similar values of ξ are allowed to mix, duplicating the diffusion term in Eq. (7): any finite-difference formulation of such a term would only consider values of ξ that are close to the point of interest. This is a physical restriction: points with similar values of ξ are most likely close to each other in physical space, so only these particles are expected to interact. However, intermittency in the interactions is also important to model the physical behaviour of mid-sized eddies transporting pockets of fluid within a large parcel of fluid. Almost all implementations of probabilistic MMC mix particles that neighbour each other in reference space, which is similar to the methodology of EMST [23]. The key differences are: that EMST enables particles to mix with multiple other particles, while MMC conventionally only pairs particles; and intermittency is introduced in EMST by an age factor causing half of the particles (on average) to interact, while intermittency is introduced in those MMC implementations by the stochastic transport of ξ reordering the particles (all particles are always mixed). The author has always introduced intermittency differently, by only mixing some particles, and requiring them to be within a diffusion-length scale of each other in reference space [8]; this method is numerically feasible for smaller Δt [24].

4.4 Conic projections

Conic projections are the standard for atlases, since they produce (with the smallest errors) uniform scaling in both directions for the entire map. To produce a conic projection (Figure 18), a point above the nearer pole is used as a vantage point, and a cone is cast over the sphere of the Earth. The points on the sphere are projected to points on the cone with the same latitude; lines of longitude intersect at the tip of the cone. Since the tip of the cone extends beyond the Earth, this is always removed before the cone is cut along a line of longitude and unravelled. Furthermore, the poles are removed from the 2-D representation owing to the infinite stretching required to render them.

Wherever the cone touches the Earth’s surface is called a “standard parallel”. Since the projection on a standard parallel is identical to the Earth’s surface, there is zero distortion of scale along a standard parallel, and distortion generally increases with increasing latitude from the standard parallel. If the cone is defined so that the Earth is completely inside—but touching—the cone, a single standard parallel is defined, and this is referred to as a tangent conic projection.

To reduce the overall distortion error, the specified cone cuts the surface of the Earth at two standard parallels (Figure 18): between the standard parallels, the Earth’s surface extends beyond the cone; outside the standard

parallels, the Earth’s surface is contained within the cone. This is referred to as a secant conic projection, and is the standard for atlases, since the largest distortion error is minimised. The errors are minimised by having two-thirds of the latitudes of interest shown between the standard parallels, since the curvature of the Earth’s surface causes greater rates of change in distortion at the edges of the map.

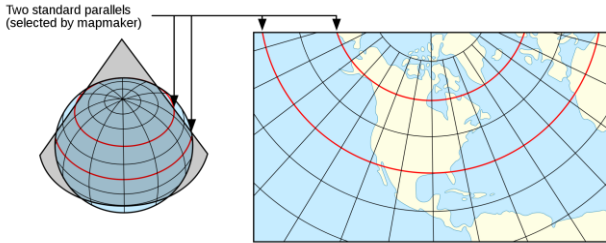


Figure 18: Methodology of Lambert conformal (“simple”) conic projection [25]. Left: the geometry of a secant conic projection; right: the resultant map.

4.5 Conic projections analogy for combustion

Conic projections impose a small distortion by converting from a curved surface into a flat surface. This geometric procedure is similar to that used to reduce dimensionality in Principal Component Analysis (PCA) [26] (taking the 3-D globe and representing it in a 2-D plane), while it is explicit in manifold behaviour [2] (taking a hyper-plane that is curved in space and representing it as a flat plane).

The two major applications of generalised MMC [27,28] use the same principles as conic projections because the reference variable ξ is defined to be a mixture fraction which is different to the mixture fraction Z that is linked to the reactive scalars. Because Z and ξ are both mixture fractions, there should be a strong correlation between the two, but the correlation is imperfect in the mapping process, analogous to the distortion error in the conic projection.

4.6 Generalised Multiple Mapping Conditioning

Generalised MMC allows any variable to be ξ instead of the conventional reference variable [29]. Instead of defining it to be a mathematical variable, in all applications it has been defined to be a variable available elsewhere in the system: the filtered LES mixture fraction [27]; or the velocity [30] or mixture fraction [28] from the binomial Langevin model [31]. (The two generalised MMC applications were developed independently and contemporaneously.) The mapping is similar to Figure 17, because the mixture fraction pdf and reference variable pdf are identical.

The major advantage of the generalised MMC applications is that the transport of ξ is embedded in a standard, familiar model. As a consequence, the challenges of defining the coefficients for transport are completely removed. Generalised MMC is therefore also better positioned as a basis for multiple conditioning variables.

While generalised MMC appears to be similar to CMC, it is different because MMC does not require the reference variable field to exactly satisfy the real mixture fraction distribution. Any errors in the reference variable transport do not affect the accuracy of the actual scalars’ fields.

5. Conclusions

MMC uses an abstract reference variable space to model turbulent combustion. Understanding how it achieves this based on the formulae is challenging. The author built his understanding during his Ph.D. [24], and has always taken a more visual approach to imagining how MMC works (e.g. Sect. 9.1 [24]). This work portrays this understanding to assist the community to better understand one of the options for modelling turbulent combustion processes.

6. Acknowledgment

The author thanks Prof. A.Y. Klimenko for “thinking in maths” and creating an environment for us to explore.

7. References

- [1] A.Y. Klimenko and S.B. Pope (2003) *Phys. Fluids* **15**, pp. 1907–1925.
- [2] S.B. Pope (2013) *Proc. Combust. Inst.* **34**, pp. 1–31.
- [3] T. Poinsoot and D. Veynante (2011) *Theoretical and Numerical Combustion*, 3rd Ed., Toulouse.
- [4] T. Echehki and E. Mastorakos (2011) *Turbulent Combustion Modeling*, Springer.
- [5] M.J. Cleary and A.Y. Klimenko (2011) in: *Turbulent Combustion Modeling*, Eds: T. Echehki and E. Mastorakos, Springer, pp. 143–173.
- [6] K. Ghai, S. De, K. Vogiatziki and M.J. Cleary (2018) in: *Modeling and Simulation of Turbulent Combustion*, Eds: S. De, A.K. Agarwal, S. Chaudhuri and S. Sen, Springer, pp. 447–474.
- [7] S. Davis (2015) *Australia South Australia City of Adelaide location map*, CC BY-SA 4.0, viewed 29th July 2019, <https://commons.wikimedia.org/w/index.php?curid=37637155>.
- [8] A.P. Wandel (2013) *Combust. Theory Model.* **17**, pp. 707–748.
- [9] R.W. Bilger (1980) In: *Turbulent Reacting Flows*, P.A. Libby and F.A. Williams (Eds.) **44**, pp. 65–113, Springer–Verlag, Berlin.
- [10] N. Peters (1984) *Progr. Energy Combust. Sci.* **10**, pp. 319–339.
- [11] N. Peters (2000) *Turbulent Combustion*, Cambridge University Press.
- [12] A.Y. Klimenko (1990) *Fluid Dynamics* **25**, pp. 327–334.
- [13] R.W. Bilger (1993) *Phys. Fluids A* **5**, pp. 436–444.
- [14] A.Y. Klimenko and R.W. Bilger (1999) *Progr. Energy Combust. Sci.* **25**, pp. 595–687.
- [15] S.B. Pope (2000) *Turbulent Flows*, Cambridge University Press.
- [16] United States Geological Survey (2005) *Mercator-projection map*, United States Department of the Interior, Public Domain, viewed 31st July 2019 https://commons.wikimedia.org/wiki/File:Usgs_map_mercator.svg.
- [17] H. Chen, S. Chen and R.H. Kraichnan (1989) *Phys. Review Letters* **63**, pp. 2657–2660.
- [18] S.B. Pope (1991) *Theor. Comput. Fluid Dyn.* **2**, pp. 255–270.
- [19] M.J. Cleary and A. Kronenburg (2007) *Proc. Combust. Inst.* **31**, pp. 1497–1505.
- [20] A. Kronenburg and M.J. Cleary (2008) *Combust. Flame* **155**, pp. 215–231.
- [21] C. Dopazo (1979) *Phys. Fluids* **22**, pp. 20–30.
- [22] J. Janicka, W. Kolbe and W. Kollmann (1979) *J. Non Equilib. Thermodyn.* **4**, pp. 47–66.
- [23] S. Subramaniam and S.B. Pope (1998) *Combust. Flame* **115**, pp. 487–514.
- [24] A.P. Wandel (2005) *Development of Multiple Mapping Conditioning (MMC) for Application to Turbulent Combustion*, Ph.D. thesis, UQ.
- [25] United States Geological Survey (2009) *Lambert conformal conic projection*, United States Department of the Interior, Public Domain, viewed 31st July 2019 https://commons.wikimedia.org/wiki/File:Lambert_conformal_conic.svg.
- [26] U. Maas and D. Thévenin (1998) *Proc. Combust. Inst.* **27**, pp. 1183–1189.
- [27] M.J. Cleary and A.Y. Klimenko (2009) *Flow, Turb. Combust.* **82**, pp. 477–491.
- [28] A.P. Wandel and R.P. Lindstedt (2019) *Proc. Combust. Inst.* **37**, pp. 2151–2158.
- [29] A.Y. Klimenko (2004) *Phys. Fluids* **16**, pp. 4754–4757.
- [30] A.P. Wandel and R.P. Lindstedt (2009) *Phys. Fluids* **21**, p. 015103.
- [31] L. Valiño and C. Dopazo (1991) *Phys. Fluids A* **3**, pp. 3034–3037.

What is important for accurate soot predictions?

Heinz Pitsch

Institut für Technische Verbrennung, RWTH Aachen University, Germany
H.Pitsch@itv.rwth-aachen.de

ABSTRACT

Modeling frameworks for Large-Eddy Simulations of soot evolution in turbulent flames include a number of submodels describing the chemistry of soot precursors, particle dynamics, heterogeneous soot chemistry, turbulent mixing, and combustion. To understand the reasons for model failure and to enhance the overall model performance, it is necessary to identify and subsequently improve model components with a leading order effect on the overall error. In this presentation, errors in soot predictions associated with gas-phase chemistry, statistical modeling of the number density function, and turbulence/chemistry/soot interaction models are isolated and quantified. Experiments in laminar flames are used to assess the chemical mechanisms, Monte Carlo simulations in laminar flames provide reference data for assessing and improving moment methods to describe the number density function, and DNS data of a sooting turbulent jet diffusion flames are used in a combined a-priori and partial a-posteriori analysis to identify errors in flamelet-based combustion models.

Sound sources in premixed flames

Mohsen Talei

Department of Mechanical Engineering, The University of Melbourne, Australia

Abstract

This paper presents a technical review of our understanding of the mechanism of sound generation by premixed flames. Examples from direct numerical simulation (DNS) studies undertaken at the University of Melbourne are provided. Furthermore, the implications of the findings for developing accurate models that can predict combustion-generated sound are discussed. This paper demonstrates that flame-flame interactions referred to as ‘flame annihilation’ are significant sources of sound in premixed flames. These localised events feature several unique characteristics that cannot be explained with existing turbulent flame theories. It is shown that flame acceleration during annihilation has a significant contribution to the radiated sound. Therefore, in the context of modelling, it is essential to predict the flame displacement speed during annihilation as accurately as possible. Analysis of the DNS data shows promising avenues to meet this requirement.

Keywords: combustion noise, premixed flames, flame annihilation

1. Introduction

One of the significant challenges we face in the 21st century is how to secure our demand for energy safely, efficiently and in an environmentally sustainable manner. This has driven a considerable effort to promote the widespread use of renewable energy and alternative fuels. Nevertheless, fossil fuels are still dominant in the energy market. The most optimistic scenario proposed by the International Energy Agency (IEA) predicts that we still rely on combustion of fossil fuels and biofuels for meeting 70% of our energy needs in 2040 [1]. This calls for further research to enhance our understanding of combustion process to advance energy-producing technologies that are cleaner and highly efficient.

Gas turbines are the prime movers in the aviation industry and account for about 20% of the installed capacity for electricity generation globally [2]. They have fast ramp up and down capabilities, which make them complementary to intermittent renewable generation. Furthermore, with the increasing interest in producing renewable hydrogen, gas turbines can play an important role in the implementation of a successful hydrogen economy.

Lean premixed combustion is the desired combustion regime in industrial gas turbines. It results in a low level of NO_x emissions due to operating at lower temperatures and facilitates better combustion efficiency. However, the primary issue with operating gas turbines in this regime is thermoacoustic instability, commonly initiated by combustion-generated sound. To avoid this type of instability, the mechanism of sound generation by premixed flames needs to be fully understood. Numerous theoretical, numerical, and experimental studies have explored this problem from various angles. An interested reader is referred to the review articles by Candel [3], Dowling and Mahmoudi [4] and Ihme [5].

To characterise combustion noise, many past studies have considered unconfined flames. They generally conclude that combustion noise features a broadband spectrum and that the sound spectra show some degree of universality in terms of the frequency of peak emission and the slope of the spectrum in the low and high frequency ranges. The experimental study by Rajaram et al. [6] is an example of a comprehensive

experimental dataset of sound generation by premixed flames for different fuels, equivalence ratios and flow parameters. They show that the frequency of peak emission can be estimated as a function of the average flame length and burner diameter.

Another important observation in the literature is that the fluctuating heat release rate is an important source of noise [3]. Many past studies have demonstrated this and used a framework such as acoustic analogies to further analyse this problem. As demonstrated in the literature and discussed further in this paper, flame-flame interaction or flame annihilation is a significant source of heat release rate fluctuations.

Numerical simulation is a tool that can provide a further understanding of this problem. Amongst different numerical approaches, direct numerical simulation (DNS) is a promising tool due to its ability to resolve all length and time scales in the problem. This paper therefore aims to review the DNS studies in this regard, primarily undertaken at the University of Melbourne. It will be shown how DNS can provide unprecedented detail about the source of sound in premixed flames and how this information can be used for developing new models that can predict sound generation by premixed flames for practical problems.

2. Acoustic Analogy

Acoustic analogies have been extensively used to study the mechanism of sound generation by different types of flows. In general, they are a rearrangement of the Navier-Stokes equations into various forms of an inhomogeneous wave equation. The source terms on the right hand side of acoustic analogies can then be used to interpret the sound generation mechanism. Lighthill [7,8] proposed the first and best known acoustic analogy by rearranging the continuity and momentum conservation equations into a wave equation. This equation was reformulated by Dowling [9] to examine sound generation by combusting flows,

$$\begin{aligned}
\frac{1}{c_\infty^2} \frac{\partial^2 p}{\partial t^2} - \nabla^2 p &= \frac{\partial}{\partial t} \left(\frac{\rho_\infty}{\rho} \left(\frac{Q\dot{\omega}}{c_p T} - \frac{\nabla \cdot \mathbf{q}}{c_p T} + \frac{\tau_{ij}}{c_p T} \frac{\partial u_i}{\partial x_j} \right) \right) \\
&+ \frac{\partial^2}{\partial x_i \partial x_j} (\rho u_i u_j - \tau_{ij}) \\
&+ \frac{1}{c_\infty^2} \frac{\partial}{\partial t} \left(\left(1 - \frac{\rho_\infty c_\infty^2}{\rho c^2} \right) \frac{Dp}{Dt} - \frac{p - p_\infty}{\rho} \frac{D\rho}{Dt} \right) \\
&+ \frac{\partial^2}{\partial x_i \partial t} (u_i \rho_e).
\end{aligned} \tag{1}$$

where p is the pressure, T is the temperature, c is the speed of sound, Q is the heat of combustion, $\dot{\omega}$ is the reaction rate, ρ is the density, c_p is the specific heat capacity, \mathbf{q} is the heat flux, τ_{ij} is the viscous stress tensor, \mathbf{u} is the velocity, x is the spatial coordinates and t is the time. The subscript ∞ refers to the flow field variables in the far field. Here ρ_e is the excess density, defined as,

$$\rho_e = \rho - \rho_\infty - (p - p_\infty)/c_\infty^2. \tag{2}$$

The first line on the right hand side of Equation 1 is a monopolar source term which is considered to be the main contributor to combustion noise. The second line is the so-called Lighthill's stress tensor which is a dominant source of sound in non-reacting jets. As discussed by Dowling [9], the source term in the third line is significant if there are regions of unsteady flow with different mean density and sound velocity from the ambient. The last term is a dipole source due to changes in the momentum of density inhomogeneities. Considering the first term on the right hand side of Dowling's formulation as the only source term, leads to:

$$\frac{1}{c_\infty^2} \frac{\partial^2 p}{\partial t^2} - \nabla^2 p = \frac{\partial}{\partial t} \left(\frac{\rho_\infty}{\rho} \left(\frac{Q\dot{\omega}}{c_p T} \right) \right). \tag{3}$$

Equation 3 is used in several combustion noise studies to obtain the far-field sound using Green's function solution and study the mechanism of sound generation. However, there is evidence in the literature that other source terms, such as the last source term in equation 1 can play an important role under some circumstances [10-11]. This review will demonstrate the range of validity of equation 3 under some conditions.

3. Numerical methods

3.1 Numerical solvers

Two DNS solvers were used to study sound generation by premixed flames. The first solver is NTMIX, developed at the European Center for Research and Advanced Training in Scientific Computing (CERFACS). NTMIX features a sixth-order compact scheme for spatial derivatives, combined with a third-order Runge–Kutta time integrator [12]. This solver uses a simple chemistry model and has been used extensively to study laminar and turbulent flames. The second DNS solver is S3D_SC [13] which is a modified version of S3D [14], a solver originally developed at the Combustion Research Facility at Sandia National Laboratories. This

solver features an eighth-order central differencing scheme for spatial derivatives, combined with a six-stage, fourth-order explicit Runge–Kutta time integrator.

3.2 Computational domains and numerical parameters

3.2.1 Laminar flames

Two groups of configurations are considered here. The first group includes one-dimensional (1D) domains for simulating planar, axisymmetric and spherically symmetric annihilation events. Figure 1 shows a schematic of these configurations. Figure 1a shows the configuration for a planar flame annihilation and half of the domain is considered by using a symmetry line on the left hand side. The outflow boundary is located on the right hand side. The flame is initialised in the middle of the domain with the unburnt gas trapped between the flame and the symmetry line. As a result of this initialisation, the flame propagates towards the symmetry line until it annihilates. Figure 1b shows the configuration for axisymmetric and spherically symmetric annihilation events. For these cases, spherical and cylindrical flames are initialised at a given radius with the unburnt gas trapped inside them. The flame therefore propagates toward the origin until it completely collapses.

The second group consists of a two-dimensional (2D) laminar flame, forced at the inlet for a range of frequencies (see Figure 1c). The boundary conditions are imposed at the inflow, while non-reflecting boundary conditions are used at the outflow boundaries. For the baseline case (i.e. 1D planar), the temperature ratio T_b/T_u is considered to be 4, the Zel'dovich number β is 8, the non-dimensional laminar flame speed S_L/c_∞ is 0.01, the Lewis number is unity and the Prandtl number is 0.75. More details of the simulation and computational domain parameters can be found in [15,16].

3.2.2 Turbulent flames

Figure 3 shows a schematic of the computational domain for the turbulent flames considered. In these cases, turbulent premixed flames at two equivalence ratios of 0.7 and 1 were considered. A careful treatment of boundary conditions was undertaken to avoid spurious noise at the boundaries. For instance, a sponge layer at the outflow was considered to avoid reflection from the outflow boundary. The jet Reynolds number was 5300 and the inlet Mach number was 0.35. More details of the simulation and computational domain parameters can be found in [18].

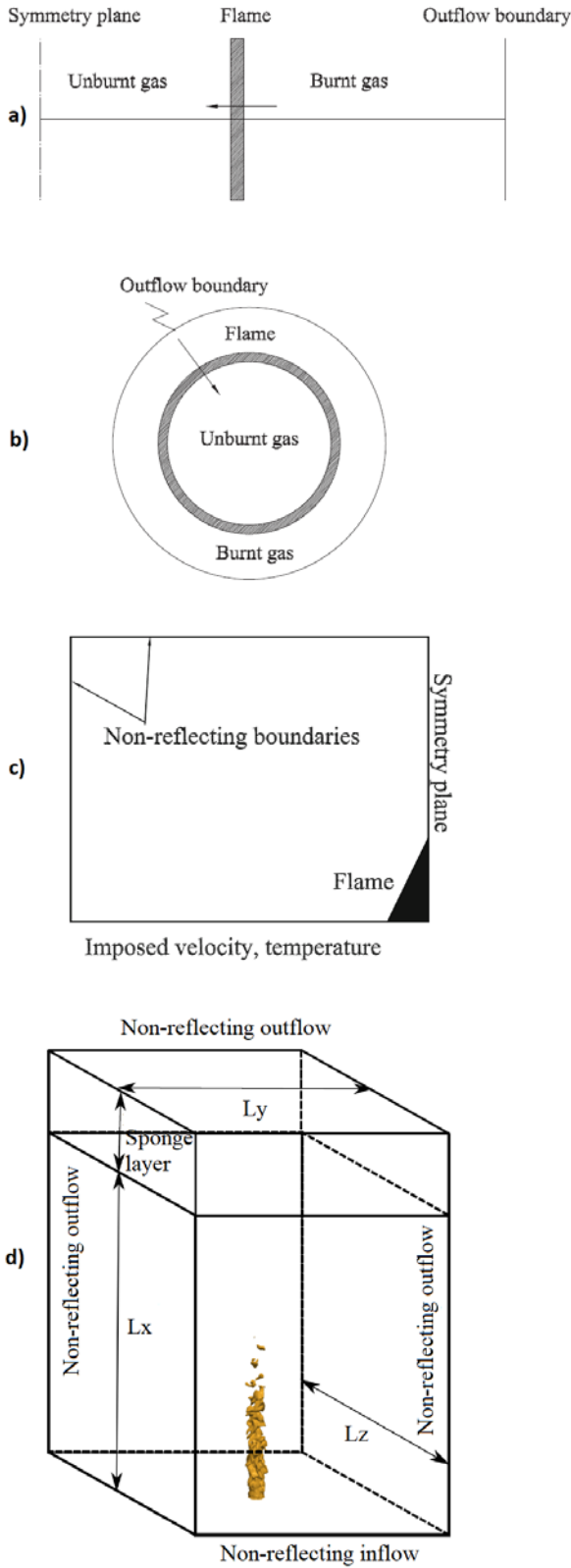


Figure 1: Computational domains for a) planar, b) axisymmetric and spherically symmetric annihilation, c) acoustically forced premixed flame and d) turbulent premixed flame.

4. Results

Annihilation events are a significant source of heat release rate fluctuations. To understand the mechanism of sound generation by these events, simple geometries including planar, axisymmetric and spherically symmetric cases will be first examined in this section [15,16]. Using the theoretical framework discussed in section 3, the proposed scaling laws to estimate sound generation by these events will be reviewed [15]. Using these scaling laws and DNS results, the impact of the key flame parameters such as flame thickness, laminar flame speed, temperature ratio, Zel'dovich number and Lewis number on the produced sound will be discussed [16]. Next, the significance of these events in 2D forced laminar flames will be investigated [17]. This follows by reporting a 3D DNS of sound generation by turbulent premixed flames [18]. An algorithm for identifying annihilation events will be presented and the contribution of these events to the overall produced sound will be quantified [19]. Finally, the implications of these results for modelling will be discussed [20].

4.1 Sound generation by 1D flame annihilation

4.1.1. Planar flame annihilation

Figure 2 shows pressure and heat release rate profiles for several instants before, during and after flame annihilation in the planar configuration discussed in section 3 (see Figure 1a). The top row shows the reaction rate as a function of distance, featuring a flame propagating towards the unburnt mixture. As can be seen, when the flame is approaching the symmetry line, the peak reaction rate slightly increases. This increase correlates with a pressure rise at the symmetry line shown in the bottom row of Figure 2. After annihilation, a pressure wave with a large negative amplitude propagates towards the outflow. As the wave propagates at the speed of sound in the burnt region, this negative amplitude remains constant (not shown here for brevity).

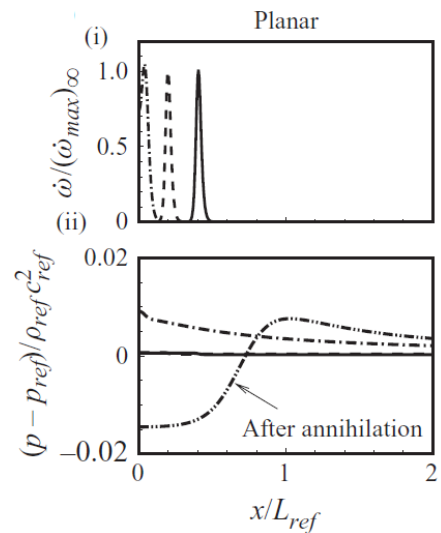


Figure 2: (i) Normalised reaction rate and (ii) pressure fluctuations before (solid, dashed), during (dash-dotted) and after flame annihilation (dash dot-dot).

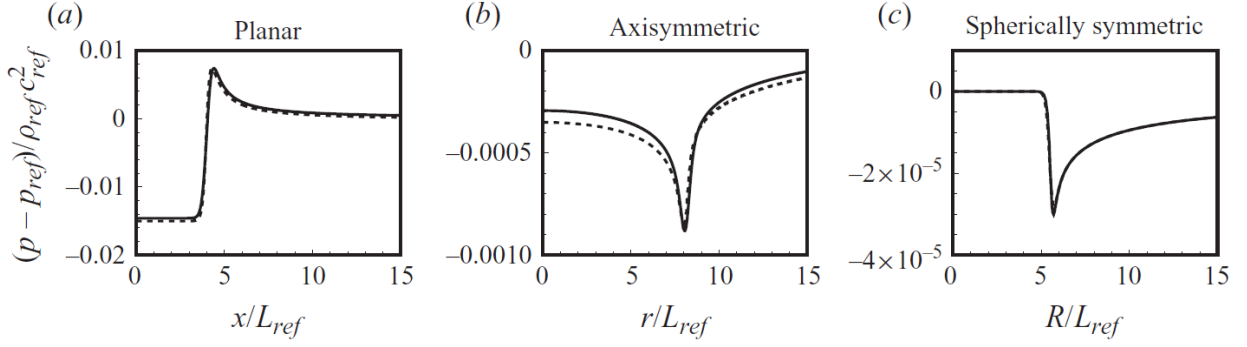


Figure 3: Comparison of the far-field pressure fluctuations from the DNS (solid line) and the solution of equation 3 (dashed line) for a) planar, b) axisymmetric and c) spherically symmetric annihilation.

4.1.2. Axisymmetric and spherically symmetric flame annihilation

For the axisymmetric and spherically symmetric annihilation events, the pressure wave produced by these events are shown in Figure 3. These pressure waves only feature negative values. In order to understand the source of these pressure waves, equation 3 is solved for these simple configurations using free-space Green's functions. There is a good agreement between this solution and the DNS results, confirming the dominance of the heat release rate fluctuations as a source of sound. Since annihilation events are responsible for destruction of the flame surface area, i.e. negative fluctuations of the heat release rate, it is expected to observe negative pressure fluctuations as a result.

4.1.3. Scaling laws

In this section, a scaling law will be presented to investigate the mechanism of sound generation by annihilation events. Using the analytical solution of equation 3 for all types of annihilation events with their corresponding Green's functions, a scaling law can be obtained to relate the generated sound p' to key flame parameters [15,16]:

$$\frac{p'}{\rho_u c_u^2} = \left(\frac{S_L}{c_u}\right)^{1+\frac{n}{2}} \left(\frac{\delta}{\zeta}\right)^{\frac{n}{2}} \left(1 - \frac{T_u}{T_b}\right) \left(\frac{T_b}{T_u}\right)^{\frac{2-n}{4}} g\left(\frac{T_b}{T_u}, \beta, Le, \zeta, t\right) \quad (4)$$

where $n = 0$ for planar, 1 for axisymmetric and 2 for spherically symmetric annihilation events. The variable δ is the flame thickness, ζ is the distance between the observer and the origin, $\frac{T_b}{T_u}$ is the temperature ratio, β is the Zel'dovich number and Le is the Lewis number.

Equation 4 explains how different configurations affect the radiated sound. While the flame thickness does not play a role for planar annihilation, it becomes an increasingly important parameter when the configuration changes from axisymmetric to spherically symmetric. This scaling shows that thicker flames will produce more sound when $n=1$ and 2. The dependency on S_L also becomes stronger as we move from planar to spherically symmetric annihilation. One should also note that the proposed scaling cannot fully explain the importance of parameters such as temperature

ratio, Zel'dovich number and Lewis number as all shown as parameters in the unknown function g . This motivated a separate DNS study, discussed in section 4.1.4.

4.1.4. Effects of key flame parameters on sound generation

In a series of DNS studies, the effects of parameters such as flame thickness, laminar flame speed, Zel'dovich number, temperature ratio and Lewis number on the generated sound by annihilation events were investigated [16]. Consistent results with the proposed scaling was generally observed. Amongst different parameters, the impact of Lewis number was particularly of interest. Three cases with the Lewis numbers of 0.5, 1 and 2 were considered. For the $Le=2$ case, a similar behaviour to the $Le=1$ case was observed except for a higher peak amplitude of the heat release rate during annihilation for the $Le=2$ case. This led to generation of a pressure wave featuring a large positive peak as well as the same negative pressure amplitude as the $Le=1$ case. This is linked to the fact that the preheat layer is thicker than the mass diffusion layer for $Le=2$, leading to the merging of the preheat layers at the initial stage of annihilation and therefore, providing additional heat. This then causes a higher peak amplitude for the heat release right before annihilation. For the $Le=0.5$ case, the mass diffusion layer is thicker. As a result, during annihilation, the unburnt gases are depleted and the flame is extinguished before it reaches the symmetry line. This process is relatively slow and therefore leads to generation of a pressure wave that has a large wavelength but the same negative pressure amplitude as the $Le = 1$ and 2 cases.



Figure 4 : Non-dimensional temperature fields at $St = 1$ (left column), $St = 0.1$ (middle column) and $St = 0.025$ (right column) of the perturbed flame at several instants during a forcing cycle. The Strouhal number is defined here as $St = fL_{ref}/c_{ref}$ where L_{ref} is half of the inlet width and c_{ref} is the speed of sound at the inlet.

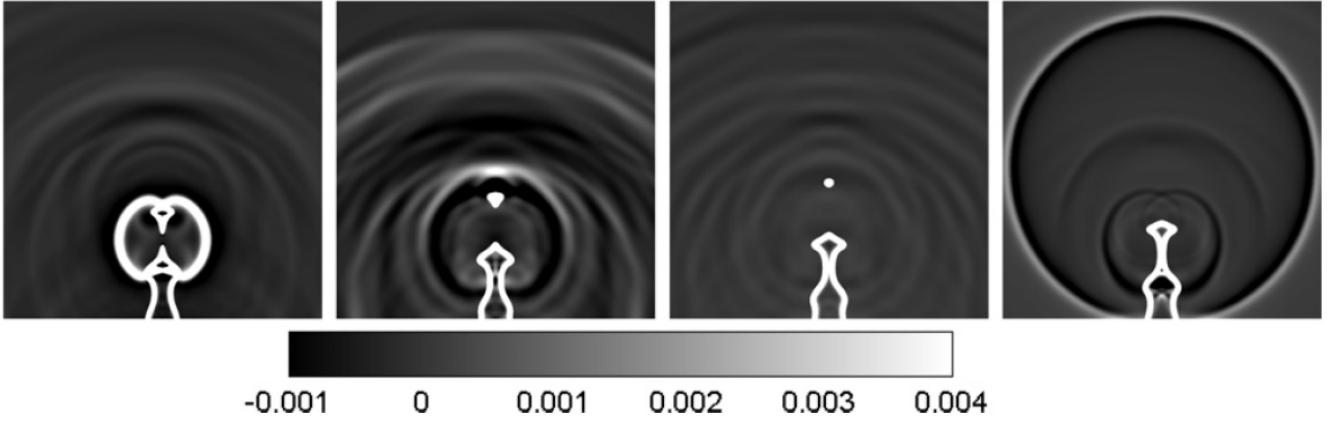


Figure 5: Dimensionless dilatation ($\nabla \cdot \mathbf{u}$) field for the $St=0.025$ case for several instants during a forcing cycle.

4.1.5. The importance of displacement speed

In a series of DNS and theoretical studies, the flame displacement speed was identified as a key parameter contributing to the radiated sound [15,16]. An example of a theoretical study is provided here. Considering the reaction rate as a delta-function with a constant consumption speed, i.e.,

$$\dot{\omega} = \rho_u S_L \delta(\zeta_f(\tau) - \zeta), \quad (5)$$

where ζ_f is the instantaneous flame location and ζ is the spatial coordinates, the pressure fluctuations in the far field can be described using the Green's function solution of equation 3. The solution for a spherically symmetric annihilation event is only expressed for brevity:

$$p'(R, t) = -2\rho_u S_L \left(1 - \frac{T_u}{T_b}\right) \times \zeta_f(t - R/c_b) V_f(t - R/c_b) H(t - R/c_b), \quad (6)$$

where V_f is the flame propagation velocity, R is the flame radius and H is a Heaviside step function. The flame propagation speed V_f can be described as a function of the gas velocity and the flame displacement speed:

$$V_f = u + S_d. \quad (7)$$

During annihilation, the flame experiences a large variation of S_d , therefore contributing to sound generation. The displacement speed can also be used as a marker to identify annihilation events as will be discussed in section 4.3.

4.2 Sound generation by 2D laminar flames

To further investigate the mechanism of sound generation in premixed flames, acoustically forced 2D flames are now considered. These flames are perturbed by imposing velocity fluctuations at the inflow. Figure 4 shows the instantaneous temperature fields for three forcing frequencies. The flame does not respond at the highest forcing frequency, corresponding to short acoustic wavelengths. As the forcing frequency decreases, increased flame wrinkling is observed, and a disturbance propagates along the flame surface at the convective wavelength U_{in}/f where U_{in} is the mean flow velocity. For the lowest forcing frequency, a high degree of wrinkling is observed. At some stage during the forcing period, this forms an elongated flame leading to a 'flame pinch-off' event, as a result of which a pocket of unburnt reactants is detached from the flame. This pocket is gradually consumed as it convects further downstream. The consumption of this pocket is referred to as an 'island burn-out' event.

Figure 5 shows the dilatation ($\nabla \cdot \mathbf{u}$) field at instants during one period of excitation for the $St = 0.025$ case. The dilatation is commonly used in aero-acoustic studies to identify sound, as pressure and dilatation are related for small Mach number flows. In the present study, the dilatation has the added property that it simultaneously shows the flame as well as the generated sound. It can be observed that the flame pinch-off and island burn-out events are strong sources of sound. The flame pinch-off event can be considered as a planar like annihilation event whereas the island burn out is analogous to an axisymmetric annihilation

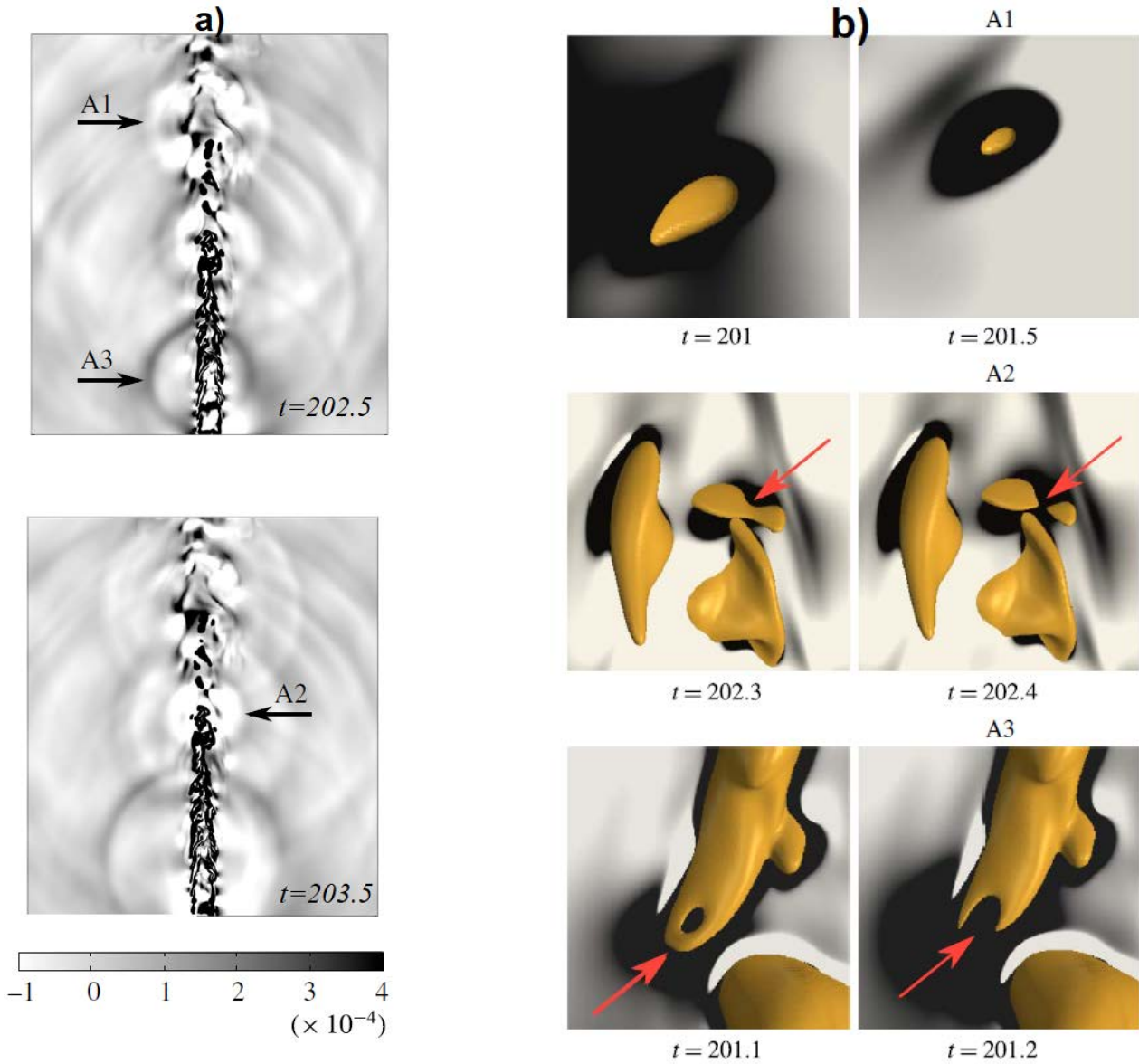


Figure 6: a) Dimensionless dilatation field for the $\phi=1$ case and b) iso-surface of progress variable superimposed on the dilatation field for the selected events A1-A3.

event both of which studied earlier in detail [15,16]. The next question is whether annihilation events are significant noise sources in turbulent premixed flames. This motivated the DNS study discussed in section 4.3.

4.3 Sound generation by turbulent flames

Sound generation by 3D turbulent flames described in section 3.2.2. is now examined. An instantaneous snapshot of the dimensionless dilatation field on the central x - y plane through the jet is shown for the $\phi=1$ case in Figure 6a. The presence of numerous spherical acoustic waves suggest that the acoustic field is dominated by monopolar noise sources. To further examine these sources, three events resulting in pressure waves shown with A1, A2 and A3 in the dilatation field are selected.

Figure 6b shows a flame iso-surface of progress variable for events A1, A2 and A3 in figure 3 superimposed on the dilatation field. The selected iso-surface corresponds to the point of the peak heat release in a one-dimensional premixed

flame with the same chemistry. The event A1 involves the consumption of a pocket of unburned gases in the downstream region near the flame tip. Consistent with our earlier studies [17], this phenomenon is referred to as ‘flame island burn out’. Event A2 is referred to as a ‘flame pinch-off’, with a pocket of unburned gases detaching from the flame surface. Finally, the event A3 takes place when flame-to-flame interaction first results in the formation of a tunnel of burned gas, and then the local flame area is lost due to cusp retraction associated with another pinch-off event. This first event is called ‘tunnel formation’. Figures 6b together with the results shown in figure 6a suggest that these frequent flame annihilation events play an important role in the generation of sound.

To accurately quantify the contribution of these events to the overall radiated sound by the flame, annihilation events were identified in a separate work by finding the critical points in the progress variable field [19]. An algorithm was developed to find these events in an automated process and track their position such that their individual contribution can be



Figure 7: A snapshot of the flame with the identified annihilation events using the critical points in the progress variable field. The two iso-surfaces represent the progress variable range used in the searching algorithm.

determined. The technique also allowed the categorisation of these events based on their topologies. In addition to the previously found topologies, i.e. tunnel formation, pinch-off and island burn out events, a new type referred to as multi-feature event was identified. In this type, a combination of 2 or 3 events from the first group occurs in the vicinity of each other such that they cannot be categorised as an individual event (see Figure 7).

Two important observations were made in this study. First, different topologies are very similar in terms of the magnitude of the pressure fluctuations as well as the duration of the pressure wave. The second observation was related to the contribution of these events to the far-field sound. It was shown that the high frequency side of the sound spectrum ($St > 1$, where $St = fD/U_{in}$) can be fully explained by these events while they are not the main sound source but still important on the low frequency side. This suggests appropriate models for these short time scale events need to be developed such that the overall sound generated by premixed flames can be predicted accurately.

4.4 Implications for modelling

Markstein theory has been extensively used to study the variation of displacement speed as a function of curvature or Karlovitz number Ka for unsteady flames:

$$\frac{S_d}{S_L} = 1 - Ma Ka, \quad (8)$$

where Ma is the Markstein number and,

$$Ka = \frac{\delta}{S_L} (a_T + Sd(\nabla \cdot \mathbf{n})). \quad (9)$$

The variable a_T is the tangential strain rate and $\mathbf{n} = \frac{\nabla Y}{|\nabla Y|}$ where Y is the progress variable.

This theory is particularly relevant for a level-set type combustion model where the evolution of the flame surface is the phenomenon of interest:

$$\rho \frac{\partial G}{\partial t} + \rho u_i \frac{\partial G}{\partial x_i} = \rho_0 S_d |\nabla G| \quad (10)$$

where G represents the flame front and ρ_0 is the fresh gas density. As can be seen, a correct estimation of S_d as a function of the local properties such as curvature and strain rate is an important part of this model.

As discussed in section 4.1.5., the displacement speed plays an important role in the generation of sound by annihilation events. To investigate whether Markstein theory is applicable for estimation of S_d , a joint PDF of S_d^*/S_L and Ka is shown in Figure 8. Note that $S_d^* = \rho S_d / \rho_u$. The iso-surface of the progress variable corresponding to the maximum reaction rate is chosen to collect the data. First, the entire flame surface is considered. As can be seen, there is a strong correlation between the displacement speed and Karlovitz number. The joint PDF for annihilation events identified by the points on the surface featuring $S_d^*/S_L > 5$ is shown in Figure 8b. A stronger correlation between the displacement speed and Karlovitz number is observed for these events. Least-squares fitting over the DNS data showed that a modified Markstein number referred to as *annihilation* Markstein number can reasonably describe the dynamics of annihilation events. This number was in agreement with that calculated by averaging the Markstein numbers of axisymmetric and spherically symmetric annihilation events under the same conditions as the turbulent flames.

5. Future work

The analyses presented for annihilation events showed that these events need special attention in terms of modelling. This is particularly important for large-eddy simulation (LES) of sound generation by premixed flames. The future work will therefore focus on developing combustion models for annihilation events using *a priori* and *a posteriori* analyses of the DNS data. This will provide grounds for testing these models under more realistic conditions (e.g. more relevant Reynolds numbers) obtained in experimental setups. As discussed in section 1, sound generation plays a key role in initiating thermoacoustic instability and therefore the ultimate goal is developing more accurate models that

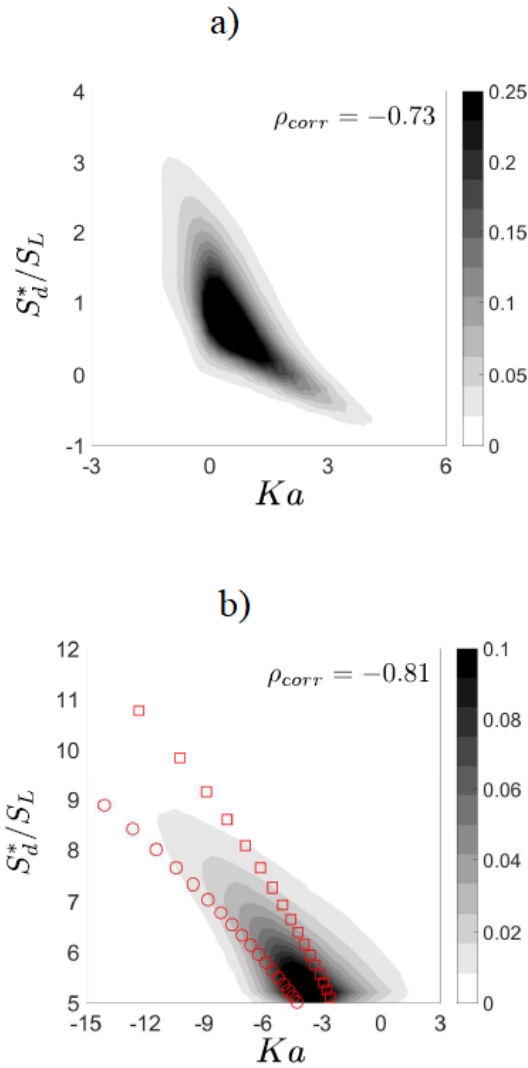


Figure 8: Correlation of the normalised stretch (Ka) with S_d^*/S_L for $\phi=1.0$ for a) the entire flame surface and b) considering only the annihilation events.

can be used to predict thermoacoustic instability in gas turbines.

6. Conclusions

This paper presented a technical review of our understanding of the mechanism of sound generation by premixed flames. Examples from the work undertaken at the University of Melbourne, mainly focused on direct numerical simulation (DNS) were provided. First, annihilation events as a significant source of heat release rate fluctuations and therefore sound generation were considered. To understand the mechanism of sound generation by these events, simple geometries including planar, axisymmetric and spherically symmetric annihilation events were examined. Scaling laws were proposed to estimate sound generation by these events. Then, the effect of key flame parameters such as flame thickness, laminar flame speed, temperature ratio, Zel'dovich number and Lewis number on the generated sound were investigated. Next, the significance of these events in 2D forced laminar flames and 3D turbulent

premixed flames was examined. An algorithm for identifying annihilation events was presented and the contribution of these events to the overall produced sound was shown to be significant, particularly on the high frequency side of the far-field pressure spectrum.

Furthermore, the implications of our findings for developing accurate models that can predict combustion-generated sound were discussed. It was shown that acceleration of the flame surface during annihilation has a significant contribution to the sound radiated by these events. Therefore, in the context of modelling, it is essential to model the annihilation process carefully. Analysis of the DNS data showed promising avenues to meet this requirement.

7. Acknowledgments

This work was supported by the Australian Research Council (ARC) [grant DP120102723 and DE180100416]. The author is grateful to the support of his PhD supervisors, Professor Michael Brear from the University of Melbourne and Professor Evatt Hawkes from the University of New South Wales (UNSW), former and current PhD students, Dr. Ali Haghiri and Mr. Davy Brouzet from the University of Melbourne, and Dr. Benedicte Cuenot from CERFACS for her help with NTMIX. This research was undertaken with the assistance of resources and services from the National Computational Infrastructure (NCI), which is supported by the Australian Government. This work was also supported by resources provided by the Pawsey Supercomputing Centre with funding from the Australian Government and the Government of Western Australia.

8. References

- [1] World Energy Outlook 2018, International Energy Agency, 2018.
- [2] Global Power Plant Database, <http://datasets.wri.org/dataset/globalpowerplantdatabase> (12/10/2019).
- [3] S. Candel; D. Durox; S. Ducruix; A.-L. Birbaud; N. Noiray; T. Schuller, *Int. J. Aeroacoust.* **8** (1) (2009) 1-56.
- [4] A. P. Dowling, Y. Mahmoudi, *Proc. Combust. Inst.* **35** (2015) 65–100.
- [5] M. Ihme, *Annu. Rev. Fluid Mech.* **49** (2017) 227–310.
- [6] R. Rajaram, T. Lieuwen, Acoustic radiation from turbulent premixed flames, *J. Fluid Mech.* **637** (2009) 357–38.
- [7] M.J. Lighthill, *Proc. R. Soc. London* **211** (1951) 564–587.
- [8] M.J. Lighthill, *Proc. R. Soc. London* **222** (1954) 1–31
- [9] A.P. Dowling, *Modern Methods in Analytical Acoustics*, Springer (pp. 378–403).
- [10] Brear M.J., Nicoud F., Talei M., Hawkes E. R., Giauque A., *J. of Fluid Mechanics*, **707**, (2012) 53-73.
- [11] Talei, M., Brear M. J., Hawkes E. R., *Theor. Comp. Fluid Dyn.* **28** (2014) 385-408.
- [12] B. Cuenot, B. Bedet, A. Corjon, *NTMIX3D user's guide manual* (1997) CERFACS.
- [13] J.H. Chen et al. *Comput. Sci. Disc.* **2** (2009) 015001.
- [14] S. Karami, E.R. Hawkes, M. Talei, J.H. Chen *J. Fluid Mech.* **777** (2015) 633–689.
- [15] Talei, M., Brear, M.J., Hawkes, E.R., *J. Fluid Mech.* **679** (2011) 194–218.
- [16] M. Talei, M.J. Brear, E.R. Hawkes, *Combust. Flame* **159** (2012) 757–769.
- [17] Talei, M., Brear, M.J., Hawkes, E.R., *Proc. Combust. Inst.* **34** (2013) 1093-1100.
- [18] A. Haghiri, M. Talei, M.J. Brear, E.R. Hawkes, *J. Fluid Mech.* **843** (2018) 29-52.
- [19] D. Brouzet, A. Haghiri, M. Talei, M.J. Brear, *Combust. Flame* **204** (2019) 268–277.
- [20] A. Haghiri, M. Talei, M.J. Brear, E.R. Hawkes, to appear in *Flow, Turb. Combust.* (2019).

Industrial Gas Turbine Combustor Design: Exhaust CO Emissions

Robert L. Gordon*

Department of Mechanical Engineering, The University of Melbourne, Victoria, Australia

Abstract

An industrial gas turbine (IGT) that is not compliant with emissions regulations on NO_x and CO will not be purchased. Similarly, an IGT that is used in a way that exceeds emissions limits will bring large financial penalties to the operator. Hence, the fundamental and applied study of CO formation and oxidation has occupied the gas turbine combustion research community for decades. Laboratory-scale combustors have generated CO emission data with seemingly contradictory trends to gas turbine engine trends. Emissions scaling correlations that have been developed cannot be used outside of their window of relevance, and CFD models are often limited by reduced chemistry and flamelet assumptions, even when incorporating non-adiabatic combustion models. The timescale competition between flow structures and CO oxidation chemistry is key to the prediction of CO emissions. These processes can be described by an inverse Damköhler number. However, determining and predicting these timescales is challenging. Recent work has demonstrated that finite cooling gradients, in addition to the residence time in an oxidising environment, play a key role in determining CO oxidation, and hence combustor emissions. In this context, flame-wall interaction (FWI) and flame-cooling-air interaction (FCAI) are shown to impact exhaust CO emission (CO_{ex}). It is then demonstrated that these concepts can represent the CO Turndown trends of an IGT combustor.

Keywords: Gas Turbine Emissions, Flame-Wall Interaction, Flame-Cooling Air Interaction, CO oxidation, DNS.

1. Introduction

Industrial Gas Turbines (IGTs) form an integral element in the transition to a sustainable energy economy [1]. Their role in energy systems with increasing penetration of non-dispatchable generation, such as wind and solar PV, will lead to an increased demand for operational flexibility. The operation of a gas turbine at part-power is limited by the increase of carbon monoxide (CO) emissions above regulated limits (e.g. 25ppmvd@15% O_2). This is known as CO Turndown. Typically, aero-derivative IGTs have a CO Turndown of around 80%, whereas large Frame IGTs have limits of 50% [2].

Optimising the combustor performance within the IGT requires trade-offs between competing design constraints of emissions limits (NO_x , CO, Soot), maximising efficiency, increased fuel flexibility and operability. For example, generally increasing residence time in the combustor will lead to lower CO, yet it will also enhance the production of NO_x , potentially beyond legislated limits. Higher temperatures lead to higher efficiency and lower CO but reach material design limits and NO_x emission limits. Material limits can be mitigated through using cooling air, but this removes from the air available for power generation in the combustion, reducing efficiency, and the increased use of cooling air has also been correlated with increased CO [3]. For a combustor design, the primary goal is to maximise the region between the high temperature limits due to NO_x emissions, and the low temperature limits due to CO emissions. This region is marked in Figure 1.

The challenges of predicting CO trends for a given combustor design are significant. Whereas the chemical pathways and timescales for thermal and prompt NO_x production have been reasonably well documented [4], CO oxidation in the flame, post-flame and quenching regions is still an area of active research.

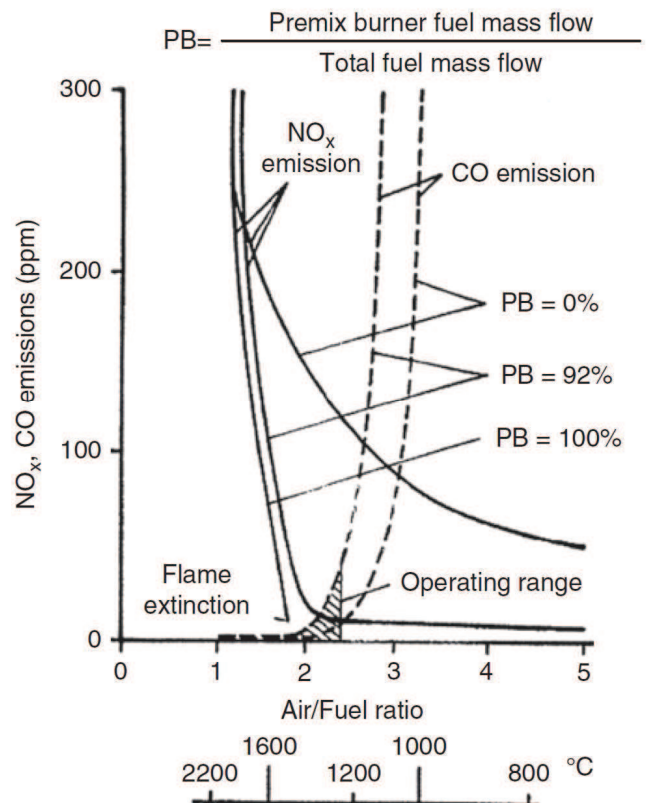


Figure 1: Representation of Industrial Gas Turbine emissions trends with respect to a representative combustor temperature or air/fuel ratio, adapted from [5].

From the equilibrium CO results in Table 1, ‘simple’ scalings do not describe the observed CO trends for IGTs. In case 1→2, increasing inlet or adiabatic flame temperatures (T_{in} , T_{adiab}) increases, not decreases, CO. For case 1→3, increasing pressure does indeed reduce CO, but increasing pressure through adiabatic compression, as in case 1→4, increases CO. In case 1→5, increasing the stoichiometry to the same T_{adiab} as case 2 increases CO

more than just the effect of the temperature increase alone. Where the equilibrium concentrations dominate, the coupling of these changes throughout the GT load range will produce behaviours that convolve these effects.

Table 1: Constant pressure equilibrium CO concentrations for a premixed methane-air flame, calculated with GasEq [6].

Case	Φ	T (K)	P (bar)	T _{adiab} (K)	CO _{eq} (ppmv)	CO _{eq} (ppmvd, 15%O ₂)
1	0.6	300	1	1665	10	5
2	0.6	600	1	1892	108	55
3	0.6	300	11.3	1665	3	1
4	0.6	600	11.3	1895	33	17
5	0.73	300	1	1887	151	66

The principal approaches for CO prediction in the gas turbine contexts have been through (a) empirical correlations, (b) semi-empirical correlations, and (c) numerical simulation. Empirical correlations are typically only valid for the combustor from which they were derived, so are limited in application. Semi-empirical correlations for CO draw on theoretical assumptions for a class of combustor, and then correlate emissions results to a pre-defined functional form. Numerical modelling, such as combustion CFD, attempts to simulate the combustor flow field and incorporate modelling assumptions for combustion species outputs.

This technical review will outline frameworks and achievements in this field, and draw attention to contemporary topics, such as flame-wall and flame cooling air interactions (FWI and FCAI). Section 2 introduces semi-empirical correlations and their theoretical foundations and limitations. As empirical correlations are engine specific, they are only briefly reviewed. Section 3 reviews the progress in non-adiabatic CO experimental studies that can be used to inform model development. Section 4 then demonstrates the challenges for CO modelling in CFD implementations. Section 5 highlights recent work, investigating the role of competing time scales in CO oxidation. Section 6 demonstrates a CO Turndown analysis (CO emissions response to part load) for an axially staged IGT combustor.

2. Semi-empirical correlations for CO

Through the 1970s, significant advances were made in aviation gas turbine combustion that reduced the soot and NO_x emissions by several orders of magnitude. Initially, empirical correlations were created to correlate combustor dimensions, design features, and operating conditions, as well as fuel type and fuel spray characteristics [3]. For the engine they are tuned to, they provide an excellent design tool for input parametric variations, and as such are the most commonly used tools in industry. However, they lack robustness for off-design investigation or combustor concept optimization, so are limited in use for future combustor development. This limitation led to analysis of the underlying physical and chemical processes in different combustor classes. Semi-empirical correlations have been created by combining these theoretical frameworks into

non-dimensional parameters, which are then plotted against engine emissions data for several engine types to determine the correlation coefficients. Scaling laws were determined for liquid fuel evaporation, bluff body wake residence times, shear-layer residence times, and chemical processes such as thermal NO_x formation and CO oxidation. The emissions behavior naturally followed a Damköhler number scaling of the representative flow time scales and chemical time scales.

The development of semi-empirical correlations for CO emissions for non-premixed combustion in aviation gas turbines was based on a linear relationship to an inverse Damköhler number representative of the quenching shear layer residence time and CO oxidation time. This was first proposed in Tuttle et al. [7], and modifications were required for these to be applicable to ‘utility combustion turbines’ to account for lean stoichiometries and gaseous fuels [8]. Conners et al. [9] proposed a modification for lean gaseous fueled ‘utility’ GTs which can be written:

$$COEI = a \frac{\tau_{CO}/\Phi_{py}}{\tau_{sl,CO}} + b \quad (1)$$

where COEI is the CO emissions index in g/kg of fuel, while a and b are the linear correlation coefficients for the data fitting. The stoichiometry of the primary zone as defined in the paper, is denoted by Φ_{py} , and the two time scales, τ_{CO} and $\tau_{sl,CO}$ are for the oxidation chemistry (Eq. 2) and the flow residence time in the shear layer of the bluff-body burner (Eq. 3), respectively.

$$\tau_{CO} = 0.001 \exp(10,760/R\bar{T}) \quad (2)$$

$$\tau_{sl,CO} = l_{quench}/V_{ref} \quad (3)$$

Here R is the universal gas constant, \bar{T} is the average of the inlet temperature and the adiabatic flame temperature at the total overall stoichiometry, l_{quench} is the length of the CO oxidation region from fuel injector to the end of oxidation region, and V_{ref} is a reference velocity given in Eq. 4.

$$V_{ref} = \frac{\dot{m}_a R_a T_{in}}{P_{in} A_{comb,max}} \quad (4)$$

The reference velocity is determined at the combustor inlet T_{in} and P_{in} . R_a is the gas constant for air. The total combustor air mass flow rate is \dot{m}_a , and the maximum area of the combustor is $A_{comb,max}$.

Such correlations demonstrated significant benefits in emissions prediction over empirical correlations tuned to individual engines. One of the most important advances was identifying that the flow time scales responsible for CO and NO_x were to some extent independent, enabling an optimization to occur to minimize both. Yet as critics have noted, these approaches are reliant on assumptions that have been tuned and cannot be applied across burner concepts (see comments section of [7,10]). Notably, a bluff-body combustor correlation, such as Eq. 1, cannot be used for a swirled burner, and Rich-Quench-Lean (RQL) correlations based on diffusion flames cannot be used for

Dry Low Emissions (DLE) combustors based on lean premixed flames. Concepts such as l_{quench} can only ever be an approximation of the turbulent combustion processes, and the treatment of the non-adiabatic combustion and quenching processes is not robust. That being said, these empirical and semi-empirical approaches are in active use industrially. Predictive Emission Monitoring Systems (PEMS) rely on simplified correlations to enable the control systems for IGTs to determine operating condition control. Hackney et al. [11] demonstrate the tuning of a Siemens IGT emissions control system through empirical correlation validated with Chemical Reactor Network (CRN) modelling.

3. Experimental Investigation of CO oxidation and quenching

3.1 CO from flame quenching in a swirl combustor

Recent investigation of IGT-relevant combustion conditions was undertaken by Marosky et al. [12]. The experiment was a GT-like swirling combustor, in a combustion rig capable of increased pressure, and fitted with CO probe sampling ports (see Fig. 2). These were positioned such that the in-flame CO could be sampled, as well as downstream of the combustion in the oxidation, or post-flame zone. Peak CO results of around 3000 ppmvd were measured, which are below the corresponding equilibrium values at the local temperatures.

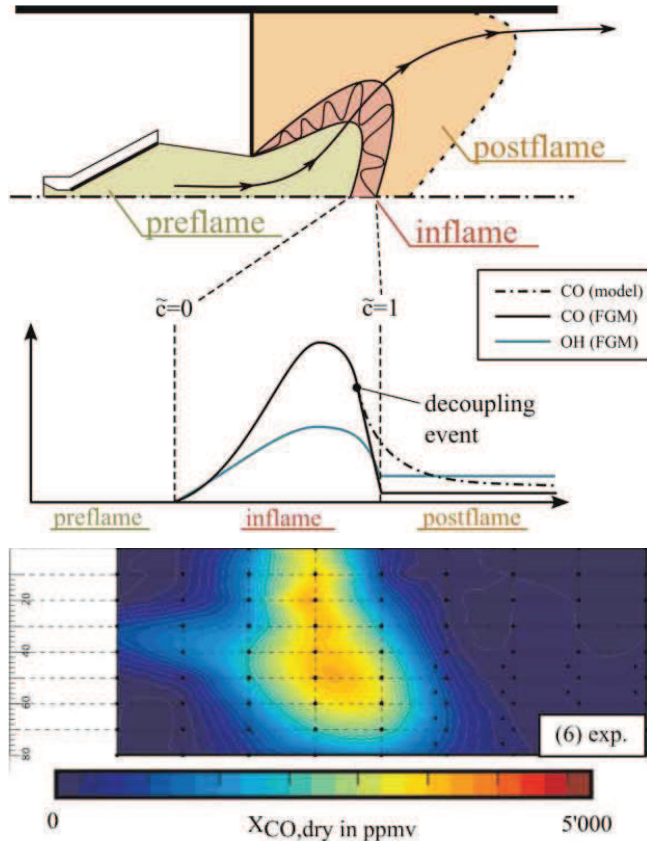


Figure 2: Schematic of the Marosky et al. experiment [12] (top) with CO regions identified. Centre image shows the decoupling of the CO from the flamelet manifold at the end

of the flame zone. Bottom image shows experimental CO[ppmv]. Adapted from [13].

Such data, combined with residence time assumptions, enables estimations of the oxidation source terms for model development.

3.2 Flame-wall Interaction on CO

Flame-wall interaction (FWI) has been shown to produce increased local CO concentrations [14]. Consequently, an understanding of FWI is necessary to determine how it could contribute to CO exhaust concentrations.

Mann et al. studied a Head-on Quenching configuration (HOQ) in [15] and demonstrated that the T-CO manifold for transient quenching events differed from the steady state quenching, confirming the impact of oxidation timescales on the local flame CO. In the same group, a novel side-wall quenching (SWQ) experiment has been developed [16]. An example of results are shown in Fig 3.

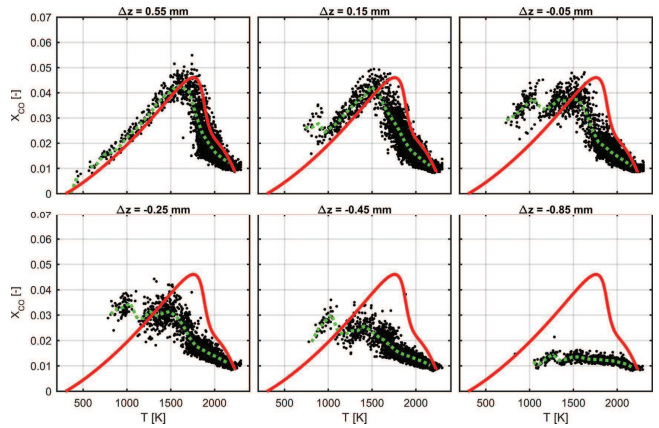


Figure 3: Scatter plots at bins of Δz . The quenching point is included in data at $z \approx -0.05$ mm. The green line represents the moving average of the measurement data and the red line is the profile of a freely propagating laminar flame. Experimental data for $\phi = 1$. Adapted from [16]

Conditional data upstream, within and downstream of the flame-wall interaction quantified the evolution of the flame-affected region and provided a database for the validation of numerical models. It was determined through the analysis of these results that the reaction term is negligible in the near wall transport of CO, and that convection and diffusion are the most important in this region.

The FWI investigations of Rivera et al. [17] focused on the CO emissions slightly downstream of the flame and at the exhaust, while perturbing the flame to determine what effects could be detected in the exhaust CO. Forcing frequency and amplitude were varied to investigate the transient effects, and the wall cooling was adjusted. While many of the parameters did not affect the semi-local results, the wall cooling altered the semi-local and exhaust CO (Fig. 4).

3.3 Flame-Cooling Air Interaction on CO

In effusion-cooled walls, holes in the combustor liner allow the cooling air to form a protective layer between the liner

and the flame, including the hot exhaust. The mass flow rate of this cooling air has been previously correlated with gas turbine exhaust CO emissions [18]. Effusion-cooled walls can induce flame-cooling-air interaction (FCAI) [19] which is theorised to be another source of engine-out CO [8]. Due to the difficulty of experimentally and numerically investigating FCAI, few studies have been done regarding this phenomenon. A model gas turbine combustor with an effusion-called wall has recently been commissioned for such an investigation [19,20].

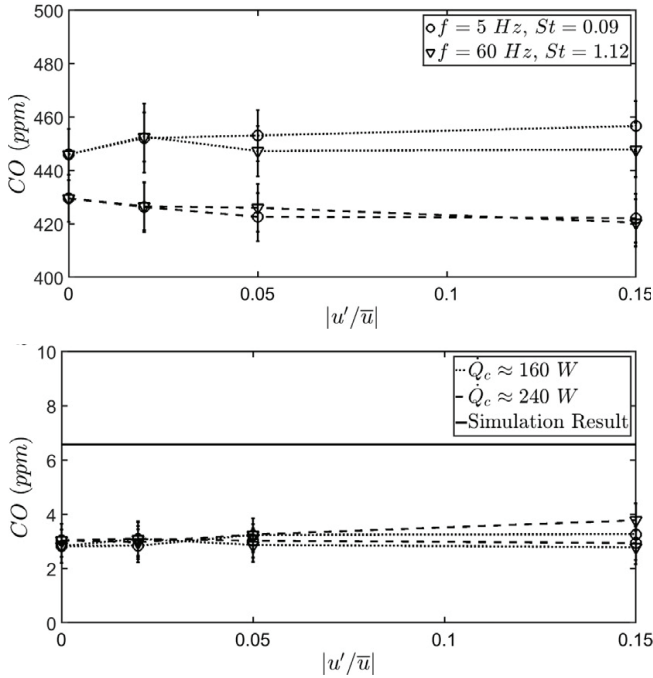


Figure 4: Amplitude response of CO emissions for semi-local (top) and end-gas (bottom). The results are shown for $f = 60 \text{ Hz}$ or $St = 1.12$ (triangle), $f = 5 \text{ Hz}$ or $St = 0.09$ (circle), $\dot{Q}_c \approx 160 \text{ W}$ (dots) and $\dot{Q}_c \approx 240 \text{ W}$ (dashed) cases, as well as the simulation result (solid). Adapted from [17].

It is unclear whether the measured CO comes from flame-cooling-air interaction (FCAI), or diversion of primary combustor air. A parametric study of post-flame and exhaust CO from FCAI in a premixed propane flame was undertaken by Rivera et al. [21] which revealed CO reduction with cooling and dilution in a laminar flame (Fig. 5). Residence times to the exhaust are of order 200ms, or an order of magnitude larger than GT combustor residence times, but sampling 40mm downstream of the flame was able to identify distinct CO profile impacts that prompted further investigation into the residence time and cooling trajectory of the exhaust gas.

In response to FWI and FCAI in a laminar premixed burner, decreasing CO_{ex} downstream of the flame correspond to decreased exhaust temperatures (T_{ex}), and increased diluent O_2 concentration. Reduced T_{ex} and increased exhaust O_2 concentration directly and independently produce decreased post-flame CO concentrations [17]. Calculation of equilibrium CO concentrations (CO_{eq}) indicated that this behaviour is due to thermodynamic favouring of CO oxidation under these conditions.

4. Challenges for CO modelling

Progress has been made in providing high-fidelity combustion emissions chemistry kinetics to tractable fluid dynamic modelling, such as the coupling of CFD with detailed kinetics reactor networks (CFD-CRN, e.g. [22–24]). However for CO, the inherent coupling of the flow and kinetic processes limits the applicability of CFD-CRN approaches for CO Turndown analysis.

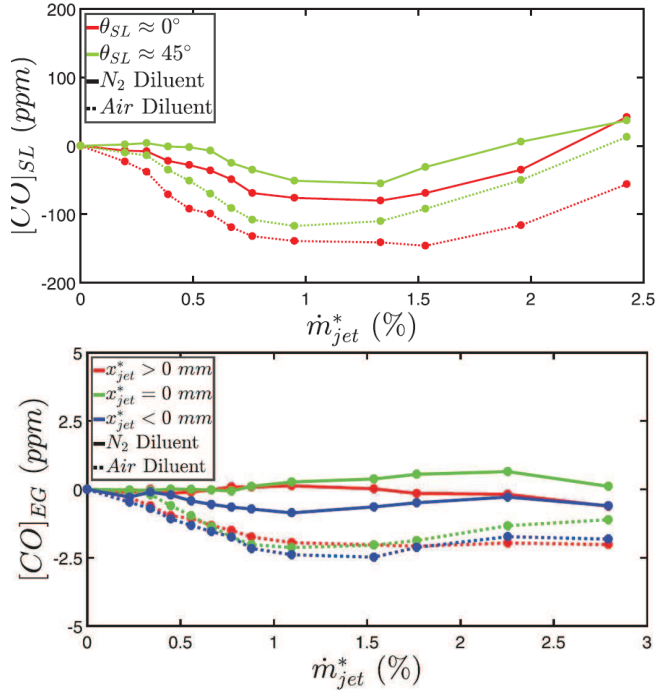


Figure 5: Semi-local CO_{SL} and exhaust gas CO_{EG} at different dilution rates and locations. CO_{SL} presented for sampling aligned with ($\theta_{\text{SL}} = 0^\circ$) and between ($\theta_{\text{SL}} = 45^\circ$) the cooling air jets. Results are shown for $x_{\text{jet}}^* > 0 \text{ mm}$ (red), $x_{\text{jet}}^* = 0 \text{ mm}$ (green) and $x_{\text{jet}}^* < 0 \text{ mm}$ (blue), for air (dots) and N_2 (solid) diluents. CO_{EG} values offset by the values at 0% dilution to aid comparison, adapted from [21].

4.1 Flame stretch and cooling effects

When modelling part-load, swirling, high Reynolds and Karlovitz number gas turbine combustors, combustion model assumptions that rely on adiabatic flames and unstretched flames tend to over-predict the combustion source term or reaction rate. As this is the first component of CO production, such discrepancies hinder the goal of predictive CO emissions modelling.

CFD combustion models such as the Flamelet Generated Manifolds (FGM) approach typically rely on tabulated adiabatic flamelet data. Recently Klarmann et al. implemented corrections to this modelling for both flame stretch and heat loss to investigate CO oxidation [25]. The flame stretch model adjustment could only explicitly account for strain as a proxy for total stretch. Heat loss is a modification to the energy transport equation to incorporate non-adiabatic enthalpy. These effects were demonstrated individually to improve the model results, and necessary to

be jointly implemented to correctly predict the flame location.

Other implementations for non-adiabatic flamelets have been developed (e.g. Ketelheun [26] as used in Heinrich et al. [27] for SWQ studies), the Flame Prolongation of ILDM (FPI, [28]), which lead to the REDIM (REaction and DIffusion Manifold, [29]) as demonstrated for HOQ [30] and SWQ [31]. The most recent development is the use of Quenching Flamelet Manifolds (QFM) to provide near-wall reaction and varying cooling rates [32].

4.2 Chemical kinetics and CO models

Accounting for heat loss and flame stretch in the combustion model has been demonstrated to be a necessary requirement for determining the flame position and source terms correctly. However, it was also demonstrated that this still not fully capture the behavior of CO oxidation. Klarmann et al. [13] implemented a decoupling of CO oxidation from the flamelet lookup table, and makes assumptions regarding the locally available OH in the post-flame gases. This approach incorporates heat loss and stretch effects into a transport equation for CO. This transport equation has a conditional source term that draws from peak equilibrium data in the flame when modified for stretch and heat loss. In the post-flame zone, an oxidation time scale is determined based on a locally determined Damköhler number connected to the OH radical chemistry. The impact of these effects is shown in Figure 6, and compares favourably with the measured CO data in the corresponding experiment in [12] (see Fig. 2).

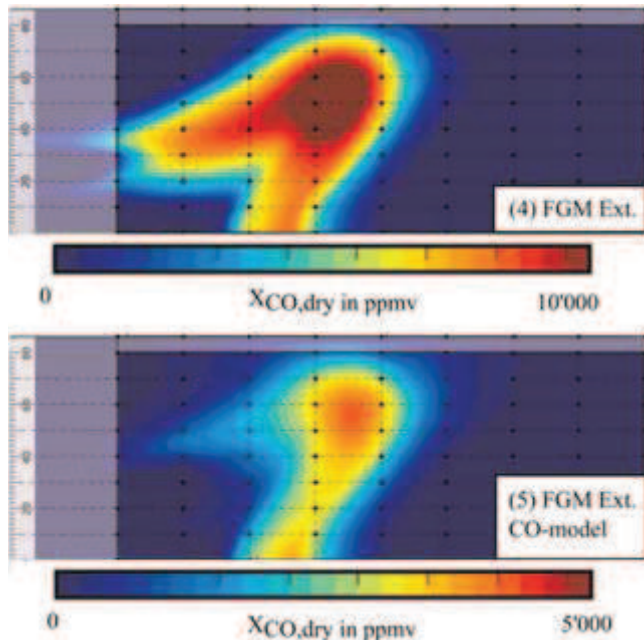


Figure 6: CO [ppmvd] from an FGM model modified for heat loss and flame stretch (top) and with an explicit CO transport and oxidation model (bottom). Adapted from [13].

It was also noted that this approach precluded the use of reduced chemical kinetic mechanisms. High fidelity is required in the equilibrium OH prediction. Errors in these

values can lead to several orders of magnitude underprediction of CO oxidation timescales.

5. Non-adiabatic DNS and kinetic studies of exhaust CO

5.1 DNS of Flame-Wall Interaction effects on CO

Direct Numerical Simulation of transient FWI with detailed chemistry and non-adiabatic walls has been undertaken recently to explore the impact of SWQ and HOQ on CO [33]. Figure 7 shows the CO contour map for an anchored premixed stoichiometric methane flame in a channel, simulated with NTMIX-CHEMKIN [34]. During the transient cycle, the flame is pushed away from the wall, re-approaches the wall in a SWQ configuration then pulls back to a HOQ configuration. The near-wall CO structures in the flame weaken during the cycle, and the post-flame oxidation results in lower CO at the domain exit. CO pockets, however, can be seen to be left behind of the upstream moving flame and are not then oxidized until the flame returns in its cycle.

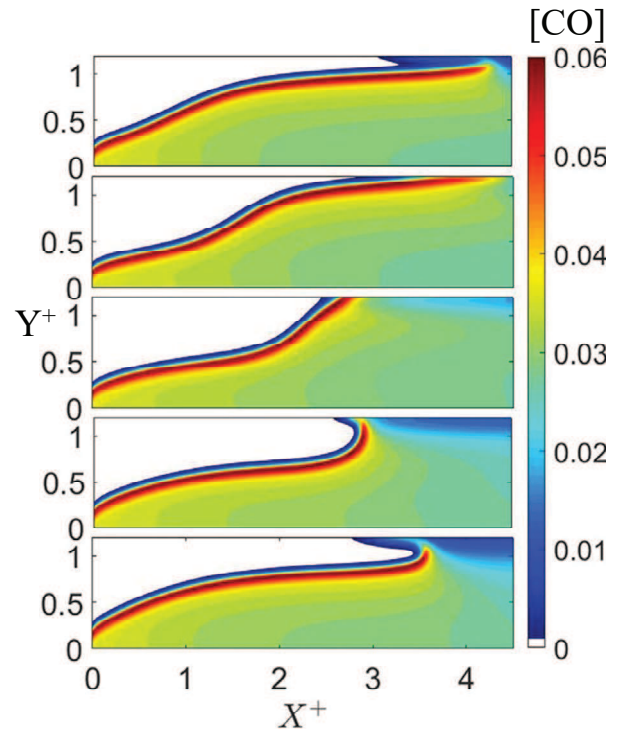


Figure 7: Contour plots of CO mass fraction for $St = 1$ at several instants during one cycle. Adapted from [33]

T-CO scatter plots at the same five reference times in the cycle are presented in Fig. 8, along with the 1D CHEMKIN freely propagating flame and head on quenching profiles. At $t = 0$ the 1D FPF solution provides an upper bound for a large range of temperatures. The near-wall CO is non-zero. As the flame gets closer to the wall ($t = T_p/5$), the near-wall CO increases and now the combination of the 1D HOQ and 1D FPF solutions set the limit to Y_{CO} . Large fluctuations of Y_{CO} at a given temperature are observed at different instants, and the distance from the wall does not seem to be responsible for these fluctuations. The level of fluctuations in the vicinity of the wall (where $T \sim T_{wall} = 800$ K) decreases for $t = 0$ and $4T_p/5$. These are the instants which

show SWQ-like behaviour. However, the instants showing the HOQ-like interaction show a higher spread of CO concentration. This shows the complex nature of transient FWI which presents a challenge in describing the near-wall.

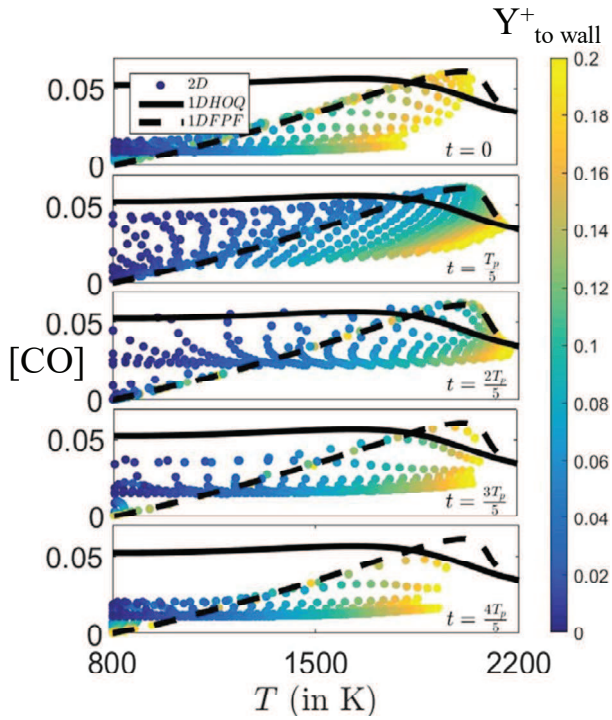


Figure 8: Scatter plots of CO mass fraction versus T (K) at several time instants in a forcing cycle for $St = 1$. Sample window width = 10 thermal flame thicknesses (δ_{th}) either side of the flame tip and height = $2\delta_{th}$ from the wall. 1D HOQ and 1D FPF are shown for reference. Points are coloured by distance from the wall. Adapted from [33]

It has also been determined that the wall can affect combustion mode if autoignition-based reactions such as found in Moderate to Intense Low Oxygen Dilute (MILD) combustion are present, and this may have consequences for CO oxidation timescales [35].

In Rivera et al. [21], 1D DNS with exhaust cooling and dilution is presented to improve understanding of FCAI impacts on CO. As the flame front is stabilized against the incoming premixture velocity only, only a limited range of residence time conditions is explored. These results identified, however, that cooling gradients and dilution of exhaust gases could have significant impact on exhaust CO.

5.2 Predicted CO Sensitivity to Cooling Rates

Sensitivity of CO concentration to varying ΔT and t_{cool} have been explored in [21]. A chemical kinetic analysis of a propane-air flame was undertaken with a Connected Reactor Network consisting of a freely propagating flame (FPF), a perfectly stirred reactor (PSR) to simulate the cooling and dilution air, then a non-adiabatic plug flow reactor (PFR) with various cooling profiles. The ΔT conditions in the PFR were chosen to achieve three T_{end} values representing GT-relevant exhaust temperatures. A T_{end} value of 1770 K represents combustor exit temperatures, while 860 K represents compressor exit

temperatures, and finally, 430 K represents engine-out exhaust temperatures [3,36]. The temperature profiles were generated with $\dot{q}_{wall} = \bar{\lambda}C_w(T - T_w)$ from Kosaka et al. [37], with T_w equal to the previously discussed T_{end} values, and with C_w varied to achieve these T_{end} values at a variety of t_{cool} values from 5 to 2000 ms. The CO trajectory values are presented in Fig 9, and the final values in Fig 10.

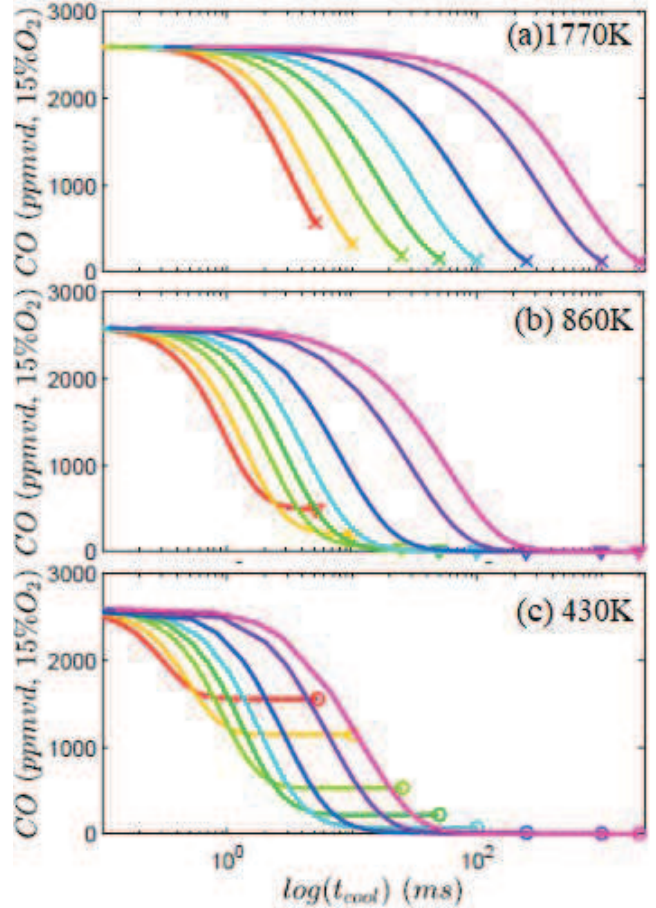


Figure 9: Profiles of CO (right column) in the PFR at varying maximum t_{cool} . T_{end} values of 1770 K (crosses), 860 K (triangles) and 430 K (circles). The CO results are shown in logarithmic time scale to highlight differences in CO_{end} . Adapted from [21]

For $T_{end} = 1770K$, given the only 354 K drop in temperature, the temperature profiles are almost linear with time. The CO_{end} for shorter maximum t_{cool} values are higher than for longer maximum t_{cool} values, despite T_{end} being identical for each t_{cool} case. This demonstrates that while CO_{eq} thermodynamically favours CO oxidation, it can be limited by the overall t_{cool} .

For the $T_{end}=860$ K case, the larger ΔT of 1264 K has non-linear monotonically decreasing temperature profiles. As $t_r > t_{cool}$, the CO profile gradients flatten, due to reduced CO oxidation rates. Hence CO oxidation is dependent on the exhaust cooling gradient, not only the absolute temperature.

For the $T_{end} = 430$ K case, the CO profiles also show the gradient flattening behaviour as $t_{cool} \rightarrow \max(t_{cool})$, similar to the $T_{end} = 860$ K case. However, the CO_{end} values that these correspond to are higher for the $T_{end} = 430$ K case. The

increased cooling rate of this case, due to the higher temperature drop can result in significant inhibition of CO oxidation, leaving values of CO_{end} greater than 1500 ppm.

The CO_{end} values for these cases are summarised in Fig. 10. For $T_{end} = 1770$ K, CO_{end} presents a decreasing trend with increased $\max(t_{cool})$, converging to a value of 115.7 ppm at $\max(t_{cool}) = 2000$ ms. This value is close to the CO_{eq} value of 113.1 ppm at this T_{end} . This can be considered as reaching equilibrium and implies an approximately zero net oxidation rate. This oxidation regime can be described as “equilibrium-dominated” since the oxidation behaviour is largely dictated by the equilibrium state. For $T_{end} = 860$ K, a similar decrease in CO_{end} is seen as $\max(t_{cool})$ is increased but converges to a lower CO_{end} value of 0.005 ppm at $\max(t_{cool}) = 2000$ ms. The CO_{end} value at this condition is due to the CO_{eq} of 0.002 ppm at a $T_{end} = 860$ K. This difference in CO_{end} highlights the temperature dependence of CO oxidation, not only due to the rate constant, but also due to the CO_{eq} imposed by the temperature.

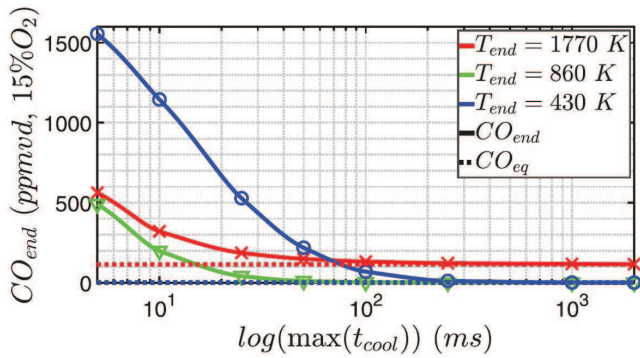


Figure 10: Exhaust CO determined for a combination of exit target temperatures. Each symbol represents the result of a different cooling residence time to achieve the T_{end} . Equilibrium CO lines are also shown, dashed [21].

At $T_{end} = 430$ K the CO_{end} value of 0.12 ppm at $\max(t_{cool})$ is three orders of magnitude larger than the corresponding CO_{eq} value of 0.0009 ppm. Given the flattening of the CO profiles shown in Fig. 11, this is evidence of decreasing temperatures inhibiting CO oxidation despite CO_{eq} thermodynamically promoting CO oxidation. Thus, this regime of oxidation behaviour can be described “kinetically-dominated”, where oxidation is limited by the kinetic rate despite being thermodynamically favoured. Under this condition, high CO_{end} values are achieved, with 68.7 ppm produced at $\max(t_{cool}) = 100$ ms.

5.3 CO Turndown for an axially staged combustor

Where residence time is fixed by some geometric constraint such as the combustor size and a prescribed flow factor, the combined effects of fuel stoichiometry, inlet pressure and temperature, and exhaust target temperature due to part-load operation can be mapped to determine the first order response of CO turndown (Fig. 11). Here, minimum CO values are found at intermediate exhaust temperatures, and high and low exhaust temperatures lead to increases in CO. An axially staged combustor for an IGT splits the fuel mass flow between consecutive primary (Py) and secondary (Sy)

combustion chambers, then a discharge nozzle (DN) distributes the combustion gases to the turbine. The bulk flow residence times for the whole combustor can be estimated and then used as a budget for the design choices for the Py, Sy and DN sectors. Scaling of temperatures, pressures and fuel flow choices can be made to develop a representative part-load map of operating conditions.

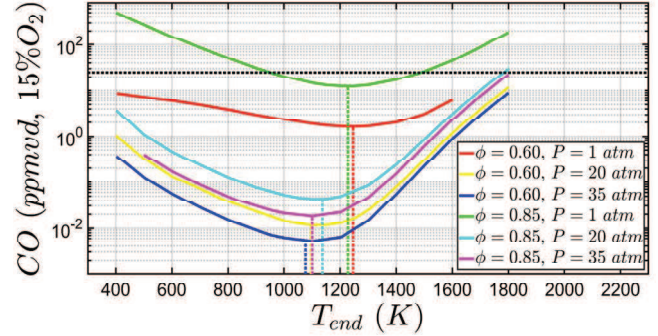


Figure 11: Combustor exit CO versus T_{end} for a 20 ms residence time with varying stoichiometry and pressure.

Figure 12 summarises the result of one such analysis from work recently submitted [38]. The low- and high-power behavior of the CO concentrations are highly representative of observed IGT trends of compliant CO down to a given power level, then sudden increases in CO concentration.

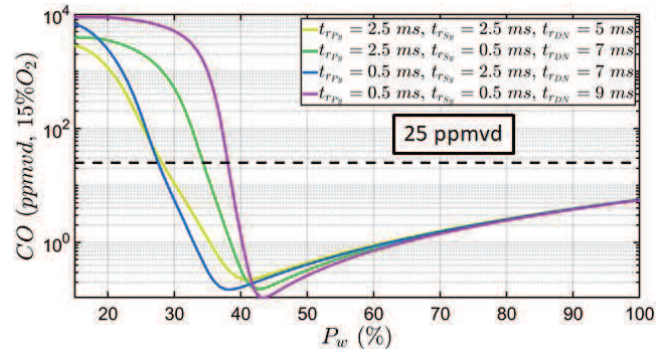


Figure 12: Combustor exit CO at various representative loads P_w , for different combinations of axially staged combustor residence times.[38]

6. Conclusions

This technical review summarises research into exhaust CO emissions measurement and prediction in industrial gas turbine contexts. The goal is to enable the prediction of CO trends for part-load operation, also known as the CO Turndown. Semi-empirical correlations are reviewed to highlight the issues of competing timescales in CO oxidation, noting that the challenges can be expressed in terms of CO oxidation timescales and relevant fluid dynamic timescales. The challenges lie in evaluating these timescales, and their effects on the CO manifold. The progress of modelling efforts has also been examined, including where flame stretch and heat loss effects have been considered. Explicit transport of CO may be required to enable the decoupling of post-flame oxidation from flamelet approximations, and the modelling of this is sensitive to the selection of chemical kinetic mechanism.

Recent and ongoing studies into the discrepancies between equilibrium CO and the quenching of the CO oxidation reactions have highlighted that not only are CO oxidation residence times important, the gradient of the quenching cooling rate is a key parameter. When such concepts are employed in representative kinetic studies, the approximate CO Turndown trends of an IGT may be approximated.

7. Acknowledgments

The significant efforts of the FWI research group at the University of Melbourne is acknowledged: Dr Mohsen Talei, Jacob Rivera, Rahul Palulli, Bin Jiang. The support of the European Centre for Research and Advanced Training in Scientific Computation (CERFACS, <http://www.cerfacs.fr>) is acknowledged in providing the source code for NTMIX-CHEMKIN. Aspects of this work have been supported by the Australian Research Council (ARC) [grant DE180100416] and the University of Melbourne through the Melbourne Research Scholarship. This research was undertaken with the National Computational Infrastructure (NCI), and by the Pawsey Supercomputing Centre with funding from the Australian Government and the Government of Western Australia.

8. References

- [1] M.J. Brear, M. Jeppesen, D. Chattopadhyay, C.G. Manzie, R. Dargaville, T. Alpcan, Least Cost, Utility Scale Abatement from Australia's National Electricity Market (NEM). Part 2: Scenarios and Policy Implications, *Energy*. 101 (2016) 621–628.
- [2] G. Bourque, Private communication, (2019).
- [3] A.H. Lefebvre, D.R. Ballal, Gas turbine combustion: alternative fuels and emissions, 3rd ed., CRC Press, Boca Raton, FL, 2010.
- [4] P. Versailles, A. Durocher, G. Bourque, J.M. Bergthorson, Nitric oxide formation in lean, methane-air stagnation flames at supra-atmospheric pressures, *Proc. Combust. Inst.* 37 (2019) 711–718.
- [5] H. Maghon, A. Kreutzer, H. Termuehlen, The V84 Gas Turbine Designed for Base-Load and Peaking Duty, *Proc. Am. Power Conf.* 60 (1988) 218–228.
- [6] C. Morley, GasEq: A Chemical Equilibrium Program for Windows (GasEq.co.uk), (2005).
- [7] J.H. Tuttle, M.B. Colket, R.W. Bilger, A.M. Mellor, Characteristic times for combustion and pollutant formation in spray combustion, *Symp. Combust.* 16 (1977) 209–219.
- [8] S.M. Correa, Carbon Monoxide Emissions in Lean Premixed Combustion, *J. Propuls. Power.* 8 (1992) 1144–1151.
- [9] C.S. Connors, J.C. Barnes, A.M. Mellor, Semiempirical predictions and correlations of CO emissions from utility combustion turbines, *J. Propuls. Power.* 12 (1996) 926–932.
- [10] J.B. Howard, G.C. Williams, D.H. Fine, Kinetics of carbon monoxide oxidation in postflame gases, *Symp. Combust.* 14 (1973) 975–986.
- [11] R. Hackney, S.K. Sadasivuni, J.W. Rogerson, G. Bulat, Predictive emissions monitoring system for small siemens dry low emissions combustors: Validation and application, *Proc. ASME Turbo Expo.* 4B-2016 (2016) 1–8.
- [12] A. Marosky, V. Seidel, T. Sattelmayer, F. Magni, W. Geng, Impact of cooling air injection on the combustion stability of a premixed swirl burner near lean blowout, *Proc. ASME Turbo Expo.* 1 A (2013) 1–9.
- [13] N. Klarmann, B.T. Zoller, T. Sattelmayer, Numerical modeling of co-emissions for gas turbine combustors operating at part-load conditions, *J. Glob. Power Propuls. Soc.* 2 (2018) 376–387.
- [14] A. Dreizler, B. Böhm, Advanced laser diagnostics for an improved understanding of premixed flame-wall interactions, *Proc. Combust. Inst.* 35 (2015) 37–64.
- [15] M. Mann, C. Jainski, M. Euler, B. Böhm, A. Dreizler, Transient flame-wall interactions: Experimental analysis using spectroscopic temperature and CO concentration measurements, *Combust. Flame.* 161 (2014) 2371–2386.
- [16] C. Jainski, M. Reißmann, B. Böhm, J. Janicka, A. Dreizler, Sidewall quenching of atmospheric laminar premixed flames studied by laser-based diagnostics, *Combust. Flame.* 183 (2017) 271–282.
- [17] J.E. Rivera, R.L. Gordon, M. Talei, Flame-wall interaction of a forced laminar premixed propane flame: Flame dynamics and exhaust CO emissions, *Proc. Combust. Inst.* 37 (2019) 5385–5392.
- [18] G. Andrews, M. Kim, The influence of film cooling on emissions for a low NOx radial swirler gas turbine combustor, in: *ASME Turbo Expo*, 2001: pp. 2001-GT-0071.
- [19] J. Hermann, M. Greifenstein, B. Böhm, A. Dreizler, Experimental Investigation of Global Combustion Characteristics in an Effusion Cooled Single Sector Model Gas Turbine Combustor, *Flow, Turbul. Combust.* 102 (2019) 1025–1052.
- [20] M. Greifenstein, J. Hermann, B. Boehm, A. Dreizler, Flame-cooling air interaction in an effusion-cooled model gas turbine combustor at elevated pressure, *Exp. Fluids.* 60 (2019) 1–13.
- [21] J.E. Rivera, R.L. Gordon, D. Brouzet, M. Talei, Exhaust CO emissions of a laminar premixed propane – air flame interacting with cold gas jets, *Combust. Flame.* 210 (2019) 374–388.
- [22] R.F.D. Monaghan, A. Cuoci, G. Bourque, M. Fu, R.L. Gordon, T. Faravelli, et al., Detailed multi-dimensional study of pollutant formation in a methane diffusion flame, *Energy & Fuels.* 26 (2012) 1598–1611.
- [23] R.F.D. Monaghan, R. Tahir, G. Bourque, R.L. Gordon, A. Cuoci, T. Faravelli, et al., Detailed Emissions Prediction for a Turbulent Swirling Nonpremixed Flame, *Energy & Fuels.* (2014).
- [24] S. Yousefian, G. Bourque, R.F.D. Monaghan, Review of Hybrid Emissions Prediction Tools and Uncertainty Quantification Methods for Gas Turbine Combustion Systems, in: *Proc. ASME Turbo Expo 2017*, American Society of Mechanical Engineers, Charlotte, USA, 2017: pp. GT2017-64271.
- [25] N. Klarmann, T. Sattelmayer, W. Geng, F. Magni, Flamelet generated manifolds for partially premixed, highly stretched and non-adiabatic combustion in gas turbines, 54th AIAA Aerosp. Sci. Meet. (2016).
- [26] A. Ketelheun, G. Kuenne, J. Janicka, No Title Heat transfer modeling in the context of large eddy simulation of premixed combustion with tabulated chemistry, *Flow, Turbul. Combust.* 91 (2013) 867–893.
- [27] A. Heinrich, S. Ganter, G. Kuenne, C. Jainski, A. Dreizler, J. Janicka, 3D Numerical Simulation of a Laminar Experimental SWQ Burner with Tabulated Chemistry, *Flow, Turbul. Combust.* 100 (2018) 535–559.
- [28] B. Fiorina, R. Baron, O. Gicquel, D. Thevenin, S. Carpentier, N. Darabiha, Modelling non-adiabatic partially premixed flames using flame-prolongation of ILDM, *Combust. Theory Model.* 7 (2003) 449–470.
- [29] V. Bykov, U. Maas, The extension of the ILDM concept to reaction-diffusion manifolds, *Combust. Theory Model.* 11 (2007) 839–862.
- [30] G. Steinhilber, V. Bykov, U. Maas, REDIM reduced modeling of flame-wall-interactions: Quenching of a premixed methane/air flame at a cold inert wall, *Proc. Combust. Inst.* 36 (2017) 655–661.
- [31] S. Ganter, C. Straßacker, G. Kuenne, T. Meier, A. Heinrich, U. Maas, et al., Laminar near-wall combustion: Analysis of tabulated chemistry simulations by means of detailed kinetics, *Int. J. Heat Fluid Flow.* 70 (2018) 259–270.
- [32] D. V. Efimov, P. de Goey, J.A. van Oijen, QFM: quenching flamelet-generated manifold for modelling of flame-wall interactions, *Combust. Theory Model.* 7830 (2019) 1–33.
- [33] R. Palulli, M. Talei, R.L. Gordon, Unsteady flame-wall interaction: Impact on CO emission and wall heat flux, *Combust. Flame.* 207 (2019) 406–416.
- [34] M. Baum, T.J. Poinso, D.C. Haworth, N. Darabiha, Direct numerical simulation of H₂/O₂/N₂ flames with complex chemistry in two-dimensional turbulent flows, *J. Fluid Mech.* 281 (1994) 1–32.
- [35] B. Jiang, R.L. Gordon, M. Talei, Head-on quenching of laminar premixed methane flames diluted with hot combustion products, *Proc. Combust. Inst.* 37 (2019) 5095–5103.
- [36] T. Lieuwen, V. Yang, Gas Turbine Emissions, Cambridge University Press, New York, 2013.
- [37] H. Kosaka, F. Zentgraf, A. Scholtissek, L. Bischoff, T. Häber, R. Suntz, et al., Wall heat fluxes and CO formation/oxidation during laminar and turbulent side-wall quenching of methane and DME flames, *Int. J. Heat Fluid Flow.* 70 (2018) 181–192.
- [38] J.E. Rivera, R.L. Gordon, M. Talei, G. Bourque, Optimisation of Co Turndown for an Axially Staged Gas Turbine Combustor, *ASME GT Expo.* (2020) (abstract accepted).

Combustion strategies for multi-fuel capable compression ignition engines

S. Kook*, H. Goyal and Y. Zhang

School of Mechanical and Manufacturing Engineering, The University of New South Wales, Sydney, Australia

Abstract

Optimising combustion strategy in relation to variation in fuel types is crucial in achieving high efficiency and low air pollution emissions in compression ignition (CI) engines. This study conducts optical/laser-based imaging diagnostics in a CI engine fuelled with a conventional diesel fuel and a gasoline-like low ignition quality fuel to explore the potential of multi-fuel capable CI engines. In the optically accessible engine, planar laser-induced fluorescence imaging of formaldehyde (HCHO-PLIF), hydroxyl (OH-PLIF), and fuel (fuel-PLIF) has been performed. For gasoline CI (GCI) combustion, not only single injection but also double injection strategies were investigated, which was to increase the mixture homogeneity and thereby reducing soot and NO formation. The results showed that, for single-injection GCI combustion, the OH radicals first develop from the HCHO distributed along the piston-bowl wall, displaying multiple ignition kernels that progressively merge to form larger high-temperature reaction zones. This ignition process was very different to diesel combustion in which HCHO and OH first appear on the jet axis and co-exist near the bowl wall during the transition from low- to high-temperature reactions. The double-injection GCI combustion had higher charge premixing than the other cases and, due to very early first injection, the mixture homogeneity was also much higher. This was evidenced by a higher consumption rate of HCHO and faster development of OH across the entire reaction zones, indicating faster low- to high-temperature reaction transition. The engine efficiency and emissions of this double-injection GCI combustion was further exploited in a single-cylinder non-optical version of the same engine. From the tests performed for various engine speeds, it was demonstrated that the double-injection GCI could achieve higher efficiency and simultaneous reduction of smoke and NO_x emissions compared to diesel combustion.

Keywords: CI engine, Gasoline compression ignition, Diesel combustion, Optical engine, Engine efficiency

1. Introduction

Reduced engine-out emissions of nitrogen oxides (NO_x) and particulate matter (PM) without compromising thermal efficiency and fuel economy is a critical concern for the future survival of automotive diesel engines. On the in-cylinder control side, much effort is made to extend the ignition delay for higher charge premixing and mixture homogeneity, which is limited due to high ignition quality of diesel fuels [1]. Therefore, gasoline-burning compression ignition (GCI) combustion has been extensively investigated [2,3] in which gasoline as a low ignition quality fuel is delivered into the combustion chamber directly to realise partially premixed charge combustion [4–8]. Compared to conventional diesel combustion, it has been shown that the increase in charge premixing and enhanced mixture homogeneity results in much lower particulates and NO_x emissions [9,10]. In addition to this emissions benefit, GCI combustion has a great potential to achieve multi-fuel capable engines in which both gasoline and diesel could be used in a single platform.

The partial premixing differentiates GCI combustion from homogeneous charge compression ignition (HCCI) combustion [11–16] or its variants such as stratified charge compression ignition (SCCI) [17,18] and premixed charge compression ignition (PCCI) [19]. In the GCI engine, the fuel injection event is closely coupled with the combustion phasing and thereby extending the operation range compared to HCCI [9,20]. This is achieved by forming “partially” premixed charge – i.e. higher premixing and mixture homogeneity than conventional diesel but lower charge premixing/homogeneity than HCCI [21–25].

The fuel injection strategy in GCI engines make a substantial impact on both efficiency and emissions [3,26]. For instance, a double-injection strategy has shown the independent control of mixture homogeneity of the early first injection and charge premixing of the late second injection, which cause a lower rate of pressure rise, extended high-load limit and better combustion stability [6,10,27,28]. Due to a stretched heat release rate profile over wider crank angles and direct combustion phasing control [3], double-injection strategy also results in lower fuel consumption compared to single-injection GCI combustion [27]. Moreover, enhanced mixture homogeneity, i.e. lean mixtures uniformly distributed inside the cylinder, contributes to suppressed thermal NO and soot formation simultaneously, similar to HCCI combustion [29–31], while the uHC and CO emissions are lower by maintaining adequate high combustion temperature in the partially premixed charge.

Previous studies evaluated the engine performance and emissions of GCI combustion [2,3,9,21,24,32] from which a good understanding of engine efficiency and engine-out emission trends has been developed. Recent studies also showed the development of low- and high-temperature reactions during the ignition process in GCI engines [33–36]. This is because the low temperature reaction and high temperature reaction during the ignition process of GCI combustion could play a crucial role in controlling the combustion phasing. It was shown that, during the low-temperature reaction, formaldehyde (HCHO) formation occurs [37–40], which is followed by hydroxyl (OH) radical formation [41–44]. Recent GCI engine studies reported that HCHO initially fills the entire combustion chamber due to extended ignition delay and increased

* Corresponding author. Email: s.kook@unsw.edu.au

charge premixing, which is consumed to generate OH radicals in the ignition kernels from which the flame front develops [33,34]. Similarly, an innovative research implementing 36-kHz high-speed planar imaging of fuel and HCHO showed that the ignition develops from fuel-rich mixtures formed in the jet-jet interaction region, which is followed by subsequent ignition at the mixture periphery [36].

This paper provides a summary of the major findings made from various experimental studies conducted at the UNSW Engine Research Laboratory with an aim to advance our understanding of GCI combustion [6,8,10,27,35,45,46]. For the past four years, both engine efficiency and emissions testing [6,8,10,27,46] and optical combustion diagnostics [35,45] were conducted in a metal and optical version of the same single-cylinder automotive CI engine. The results provide a unique opportunity to directly compare diesel and GCI combustion in the same engine while also offering a comparative analysis of engine performance and emissions with a help of fundamental knowledge gained from the optical combustion diagnostics.

2. Experiments

2.1 Optical compression ignition engine

The schematic diagram of the single-cylinder diesel engine and optical/laser-based diagnostics setup used in the present study is illustrated in Fig. 1. The specifications of this 0.5-litre engine are listed in Table 1. The laser sheet represented by a green dashed line was inserted into the combustion chamber through a 45-mm-wide liner quartz window and 35-mm-wide bowl-rim quartz window. To understand the flame development in vertical direction, two laser planes were selected at 8 and 10 mm below the cylinder head, as shown in Fig. 1(top-left). The images were captured through the quartz piston top and a 45° mirror placed within the hollow space of the extended piston. This resulted in 43

mm circular field of view for the bottom-view image.

Out of various optical/laser-based imaging diagnostics performed in the engine, four images of cool-flame chemiluminescence, OH* chemiluminescence, planar laser-induced fluorescence of formaldehyde (HCHO-PLIF) and PLIF of hydroxyl (OH) are to be discussed in this paper with an emphasis on ignition process. The images were capture using an ICCD camera (LaVision NanoStar) and a 105-mm lens at f/4.5 with UV-enhanced optics for 85% transmission. For cool-flame imaging, the camera gain was set at 90% of the maximum value while the exposure time was set at 100 μ s. For OH* chemiluminescence imaging, additional filters were used to block the interference signals, which included two WG-295 and two WG-305 filters as well as a 300-nm band pass filter (40-nm FWHM). The selected camera gain was 80% of its peak value and the exposure time was set at 70 μ s. For OH-PLIF imaging, an Nd:YAG laser (SpectraPhysics Quanta-Ray Pro-230) was used to pump a dye laser (Sirah CobraStretch) filled with Rhodamine-6G. This set of lasers was used to generate 10-Hz laser pulses at desired wavelength. Through dichroic mirrors and sheet-making optics constituting a combination of plano-concave and plano-convex lenses, a 35 mm wide and 0.3 mm thick laser sheet was generated, which was then directed towards the cylinder liner and piston bowl-rim windows as mentioned previously. For OH-PLIF, a 284 nm laser beam with high energy of 22 mJ/pulse was utilised. This was to image the fluorescence signals emitted in the wavelength range of 308-320 nm when excited OH radicals return to their ground state. On the ICCD camera, the same filter pack as that of OH* chemiluminescence was used and the gain was set at 90% of its maximum value with short exposure time of 160 ns. For HCHO-PLIF imaging, a third harmonic (i.e. 355 nm) of the Nd:YAG laser at very high energy of 120 mJ/pulse was used. As a good marker of low-temperature reaction, HCHO fluorescence signals are emitted in the wavelength range of 380-450 nm, which was recorded using the same ICCD camera as other diagnostics

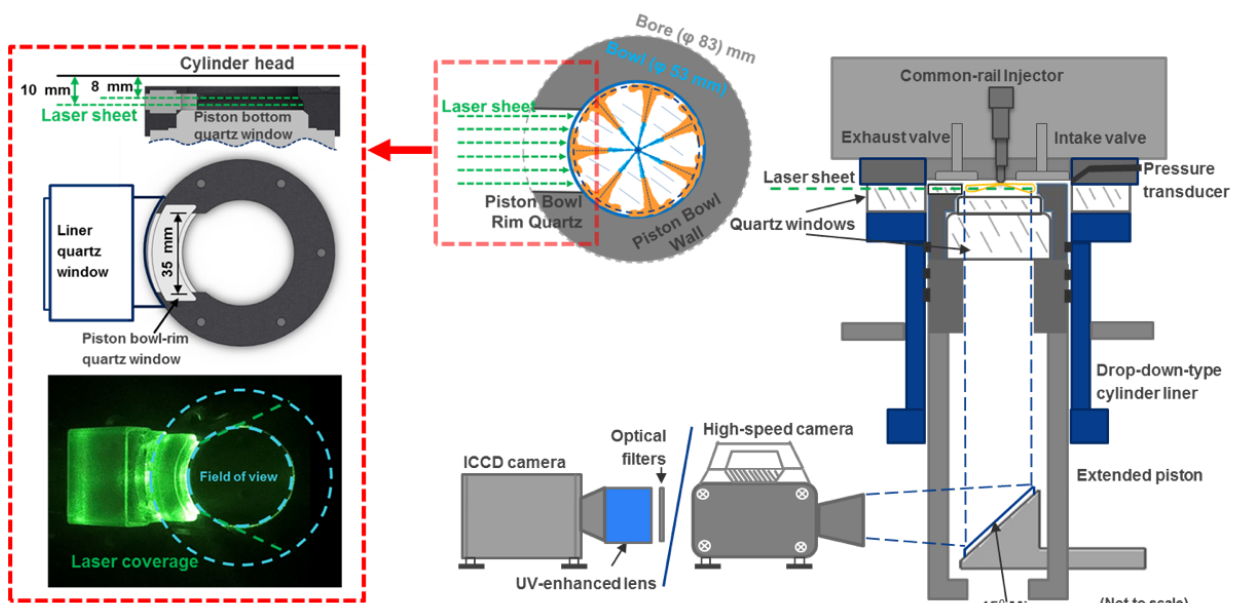


Figure 1: Illustration of a single-cylinder optical engine and diagnostics setup (right) and the laser sheets below the cylinder and the field of view of PLIF imaging (left).

with the gain setting at 60% and exposure time of 100 ns. To isolate the HCHO signals from other interference signals such as laser light scattering, soot incandescence or fluorescence from other species, a combination of 385 nm long pass filter, 430 nm band pass (10 nm FWHM) filter and a short-pass filter (450 nm) was used. It is to be noted that all the diagnostics performed in the present study were implemented one at a time.

The selected engine operating conditions for the diagnostics are summarised in Table 2. The engine speed was maintained at 1200 revolutions per minute (rpm) using an AC motor. During the engine operation, a 10-skip firing mode with one firing cycle followed by nine motoring cycles was implemented so that the thermal stress on the quartz windows can be minimised while expelling the remaining combustion products from the preceding firing cycles. The engine was naturally aspirated and the intake

Table 1: Engine specifications

Displacement (single cylinder)	497.8 cm ³
Bore	83 mm
Stroke	92 mm
Piston	Cylinder bowl (ϕ55 mm)
Number of valves	2 intake and 2 exhaust
Compression ratio	17.7:1 (Geometric)
Swirl ratio	1.4
Injection system	7-hole common-rail (Bosch CP3) Nominal hole diameter: 134 µm Included angle: 150° K-factor: 1.5 Discharge coefficient: 0.86 HFR: 400 cm ³ for 30 s at 10 MPa

Table 2: Engine operating conditions for optical/laser-based imaging diagnostics

Engine speed [rpm]	1200		
Coolant (water) temperature [°C]	90		
Common-rail pressure [MPa]	50		
Fuel	GCI	Diesel	
Cetane number	30	51	
Octane number (estimated)	~60	~10	
Fuel injection strategy	Single	Double	Single
1 st injection timing [°CA bTDC]	12	170	5
2 nd injection timing [°CA bTDC]	-	9	-
1 st injection proportion [%]	-	40	-
1 st injection signal duration [ms]	0.635	0.464	0.625
2 nd injection signal duration [ms]	-	0.512	-
Combustion phasing [°CA aTDC]	~12		
Total injected fuel mass [mg/cycle]	9		
Total energy input [J/cycle]	~391		
Overall equivalence ratio [ϕ]	0.24		

air temperature was fixed at about 30°C during the experiments. The wall temperature of the engine head and cylinder liner were heated to 90°C using a water heater/circulator (ThermalCare Aquatherm RA Series) to simulate warmed-up engine conditions. The common-rail pressure was kept constant at low 50 MPa because our previous study [46] showed higher common-rail pressure causes significant wall-wetting and fuel-film formation, and thereby increasing smoke and uHC emissions. The experiments were performed using a conventional diesel fuel with cetane number of 51, and a low-ignition quality fuel with cetane number of 30. For the single-injection GCI combustion, the injection timing was fixed at 12°CA bTDC while for the double-injection, the first injection timing was fixed at 170°CA bTDC, similar to our previous studies [6,10] with the second injection timing of 9°CA bTDC. The combustion phasing (i.e. CA50) was fixed at 12°CA aTDC. Also, 40% first injection proportion was selected for double-injection strategy based on our previous tests to find optimised mixture homogeneity of the first injection and charge premixing level of the second injection [10]. The two GCI injection conditions were compared with the single-injection diesel reference case. Regardless of the tested fuel and injection strategy, the total injected fuel mass per firing cycle was held constant at 9 mg with an overall equivalence ratio of 0.24.

2.2 Single-cylinder metal engine

The schematic diagram of a single-cylinder common-rail diesel engine for efficiency and emissions testing is shown in Fig. 2. The engine shares the same hardware as the optical engine except the optical liner and extended piston being removed. Also, this engine is connected to Eddy Current (EC) dynamometer (FroudeHoffmann AG-30HS) to enable higher load operation – e.g. 910 kPa of indicated mean effective pressure as in this study. Table 3 shows the selected engine operating conditions for the efficiency and emissions testing. It is noted that the engine was run at higher load conditions than the optical engine, and the test was conducted for various speeds, which were to evaluate the real performance of GCI combustion in comparison to diesel combustion.

In this engine setup, the in-cylinder pressure was recorded using a piezoelectric pressure transducer (Kistler 6056A1) for 100 consecutive firing cycles, which was used to obtain the average in-cylinder pressure trace, indicated power, efficiency, and specific fuel consumption (ISFC). The engine-out emissions of smoke (opacity), NO_x, and unburnt hydrocarbon (uHC) and carbon monoxide (CO) were also measured using an opacimeter (Horiba MEXA-600S, accuracy: ±0.15 m⁻¹ light absorption coefficient), a chemiluminescence-type gas analyser (Ecotech 9841AS, 1% accuracy), and a non-dispersive infrared (NDIR) analyser (Horiba MEXA-584L, 1.7% accuracy), respectively. For the sake of brevity, the discussion will be limited to NO_x and smoke emissions in this paper.

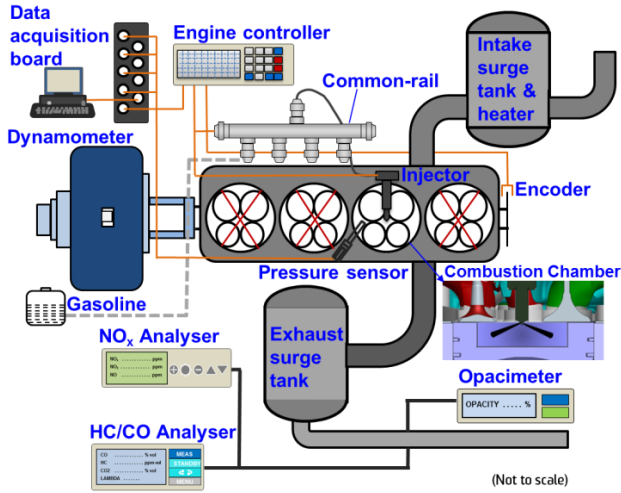


Figure 2: Schematic diagram of the single-cylinder engine setup for efficiency and emissions testing

Table 3: Engine operating conditions for efficiency and emissions testing

	GCI			Diesel
	1200	1600	2000	2000
Engine speed [rpm]	1200	1600	2000	2000
Common-rail pressure [MPa]	50			130
Net IMEP [kPa]	~910			
Fuel injection strategy	Double injection			Single
Fuel injection timing	1 st injection [°CA bTDC]	170		
	2 nd injection [°CA bTDC]	12, 9, 6, 3, 0, -3		
Injected fuel mass	1 st injection [mg]	5.04	7.2	7.2
	2 nd injection [mg]	13	13	14.8
Overall equivalence ratio (ϕ)	0.48	0.53	0.58	0.66

3. Results and discussion

3.1 Optical/laser-based imaging diagnostics

Figure 3(top) shows individual and ensemble-averaged in-cylinder pressure traces for diesel, single-injection and double-injection GCI combustion strategies (GCI:Single and GCI:Double). By plotting the in-cylinder pressure traces for all measured cycles, it was confirmed that cyclic variations are minimal such that the pressure gap associated with combustion strategies well exceed the inherent cycle-to-cycle variations. For each strategy, the injection timing was adjusted so that the combustion phasing could be fixed. The corresponding apparent heat release rate (aHRR) traces are shown at the bottom wherein actual fuel injection timing and duration for each combustion strategy is illustrated. The figure shows that, for all three combustion strategies, the start of combustion occurs at about 5°CA aTDC and the peak aHRR is positioned at about 8.5°CA aTDC (or CA50 at 12°CA aTDC). Since the start of

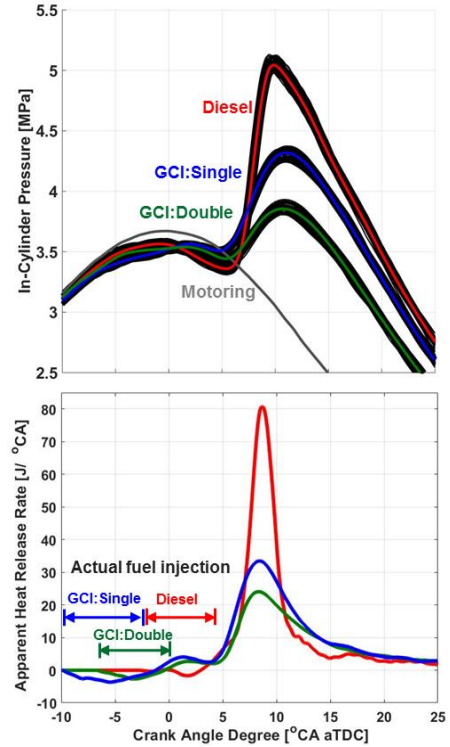


Figure 3. The in-cylinder pressure traces of all individual cycles and their ensemble average for diesel, GCI:Single and GCI:Double (top). Shown at the bottom are the corresponding apparent heat release rate traces

injection was different, this fixed combustion phasing means that the ignition delay and pre-combustion mixing time for GCI:Single was almost twice longer than diesel, achieving a partially premixed charge due to the use of a low ignition quality fuel. The GCI:Double also shows longer ignition delay than diesel. It was thought the early first injection caused a well-mixed homogenous charge while the late second injection initiated the high-temperature reaction. From the figure, it is observed that diesel combustion leads to higher peak of in-cylinder pressure and aHRR than the two GCI strategies with the single-injection GCI showing higher peak values than the double-injection GCI mode. For the two GCI modes, a small peak in the aHRR at about 2°CA aTDC is noticeable. This was due to low-temperature reaction during the first-stage ignition. That is, the extended ignition delay and increased charge premixing for GCI combustion modes created an environment for distinctive low-temperature reaction period. Between the two GCI modes, GCI:Double shows lower peak of aHRR as the mixture homogeneity was enhanced due to the early first injection.

The transition of low-temperature reaction to high-temperature reaction was investigated using cool-flame and OH* chemiluminescence imaging. Figure 4 shows, for diesel combustion, the cool-flame signals start to develop from 2°CA aTDC with the first signals emerging along the jet axis and then growing near the jet-wall impingement point. This is followed by OH* chemiluminescence signals observed at 6°CA aTDC, also forming on the jet axis first and then developing near the bowl-wall region. Each OH* signal pocket corresponding to each fuel jet then grows and

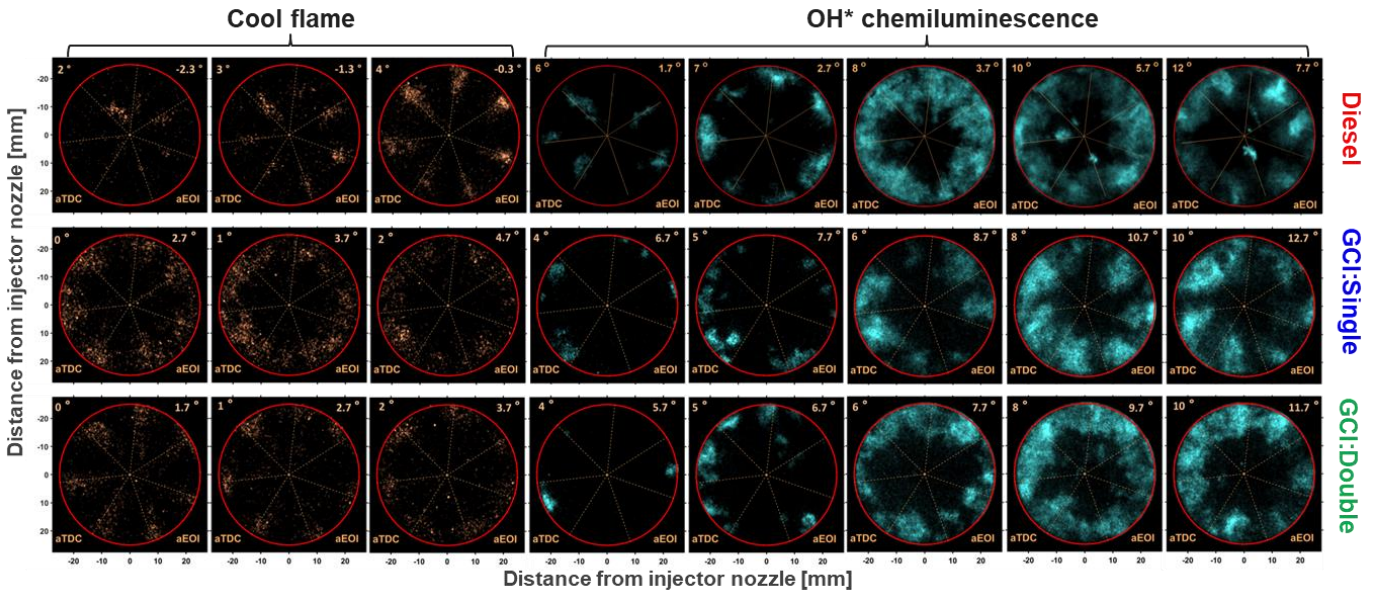


Figure 4: Cool-flame and OH* chemiluminescence images for diesel. GCI:Single and GCI:Double

interacts to fill up most of the combustion chamber until the signals decline and exhibit the distinctive seven pocket structure again in the late cycle.

For GCI:Single, the cool-flame signals are firstly found further downstream, i.e. near the bowl wall, which show a wider spatial coverage than diesel. This suggests more premixed charge was made due to extended ignition delay time. An interesting trend observed from the OH* chemiluminescence images at 4 and 5°CA aTDC is that multiple signal pockets, which would be interpreted as ignition kernels, form within the near-wall region where the cool-flame signals were almost uniformly distributed (e.g. 1°CA aTDC). These small pockets progressively merge to form a larger OH* zones. Compared to diesel combustion, the OH* chemiluminescence signals do not show distinctive jet structures corresponding to seven nozzle holes, with only vague boundaries being identified later at 8 and 10°CA aTDC. The GCI:Double shows cool-flame and OH* chemiluminescence images strongly affected by two split injections. For example, cool-flame signals show a distinctive and clear seven jet structure, which was predominantly due to the late second injection that lasted until TDC. The cool-flame signals appear all the way from the near nozzle to the bowl-wall region, which gradually disappear from the near nozzle region. Prior to the OH* dominant high-temperature reaction phase, the cool-flame signals decline, leaving the last signals near the bowl wall. The OH* signals develop in a similar pattern as the GCI:Single with multiple ignition kernels, which were likely from the second-injection mixtures. However, the OH* distribution is more spread and uniform, indicating the strong influence of the early first-injected fuel. The seven jet structure is hardly found from the OH* chemiluminescence images for GCI:Double.

Figure 5 shows the combined HCHO- and OH-PLIF images during the ignition and main combustion period for diesel, GCI:Single and GCI:Double strategies at 8 mm and 10 mm below the engine cylinder.

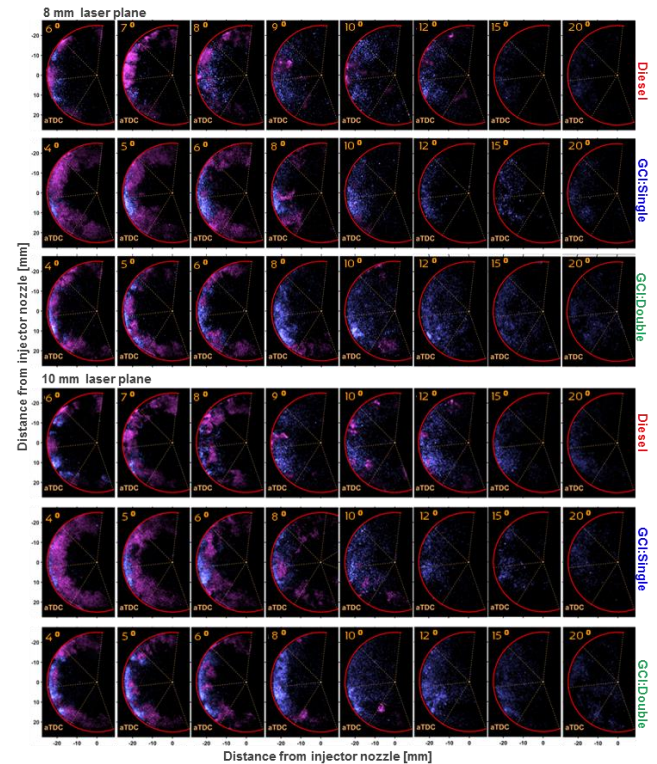


Figure 5: The combined HCHO- and OH-PLIF images during the ignition and main combustion period for diesel, GCI:Single and GCI:Double at 8 mm and 10 mm below the engine cylinder

temperature reaction at 6°CA aTDC. At later crank angles, the OH radicals replace the HCHO, which happens in the jet-wall interaction region and then progresses towards jet-jet interaction region. By 9°CA aTDC, other than the suspected PAH interference, only the OH-PLIF signals are observed. This timing corresponds to peak aHRR (Fig. 3), suggesting strong high-temperature reactions. By contrast, for GCI:Single strategy, the isolated OH-PLIF signals grow out of the HCHO-PLIF region from the jet-wall interaction point, which occurs between 4 and 6°CA aTDC. The

development pattern of OH radicals is more sequential than diesel combustion such that the first OH zone appears within the HCHO region and then grows in both radial and axial directions. This is consistent with the expected higher charge premixing condition of GCI combustion. It is also consistent with the OH* chemiluminescence images showing the multiple ignition kernels and their gradual merger to form a large high-temperature reaction zone (Fig. 4). In comparison, the GCI:Double strategy shows wider spread OH signals due to higher mixture homogeneity from the early first injection. It is noticeable that, between 4 and 8°CA aTDC, the OH develops faster across the entire reaction zones, meaning the HCHO to OH transition occurred at a higher rate than that of GCI:Single. This explains why the spatial coverage of cool-flame (Fig. 4) and HCHO signals for GCI:Double is less compared to GCI:Single. That is, the early first injection produced a more homogenous premixed charge, which, upon the start of combustion initiated by the late second injection, led to a faster transition of low-temperature reaction to high-temperature reaction. For GCI engine applications, this would result in better combustion stability and thereby extending the low load limit.

3.2 Engine efficiency and emissions testing

The GCI:Double combustion strategy was further investigated for efficiency and emissions at more practical and wider operating conditions. As an example, the in-cylinder pressure and aHRR traces at three different engine speeds of 1200, 1600, and 2000 rpm are shown in Fig. 6. In each plot, the data is shown for various second injection timings with fixed first injection timing of 170°CA bTDC. From the figure, a clear trend is found that the peak of in-cylinder pressure decreases with increasing engine speed at any fixed second injection timing. The same trend is also

found in the peak aHRR shown in the middle row. However, care should be taken to interpret the observed trend as the physical time available per each crank angle is shorter at higher engine speed. Indeed, when the aHRR is plotted for J/ms (bottom row) instead of J/°CA (middle row), the trend is reversed that the peak aHRR increases with increasing engine speed. This could be explained by the increased energy input as the injected fuel mass was increased to maintain the target power output. Also, the heat loss was expected to be decreased due to the limited time at higher engine speed.

The engine efficiency plotted in Fig. 7 shows a decreasing trend with increasing engine speed. At fixed engine speed, the advanced injection timing resulted in higher efficiency and lower indicated specific fuel consumption (ISFC) due to higher in-cylinder pressure. Figure 7 shows that high net indicated efficiency of 50% and low ISFC of 160 g/kWh could be achieved at 12°CA bTDC second injection and 2000 rpm conditions. In comparison, the diesel reference case with a similar aHRR profile (see Fig. 6) shows 41% efficiency and 210 g/kWh ISFC. This means 22% increase in the net indicated efficiency and 23.8% decrease in ISFC using the GCI combustion implementing a double injection strategy.

The smoke opacity results are shown in Fig. 8(top). Trends are clear that the advanced second injection and thus advanced combustion phasing (Fig. 6) leads to smoke reduction regardless of the engine speed. The observed trends could be explained by the ignition delay time. That is, at earlier second injection timing, the increased ignition delay caused extended time for premixing and decreased locally rich mixtures. The same explanation applies to engine speed variations: lower engine speed leads to increased premixing time (in physical time domain) and

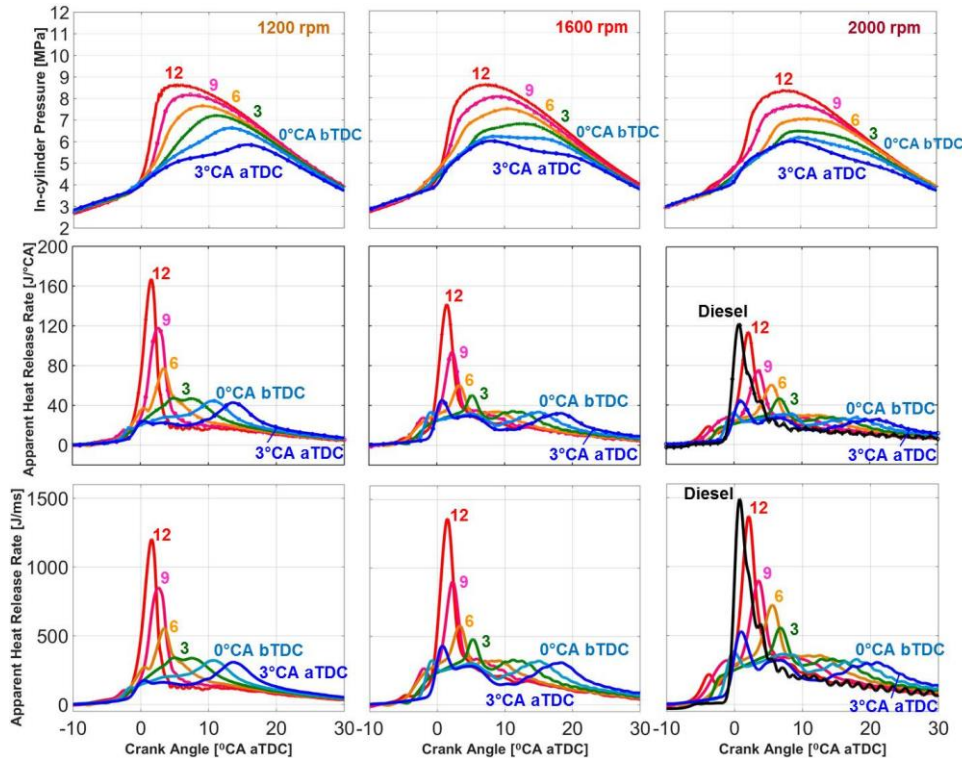


Figure 6: In-cylinder pressure and apparent heat release rate (aHRR) in crank angles and milliseconds for various second injection timings of the double injection strategy at three different engine speeds

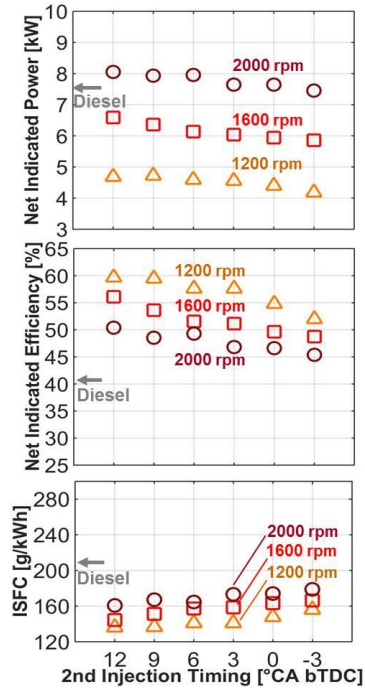


Figure 7: Net indicated power, efficiency and ISFC for various second injection timings of the GCI double injection strategy at three different engine speed conditions

thus lower smoke emissions. Compared to the diesel reference case showing 13% opacity, the corresponding GCI:Double combustion (12°CA bTDC/2000 rpm) exhibits much lower opacity of 2%, which is also due to the increased charge premixing and mixture homogeneity.

The engine-out emissions of NO_x , plotted in Fig 9(top), show an interesting trend of decreasing and increasing emissions with advanced second injection timing. The minimum emission is found for second injection timing of 3°CA bTDC. At the earlier second injection timing, the advanced second injection led to increased NO_x emissions, which is consistent with increased peak aHRR as shown in Fig. 9(bottom), suggesting higher thermal NO formation. At the later timings than 3°CA bTDC, however, the peak aHRR is lower, which cannot explain the significant increase in NO_x emissions. Note that for these two second injection timings of 0 and -3°CA bTDC, the second injection occurred after the start of combustion, *i.e.* fuel injection into the existing flames, which was thought to increase local flame temperatures although they might not show up in the bulk-gas-averaged aHRR. Except these late second injection timings, the smoke opacity (Fig. 7) and NO_x emissions show a trade-off characteristic, similar to diesel combustion. In other words, the advanced injection led to increased premixing and higher peak aHRR resulting in decreased smoke but increased NO_x emissions. Regarding the engine speed variations, figure 9 shows decreased NO_x emissions with increased engine speed, which also follows the trade-off characteristic. As mentioned previously in Fig. 8, the premixing time in the physical time domain was reduced as the engine speed was higher, which led to increased smoke emissions and reduced thermal NO formation. Compared to the diesel reference case with 2.8 g/kWh of NO_x emissions, the GCI

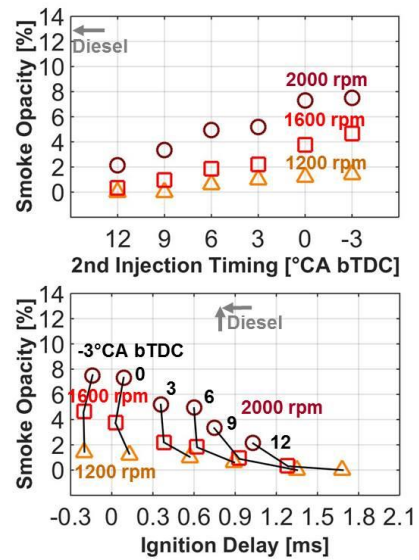


Figure 8: The smoke opacity for various second injection timings of the GCI double injection strategy at three different engine speed conditions. Shown at the bottom is the smoke opacity versus ignition delay time

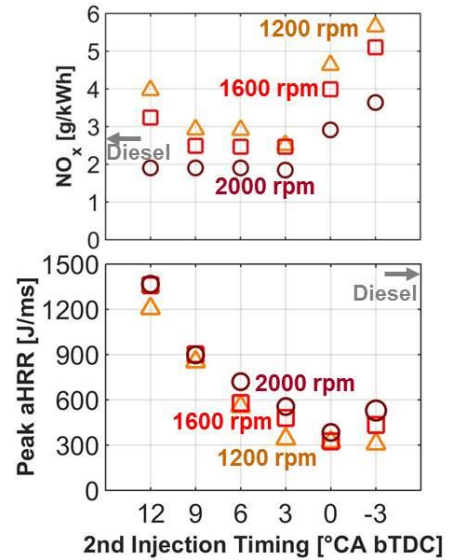


Figure 9: Engine-out emissions of oxides of nitrogen (NO and NO_2) and peak aHRR for various second injection timings of the GCI double injection strategy at three different engine speed conditions

combustion (12°CA bTDC/2000 rpm) achieves 35.7% lower emissions at 1.8 g/kWh, demonstrating the simultaneous reduction of smoke and NO_x emissions.

4. Conclusions

By performing optical/laser-based imaging diagnostics for diesel, GCI:Single and GCI:Double combustion strategies in an optical compression ignition engine, fundamental knowledge was gained to develop a multi-fuel capable compression ignition engine, which can be summarised as follows:

1. For diesel combustion, the low-temperature reaction initiates from the jet-axis and then spread downstream towards the bowl wall, showing a clear seven-jet

structure corresponding to each nozzle hole. The high-temperature reaction also follows a similar development pattern with distinctive reaction zones first forming on the jet axis and then near the bowl wall. The HCHO and OH radicals co-exist near the bowl wall during the ignition process.

- The single-injection GCI combustion shows low-temperature reactions occurring from the bowl wall region with wider spatial coverage of HCHO due to increased charge premixing. The OH radicals grow out of HCHO region near the bowl wall in a more sequential manner compared to diesel combustion. This transition from low- to high-temperature also involves multiple ignition kernels that progressively merge to form a larger high-temperature reaction zone.
- The double-injection GCI combustion shows low-temperature reactions occurring from the jet-wall impingement point with distinctive seven-jet structures while the spatial coverage of HCHO is less than the single-injection GCI strategy. However, the high-temperature reaction shows wider spread and more dispersed signals along the bowl-wall due to the early first injection causing a homogeneous premixed charge. During the low- to high-temperature reaction transition, the HCHO consumption to form OH radicals is higher, indicating faster transition for better combustion stability.

The GCI:Double combustion strategy was also tested for efficiency and emissions at more practical operating conditions with variations in engine speed. The level of charge premixing, which was found to make a predominant effect on ignition process from the optical combustion diagnostics, was identified again as a key player. The major findings from this test are summarised as follows:

- The increased engine speed leads to lower efficiency and higher ISFC. In the physical time domain, the heat release rate increases with increasing engine speed but the combustion phasing does not change. A typical smoke-NO_x trade-off is found with increased smoke and decreased NO_x emissions at higher engine speed, which is related to reduced charge premixing time.
- Compared to a selected diesel reference case at 2000 rpm, the corresponding GCI:Double combustion strategy with a similar aHRR profile shows 22% increase in net indicated efficiency and 23.8% decrease in ISFC by implementing a double injection strategy. The smoke level is decreased as evidenced by a significant reduction of opacity from 13 to 2% and simultaneously, the NO_x emissions are reduced by 35.7%.

Acknowledgments

The experiments were performed at the UNSW Engine Research Laboratory, Sydney, Australia. The authors appreciate the financial support provided by the Australian Research Council via Linkage Project scheme, and in part by CCDC Army Research Laboratory and ITC-PAC.

References

- Yang J, Culp T, Kenney T. SAE Pap. 2002-01-2832, 2002.
- Kalghatgi GT, Risberg P, Ångström H-E. SAE Pap. 2006-01-3385.
- Kalghatgi GT, Risberg P, Ångström H-E. SAE Pap. 2007-01-0006.
- Fridriksson H, Sundén B, Hajireza S, Tuner M. SAE Pap. 2011-01-1838.
- Solaka H, Aronsson U, Tuner M, Johansson B. SAE Pap. 2012-01-0684.
- Goyal H, Kook S, Hawkes E, Chan QN, Padala S, Ikeda Y. SAE Pap. 2017-01-0742.
- Fang C, Tunestal P, Yin L, Yang F, Yang X. Appl Therm Eng (2018) 148:219-228.
- Liu X, Goyal H, Kook S, Ikeda Y. SAE Pap. 2019-01-1148, 2019.
- Kalghatgi G, Hildingsson L, Johansson B. J Eng Gas Turbines Power (2010) 132:092803.
- Goyal H, Kook S, Ikeda Y. Fuel (2019) 235:1207-15.
- Dec JE. Proc Combust Inst (2009) 32:2727-42.
- Liu H, Zheng Z, Yao M, Zhang P, Zheng Z, He B, Appl Therm Eng (2012) 33-34:135-43.
- Liu H, Yao M, Zhang B, Zheng Z. Energy Fuels (2009) 23:1422-30.
- Saurya RK, Agarwal AK. Appl Energy (2011) 88:1169-80.
- Bahng GW, Jang D, Kim Y, Shin M. App Th Eng (2016) 98:810-5.
- Singh G, Singh AP, Agarwal AK. Sustain Energy Technol Assessments (2014) 6:116-28.
- Sjöberg M, Dec JE. SAE Pap. 2006-01-0629.
- Krisman A, Hawkes ER, Kook S, Sjöberg M, Dec JE. Fuel (2012) 99:45-54.
- Kobashi Y, Tanaka D, Maruko T, Kato S, Kishiura M, Senda J. SAE Pap. 2011-01-1768.
- Sellnau M, Foster M, Hoyer K, Moore W, Sinnamon J, Husted H. SAE Int J Engines (2014) 7:835-51.
- Manente V, Johansson B, Tunestal P, Cannella W. SAE Int J Engines (2009) 2:71-88.
- Manente V, Johansson B, Cannella W. Int J Engine Res (2011) 12:194-208.
- Splitter D, Hanson R, Kokjohn S, Reitz RD. SAE Pap. 2011-01-0363.
- Sellnau MC, Sinnamon J, Hoyer K, Husted H. SAE Int J Engines (2012) 5:300-14.
- Jain A, Singh AP, Agarwal AK. Appl Energy (2017) 190:658-69.
- Tang Q, Liu H, Li M, Yao M. SAE Int J Engines (2016) 9:2185-93.
- Goyal H, Liu X, Kook S, Ikeda Y. FISITA World Congr., 2018.
- Jain A, Singh AP, Agarwal AK. Energy (2017) 122:249-64.
- Zhao F, Asmus TN, Assanis DN, Dec JE, Eng JA, Najt PM.. SAE International; 2003.
- Gray III AW, Ryan III TW. SAE Pap. 971676, 1997.
- Thring RH. SAE Pap. 892068, 1989.
- Lilik GK, Herreros JM, Boehman AL. Energy & Fuels (2009) 23:143-50.
- Tang Q, Liu H, Li M, Yao M. Appl Energy (2017) 185:708-19.
- Tang Q, Liu H, Li M, Yao M, Li Z. Combust Flame (2017) 177:98-108.
- Goyal H, Kook S, Ikeda Y. Fuel, JFUE-S-18-06120, in review.
- Wang Z, Stamatoglou P, Lundgren M, Luise L, Vaglieco BM, Andersson A, Proc Combust Inst (2019) 37(4): 4751-4758.
- Musculus MPB, Miles PC, Pickett LM. Conceptual models for partially premixed low-temperature diesel combustion. Prog in Energy Combust Sci (2013) 39:246-283.
- Richter M, Collin R, Nygren J, Aldén M, Hildingsson L, Jonansson B. JSME Int J Ser B (2005) 48:701-7.
- Collin R, Nygren J, Richter M, Aldén M, Hildingsson L, Johansson B. SAE Pap. 2003-01-3218, 2003.
- Genzale CL, Reitz RD, Musculus MPB. Proc Combust Inst (2009) 32:2767-74.
- Musculus MPB. SAE Pap. 2006-01-0079.
- Le MK, Kook S, Hawkes ER. Fuel (2015) 140:143-55.
- Le MK, Zhang R, Rao L, Kook S, Hawkes ER. Fuel (2016) 166:320-32.
- Dec JE, Coy EB. OH radical imaging in a DI diesel engine and the structure of the early diffusion flame. SAE Pap. 960831, 1996.
- Goyal H, Zhang Y, Kook S, Kim KS, Kweon C-B, SAE Int J Engines, JENG-2019-0028_R1, in review.
- Woo C., Goyal H., Kook S., Hawkes E.R., Chan Q.N., SAE Pap. 2016-01-2303.

Combustion Regime Analysis of a Supersonic Turbulent Mixing Layer

Nicholas N. Gibbons^{1,*} and Vincent Wheatley¹

¹School of Mechanical and Mining Engineering, University of Queensland, St. Lucia QLD 4072, Australia

Abstract

A turbulent supersonic reacting mixing layer is studied numerically using Direct Numerical and Large Eddy Simulation, combined with a 13 species, 33 reaction detailed chemical kinetic model. Of interest are the predicted combustion regimes, characterised by the nondimensional turbulent Damkohler number (Da_t) and turbulent Reynolds number (Re_t). Knowledge of these regimes is important to appropriately modelling turbulence/chemistry interaction in these flows. The present case consists of a temporally developing mixing layer between high velocity air and pure hydrogen fuel, with temperatures of 1500K and 1400K respectively, an initial differential velocity of 2834 m/s, and a uniform pressure of 101kPa. The simulations are sustained for $\approx 100\mu s$, with transition to fully turbulent behaviour occurring around $\approx 20\mu s$. Comparison of the combustion regimes computed using the DNS and LES simulations reveal only minor differences; the DNS regimes spanning a broader and somewhat slower range of the parameter space. These results imply that LES can be used in supersonic propulsion applications to compute regime information relevant to practical design problems.

Keywords: Hypersonics, Direct Numerical Simulation, Turbulent Combustion, Supersonic Combustion

1. Introduction

Cutting edge simulations of supersonic reacting flows are presently subject to a high degree of uncertainty. These simulations are often applied to supersonic combustion ramjets (scramjets), an experimental propulsion technology that mixes and burns fuel at high velocity to prevent losses from slowing the flow to subsonic speeds. In this kind of environment reactions must complete in milliseconds, and minor errors in ignition delay can lead to large errors in performance as predicted by Computational Fluid Dynamics (CFD). Scramjets also contain complex turbulent flow fields, including separations, shockwave turbulent boundary layer interactions, and fuel injection structures that CFD models frequently struggle to replicate. Critically, turbulence and combustion do not just exist in isolation but interact strongly at the smallest possible scales. Turbulent vortices are responsible for sweeping up fuel and incoming air and increasing the available surface area for them to mix at the molecular level. Once ignition begins the interaction continues and may even become stronger, as the flame structure is disrupted by turbulent eddies that break apart layers of intermediate species and recycle and mix them anew.

Many decades of research by the combustion community has produced an impressive array of predictive models to handle this Turbulence/Chemistry Interaction (TCI), but progress has been mostly concentrated on low speed flows. In [1] we have reviewed a large number of supersonic, reacting simulations that use high-fidelity turbulence modelling and found little consensus on which models are best suited to compressible TCI. This uncertainty is important because the results of computational simulations are embedded in supersonic flight experiments at every level. CFD is used to design individual engine components, to optimize the overall vehicle design and flight trajectory, to interpret and design wind tunnel tests, and to ensure that fully integrated flight tests are successful and return useful scientific data.

*Corresponding Author. Email: n(dot)gibbons(at)uq.edu.au

This paper is part of a broader campaign to understand the phenomenon of turbulent combustion in supersonic flows. We focus on a basic question: How to classify the combustion occurring in a typical scramjet flow into *combustion regimes* — areas of the parameter space where a coherent physical picture or set of simplifying assumptions can be identified. Since different TCI models make different simplifying assumptions, the regime information can then be used to choose a model from the existing menu or to assist in developing new ones if required.

Computational simulations can be used to estimate these regimes, but without prior knowledge of the regimes one cannot choose an appropriate model, and without a model one cannot quite be sure that the simulated regimes are accurate. This chicken-and-egg problem is addressed in this paper by using Direct Numerical Simulation (DNS) of a simple fundamental supersonic reacting flow to estimate the combustion regimes with an established technique. Since the DNS resolves all of the chemical and turbulent structures down to the smallest scales, the turbulence/chemistry interaction is computed directly with no additional modelling required, and the regime analysis should be trustworthy. These results are then compared to an identical simulation using an approximate turbulence model, a high-fidelity Large Eddy Simulation without an explicit TCI model (otherwise known as quasi-laminar combustion). If the results are the same then the LES technique can be applied in the future to estimate the regimes in more practical engine-like flows without fear of the regimes being inaccurate, and if they differ then the simulations might offer clues as to why.

2. Flow Description

The flow configuration for a Direct Numerical Simulation must be chosen carefully. Turbulence produces a vast range of scales that are difficult or impossible to resolve in a practically sized object such as an engine or aircraft wing, given finite computing time and memory limits. Instead, prior work on compressible high-speed DNS has focused on simple fun-

damental flows that replicate the physics of supersonic mixing and combustion one-at-a-time in a reasonably sized geometry. The simplest of these arrangements is isotropic homogeneous turbulence [2] [3], a statistically amorphous mass of randomly fluctuating flow that convects through a domain with periodic boundaries. More complicated examples include boundary layer flows [4] [5], and spatially developing mixing layers [6] [7] [8] where two initially separate streams of fuel and oxidiser flowing in the same direction mix and burn as they move downstream. There have also been studies of temporally developing mixing layers [9], where the two streams begin with opposing velocities and the mixing layer develops between them while contained within a set of periodic boundary conditions. Mixing layers are a particularly interesting fundamental flow in the present context due to their importance in scramjet combustors, and temporally developing mixing layers in particular typically require fewer computational resources than spatially developing ones since the domain size is smaller.

For these reasons the flow configuration chosen for this investigation is a temporally evolving mixing layer documented in figure 1. The initial condition consists of one layer of pure hydrogen fuel and another of air, confined in a periodic cubic-shaped domain with a high opposing velocity and allowed to evolve in time. The domain itself is quite small, with all side lengths set to 20mm. This limits the amount of time the mixing layer can be sustained, since eventually the largest turbulent structures will span the entire domain, but the small size ensures that the computation is tractable in terms of computational expense.

At the interface between layers, the gas properties are blended over a $\approx 0.6\text{mm}$ hyperbolic tangent function, to help make different simulations on different grids comparable. This interface is also perturbed by a sinusoidal function with amplitude 0.2mm and wavelength 3.3mm, to ensure rapid and consistent transition of the LES simulation. Additionally, the top and bottom surfaces of the domain have extra blocks of cells added to them with cells that stretch rapidly in the Z direction, which damps out any waves and prevents them from reflecting off the symmetry boundary conditions at $Z = 16.5\text{mm}$ and $Z = -16.5\text{mm}$. These extra blocks are excluded from the visualizations to come so that the images can be larger, and because the flow in them is non-physical.

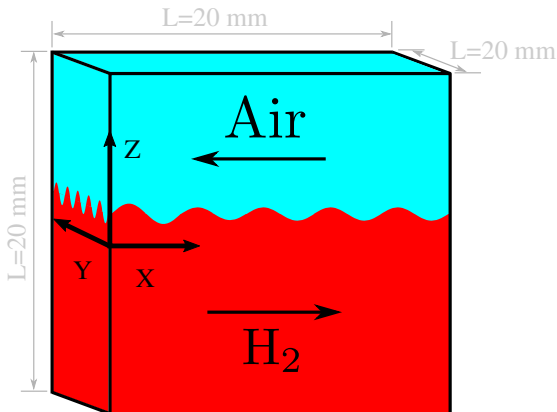


Figure 1: Supersonic Mixing Layer initial state

The initial flow conditions are documented in table 1. These numbers are roughly analogous to the initial state of fuel and air in a scramjet engine but are not completely representative of these states. The relative velocity of the two layers has been increased to ensure rapid transition to turbulence, and the fuel temperature is also higher than a typical wind-tunnel test to ensure that the flow reacts during the brief period the mixing layer can be sustained. The simulations are intended to test the modelling methodology and investigate some of the physics of the subgrid field, not to precisely emulate the conditions in a scramjet engine, so the initial conditions were chosen to reflect this goal.

Table 1: Supersonic Mixing Layer Initial Conditions.

Air:		Fuel:	
p	101,000 (Pa)	p	101,000 (Pa)
T	1,400 (K)	T	1,500 (K)
u	-1,168.89 (m/s)	u	1,665.89 (m/s)
Y_{N_2}	0.767	Y_{H_2}	1.0
Y_{O_2}	0.233		

3. Simulation Methodology

The simulations in this work are performed using the computer code Unstructured 3D (US3D), a hybrid structured/unstructured finite-volume compressible flow code for aerospace applications, developed at the University of Minnesota [10]. US3D is equipped for complex thermochemical non-equilibrium including finite-rate chemical kinetics and two-temperature gas modelling, as well as the presence of turbulence through both Reynolds Averaged Navier-Stokes (RANS) and Wall-Modelled Large Eddy Simulations (LES). The results to come are compiled from two distinct simulations of the same flow; a Large Eddy Simulation that models subgrid scale turbulent transport using the IDDES method of [11], and a Direct Numerical Simulation that uses a very fine grid to actually compute the fine-scale turbulent fluctuations instead. Both simulations model chemical reactions using a 13 species, 33 reaction detailed chemical kinetic model for hydrogen combustion [12]. Time advancement is computed using the second order implicit Full-Matrix Point Relaxation (FMPR) method [13], and the inviscid fluxes are computed using the low-dissipation gradient reconstruction [1]. This scheme switches between a symmetric 6th order accurate gradient reconstruction method in smoothly varying regions of the flow, and a highly dissipative scheme based on [14, ?] near shockwaves and discontinuities. The switching function of [15] is used for this purpose.

Table 2: Solver settings for Supersonic Mixing Layer.

SML Parameters	DNS	LES
Turbulence Model	None	IDDES [11]
Grid Size	299 ³	99 ³
Solver		US3D [10]
Chemistry		13s33r [12]
Time Advancement		FMPR 2nd [13]
Inviscid Fluxes		Grad. Recon. 6th[1]
Domain Size		20mm

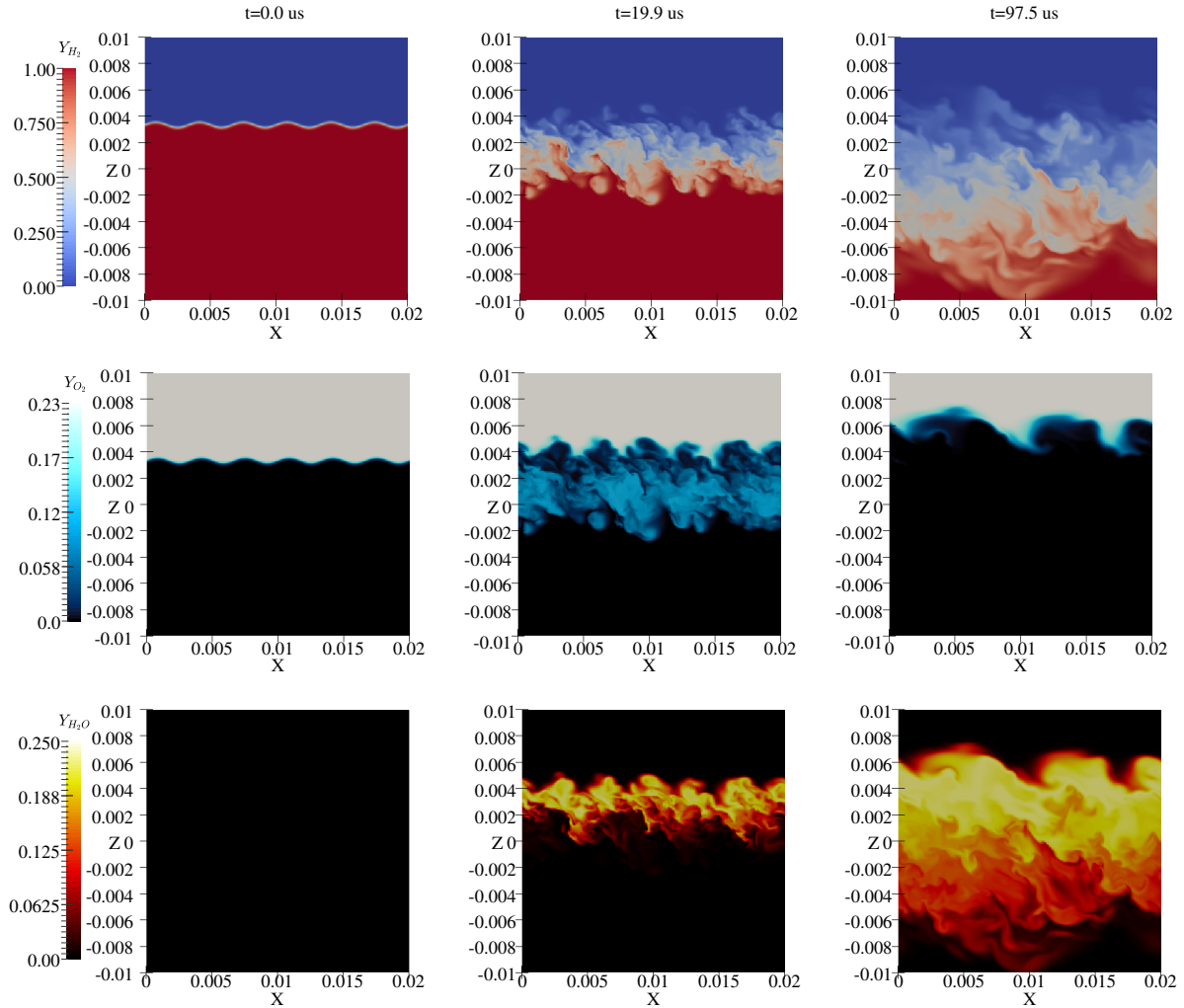


Figure 2: DNS time evolution of Fuel H_2 (TOP), oxidiser O_2 (MIDDLE), and product H_2O (BOTTOM).

4. Flow Structure

This section uses the DNS results to explore the flowfield and draw general conclusions about the overall behaviour of the mixing layer. Figure 2 shows several colour maps of the key variables, visualizing the x - z plane through $y=0.01$ in the centre of the domain. The upper layer of flow is travelling to the left, and the lower layer to the right. The first column shows the simulation at time zero. Its only visible feature being the interface discussed in an earlier section, which has been raised slightly above the center of the domain to counteract an observed drift in the location of the shear layer as the simulation develops. The sinusoidal perturbations in the interface location use a nominal wavenumber of six and are used to accelerate the transition to turbulence and ensure that the two simulations have similar initial conditions.

The second column is a snapshot of the flow at $\approx 20\mu s$, just as the flow is transitioning to turbulence. Combustion is just beginning as well, as evidenced by the ribbon of H_2O visible in the bottom image, on the top (air) side of the mixing layer. This ribbon is unable to propagate deeper into the mixing layer due to the richness of the mixture in the center, but by the time of the final column, $\approx 100\mu s$, the combustion zone has grown to encompass most of the domain. At this point

the simulation was stopped, since the coarse cells at the bottom and top of the domain would soon begin to compromise the results.

Overall then, the simulation displays rapid transition to turbulence and robust combustion over the time period. These two effects interact strongly in the mixing layer, leading to strong coupling between the turbulence and the chemistry, confirming the simulation is behaving appropriately for its purpose.

5. Combustion Regime Analysis

A useful first step in attempting to model turbulent combustion is to characterize the system of interest using some dimensionless parameters. Often a very large or very small parameter will suggest a physical effect that is dominant, or one that can be ignored, or if two parameters are approximately equal sometimes a model can be built that assumes a ratio of them is order unity. Areas in the parameter space where this happens can be called regimes, and it is helpful to ask which regime turbulent combustion in scramjets occurs in, to determine which of the existing models will be appropriate, or to assist in developing new ones if none are suggested.

This analysis follows the overall method of Balakrishnan and Williams, 1994 [16]. The authors identify two important dimensionless parameters that can be used to classify the combustion into physically distinct types. The first is the turbulent Damkohler Number Da_t :

$$Da_t = \frac{\tau_t}{\tau_c} \quad (1)$$

Defined as the ratio between the turbulent timescale and the chemical timescale. Large values of Da_t indicate fast chemistry that reacts quickly relative to the turbulent motion, and small values represent slow reactions where the turbulence controls mixing and stirring of the reactants in a distributed reaction zone. To compute this quantity, first the characteristic turbulent timescale τ_t is required. This represents the turnover time of a large eddy computed using the integral timescale to set the length and the turbulent kinetic energy k_t to estimate a velocity. An expression from this is taken from [17], and includes the turbulent dissipation ε , defined in equation 5:

$$\tau_t = \frac{k_t}{\varepsilon} \quad (2)$$

k_t is the energy per unit mass tied up in turbulent motion (the turbulent kinetic energy or TKE). The TKE can be estimated by splitting it into two parts, a resolved energy based on the fluctuating velocity field, and a subgrid component representing the energy tied up in the modelled eddies that are filtered out by the LES.

$$k_t = k_r + k_{sgs} \quad (3)$$

The resolved TKE is computed from the fluctuating velocities $u'_i = u_i - \bar{u}_i$, where the overline indicates the 1-d spatial average from equation 16 and u_i is the velocity vector. The subgrid TKE is computed using an estimation technique also from [17], which uses Δ as the filter width (grid cell size), ν_t as the turbulent dynamic viscosity, and c_v^k a constant equal to 0.07:

$$k_{sgs} = \frac{\nu_t^2}{(c_v^k \Delta)^2} \quad k_r = \sum_i \frac{1}{2} u'_i u'_i \quad (4)$$

The turbulent dissipation ε represents the rate at which energy in the form of turbulent motion is being transformed into heat in the form of disordered molecular motion. It is also composed of two parts, a resolved component computed from the actual eddies present in the solution, and a subgrid component contributed by the LES model.

$$\varepsilon = \varepsilon_{sgs} + \varepsilon_r \quad (5)$$

An expression for the resolved dissipation is taken from the turbulent kinetic energy transport equation, derived in [18]. This transport equation has a dissipation term that can be interpreted as ε_r , computed using the fluctuating strain rate tensor S'_{ij} .

$$\varepsilon_r = 2\nu \sum_i \sum_j \overline{S'_{ij} S'_{ij}} \quad S'_{ij} = \frac{1}{2} \left[\frac{\partial u'_i}{\partial x_j} + \frac{\partial u'_j}{\partial x_i} \right] \quad (6)$$

The subgrid dissipation is computed from an expression derived by [17], which combines the Kolmogorov scaling laws

for isotropic homogeneous turbulence to estimate ε_{sgs} from the turbulent viscosity.

$$\varepsilon_{sgs} = \frac{0.931 k_{sgs}^{3/2}}{\Delta} \quad (7)$$

Note that in the DNS simulation, both k_{sgs} and ε_{sgs} are set equal to zero.

The other component of Da_t is the chemical timescale τ_c . What this timescale represents conceptually is less clear than for the turbulent one: Essentially it is how long one has to wait before a significant change occurs in the species concentrations due to chemistry, although the threshold of ‘significance’ is somewhat open to interpretation. This work uses Chemical Explosive Mode Analysis (CEMA) [19] to compute τ_c , as the method is quite general and has performed well in comparative testing [1]. In CEMA, a timescale is extracted from the reaction dynamics by starting with the chemical source term Jacobian:

$$J_{sj} = \frac{\partial \dot{\omega}_s}{\partial U_j} \quad (8)$$

Where $\dot{\omega}_s$ is the formation rate of each species in $kg/m^3/s$, and U_j is a vector of conserved variables. A standard numerical linear algebra routine is then used to obtain the eigenvalues of the matrix J_{sj}

$$\lambda_n = evals(J) \quad (9)$$

Each eigenvalue is associated with a certain *chemical mode*. These modes are abstract vectors that are combined linearly to produce the change in composition due to chemistry at each timestep. Each chemical mode is an exponential function of time, and the eigenvalues are the time constants in these functions, where positive real parts indicate the mode is departing explosively from an equilibrium state, and negative indicates a mode approaching equilibrium. The positive ones, the ‘Explosive Modes’, are used to estimate the chemical timescale by simply choosing the largest real component from the set of eigenvalues λ_n (which have units of s^{-1}) and computing the inverse to get a timescale:

$$t_c = \max \left(\frac{\lambda_n + \lambda_n^*}{2} \right)^{-1} \quad (10)$$

Where λ_n^* is the complex conjugate of the n^{th} eigenvalue.

The last component of the regime analysis is the turbulent Reynolds number Re_t . This number quantifies the intensity of the turbulence, as determined by the ratio of the inertia of the turbulence at large scales and the strength of the viscous forces that oppose it. Large values of Re_t intensify the Turbulence/Chemistry Interaction that may be present in a particular regime. It is computed from various quantities already introduced, plus the kinematic viscosity ν .

$$Re_t = \frac{k_t}{\varepsilon \nu} \quad (11)$$

These two numbers can be computed for each point in the flow field and mapped onto a Da_t vs Re_t parameter space, an approach suggested by [16] and updated by various authors including [17]. Areas in the parameter space where the

points cluster suggest relevant combustion regimes, where simplifying assumptions can be made and appropriate turbulent combustion models can be applied. The actual physical characteristics of each regime differ between premixed and nonpremixed combustion, and are likely to be different in this contrived flow situation compared to in a real engine. For this reason we spend little time analysing what the regimes are and focus more on the comparison between the LES and the DNS.

Figure 3 compares the regime diagrams using a heatmap approach where the colour scale indicates the number of cells found within a small region of the Re_t/Da_t space. A map is computed for each simulation, one each at the early ($20 \mu s$) and late ($100 \mu s$) times that we have been examining. Cells with low TKE ($k_t < 1.0$) and extremely slow reactions ($t_c > 1.0$) have been excluded, leading to varying numbers of

points in each heatmap.

The results show that the LES computes very similar regimes to the DNS. Both indicate some kind of thin flame would be present, possibly with significant disruptions of the flame structure due to locally intense turbulence. There are however some minor differences as well. The DNS results span a broader range of the parameter space, particularly at the later time, and tend to be lower on the diagrams indicating slower reactions relative to the turbulent timescales. Interestingly the LES results tend to be a bit further in the radial direction, a result that would indicate slightly stronger TCI effects to someone viewing only the LES results. But the difference is not a major one — both diagrams would license the same conclusions about which model to use if one needed to compute the subgrid turbulent chemistry accurately.

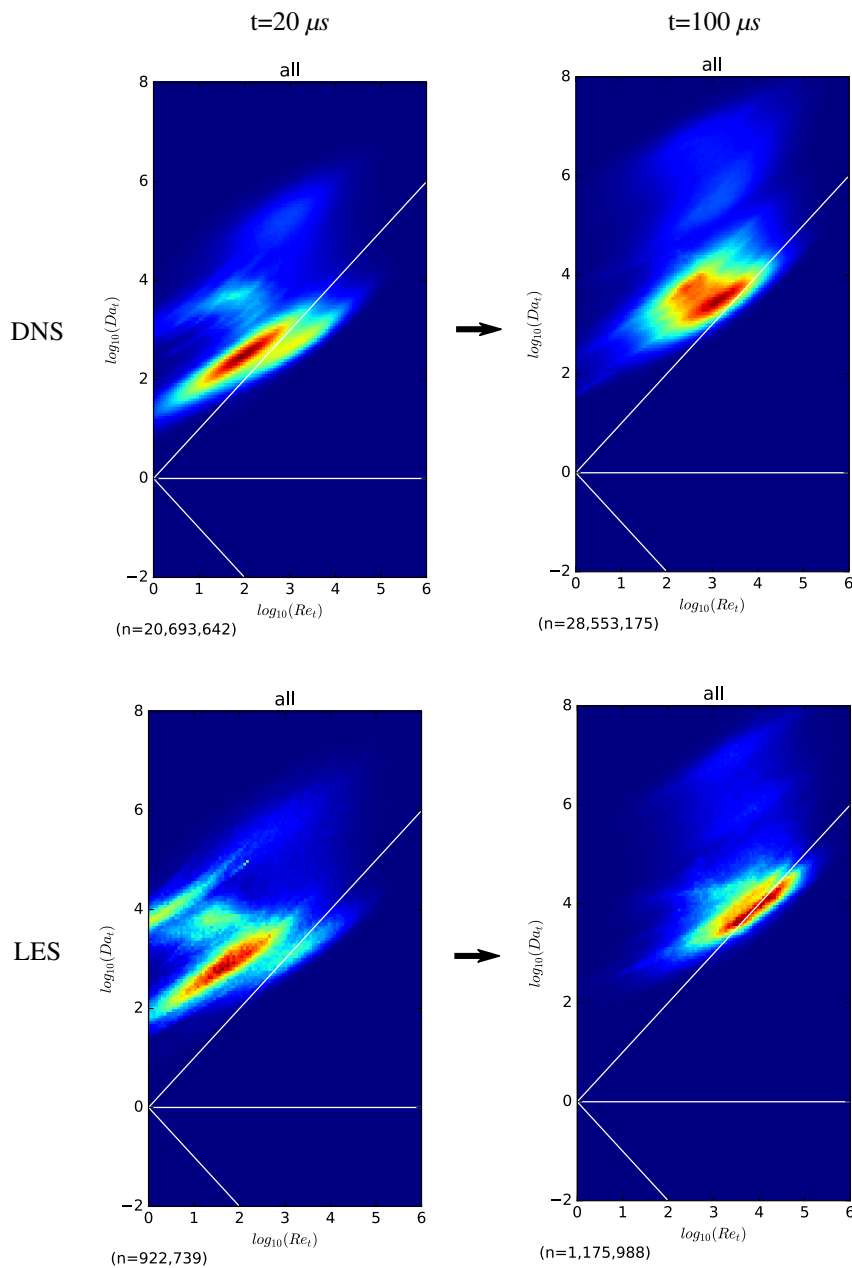


Figure 3: Regime heatmap comparison. Left: $20 \mu s$. Right: $100 \mu s$. Top: DNS. Bottom: LES

6. Simulation Quality

This section applies a mixture of approximations, averaging, and rules of thumb to critically examine the numerical setup used for the simulations already presented.

6.1 DNS Spatial Resolution

Among the most important of these issues is the matter of spatial discretisation, especially for the DNS. The simulation domain must contain sufficient size to support realistic turbulent flow inside it. Should the large scales of the flow grow too large relative to the domain size, the periodic boundaries will start to affect the results, as they are no longer far enough apart to be representative of a real flow. Additionally, at the smallest scales the cell sizes should be sufficient to resolve the fine detail of the turbulent cascade, ensuring that enough of the dissipation range is present that energy is not unphysically trapped in the middle scales. These requirements are examined here by using the flow field to estimate various scale sizes using approximate formulae derived from dimensional analysis of idealised turbulence.

The first length scale of interest is the integral length scale l_0 , roughly the size of the largest eddies in the flow. This can be computed [17] using the turbulent kinetic energy k_t and the turbulent dissipation ε :

$$l_0 = \frac{k_t^{3/2}}{\varepsilon} \quad (12)$$

The second scale of interest, moving down the turbulent cascade, is the Taylor scale λ . It is an abstract length scale associated with the turbulent dissipation, lying somewhere in the inertial range where the turbulence becomes approximately scale free. Estimating it additionally requires the kinematic viscosity (ν), from [17]:

$$\lambda = \sqrt{\frac{10\nu k_t}{\varepsilon}} \quad (13)$$

The final and smallest scale used here is the Kolmogorov microscale η , the size range where viscosity dominates and turbulent structures cannot persist. From [20]:

$$\eta = \left(\frac{\nu^3}{\varepsilon}\right)^{1/4} \quad (14)$$

These numbers are aggregate properties of an entire turbulent cascade. They emerge from dimensional analysis and energy scaling laws discovered for homogeneous isotropic turbulence in equilibrium, an idealization that captures some of the statistical properties of a real turbulent flow in spite of its complexity. This means that computing each of them at each point in the current flow produces a field of length scales without a clear physical interpretation. A sensible method for resolving this issue is to aggregate the results using some kind of averaging process, after which they can be interpreted statistically as in the original definition of each quantity. The present case is highly unsteady and ill-suited to time averaging, but a spatial average can be substituted by assuming that the 3D turbulent fluctuations are superimposed on a bulk

flow field that varies only in the z direction. Defining a slab-shaped filter centered on a point Z and spanning the entire x and y directions as:

$$F(z, Z, d) = \begin{cases} 1 & : Z - d/2 < z < Z + d/2 \\ 0 & : \text{else} \end{cases} \quad (15)$$

The flowfield can be filtered into a one dimensional line at each timestep, mapping a set of z positions Z_k and any flow variable ψ into a set of filtered quantities $\bar{\psi}_k$:

$$\bar{\psi}_k = \frac{\sum_j F(z_j, Z_k, d) \psi_j V_j}{\sum_j F(z_j, Z_k, d) V_j} \quad (16)$$

Where the index k varies over 100 non-overlapping slabs (50 for the LES) that move vertically up the domain, and the index j varies over each cell in the full 3D flowfield. Additionally V_j and z_j are the volume and z position of cell j . This operation reduces the flow to a set of time-varying 1D distributions that are stable from run to run and can be used to easily compare the two simulations and understand their overall behaviour.

Figure 4 displays the one-dimensionalized turbulent length scales \bar{l}_0 (Integral), $\bar{\lambda}$ (Taylor), and $\bar{\eta}$ (Kolmogorov), computed using the DNS at two important times.

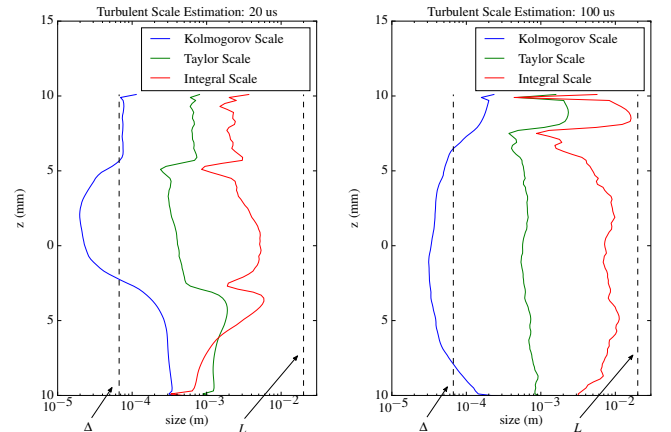


Figure 4: One-dimensionalized turbulent scales, SML DNS.

The results are split into two figures, which display the distribution of averaged scales for each z position in the mixing layer, plotted using a logarithmic horizontal axis for the dependant variable. The left figure is the early time measurement ($\approx 20\mu s$) taken just as the flow becomes fully turbulent, and the right one is the late time ($\approx 100\mu s$) one just before the simulation ends. The grid spacing Δ is marked using a vertical line, and so is the domain size L . The curves show that the integral scale is properly contained within the domain, increasing over time but still less than L at the end of the simulation time. The Taylor scale too stays roughly centered in the scale space, indicating the presence of an inertial range where fully developed turbulent effects are present, and also a substantial range of resolve scales below this. The Kolmogorov scale is represented by the blue line in the diagrams, which does dip below the grid

size limit represented by the dotted line, though the scales are within a factor of two or three of each other at worst. It is possible that the grid in this simulation is partially cutting off the smallest end in the dissipation range, but enough of it is being resolved for the simulation to run stably without excessive energy build-up at high wavenumbers. Additionally, other DNS simulations[3] found have found the smallest reacting structures are around 10 Kolmogorov length scales in size, and it is possible that η is a overly conservative benchmark for Δ for this reason. Future simulations should address this concern, but for the present purposes it appears as if enough of the dissipation range is being computed that the results of the analysis are still useful.

6.2 LES Spatial Resolution

To evaluate the level of discretisation used in the LES, we estimate the subgrid turbulent kinetic energy (TKE) and compare it in magnitude to the resolved TKE present in the flow [17]. According to a classical definition of a well resolved LES, the resolved flow should account 80% or more of the total TKE k_r [20]. This rule of thumb can be translated into a concrete metric, the resolved kinetic energy fraction R , using the equation 4:

$$R = \frac{\bar{k}_r + \epsilon}{\bar{k}_r + \bar{k}_{sgs} + \epsilon} \quad (17)$$

This definition uses a small number ($\epsilon = 1 \times 10^{-6}$) to force the metric to approach 1 (fully resolved flow) whenever both numbers are small, i.e. in laminar conditions.

With the LES filter width being fairly close to the DNS level, (a reduction by a factor of 3 in cell size), it might be expected that the LES resolution will be quite good. Computing the resolved turbulent kinetic energy fraction R confirms this is the case. Figure 5 shows the one-dimensionalized representation of this quantity at $20\mu s$ and $100\mu s$ of simulation time, which is well above 80% for the entire domain.

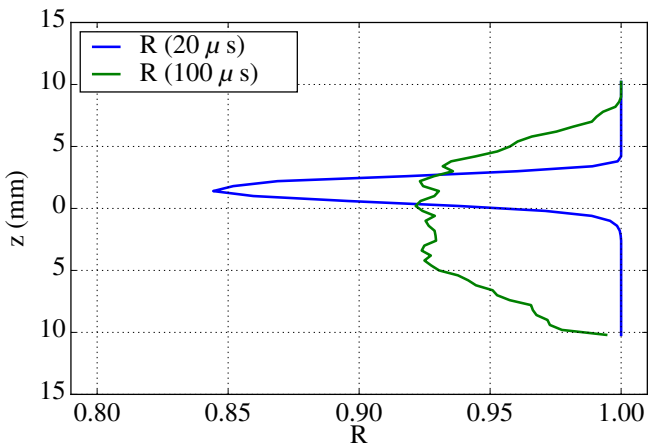


Figure 5: One-dimensionalized resolved kinetic energy fraction, SML LES.

6.3 Turbulence Reynolds Number

The last quality check is on the state of the turbulence itself. At any one point in time the state of the turbulence can be parameterized by a Reynolds number, assuming a velocity, kinematic viscosity, and length scale relevant to the flow problem can be defined. Following [21], we use Δu , the relative velocity of the two layers, as the velocity scale, and the so-called vorticity thickness δ_ω as the length scale:

$$\delta_\omega = \frac{\Delta u}{\text{MAX}\left(\frac{\partial \bar{u}}{\partial z}\right)} \quad (18)$$

The velocity gradients used in this calculation are computed using forward differencing from the one-dimensionalized x-velocity \bar{u} . The kinematic viscosity $\bar{\nu}$ is computed from the one-dimensionalized mean properties midway through the mixing layer. The shear-layer Reynolds number is then:

$$Re = \frac{\Delta u \delta_\omega}{\bar{\nu}} \quad (19)$$

Charting the evolution of this quantity over time provides an overall view of the time evolution of the turbulent flow in the domain, as in figure 6.

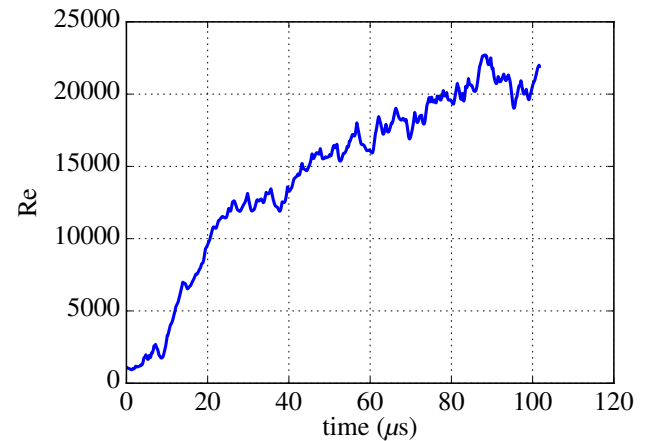


Figure 6: Shear layer Reynolds number vs time in microseconds.

In Ref. [21], fully developed turbulent behaviour was observed above $Re \approx 10,000$, a useful threshold for verifying that the apparently turbulent flow in the images in figure 2 is representative of turbulence in general. Figure 6 shows that the flow quickly reaches this threshold and stays above it for the rest of simulation, climbing over time as the mixing layer grows in size, the increased length scale dominating over the increase in viscosity that occurs due to the rising temperature, eventually reaching just over $\approx 20,000$. The result confirms that the DNS is representative of the fully developed, high Reynolds number turbulence that occurs in a full-sized engine, in spite of the limited physical size of the domain.

7. Conclusions

In this work a Direct Numerical Simulation is used to compute combustion regime data in a supersonic turbulent mixing layer. Though the regimes themselves are somewhat artificial, they have been compared to the results of a similar calculation that uses an approximate turbulence model; a Large Eddy Simulation or LES. This LES did not include an explicit model for the filtered reaction rates, assuming that they can simply be computed from the filtered composition and temperature as in quasi-laminar combustion. Although this assumption is known to cause minor errors in the reaction rates, the combustion regimes computed by the two simulations are similar, differing in location in parameter space by ≈ 0.5 units at the $20\mu s$ mark, and ≈ 1.0 at the $100\mu s$ mark. This suggests that the quasi-laminar LES methodology can be used to investigate the regimes in larger flowfields that are more representative of real supersonic propulsion systems, at least to the extent that the DNS/LES correspondence in this study is maintained at the larger scales.

Further research should aim to test this correspondence, in addition to the goal of regime characterisation. The DNS and LES used in this study are rather close in scale, with cell sizes within a factor of 3, and the combustion they model is quite fast compared to the milder conditions encountered in a scramjet flowpath. Relaxing these concerns by matching the scale separation and combustion speed will increase the confidence in the conclusions of this paper, and assist greatly with developing new models to address the significant challenges ahead.

8. Acknowledgements

The authors would like to thank Professor Graham Candler's research group for providing the research CFD code used. Supercomputer time was provided by the National Computational Infrastructure (NCI) at the ANU and by the Pawsey Supercomputing Centre in WA, supported by an award under the NCI Merit Allocation Scheme and funding from the Australian Government.

References

- [1] N. N. Gibbons (2019) Ph.D. dissertation, The University of Queensland, School of Mechanical and Mining Engineering, St Lucia, QLD 4072.
- [2] M. P. Martin and G. V. Candler (1998, July) *Physics of Fluids*, **10**, pp. 1715–1724.
- [3] M. Tanahashi, M. Fujimura, and T. Miyauchi (2000) *Proceedings of the Combustion Institute*, **28**, pp. 529–535.
- [4] M. P. Martin, V. G. Weirs, D. Olejniczak, and G. V. Candler (1998, June) in *29th AIAA Fluid Dynamics Conference*, no. 1998-2817.
- [5] L. Duan and M. P. Martin (2011, October) *AIAA Journal*, **49**.
- [6] D. Chakraborty, P. J. Paul, and H. S. Mukunda (2000) *Combustion and Flame*, **121**, pp. 195–206.
- [7] C. Pantano (2004) *Journal of Fluid Mechanics*, **514**, pp. 231–270.
- [8] P. J. M. Ferrer, G. Lehnasch, and A. Mura (2017) *Combustion and Flame*, **180**, pp. 284–303.
- [9] C. Pantano, S. Sarkar, and F. A. Williams (2003) *Journal of Fluid Mechanics*, **481**, pp. 291–328.
- [10] G. V. Candler, H. B. Johnson, I. Nompelis, P. K. Subbareddy, T. W. Drayna, and V. Gidzak (2015, January) in *53rd AIAA Aerospace Sciences Meeting*, no. 2015-1893.
- [11] M. Shur, P. Spalart, M. Strelets, and A. Travin (2008) *International Journal of Heat and Fluid Flow*, **29**, pp. 1638–1649.
- [12] C. J. Jachimowski (1992, July) Tech. Rep. NASA TP-3224, National Aeronautics and Space Administration, Hampton, Virginia.
- [13] M. Wright, G. Candler, and M. Prampolini (1996, July) *AIAA Journal*, **34**, pp. 1371–1377.
- [14] J. Steger and R. F. Warming (1981) *Journal of Computational Physics*, **40**, pp. 263–293.
- [15] F. Ducros, V. Ferrand, F. Nicoud, C. Weber, D. Darracq, C. Gacherieu, and T. Poinso (1999) *Journal of Computational Physics*, **152**, pp. 517–549.
- [16] G. Balakrishnan and F. A. Williams (1994) *Journal of Propulsion: Technical Notes*, **10**, pp. 434–437.
- [17] R. M. Gehre (2014) Ph.D. dissertation, The University of Queensland, School of Mechanical and Mining Engineering, St Lucia, QLD 4072.
- [18] D. C. Wilcox (2002, December) *Turbulence Modelling for CFD*, 2nd ed., DCW Industries, Inc.
- [19] T. F. Lu, C. S. Yoo, J. H. Chen, and C. K. Law (2010, January) *Journal of Fluid Mechanics*, **652**, pp. 45–64.
- [20] S. Pope (2000) *Turbulent Flows*, 40 West 20th Street, New York NY, USA: Cambridge University Press.
- [21] P. E. Dimotakis (2000) *Journal of Fluid Mechanics*, **409**, pp. 69–98.

Soot particle structure variation associated with in-cylinder gas pressure/temperature in a small-bore diesel engine

L. Rao, Y. Zhang and S. Kook*

School of Mechanical and Manufacturing Engineering, The University of New South Wales, Sydney, NSW 2052, Australia

Abstract

The present study reveals the impact of fuel injection timing on in-cylinder soot processes in a small-bore optical diesel engine. Two injection timings were selected for their distinctive differences in the peak in-cylinder pressure/temperature, which was used to discuss structure of soot particles within the diesel flame. Thermophoresis-based particle sampling was performed at two different in-bowl locations and transmission electron microscope (TEM) imaging was used to visualise the sampled soot particles. Subsequently, through both visual inspection and statistical analysis, soot aggregate morphology and sub-nanoscale carbon-layer structures were discussed for the two different injection timings. The results suggest that advancing fuel injection timing directs the start of combustion closer to the top dead centre and therefore soot formation and oxidation occurred at elevated in-cylinder gas pressure/temperature. Consequently, the soot formation is further advanced as indicated by increased propensity of large and stretched soot aggregates as well as lack of small and compact soot aggregates. The carbon layer structure also shows more mature soot status as evidenced by longer carbon fringe length measured for higher in-cylinder pressure/temperature.

Keywords: Diesel engine, Soot structure, In-cylinder gas pressure/temperature

1. Introduction

As one of the most important operating parameters for modern diesel engines, fuel injection timing has significant impacts on both the engine performance and pollutant formation [1]. It is well known that advancing the fuel injection timing effectively reduces the tailpipe soot emissions [2], which could be used to meet ever-tightening regulations on diesel particulate emission. Most previous studies attributed the reduction of soot emissions to suppressed formation as a result of enhanced mixing. That is, advancing the injection timing results in extended ignition delay due to relatively lower in-cylinder pressure and temperature at the injection event, which subsequently promotes pre-combustion mixing [2,3]. However, recent studies suggest ignition delay does not always vary monotonically with injection timing [4]. For example, in a modern small-bore diesel engine, significantly reduced (even negligible) change in ignition delay was observed with injection timing variation. This is because the enhancement of air-fuel mixing through factors such as high swirl ratio dominates over the variation in in-cylinder gas conditions [5].

Another important factor that affects the in-cylinder soot processes is in-cylinder gas pressure/temperature [6]. Previous studies showed advanced injection timing elevates the in-cylinder gas temperature during the main combustion event [7]. With the increased in-cylinder gas pressure/temperature due to advanced injection timing, soot formation was increased; however, the measured engine-out emission showed lower soot emissions due to enhanced soot oxidation [7]. Given the complex nature of in-cylinder soot formation and oxidation and their trade-off characteristics in determining the engine-out emissions, further insight is required.

The present study performed soot particle structure analysis based on thermophoresis-based in-flame particle sampling in a running diesel engine. The particle sampling was performed at two in-bowl locations to capture the structural evolution of soot particle during the combustion event. The subsequent statistical analysis of the sampled soot primary particles and visual inspection of soot aggregate structure were repeated for two selected fuel injection timings that exhibited significant differences in in-cylinder pressure/temperature during the main combustion event.

2. Experiments

The soot sampling experiment was performed in a single-cylinder light-duty optical diesel engine modified from a conventional 2-litre, four-cylinder diesel engine. The simplified engine configuration is shown in Fig. 1 and the engine specifications as well as operating conditions are summarised in Table 1. The engine has a displacement volume of 497.5 cm³ with 83 mm bore and 92 mm stroke, a

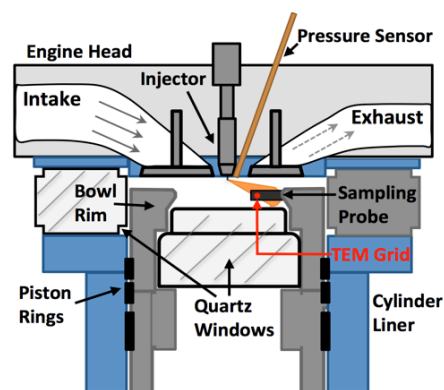


Figure 1: Schematic diagram of the optical diesel engine and soot sampling setup.

geometric compression ratio of 15.5, and a swirl ratio of 1.4. Throughout the experiments, the engine speed was held constant at 1200 rpm using an AC electric motor that is connected directly to the crankshaft. The engine was naturally aspirated and the intake air temperature was maintained at 303 K. In addition, the combustion-chamber wall temperature was kept at 363 K by implementing heated water circulation (ThermalCare Aquatherm RA series) to the cylinder head, liner and engine block. Similar to that of previous studies, methyl decanoate ($C_{11}H_{22}O_2$) was selected as the diagnostics fuel due to its low sooting propensity that helps avoiding potential soot overloading for particle sampling experiments. The existing data from planar laser-induced incandescence (PLII) imaging was also useful to determine the soot sampling locations [9], which was obtained using methyl decanoate to avoid beam attenuation issues.

The fuel was directly injected into the combustion chamber

Table 1: Engine specifications and operating conditions

Displacement	497.5 cm ³
Bore	83 mm
Stroke	92 mm
Compression ratio	15.5 (Geometric)
Engine speed	1200 rpm
Swirl ratio	1.4
Wall temperature	363 K
Intake air temperature	303 K
Injector type	Common-rail (Bosch CP3)
Number of holes	1
Nozzle type	Hydro-grounded, K1.5/0.86
Nozzle diameter	134 μ m
Included angle	150°
Fuel	Methyl Decanoate
Cetane Number	47-53
Rail pressure	100 MPa
Injection signal duration	1.5 ms
Injected fuel mass	15.3 mg
Injection signal timing	16, 13°CA bTDC

using a centrally mounted common-rail injector (Bosch CP3). Following the same approach as of previous studies, the original 7-hole injector nozzle was laser welded for a single-hole configuration, which has a hole diameter of 134 μ m and an included angle of 150°. This approach enabled the analysis of soot particles from a single jet before more practical jet-jet interaction conditions are studied in future.

For the control of fuel injection timing and duration, a universal timing synchronisation unit (Zenobalti 9013-P) was used. The fuel injection duration was held constant at 1.5 ms (electronic), which resulted in approximately 15.3 mg of fuel per injection at fixed injection pressure of 100 MPa. Two injection timings of 13 and 16°CA bTDC were carefully selected for discernible changes in in-cylinder pressure profile and combustion phasing. The present study implemented a 10 skip-firing method: fuel injection takes place every 10th motoring cycle to expel residual gases from previous firing cycle. For each engine run, the in-cylinder pressure was recorded using a piezoelectric transducer (Kistler 6056A1).

For soot sampling experiment, a 3-mm diameter TEM grid was installed at the tip of the sampling probe, which was fixed onto the piston-bowl wall. The probe tip had a 2-mm diameter hole that provides a direct exposure of the TEM grid to the hot soot-laden gases (flame). The high temperature gradient between the hot soot particles and the cold TEM grid surface induced thermophoresis effect that forced soot particles to deposit on to the grid surface with immediate reaction quenching. As shown in Fig. 2, soot sampling was performed at two different locations through rotating the piston crown by 60°. This is designed to reveal evolution of soot particles as carried by the wall jet head travelling along the wall from the flame-wall impingement region (location A) and to further downstream location (location B). At each sampling location, two TEM grids were used as the standard and lacy TEM grids for the imaging of soot aggregate structure (Fig. 2 left, highlighted by red dashed box) and the high-resolution imaging for the carbon layer fringes of soot primary particles (Fig. 2 left,

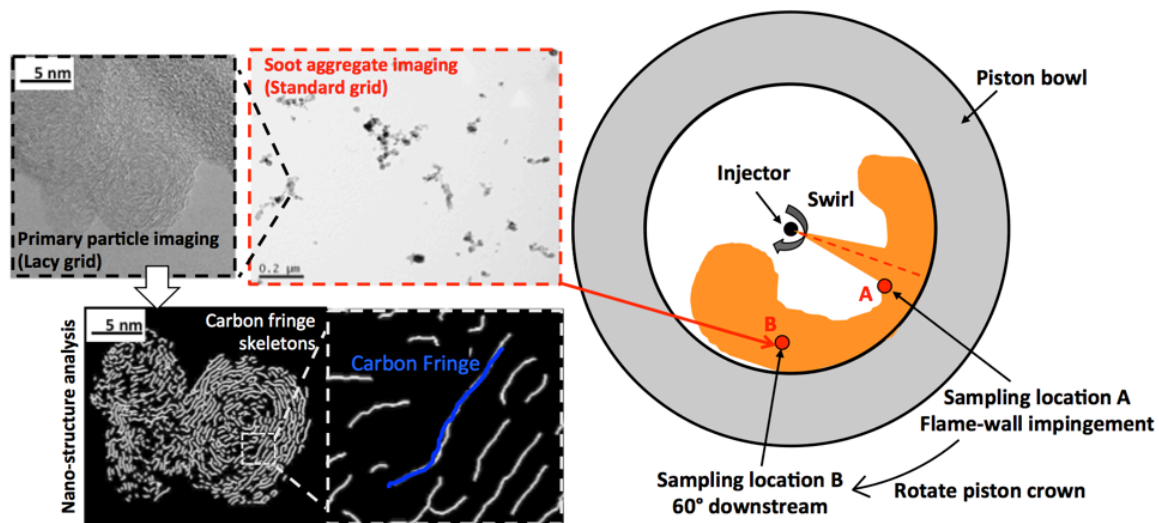


Figure 2: Illustration of the soot sampling system and example TEM images.

highlighted by black-dashed box) with respectively. For this sub-nanoscale analysis of carbon fringes, the original TEM image was converted into a skeleton image using a Matlab-based processing code. Detailed explanation of the processing procedure is found in our previous study [8]. From each carbon fringe (Fig. 2, white-dashed box), key fundamental parameters as fringe length and tortuosity (the curviness of fringes) were obtained, which are useful to understand the evolution of in-cylinder soot particles.

3. Results and Discussion

3.1 In-cylinder pressure and aHRR

Figure 3 shows the ensemble-averaged in-cylinder pressure traces and calculated apparent heat release rate (aHRR) profiles for the two selected injection timings of the present study. The actual start of fuel injection and the start of combustion are also annotated in Fig. 3. The observed trend is clear that the start of combustion becomes more advanced and the in-cylinder pressure is higher at earlier injection timing. The peak aHRR also shows higher value for more advanced injection timing. It was understood that, for the selected conditions of the present study, the higher in-cylinder pressure was not related to the level of pre-combustion mixing due to insignificant variation in ignition delay ($< 1^\circ\text{CA}$). It was the earlier start of combustion, i.e. the combustion event occurring closer to the TDC, as triggered by the advanced fuel injection event. Subsequently, the reaction occurred at elevated in-cylinder pressure and temperature conditions. This is primarily a combustion phasing effect. From our previous study [9], it was shown that the soot PLII signals are detected first at the peak in-cylinder pressure position, which is roughly 10°CA aTDC in Fig. 3. This means the soot formation and oxidation would occur at much higher in-cylinder pressure (and temperature) conditions for more advanced injection timing of 16°CA bTDC.

3.2 Soot particle structure

Figure 4 shows TEM images of the sampled soot particles from sampling location A - the jet-wall impingement point (top), and location B - 60° downstream (bottom) for the two injection timings. At location A, the sampled soot particles show structures that are best interpreted as early formation stage for both injection timings – i.e. many small soot aggregates composed of single (monomer) or double (dimer) soot primary particles. The TEM images show very similar soot structures and overall amount of soot particles sampled for the two injection timings, indicating minimal impact of in-cylinder pressure/temperature on the early formation of soot particles.

Figure 4 (bottom) shows that, compared to location A, the sampled soot particles from location B had larger soot aggregates composed of many soot primary particles. It is clear that both the quantity and size of the sampled soot increase significantly between location A and B, and the soot aggregates are not only larger but also more complex in structures. The TEM images indicate soot particle-to-

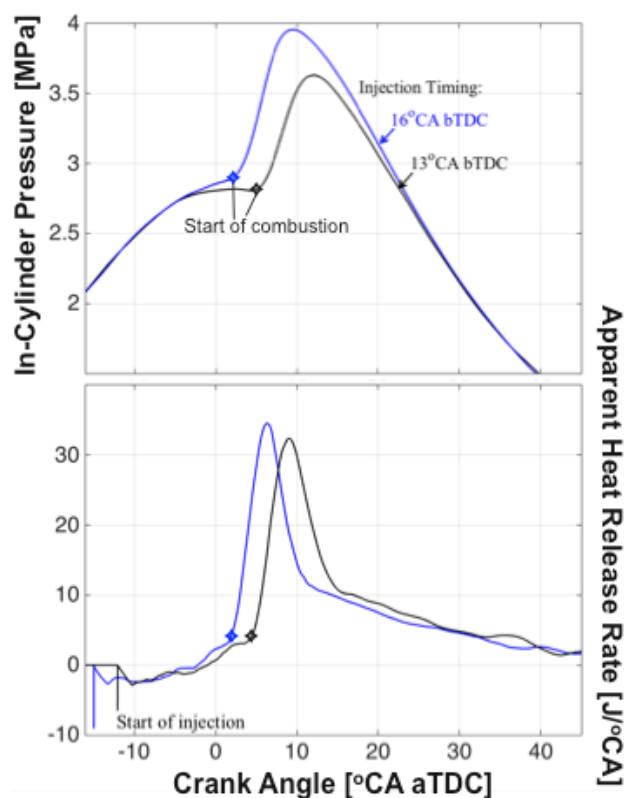


Figure 3: Ensemble-averaged in-cylinder pressure and apparent heat release traces for the two injection timing cases.

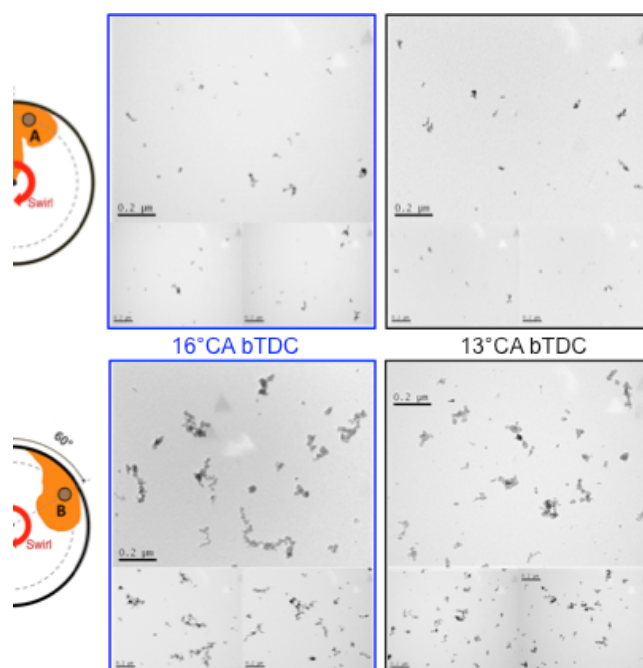


Figure 4: Transmission electron microscope (TEM) images of the sampled soot particles from location A (top) and location B (bottom) for the two injection timing cases.

particle aggregation, which resulted in a long stretched structure of the soot aggregates.

At location B (Fig. 4, bottom), the soot aggregates show a marked difference between the two injection timings. With the advanced injection timing of 16°CA bTDC, the small

and compact aggregates easily seen from the 13°CA bTDC injection are rarely found. The overall soot aggregate size is also larger for more advanced injection timing. This suggests that the soot aggregation was more significant for more advanced injection due to accelerated soot evolution at higher in-cylinder pressure/temperature.

Figure 5 (left) shows four example high-resolution TEM images of soot primary particles sampled at location A and B under the variation in injection timing. On the right, the probability density function (pdf) distributions of carbon-layer fringe length are plotted with annotations of the mean value and error range for the fringe length and tortuosity. Inspecting the raw high-resolution TEM images confirms that soot particles experienced significant oxidation at the downstream location, as the amorphous internal structure of the soot primary particles found at location A transformed into a core-shell structure at location B. This trend was observed for both injection timings. In addition, from the pdf plot shown at the right, the fringe length and tortuosity of the 16°CA bTDC injection are comparable to that of the 13°CA bTDC injection at location A, which is consistent with similar soot aggregate morphology at the early formation stage.

However, at location B, the result shows longer fringe length for more advanced injection timing. This means more mature soot that went through significant formation and oxidation reactions. In other words, the higher in-cylinder pressure/temperature enhanced soot processes (e.g. the formation and oxidation) and thus when they were sampled, the soot particles were at a later stage of soot formation/oxidation for more advanced injection timing.

4. Conclusions

The in-cylinder soot processes associated with injection

timing variation have been investigated in a small-bore optical diesel engine through thermophoresis-based particle sampling and subsequent statistical analysis of particle structure at two different in-bowl locations. The result shows advanced injection timing leads to overall larger and more stretched soot formation due to enhanced particle-to-particle aggregation occurred at higher in-cylinder pressure/temperature conditions. These soot particles underwent more significant formation and oxidation reactions for more advanced injection timing due to higher in-cylinder pressure/temperature as evidenced by longer carbon-layer fringe length.

Acknowledgments

The experiments were performed at the UNSW Engine Research Laboratory, Sydney, Australia. The financial support for this work was provided by the U.S. Army International Technology Center Pacific (ITC-PAC).

References

- [1] X. Li, Z. Xu, C. Guan, and Z. Huang (2014) *Fuel* **134**, pp. 189–195.
- [2] C. Kweon, S. Okada, et al. (2003) *SAE Tech. Pap.* 2003-01–17.
- [3] S.K. Aggarwal, X. Fu, and S. Wijeyakulasuriya (2016) *Int. J. Green Energy* **13**, pp. 431–445.
- [4] Z. Xu, X. Li, C. Guan, and Z. Huang (2014) *J. Aerosol Sci.* **76**, pp. 28–38.
- [5] S. Kook, C. Bae, et al. (2006) *SAE Tech. Pap.* 2006-01–0197.
- [6] L.M. Pickett and D.L. Siebers (2004) *Combust. Flame* **138**, pp. 114–135.
- [7] R. Zhang and S. Kook (2014) *Environ. Sci. Technol.* **48**, pp. 8243–8250.
- [8] Y. Zhang, R. Zhang, and S. Kook (2015) *SAE Int. J. Engines* **8**, pp. 2213–2226
- [9] MK. Le, R. Zhang, et al. (2016) *Fuel* **166**, pp. 320–332.

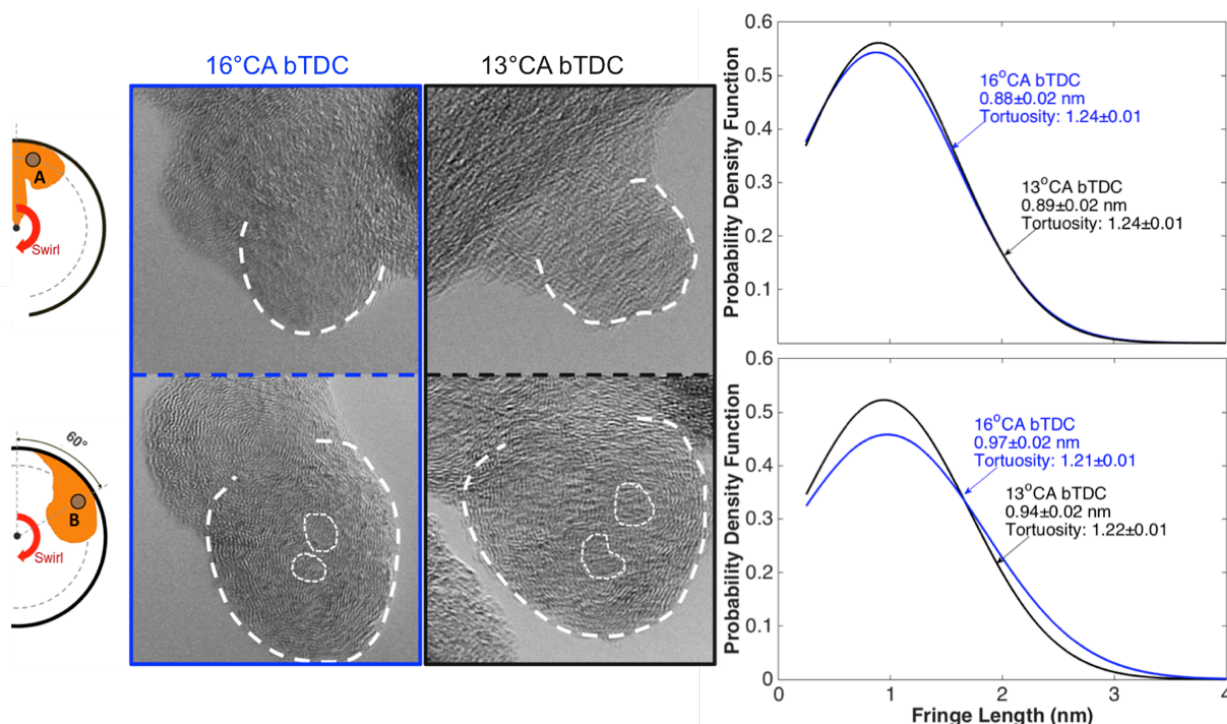


Figure 5: High-resolution TEM images (left) and processed carbon-layer fringe length in pdf (right) for the two injection timing cases. The tortuosity values are noted next to the fringe length pdf lines.

In-cylinder and exhaust soot morphology in an optical spark ignition direct injection (SIDI) petrol engine

D. Kim and S. Kook*

School of Mechanical and Manufacturing Engineering, The University of New South Wales, Sydney, NSW 2052, Australia

Abstract

Simultaneous in-flame and exhaust soot particle sampling experiments were conducted to investigate the soot formation and oxidation process in a spark ignition direct injection (SIDI) engine. Sampled soot particles were imaged through transmission electron microscope (TEM) and processed to extract soot primary particle diameter, radius of gyration of soot aggregates, and their fractal dimension. Results show that higher injection pressure resulted in higher amount of in-flame soot particles with larger particle size due to increased wall wetting and thereby more intense pool fire. However, the particles sampled from the exhaust stream showed significantly lower amount of soot with smaller and more compact particle structures, suggesting that enhanced in-cylinder soot oxidation at higher jet momentum conditions outperformed higher soot formation.

Keywords: Soot particle, SIDI engine, Pool fire.

1. Introduction

Direct injection technology has been steadily employed in gasoline engines due primarily to fuel economy benefits [1]. As spark ignition direct injection (SIDI) engines deliver fuel directly into the combustion chamber, precise and robust fuelling control is realised for various engine load and speed conditions, which outperforms port-fuel injection (PFI) systems [2]. This contributes to the reduced fuel consumption which in turn result in reduced CO₂ emissions [3]. The charge cooling effect is another significant benefit as endothermic fuel vaporisation enables the use of higher compression ratios while avoiding premature ignition and abnormal combustion, namely, knocking [4]. One major drawback of the SIDI engine is increased particulate matter (PM) emissions [5], a well-known harmful pollutant that damages human respiratory systems [6] and deteriorate the air quality [7]. Therefore, particulate emissions are strictly regulated for both mass (PM) and number counts (PN) [8], which poses a significant technical challenge for automakers and engine developers.

Elevated injection pressure is one of the widely used methods to mitigate the particulate emissions in SIDI engines. The injection pressure of SIDI engines today is already high at 20–25 MPa [9], which could be further increased up to 60 MPa [10] for shorter injection duration and improved air/fuel mixing and thereby reducing the in-cylinder formation of soot and other particulates. However, some reported an adverse effect of very high injection pressure such as increased ultra-fine particulate emission and higher PN emission [11]. To achieve significant and simultaneous reduction of PM and PN emissions, enhanced fundamental understanding is required in terms of their original formation within the flame.

The detailed fundamental behaviour of soot emission could be investigated with the thermophoresis-based particle sampling and subsequent transmission electron microscope (TEM) imaging [12]. Throughout TEM imaging, engine-out soot particles were found to have fractal-like aggregate

structures, which comprise many soot primary particles [13]. These studies provide valuable information about exhaust particle structures; however, the particles are a product of complex soot formation and oxidation processes occurring inside the cylinder of the engine [14]. Our recent study [15] bridged this gap by developing a new soot sampling system with four TEM-grid holders being installed on the piston top in an optical SIDI engine. Together with the visualisation of soot luminosity signals, this study found direct correspondence between high pool fire and large soot primary particle/aggregate sizes.

In the present study, this newly developed soot sampling system has been applied for various injection pressures at a fixed advanced injection timing, which is a problematic condition with high soot emission [16]. The simultaneous soot sampling experiments were conducted for both in-flame and exhaust particles. Detailed morphology analysis was conducted based on standard TEM images which were post-processed to extract key parameters such as soot primary particle/aggregate size and fractal dimension. To ensure statistically meaningful analysis, over 100 soot aggregates and more than 1200 primary particles were processed from at least 30 different on-grid locations for each sample.

2. Experiment

2.1 Engine specifications and operating condition

The engine and particulate sampling system are illustrated in Fig.1 and the specifications of the engine and operating conditions are tabulated in Table 1. The sampling experiments were carried out in an optical engine based on a 0.5-litre single-cylinder engine with double-overhead cam (DOHC). The bore/stroke is a square configuration of 86 mm. The cylinder has a compression ratio of 10.5. A conventional 95 RON petrol fuel was supplied to a side-mounted 6-hole injector (Continental DI XL2) with varied injection pressures from 5 to 15 MPa. The amount of fuel injected was maintained for stoichiometric condition. The fuel injection timing was intentionally selected for a wall-

wetting condition with an advanced timing of 320 °CA bTDC, which corresponds to high particulate emissions conditions. The spark ignition timing was slightly adjusted to match the combustion phasing by 1 °CA for the varied injection pressures. In order to keep a consistent in-cylinder thermal condition, the coolant water was heated to 90 °C and circulated through the cylinder engine, liner, and engine block. The intake air was supplied in the wide-open throttle position at 100 kPa absolute pressure (i.e. natural aspiration), and the intake air temperature was measured at 30°C throughout the experiments.

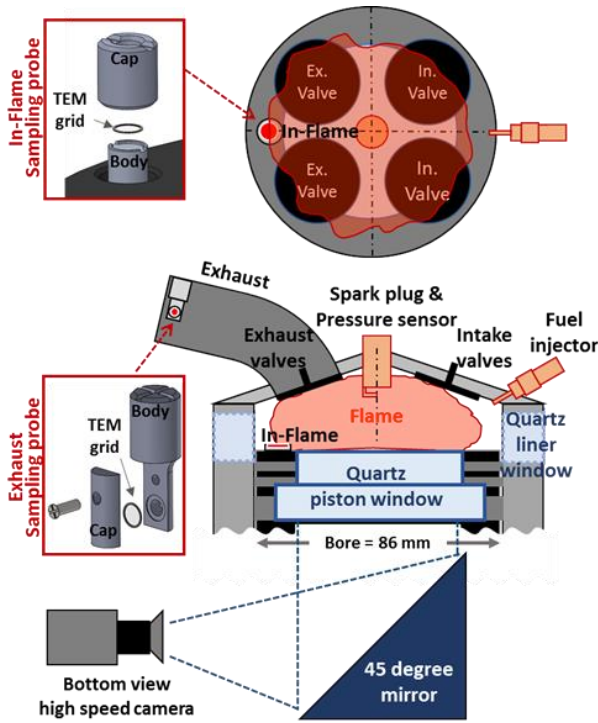


Figure 1: Illustration of the optical SIDI petrol engine and soot sampling system in top (top) and side views (bottom).

The engine speed was held constant at 1200 RPM using a 36-kW AC motor and a large flywheel. The engine was fired once in every 10th cycle (i.e. 10 skip-firing) to avoid thermally over-loaded optical quartz windows, and to completely expel the residual gas from a previous cycle before the subsequent firing. For each TEM grid, five firing cycles were applied to have sufficiently high number of particulates while avoiding the over loading of particulate on the TEM grid. This was found from the trial-and-error based preliminary tests. Then the engine run was repeated for the three different injection pressures. The injection and spark timing were controlled via a universal timing control unit (Zenobalti ZB-9013P) based on the reference signal of the crankshaft position produced from a rotary encoder (Autonics E40S8). The in-cylinder pressure was recorded using a pressure transducer integrated onto the spark plug (Optrand C822J6-SP), thus enabling to calculate the apparent heat release rate (aHRR).

2.2 High-speed flame luminosity imaging

The predominant signal from the natural combustion luminosity is released by the radiation of soot particles at high temperature [17], which shows the spatial and

temporal development of the diffusion flames with respect to the in-flame sampling probe location. A high frame rate of 10 kHz was used to obtain 0.72 °CA frame interval. A high-speed CMOS camera (VisionResearch Phantom v7.3) equipped with a Nikon Nikkor lens with 200-mm focal length were used for bottom-view imaging. The lens aperture and exposure time were set as f/8 and 20 μs for high image clarity.

Table 1: Engine specification and operating conditions.

Displacement	500 cm ³
Bore/Stroke	86/86 mm
Compression Ratio	10.5
Valvetrain	DOHC, 4 valves
Intake Valve Timing	353–113 °CA bTDC
Exhaust Valve Timing	136–360 °CA bTDC
Engine Speed	1200 RPM
Intake Pressure	100 kPa (absolute)
Intake Temperature	303 K
Coolant Temperature	363 K
Fuel-Injection Strategy	Single injection
Fuel Pressure	5, 10, 15 MPa
Fuel Injector	Continental DI XL2 (6-hole, side mounted)
Injection Timing	320 °CA bTDC
Firing Mode	10-skip firing
Number of Firing Cycles	5

2.3 Soot sampling and image processing

The particulate sampling probes were located on the opposite side of the fuel injector and exhaust port for simultaneous in-flame and exhaust soot particle sampling, as illustrated in Fig 1. The height of TEM grid for in-flame sampling was set at 1 mm above the piston top to allow for sufficient exposure of the grid to the flame before it reaches the piston surface, thus enhancing in-flame soot sampling capability. A 3-mm diameter TEM grid (Emgrid CF400-Cu) with a standard carbon film supported by copper grids was contained in each of the sampling probe tips. The temperature gradient between hot flame or exhaust gas and cold TEM grid surface would induce the thermophoresis and particulates deposition on the carbon film. It is expected that the reaction quenching would be immediate for the particulates due to high temperature difference, which would preserve the original particulate morphology [18].

The sampled particulates on the TEM grid were imaged using a TEM (JEOL 1400) with a point resolution of 0.38 nm and an accelerating voltage of 100 kV. The TEM images were recorded as digitised images via a CCD camera with a resolution of 11 mega pixels. Our previous study that conducted diesel in-flame soot sampling suggested significant variations in soot morphology depending on the TEM grid location [19]. Therefore, a total of 30 TEM images from various on-grid locations were

captured for each sample with 100k magnification. The TEM images were post-processed via in-house developed Matlab code for particulate morphology data such as soot primary particle diameter, radius gyration of particulates, and the fractal dimension. Detailed procedures of the Matlab-based image processing and determination of each morphology parameters can be found in our previous study [20].

3. Results and Discussions

3.1 In-cylinder conditions and pool fire distribution

In-cylinder pressure and combustion phasing have been matched to investigate the fundamental behavior of soot formation and oxidation process at fixed pressure and temperature environment while changing injection pressure as shown in Fig 2 (top). Despite of the consistent in-cylinder conditions, the flame luminosity due to pool fire shows significant variation with tested injection pressures as shown in Fig 2 (bottom). Figure 2 shows that, at higher injection pressure, the pool fire becomes more intense and covers wider area due to increased fuel spray penetration and wall wetting – i.e. higher fuel film formation on the piston surface and thereby higher pool fire.

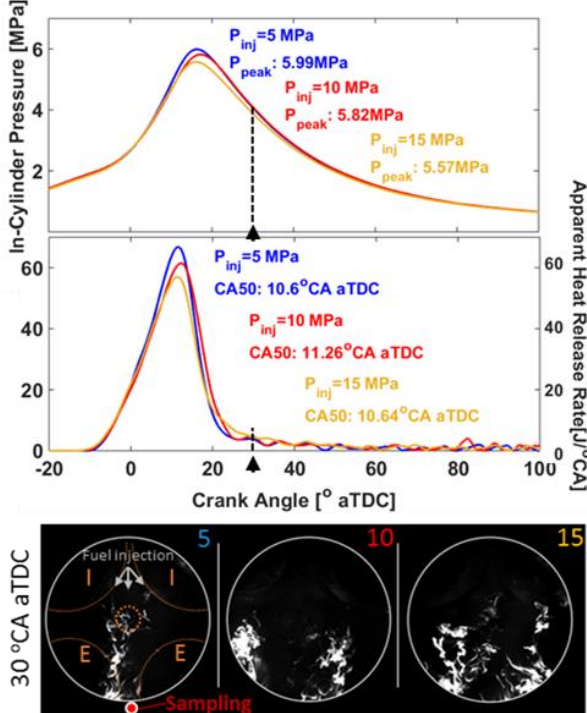


Figure 2: In-cylinder pressure and apparent heat release rate of varied injection pressure (top). Pool fire distribution at 30 °CA aTDC for the three injection pressures (bottom).

3.2 TEM images and overall soot amount

Example TEM images at 30k magnification are selected to show overall soot amount sampled for each sampling location along the injection pressure as shown in Fig 3. As injection pressure was increased, the more and larger soot particles were sampled. This is consistent with the previously observed more intensive pool fire signals at higher injection pressure, which is a well-known source of PM/PN emissions of SIDI engines [15]. Interestingly,

exhaust soot particles show opposite trend to the in-flame soot. With the higher injection pressure, less and smaller soot particles were sampled. At the lowest injection pressure of 5 MPa, stretched and chin-like structure of soot aggregates are observed, which is rarely seen for 10 and 15 MPa conditions. This indicates, despite higher pool fire and increased soot formation, the soot oxidation occurring inside the cylinder of the engine was more intense at higher injection pressure.

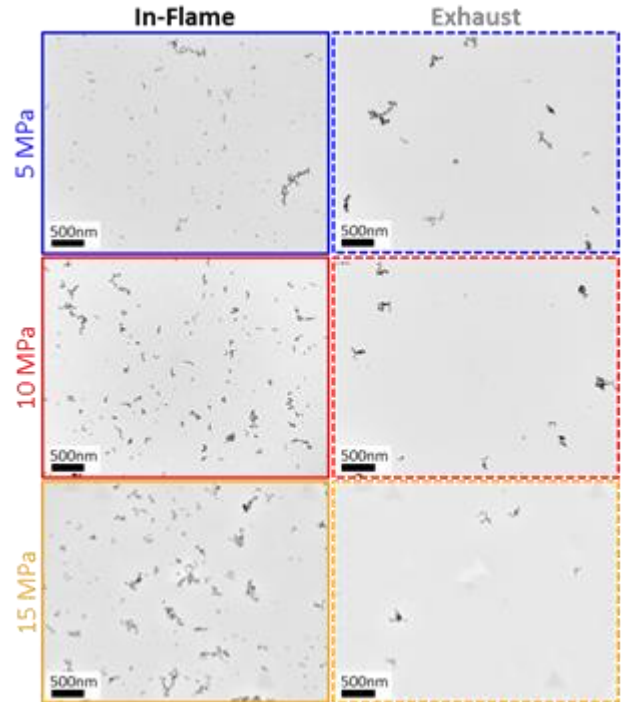


Figure 3: Example TEM images at 30k magnification from varied injection pressure for in-flame and exhaust soot aggregates. The scale bar of 500-nm are shown on the left-bottom corner for each image.

3.3 Microstructure variation between in-flame and exhaust soot particles.

To discuss further details of soot morphology change from in-flame to exhaust, soot primary particle diameter and radius of gyration of aggregates, as well as fractal dimension of each sampled soot particle have been processed with TEM images of 100k magnification, and the mean values of soot particle size and fractal dimension are shown in Fig 4. In-flame soot primary particle diameter and radius of gyration of aggregates show monotonic increasing trends as injection pressure increases. For the soot particles with 15 MPa injection pressure, the mean primary particle diameter and radius of gyration of aggregates are larger than those of 5 MPa case by 26.3% and 86.7%, respectively. This means that high injection pressure caused significant soot surface growth and agglomeration environment due to higher wall wetting and larger pool fire during the soot formation process. However, when the size variation between in-flame and exhaust particles is looked at, both soot primary particles and aggregates become smaller at higher injection pressure of 15 MPa. By contrast, at low injection pressure of 5 MPa, they show an increasing trend. The observed trends suggest the in-flame soot particles experienced more significant soot oxidation at

higher injection pressure. The higher in-cylinder soot oxidation was expected, and it was central to the development of higher pressure injection systems, as the enhanced injection momentum would enhance in-cylinder flow and turbulence. Despite higher wall wetting and increased soot formation, the accelerated soot oxidation resulted in reduced soot particles in the exhaust stream at higher injection pressure. The enhanced soot oxidation at higher injection pressure was also evident in the structural change from in-flame to exhaust, showing higher fractal dimension of exhaust soot particles at higher injection pressure.

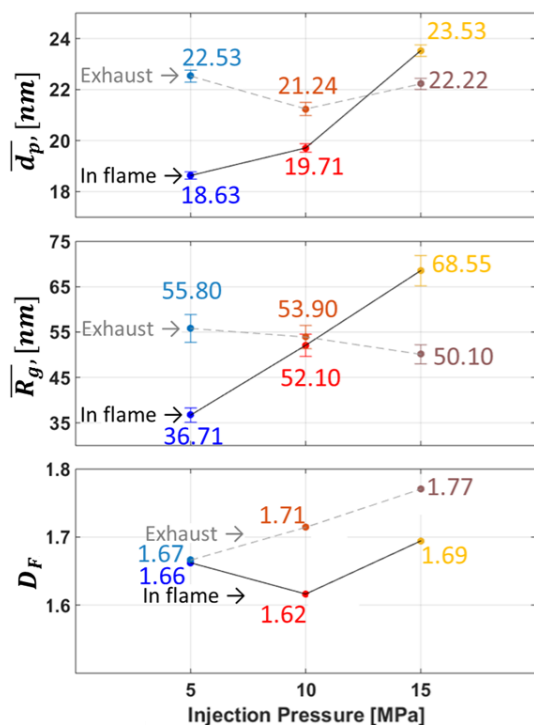


Figure 4: Mean value variations of soot primary particle diameter (top), radius of gyration of aggregate (middle), and calculated fractal dimension (bottom) along the injection pressure for in-flame and exhaust soot particles. 95% confidence intervals are annotated for each mean value.

4. Conclusions

Detailed soot morphology has been investigated with TEM images of soot particles sampled at in-flame and exhaust locations. The sampling experiment has been conducted with varied injection pressures from 5 to 15 MPa at fixed advanced injection timing to observe the soot morphology change from in-flame to exhaust. Combustion phasing has been matched by adjusting spark timing depending on the injection pressure for constant in-cylinder temperature and pressure conditions. Then, in-cylinder pool fire has been captured with high-speed imaging. The key findings of the present study are summarised as follow;

- Wider and stronger pool fire is formed with higher injection pressure due to the increased fuel wetting from the combination of longer fuel spray penetration,

supplying significant amount of fuel when the piston is close to the injector.

- TEM images show higher number counts as well as larger size of soot aggregate with higher injection pressure for in-flame soot particle, consistent with more intensive pool fire. However, the sampled soot particles from the exhaust stream are lower and show smaller sizes.
- Mean primary particle and radius of gyration for in-flame soot particles show a monotonic increasing trend as injection pressure increases, indicating high injection pressure provided significant in-flame soot formation environment.
- Despite higher soot formation at higher injection pressure, the enhanced soot oxidation leads to reduced soot size and compact structure, which explains overall lower amount of soot in the exhaust.

Acknowledgments

The experiments were performed at the UNSW Engine Research Laboratory, Sydney, Australia. The financial support was provided by the Australian Research Council via Linkage Project scheme.

References

- [1] Agency USEP (2016), United States Environmental Protection Report.
- [2] Zhao F, Lai MC, Harrington DL (1999), *Prog. Energy Combust. Sci.* **25**, pp. 437–562.
- [3] Lineman M, Do Y, Kim JY, Joo G-J (2015), *PLUS ONE*, **10**, e0138996.
- [4] Chincholkar SP, Suryawanshi JG (2016), *Energy Procedia*, **90**, pp. 666–672
- [5] Liang B, Ge Y, Tan J, Han X, Gao L, Hao L, et al. (2013), *J. Aerosol Sci.* **57**, pp. 22–31
- [6] Oberdörster G, Pulmonary (2001), *International Archives of Occupational and Environmental Health* **4**, pp. 1–8
- [7] Pöschl U (2005), *Angewandte Chemie*, **44**, pp. 7520–7540
- [8] European Commission, Commission regulation (EC) No 692/2008 of 18 July 2008, 2008
- [9] Leach F, Knorsch T, Laidig C, Wiese W (2018), *Int. Powertrains, Fuels & Lubr. Meeting*.
- [10] Postriotti L, Cavicchi A, Brizi G, Berni F, Fontanesi S, *SAE Technical Paper* No. 2018-01-0271
- [11] Wang C, Xu H, Herreros JM, Wang J, Cracknell R (2014), *Appl. Energy*, **132**, pp. 178–191
- [12] Vander Wal RL (1997), *Combust. Sci. Technol.* **126**, pp. 333–351
- [13] Miyashita K, Fukuda Y, Shiozaki Y, Kondo K, Aizawa T, Yoshikawa D, et al. *SAE Technical Paper* No. 2015-01-1872.
- [14] Tree DR, Svensson KI (2007), *Prog. Energy Combust. Sci.* **33**, pp.272–309
- [15] Kim D, Zhang Y, Clark L, Kook S, Gao Y (2018), *SAE Int. J. Engines*, **11**, pp. 1007-1022.
- [16] He X, Ratcliff MA, Zigler BT (2012), *Energy & Fuels*, **26**, pp.2014-2027.
- [17] Dec JE, zur Loye AO, Siebers DL, *SAE Technical Paper* No. 910224.
- [18] Dobbins RA, Megaridis CM (1987), *Langmuir*, **3**, pp. 254–259.
- [19] Kook S, Zhang R, Szeto K, Pickett LM, Aizawa T (2013), *SAE Int. J. Fuels Lubr.* **6**, pp. 80-97.
- [20] Zhang Y, Kim D, Rao L, Zhang R, Kook S, Kim KS, et al. (2017), *Combust. Flame*, **185**, pp. 278–291.
- [21] Chan QN, Bao Y, Kook S (2014), *Fuel*, **130**, pp. 228–240.

Fuel reactivity effects on premixed combustion in a diesel engine

Y. Zhang¹, S. Meng¹, H. Goyal¹, S. Kook^{1*}, K.S. Kim², and C.-B. Kweon²

¹School of Mechanical and Manufacturing Engineering, The University of New South Wales, Sydney, NSW 2052, Australia

²US Army Research Laboratory, Aberdeen Proving Ground, MD 21005, USA

Abstract

The present study shows temporal and spatial development of formaldehyde and hydroxyl radicals during the ignition event and how it is impacted by fuel reactivity in a small-bore diesel engine. Planar laser induced fluorescence imaging of fuel (fuel-PLIF), formaldehyde (HCHO-PLIF), and hydroxyl radical (OH-PLIF) have been performed for two different fuels with cetane number of 30 and 40 (CN30 and CN40) at fixed input energy and combustion phasing conditions. The fuel-PLIF images indicate that CN30 fuel is better mixed with air than CN40, which is consistent with longer ignition delay period measured from the in-cylinder pressure. Despite lower premixing, CN40 shows higher peaks of apparent heat release rate and in-cylinder pressure than CN30 during the premixed burn phase of the combustion. The combined HCHO-PLIF and OH-PLIF images exhibit that CN40 produced larger amount of HCHO, which was consumed faster to produce OH. This demonstrates a case that higher fuel reactivity could outperform lower charge premixing in determining the intensity of combustion during the premixed burn phase.

Keywords: Fuel reactivity, Formaldehyde, Compression ignition, Diesel engine.

1. Introduction

In a diesel engine, operating conditions set for long ignition delay time are used to increase charge premixing, which is known to increase engine efficiency and reduce soot formation [1]. This advantage has been utilised in a wide variety of advanced combustion regimes realising compression ignition of fully or partially premixed charge [2,3]. In these premixed charge compression ignition (CI) engines, the measured in-cylinder pressure and calculated apparent heat release rate (aHRR) profile show a small bump prior to the steep increase. This indicates the low-temperature reaction period during which hydrogen peroxide (H₂O₂) formation occurs before they decompose or react with formaldehyde (HCHO) before hydroxyl (OH) radical formation occurs during high-temperature reaction [4]. As HCHO persists longer in fuel-lean mixtures, the length of this persistency could imply charge premixing level [4,5]. The HCHO and OH distribution has been extensively studied in premixed charge CI engines [6] from which HCHO was found to fill the cylinder before OH radicals emerge near the piston-bowl wall first and then spread across the combustion chamber while replacing the HCHO.

The present study analyses HCHO and OH distribution in an optically-accessible compression-ignition engine similar to the previous studies but for two different fuels with cetane number of 30 and 40. Together with fuel-PLIF, the HCHO-PLIF and OH-PLIF images are for the first time used in diesel engine to discuss how charge premixing level and fuel reactivity impact ignition process and resulting in-cylinder pressure and aHRR.

2. Experiment

2.1 Engine specification and operating conditions

The schematic of the optical engine is illustrated in Fig. 1 and the selected engine operating conditions are summarised in Table 1. The single-cylinder engine used for planar laser-induced fluorescence imaging has the bore and

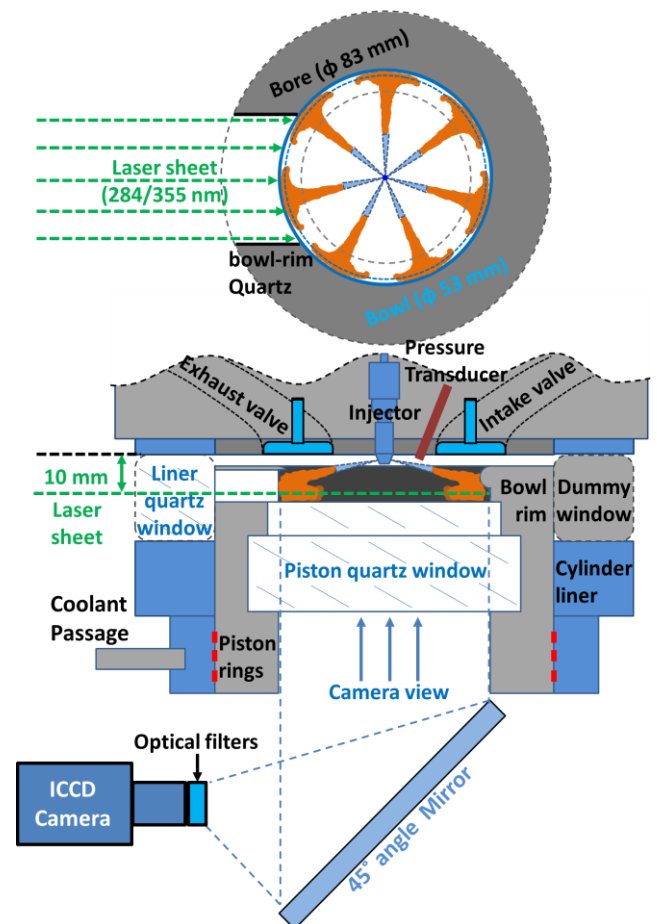


Figure 1: Illustration of the diesel engine and PLIF imaging setup in the bottom-view (top) and side-view (bottom) orientations

stroke of 83 mm and 92 mm, respectively with a displacement volume of 497.5 cm³. The combustion chamber has a geometric compression ratio of 17.7, beneath which the extended piston allows the space for a 45° reflex mirror. This mirror bridges the optical path from the quartz

Table 1: Engine specification and operating conditions

Displacement volume [mm ³]	498	
Bore/stroke [mm]	83/92	
Compression ratio	17.7	
Engine speed [rpm]	1200	
Intake air temperature [°C]	27	
Coolant temperature [°C]	90	
Common-rail pressure [MPa]	50	
Fuel	CN30	CN40
Cetane number	30	40
Fuel density at 15°C [kg/m ³]	785	796
Lower heating value [MJ/kg]	43.6	43.4
Kinematic viscosity at 40°C [mm ² /s]	4.01	4.8
Injection timing [CAD bTDC]	12	10
Injection signal duration [ms]	0.635	0.630
Olefin [Vol%]	0.7	2.8
Saturates [Vol%]	88.8	85.6
Injected fuel mass [mg/cycle]	9	
Total energy input [J/injection]	~391	

window on the piston top to the ICCD camera so that laser-induced fluorescence signals inside the combustion chamber can be captured. For laser excitation, the beam was converted into a 0.3-mm thick sheet and inserted through the quartz liner window and piston-bowl rim window at 10 mm below the cylinder head. The sheet making optics was selected to cover the entire field of view within the piston bowl.

To mimic a warmed-up engine condition, water heated to 90°C was circulated through the engine head, cylinder liner, and engine block. The tested fuels were directly injected at a fixed injection pressure of 50 MPa into engine cylinder using a common-rail injector (Bosch CP3) with the timings and durations managed in a universal control system (Zenobalti ZB-9013P). The injector nozzle has seven evenly spaced holes with nominal hole diameter of 134 μm and included angle of 150°. As listed in Table 1, two fuels with different cetane numbers were used in this study. These custom-made fuels were kerosene-based, achieving almost identical physical properties but cetane numbers (CN30 and CN40). This was made possible by slightly increasing olefins and reducing saturates for the higher cetane number fuel, while detailed analysis regarding what the cetane number is achieved upon is out the scope of this study. The total energy input was held constant at 391 Joule per injection, equivalent to 9-mg injection mass. The injection timing was more advanced for CN30 to match the start of combustion, which was required to isolate the fuel effect from in-cylinder gas temperature/pressure effects. The engine was running under 10 skip-firing mode (i.e. injection once every 10th motoring cycles) at a fixed speed of 1200 rpm. The in-cylinder pressure of the fired cycles was recorded using a pressure transducer (Kistler 6056A) and processed for the apparent heat release rate (aHRR) profile.

2.2 Planar laser-induced fluorescence imaging

The HCHO was excited using the third harmonic of an Nd:YAG laser (SpectraPhysics Quanta-Ray Pro-230) at a wavelength of 355 nm [7]. The laser was operated at 10 Hz with a beam energy of 160 mJ/pulse. The HCHO-PLIF signals in a wavelength range of 380~450 nm [7] were

isolated using a set of 385-nm long-pass filter, 430-nm band-pass (10-nm FWHM) filter, and 450-nm short-pass filter placed in front of the ICCD camera (Lavision Nanostar). The Nd:YAG laser at 532 nm was also used to pump the Rhodamine-6G filled dye laser (Sirah CobraStretch) for 284-nm excitation of OH radicals at 25 mJ/pulse. The excited OH radicals released fluorescence signals in 308~320 nm while returning to the ground state. Therefore, a 300-nm band pass filter (40-nm FWHM) together with two 305-nm long-pass filters was used to capture the OH-PLIF images. Because of the high sensitivity of OH to the excitation wavelength, OH-sourced LIF signals are known to decline sharply with the significant interference from fuel fluorescence with only 0.1-nm decrease in the laser wavelength from the 284-nm beam [8]. This characteristic was utilised to visualise the fuel distribution using the same filter pack as OH-PLIF imaging. That is, at each crank angle, OH-PLIF imaging was repeated for turned on (284 nm) and off (283.9 nm) conditions with the latter being interpreted as fuel-PLIF if, at a selected crank angle, the online and offline images were almost identical due to lack of OH-PLIF. Similarly, when the online OH-PLIF images are significantly different to the offline OH-PLIF during the main combustion event, the online OH-PLIF images were considered as OH images. In present study, the images are selected to represent certain timings using a cross-correlation approach that is justified in our previous work [8].

3. Results and discussion

3.1 In-cylinder pressure and aHRR

The black lines shown in Fig. 2 are the ensemble-averaged in-cylinder pressure traces of the 20 firing cycles in each engine run, which was repeated for the two fuels. The trend is clear that the traces are divided into two groups for each fuel with their differences well exceeding the cyclic variations. It was confirmed that the PLIF imaging was performed at highly consistent combustion conditions for each fuel. As mentioned previously, the fuel injection timing was adjusted to fix the start of combustion at 4 CA aTDC for both fuels, which is clearly shown in the in-cylinder pressure and aHRR traces. Right before the start of combustion, a small bump is shown in the aHRR trace, indicating the low-temperature reaction. This small peak in aHRR is more distinctive for CN30 due to longer ignition delay time, and it occurs earlier than that of CN40 due to earlier start of injection.

It is noticeable from the in-cylinder pressure and aHRR traces that the high-temperature reaction was more intense for CN40 than that of CN30. The peak aHRR for CN40 is about 50% higher and the peak pressure was measured about 10% higher. This was not expected as the longer ignition delay would cause higher premixing, which would lead to higher peak aHRR during the premixed burn phase. The results suggest the level of charge premixing is not the only player in determining the intensity of high-temperature reaction. Since CN40 was made to include more olefins and less saturates, the reactivity of fuel would be higher than that of CN30. Although the lower heating value was almost identical between the two fuels, the higher fuel reactivity of CN40 might cause faster high-temperature reaction, which

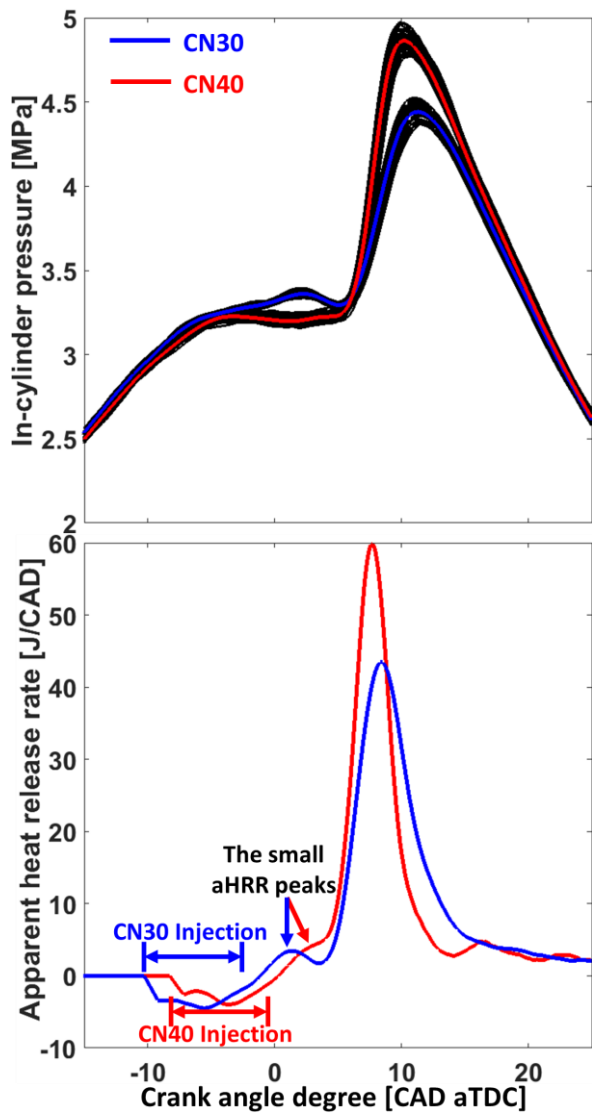


Figure 2: In-cylinder pressure and apparent heat release rate traces

could increase the aHRR and in turn in-cylinder pressure rise. Therefore, the fuel reactivity determined by its molecular structure should be considered for discussion.

3.2 Fuel-, HCHO- and OH-PLIF images

Figure 3 shows fuel-PLIF images for various crank angles. It was noted that only the left half of the piston-bowl is shown due to beam attenuation issues. Despite this limitation, the fuel-PLIF signal distribution provides useful information. For example, the signals indicate that the jet-wall impingement that occurred 2 CA earlier for CN30 due to earlier injection. The CN30 presents overall lower fuel-PLIF signals than CN40, suggesting less fuel-rich mixtures. By contrast, CN40 exhibits larger fuel-PLIF coverage with less uniform distribution of signals. Therefore, it was thought that CN30 was better mixed with air during the extended ignition delay time and thus resulted in more uniform fuel-PLIF signals.

Figure 4 shows temporal and spatial development of HCHO-PLIF signals for both fuels. Consistent with the aHRR traces, the HCHO-PLIF images indicate earlier start of low-temperature reaction for CN30 by about 2 CA. Also,

the HCHO signals last longer for CN30 with higher persistence prior to the second-stage ignition, indicating higher charge premixing [4]. Figure 4 shows that the maximum coverage of HCHO-PLIF signals are observed at 4-5 CA aTDC, which appears similar between the two fuels. However, the signal intensity is relatively higher for CN40. Since the time for pre-combustion mixing was longer for CN30, the formation of HCHO should have been higher, not lower, if the charge premixing was a dominant factor.

From Fig. 4, it was observed that the HCHO-PLIF signals start to decline from 6 CA aTDC for both fuels. This decrease occurs faster for CN40 with the HCHO-PLIF signals disappearing significantly by 8 CA aTDC, about 2 CA earlier than CN30. It is known that the consumption of HCHO indicates the reaction with H_2O_2 to produce OH or OH-induced oxidation during the transition of low-temperature reaction to high-temperature reaction [4]. Therefore, the faster disappearance of HCHO-PLIF for CN40 would mean faster development of high-temperature reaction during the ignition simply due to higher fuel reactivity.

Indeed, the overlaid images of OH- and HCHO-PLIF in Fig. 5 suggest a faster transition of low-temperature reaction to high-temperature reaction. From the start of combustion, the OH signals replace HCHO near the piston-bowl wall and then spread throughout the entire region that originally occupied by HCHO. This occurs faster for CN40 with all the HCHO being consumed in just 4 CA whereas it took 7 CA for CN30. This result confirmed that the transition from low- to high-temperature reaction was accelerated for CN40 due to higher fuel reactivity. For a given fuel, the peak in-cylinder pressure and aHRR during the premixing burn phase of combustion would be higher if the charge premixing was enhanced due to earlier injection timing. However, despite higher charge premixing observed for CN30, it was the fuel reactivity to make a predominant effect in accelerating the high-temperature reaction of CN40, and therefore the peak in-cylinder pressure and aHRR were measured higher.

4. Conclusion

The present study unveils the effect of fuel reactivity and charge premixing on the development of low-temperature and high-temperature reaction by testing two cetane number fuels of CN30 and CN40 in a diesel engine. The in-cylinder pressure and aHRR shows higher peaks for CN40 than those of CN30. The HCHO-PLIF images show that low-temperature reaction occurred earlier for CN30 and the signals persisted longer prior to the high-temperature reaction, indicating higher premixing. However, larger amount of HCHO was produced in a shorter period of time for CN40. Moreover, the consumption of HCHO to produce OH was faster for CN40, indicating accelerated transition from low-temperature reaction to high-temperature reaction. Therefore, between the tested fuels of the present study, it was higher cetane number fuel with higher fuel reactivity to cause higher peak in-cylinder pressure and aHRR despite lower charge premixing.

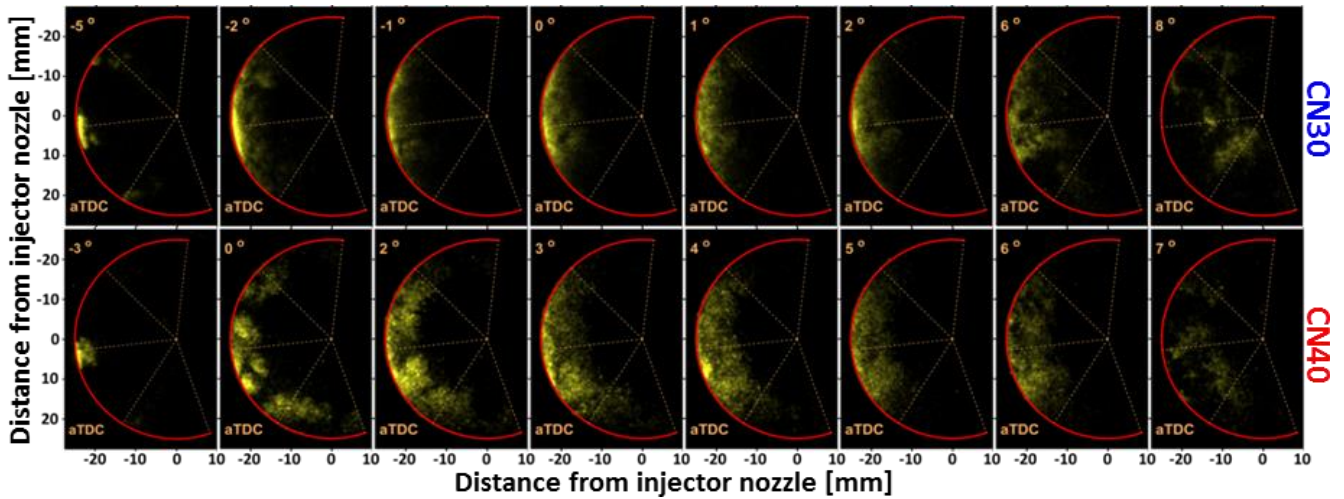


Figure 3: Fuel-PLIF images for CN30 (top row) and CN40 (bottom row).

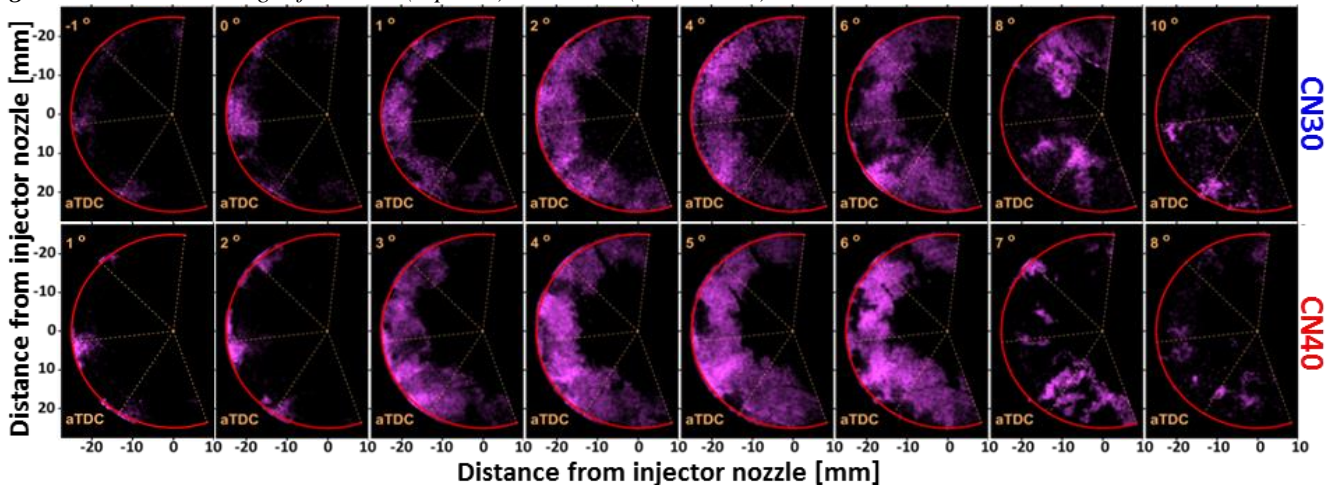


Figure 4: HCHO-PLIF images for CN30 (top row) and CN40 (bottom row).

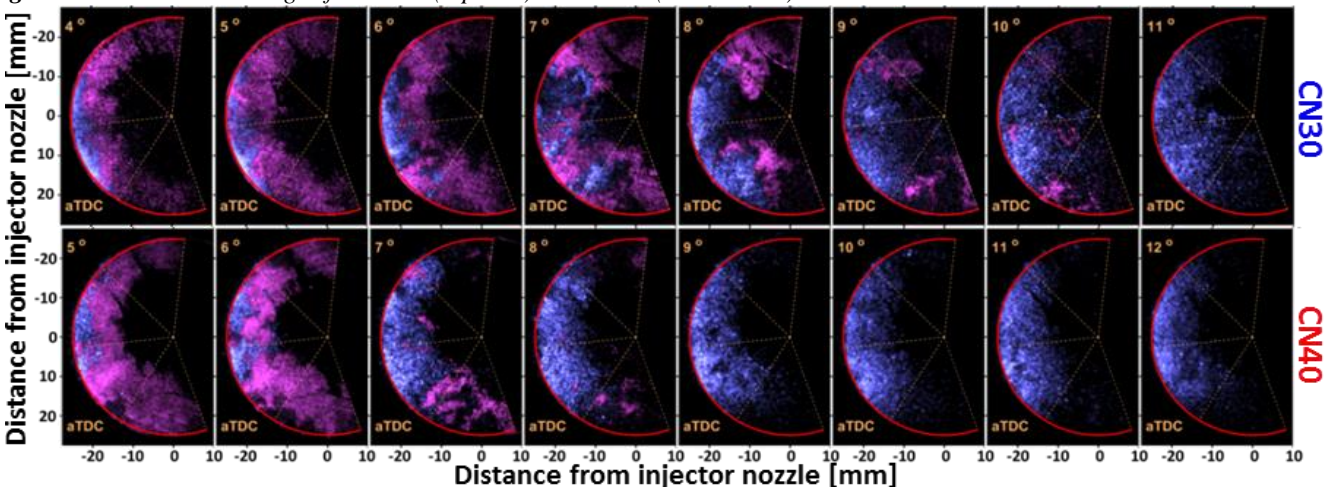


Figure 5: Overlaid HCHO- and OH-PLIF images for CN30 (top row) and CN40 (bottom row).

Acknowledgments

The experiments were performed at the UNSW Engine Research Laboratory, Sydney, Australia. The financial support for this work was provided by the U.S. Army International Technology Center Pacific (ITC-PAC).

References

- [1] M. Bobba, C.L. Genzale, and M.P.B. Musculus (2009) *SAE Int. J. Engines* **2**, pp. 911-924.
- [2] C.L. Genzale, R.D. Reitz, and M.P.B. Musculus (2008) *SAE Int. J. Engines* **1**, pp. 913-937.
- [3] U. Aronsson, C. Chartier, Ö. Andersson, B. Johansson, J. Sjöholm, R. Wellander, M. Richter, M. Alden and P.C. Miles (2010) *SAE Int. J. Engines* **3**, pp. 137-155.
- [4] M.P.B. Musculus, P.C. Miles, and L.M. Pickett LM (2013) *Prog. Energy Combust. Sci.* **39**, pp. 246-283.
- [5] H.J. Curran, P. Gaffuri, W.J. Pitz, C.K. Westbrook (1998) *Combust. Flame* **114**, pp. 149-177.
- [6] Q. Tang, H. Liu, M. Li, M. Yao, and Z. Li (2017) *Combust. Flame* **177**, pp. 98-108.
- [7] CL. Genzale, R.D. Reitz, M.P.B. Musculus (2009) *Proc. Combust. Inst.* **32**, pp. 2767-2774.
- [8] M.K. Le, R. Zhang, L. Rao, S. Kook, and E.R. Hawkes (2016) *Fuel* **166**, pp. 320-332.

One-Step Chemical Kinetic Scheme for Propane in High Temperature Applications

Raoul Mazumdar^{1,*}, Hideaki Ogawa^{1,2}, Adrian Pudsey¹, Mathew Bricalli¹

¹ School of Engineering, RMIT University, Victoria, Australia

² Department of Aeronautics and Astronautics, Kyushu University, Fukuoka, Japan

Abstract

One-step chemical mechanisms have played a prominent role in engineering, providing reduced order schemes for reacting flow simulations. In the past, these schemes have been applied to large eddy simulations (LES) and direct numerical simulations (DNS), thereby reducing the numerical computing requirements. Furthermore, applications of chemical one-step schemes have allowed fast initial sizing of combustors and an array of other components. The primary motivation in this study is to produce one-step schemes for high temperature applications, specifically air-breathing propulsion, by investigating the fitting of one-step reactions to fuels such as propane. The body of work fits global rates against detailed chemical mechanisms for propane. The kinetic parameters are optimized using a Nelder-Mead routine; in addition, a function for the temperature dependence is found using a polynomial surface fit to the optimized coefficients. These parameters in the kinetic equation are optimized across pressures of 0.5 to 1atm, and temperatures of 1000 to 1600K. The outcome yields one-step global schemes for propane and show good adherence to the full-detailed model in a perfectly stirred reactor.

Keywords: Kinetics, Propane, hydrocarbons, High-Temperature, reduced order,

Nomenclature

$\frac{dF}{dt}$	Fuel consumption rate $\frac{Kmol}{m^3s}$
$\frac{dOx}{dt}$	Oxidizer consumption rate $\frac{Kmol}{m^3s}$
[F]	Fuel concentration $\frac{Kmol}{m^3}$
[Ox]	Oxidizer concentration $\frac{Kmol}{m^3}$
T	Temperature in K
P	Pressure in atm
C_p	Specific heat at constant pressure $\frac{J}{Kmol.K}$
R_u	Universal gas constant $\frac{J}{Kmol.K}$
n	Temperature dependent
E	Activation energy $\frac{J}{Kmol}$
v	Pseudo-Vandermonde matrix
$a_{0,1..i}$	Fitting coefficients
$b_{0,1..i}$	Thermodynamic polynomials
h_f	Heat of combustion $\frac{J}{Kmol}$
A/F	Air fuel ratio
<i>Subscript</i>	
Prod	Products
Ox	Oxidizer
r	Reactors
o	Initial conditions
s	Stoichiometric
<i>Superscript</i>	
x	Fuel exponent factor
y	Oxidizer exponent factor

1. Introduction

One-step chemical reactions often lump a variety of chemical observations into a single equation involving fuel consumption. Unlike using a number of elementary reactions to represent the chemistry, a one-step scheme can substantially reduce the numerical cost via this simplification. This however can reduce the accuracy of the mechanism, and therefore benefits applications where the numerical demand outweighs the required accuracies.

This approach dates back to the foundational research conducted by Westbrook and Dryer [1] in the early 1980s. The author published global chemical kinetic reactions for a number of fuels on an Arrhenius based equation, including propane and a variety of larger hydrocarbon sources. Developments in one-step chemical schemes were also explored by Fernández-Galisteo et al. [2] in 2009. Their work investigated a one-step chemical scheme for hydrogen combustion and showed close approximation for lean fuel mixtures. More recently, Franzelli et al. [3] produced a two-step kinetic scheme for kerosene and validated the experiment against detailed baseline mechanisms. Although numerical computing power has dramatically increased over the past few decades, the increasing complexity of computational fluid dynamic solvers continues to drive numerically simplistic chemical schemes.

Large eddy simulation (LES) and direct numerical simulation (DNS) are far numerically demanding than other methods such as Reynolds averaged Navier-Stokes (RANS). That said, methods such as

* Corresponding author. Email: Raoul.mazumdar@student.rmit.edu.au

LES and DNS are increasingly popular in use, however in most cases the simulations are done with non-reacting gases; pre, or post combusted gas mixtures as mentioned by Moureau [4]. The added complexity of the methods implies a far greater numerical burden and the inability to process large chemical mechanisms. As such, providing simple mechanisms for the application of LES and DNS in reacting flows is still a key concern. Thus the continued life span of one-step chemical kinetic mechanisms are here to stay, providing simplified chemical mechanisms for small and large fuels continues to be a necessity for advanced computational fluid dynamic (CFD) practices. Whether the application is for fast one-dimensional codes, validation studies, or an applied engineering system, the use of such schemes continues to be of interest.

The method utilized for this paper involves modified global chemical reactions based on previous works [1,5], with complex polynomial fitting of temperature dependents in order to adjust pyrolysis rates. The work has similarities to the approach conducted by Naik et al. [6], in the use of chebyshev polynomials to fit kinetic rates on temperature and pressure from a mathematical approach. In this case, temperature dependent values are found initially through optimization for each reactor simulation of interest through a Nelder-Mead scheme in Scipy [7,8,9]. The dependent values then form the inputs for the three-dimensional polynomial function fitting which thereby couples with the one-step chemical reaction rate. This procedure is carried out for propane, and the results are subsequently compared against a detailed kinetic model [10] in CANTERA [11].

2. Method

The reactor model is based on the equations given in Turns [5], where the fuel reaction rate is presented by Eq. (1). Production of product species and consumption of oxidizer species are related to the primary fuel reaction rate by Eq. (2) and Eq. (3).

$$\frac{dF}{dt} = T^n A e^{-\frac{E}{T}} [F]^x [Ox]^y \quad (1)$$

$$\frac{dOx}{dt} = (A/F)_s \frac{dF}{dt} \quad (2)$$

$$\frac{dPr}{dt} = -((A/F)_s + 1) \frac{dF}{dt} \quad (3)$$

$$n = a_0 + a_1 P_o + a_2 P_o^2 + a_3 T_o + a_4 T_o P_o + a_5 T_o P_o^2 + a_6 T_o^2 + a_7 T_o^2 P_o + a_8 T_o^2 P_o^2 \quad (4)$$

The coefficients for n are calculated in two stages. First, the one-step reaction is run in a zero dimensional perfectly stirred reactor and compared

to a full detailed kinetic mechanism in a similar reactor scheme using Cantera [11]. The factor n is optimized such that the temperature profile for the one-step scheme replicates the profile of the full-mechanism via the use of a Nelder-Mead optimization routine from Scipy [7,8,9]. The routine minimizes exclusively the area between the two temperature profiles by modifying n , producing a number of optimum n values as defined by a relative convergence error of 1×10^{-4} for the routine operation.

The value n is calculated for initial reactor conditions from 1000 to 1600K and for 0.5atm to 3atm, covering reactor conditions relevant to combustion in air-breathing propulsion. Following which, a pseudo-vandermonde matrix is formed using the Scipy polyvander2d function [7,8,9]. The matrix is formed by sampling points for the reactor conditions as shown by Eq.(5) and (6), culminating in the pseudo-vandermonde matrix in Eq.(7).

$$T_r = [T_0 \quad \dots \quad T_i] \quad (5)$$

$$P_r = [P_0 \quad \dots \quad P_i] \quad (6)$$

$$v = \begin{bmatrix} 1 + P_0 + P_0^2 + T_0 + P_0 T_0 + P_0^2 T_0 + T_0^2 + T_0^2 P_0 + T_0^2 P_0^2 \\ \vdots \\ 1 + P_i + P_i^2 + T_i + P_i T_i + P_i^2 T_i + T_i^2 + T_i^2 P_i + T_i^2 P_i^2 \end{bmatrix} \quad (7)$$

The pseudo-vandermonde matrix once formed is solved [12,13] via the least squares method. This produces the coefficients for the equation that describes the optimum n for a given initial temperature and pressure in the form of Eq. (4).

The thermodynamic properties of the gas species use NASA7 polynomial scheme as described by Eq. (8). The thermodynamic data for the chemical species are taken from baseline mechanisms of Qin et al. [10]. This is sufficient to calculate the case for a zero dimensional perfectly stirred reactor.

$$\frac{C_p}{R_u} = b_0 + b_1 T + b_2 T^2 + b_3 T^3 + b_4 T^4 \quad (8)$$

Calculating the specific heat of the mixture is done via the set of Eqs. (9-13). The specific heat of the mixture is calculated as a summation of specific heats of fuel, oxidizer and products. The ratios of produced and consumed species are assumed to be consistent with a stoichiometric reaction of the particular fuel. The heat of combustion, h_f for propane is taken to be $2.2 \cdot 10^9 \frac{J}{Kmol}$. In addition, the pressure of the mixture is calculated via the Eq. (12).

$$C_{ox} = \frac{1}{4.76} C_{p,CO_2} + \frac{3.76}{4.76} C_{p,N_2} \quad (9)$$

$$C_{fuel} = C_{p,C_3H_8}[T] \quad (10)$$

$$C_{pr} = \frac{3}{25.8} C_{p,CO_2}[T] + \frac{4}{25.8} C_{p,H_2O}[T] + \frac{18.7}{25.8} C_{p,N_2}[T] \quad (11)$$

$$\tilde{C}_p = [F] \cdot C_{fuel} + [Ox] \cdot C_{ox} + [Pr] \cdot C_{pr} \quad (12)$$

$$\frac{dT}{dt} = \omega_f h_f \frac{R_u T}{P(C_p - R_u)} \quad (13)$$

$$P = R_u T ([F] + [Ox] + [Pr]) \quad (14)$$

This formulation of a one-step scheme assumes a specific ratio of produced products, in addition to a specific ratio of consume reactants. This significantly reduces the complexity of the system but can increase errors by assuming the species fraction of chemical products are conserved at all temperatures. In applying this method, consideration has been made to the rate equations supported by most computational fluid dynamic software packages. In providing a reaction rate with the Arrhenius form in the one-step scheme, an attempt is made to provide a readily convertible solution to a CFD software package.

3. Result

Following the methods discussed in the previous section, one-step global kinetic equations for fuel decomposition for propane are shown by Eq. (15). The factor n is approximated by a polynomial equation to form a portion of the kinetic rates. Using these calculated functions and running the simulations versus CANTERA and the full-baseline chemical kinetic mechanisms, the ignition profile within a perfectly stirred reactor can be examined. In which ignition is defined as the maximum gradient of temperature rise. Figure 1 shows the temperature profile of the one-step model, the behavior observed mirrors the temperature profile of the full detailed kinetic mechanism to a degree. If we examine Fig. 2, we can see the ignition trends between the one-step and full detailed mechanism are consistent across a larger array of environmental variables. The deviations are more pronounced at higher temperatures and lower pressures.

Propane:

$$n = -3.02 + (4.92E - 01)P_o + (-7.42E - 02)P_o^2 + (2.72E - 03)T_o + (-7.24E - 04)T_o P_o + (1.09E - 04)T_o P_o^2 + (-7.14E - 07)T_o^2 + (2.60E - 07)T_o^2 P_o + (-3.93E - 08)T_o^2 P_o^2$$

$$\frac{dF}{dt} = T^n \cdot (-4.8365E + 09)e^{-\frac{15098}{T}} [F]^{0.1} [Ox]^{1.65} \quad (15)$$

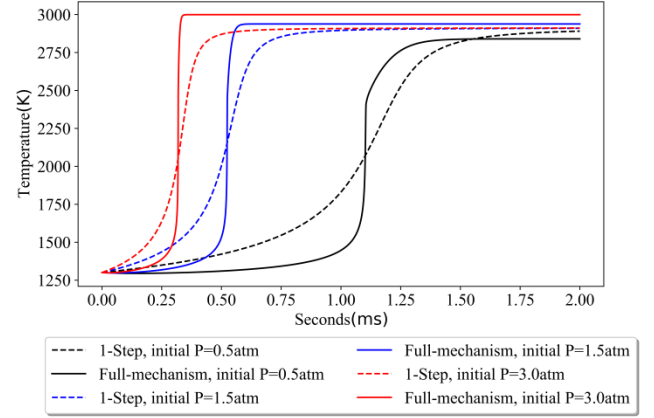


Fig 1: Temperature profile of the propane one-step model versus the detailed model in a perfectly stirred reactor at an initial starting temperature of 1300K.

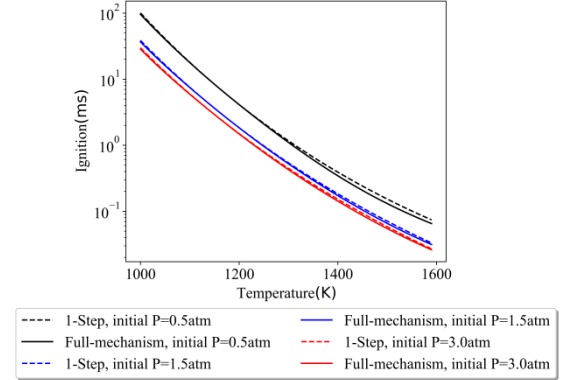


Fig 2: Propane ignition delay time for the detailed mechanism and one-step scheme.

For comparative purposes if we hold the temperature dependent value fixed and run the simulations for ignition delay time, we can see a large deviation as depicted in Fig. 3. The constant temperature dependent profile uses a value which is optimized for 1200K and 0.5 atm. The profile is capable of capturing the ignition delay time at 1200K but fails to capture any other ignition delay time, either lower or higher in temperature. This is borne out by the fact that the one-step scheme is a significant simplification of the detailed chemical kinetics, thereby requiring some form of correction in the rate.

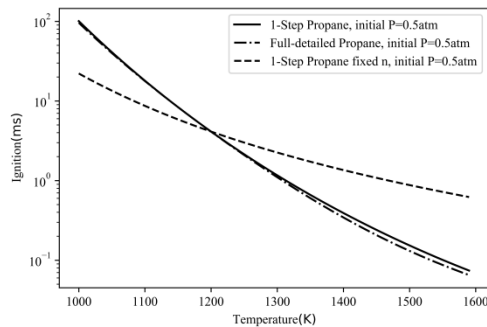


Fig 3: Propane ignition delay time for the detailed mechanism, one-step scheme and a fixed n exponent one-step scheme.

Now if we take one step outside of the zero-dimensional domain, in which the ignition delay times are calculated. We can examine one-dimensional models such as a premixed flame. To achieve this, thermodynamic data of the product species were blended and fitted together using the NASA7 polynomial form and transport properties were adopted from the GRI mechanism [14]. Using Cantera's one-dimensional features, we are able to examine the average burning velocity for a premixed propane flame. Figure 4 shows a comparison between the flame speed of the detailed and one-step scheme, at pressures of 1atm and 300K. What should be evident is that the one-step formulation is lacking proper refinement to one-dimensional flow.

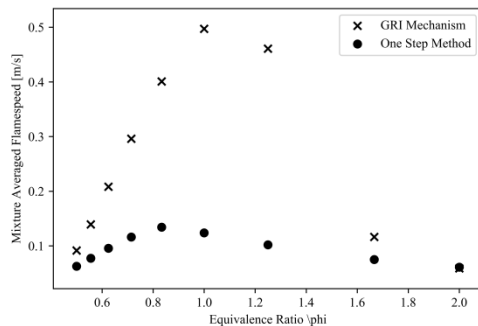


Fig 4: Premixed propane flame speed of of the one-step-scheme, compared to a GRI mechanism [14].

4. Conclusion

The method of approximating one-step chemical schemes appears to work well at predicting ignition time for hydrocarbon fuels under certain circumstances; the method of polynomial three-dimensional fitting can be used to provide complex approximations to multidimensional chemical functions. In the application of the one-step scheme for a one-dimensional flame, significant deviations are observed. This error can be attributed to the lumping of thermodynamic and

transport properties. Thus further work needs to be done on one-dimensional calibration of the model.

5. Acknowledgments

The CRC Programme supports industry-led collaborations between industry, researchers and the community. The authors would like to thank the support of the CRC-P, RMIT University, and the high performance computing resources and support from the National Computational Infrastructure (NCI), as well as the Australian government's higher education training scheme.

6. Reference

- [1] Westbrook, C. K., & Dryer, F. L. (1981). *Combustion science and technology*, 27(1-2), 31-43.
- [2] Fernández-Galisteo, D., Sánchez, A. L., Liñán, A., & Williams, F. A. (2009). *Combustion and flame*, 156(5), 985-996.
- [3] Franzelli, B., Riber, E., Sanjosé, M., & Poinso, T. (2010). *Combustion and Flame*, 157(7), 1364-1373.
- [4] Moureau, V., Lartigue, G., Sommerer, Y., Angelberger, C., Colin, O., & Poinso, T. (2005). *Journal of Computational Physics*, 202(2), 710-736.
- [5] Turns, S. R. (1996). *An introduction to combustion* (Vol. 499). New York: McGraw-Hill.
- [6] Naik, C., Carstensen, H. H., & Dean, A. M. (2002, March). In *Western States Section 2002 Spring Meeting of the Combustion Institute*, San Diego, CA.
- [7] Jones E, Oliphant E, Peterson P, et al. *SciPy: Open Source Scientific Tools for Python*, 2001-, <http://www.scipy.org/> [Online; accessed 2019-04-23].
- [8] Travis E. Oliphant. *Computing in Science & Engineering*, 9, 10-20 (2007)
- [9] K. Jarrod Millman and Michael Aivazis. *Python for Scientists and Engineers, Computing in Science & Engineering*, 13, 9-12 (2011)
- [10] Z. Qin, V. V. Lissianski, H. Yang, W. C. Gardiner, Jr., S. G. Davis and H. Wang, *Proceedings of the Combustion Institute*, Volume 28, 2000. p. 16631669.
- [11] David G. Goodwin, Raymond L. Speth, Harry K. Moffat, and Bryan W. Weber. <https://www.cantera.org>, 2018. Version 2.4.0. doi:10.5281/zenodo.1174508
- [12] Travis E, Oliphant. *A guide to NumPy, USA: Trelgol Publishing*, (2006).
- [13] Stéfan van der Walt, S. Chris Colbert and Gaël Varoquaux. *Computing in Science & Engineering*, 13, 22-30 (2011)
- [14] Smith, G. P. (1999). GRI-Mech 3.0. http://www.me.berkeley.edu/gri_mech/.

Comparative study of spray characteristics of butanol, acetone-butanol-ethanol, butanol-acetone/diesel blends.

Sattar Jabbar Murad Algayyim^{a,*}, Andrew P. Wandel^a

^a School of Mechanical and Electrical Engineering, University of Southern Queensland, Toowoomba, QLD 4350, Australia.

Abstract

Butanol is widely investigated as a renewable biofuel additive in Compression-Ignition (CI) engines due to its ability to improve diesel fuel properties and reduce emission levels. Because Acetone-butanol-ethanol (ABE) and butanol-acetone (BA) are intermediate mixtures in bio-butanol production, they present cost benefits compared to butanol production by reducing energy consumption and the number of recovery processes. This paper evaluates and compares the effect of using butanol (B), BA and ABE additives with diesel (D) on macroscopic spray characteristics. Spray tests were carried out in a constant volume vessel (CVV) under different injection conditions. A high-speed camera was used to record spray images. Macroscopic spray characteristics including spray penetration, spray cone angle and spray volume were measured. The experimental results showed that spray penetration (S) was increased as a result of addition of all alcohols to diesel fuel as well as of increased injection pressure; spray cone angle (θ) was slightly widened while it was slightly narrowed as a consequence of increase fuel injection. The spray volume of the alcohol-diesel blends showed a higher value compared to that of neat diesel due to high spray penetration length. Spray penetration and spray volume of BA-diesel blend were higher compared to ABE-diesel and B-diesel blends.

Butanol-acetone mixture; Acetone-Butanol-Ethanol mixture; spray visualization.

1. Introduction

The pollution emitted from diesel engines such as carbon monoxide and nitric oxide causes serious health risks to human beings. Reducing carbon emissions have become a necessary goal to reduce global warming [1, 2, 3]. Optimising the combustion process in internal combustion engine is necessary to reduce both the fuel consumption and the pollutant emission levels. Compression ignition (CI) engines' performance and emissions are highly impacted by fuel spray techniques [4, 5]. Hence, it is important to understand the spray behaviour and atomisation characteristics of these fuels as individuals and mixtures especially when using these fuels directly in non-modified or slightly modified diesel engines [6, 7]. One way to reduce the reliance on fossil fuel is to blend it with additives. Butanol is a potential renewable resource of alcohol which can be blended with diesel. Butanol has some advantages compared to ethanol, such as being stable with diesel at any ratio without any phase separation. being less corrosive, having a higher flash point which means it is a safer option for storage and distribution, having a higher energy content and lower vapour pressure and high burning velocity which reduces emissions (such as soot, smoke, NO_x and CO) [8]. However, the cost of butanol production is the major issue of limiting its use as a fuel in internal combustion (IC) engines. It is preferable to use ABE or BA as a mixture because butanol is the most abundant component in the ABE and BA mixture and the purification cost would be minimised as a consequence of reduce energy consumption and recovery processes[1].

Algayyim et al. [3] studied the macroscopic spray characteristics of butanol-acetone mixture (BA) as additive for diesel fuel under two injection pressures 300 bar and 500 bar. Two butanol types (normal butanol and iso-butanol: iso-BA and n-BA) were investigated as

components in a BA mixture. The experimental result showed that all BA mixture enhanced spray penetration. Spray penetration of n-BA-diesel was slightly higher than that of iso-BA-diesel blend. Therefore, an ABE or BA mixture can enhance the evaporation rate which improves the combustion rate. Liu et al. [9] used an optical CVV to compare the effects of ethanol and butanol as separate additives in biodiesel fuel on the spray and, combustion characteristics. The experimental results showed that ethanol and butanol blend can enhance spray and combustion characteristics of biodiesel. Wu et al. [10] examined the effect of butanol and ABE on spray behaviour under different temperatures and oxygen content in a CVV. The images of the experimental results showed that liquid penetration with n-butanol or ABE is much shorter than diesel under all tested conditions. Almost all the physical properties change with temperature: an increase in ambient temperature causes viscosity and surface tension to decrease and vapour pressure to increase; these changes significantly accelerate the atomisation and evaporation of the liquid spray.

A study by Chen et al. [11] investigated the spray and atomisation characteristics for commercial diesel fuel, biodiesel (FAME) derived from waste cooking oil (B100), and 20% biodiesel blended with diesel (B20). The experimental work was conducted at room temperature and pressure via a common-rail high-pressure fuel injection system with a single-hole nozzle for different injection pressures (300, 500, 800 and 1000 bar). The experimental results showed that biodiesel had different structures compared with conventional diesel fuel. Spray tip penetration was longer and droplet diameters were larger of pure biodiesel (B100).

Spray visualization of three fuel additives—butanol (B), BA and ABE has been investigated to determine the best

type of alcohol blend to be used as an additive to conventional diesel.

2. Experimental apparatus

2.1 Fuel preparation and properties.

Analytical grade acetone (99.5% purity), normal butanol (99.5%) and ethanol (99.8%), supplied from Chem Supply Australia, were used. In this study, n-butanol (B) was the only butanol isomer used. In line with the intermediate products when producing B by fermentation, the volumetric ratio of acetone, butanol and ethanol was 3:6:1 in ABE and the volumetric ratio of butanol and acetone was 2.9:1 in BA. All alcohol blends were mixed together using splash blending at 4,000 rpm to simulate the composition of the above-mentioned ABE and BA fermentation products. Conventional diesel fuel supplied from a local petrol station in Toowoomba was used as the baseline fuel in this study. B, BA and ABE mixtures were blended with diesel by 10% volume and denoted 10B90D, 10BA90D and 10ABE90D, respectively. The miscibility and stability of B, BA and ABE-diesel blends were monitored over a three-month period before the tests were carried out on the engine. The samples were stored in glass bottles and visually observed every 30 days, with all blends maintaining a good homogeneous mixture. The density was measured for all fuel blends according to ASTM 1298. The dynamic viscosities of the test fuel were measured according to the ASTM 445-01 fuel standards by using a Brookfield DV-II+Viscometer, then the kinematic viscosity was calculated. The heating values of the blends were measured using a Digital Oxygen Bomb Calorimeter (XRY-1A) following ASTM D240. Each test was carried out in triplicate. The properties of diesel, acetone, butanol, ethanol and measured properties of fuel blends are listed in Table 1.

Table 1. Measured properties of fuel blends.

Blend	Density @ 20°C (g/L)	Viscosity @ 40°C (mm ² /s)	Heating value (MJ/kg)
Diesel	0.86	2.46	42.6
ABE	0.80	1	31.4
BA	0.79	1.03	32.2
10B90D	0.83	2.13	41.8
10ABE90D	0.83	2.21	41.4
10BA90D	0.82	2	41.3

2.2 Spray test setup

The experiment of spray test was conducted at atmospheric condition and consisted of: (1) A constant volume vessel (CVV), (2) a high pressure injection common rail system with Bosch electromagnetic (solenoid type injector was used due to this injector type widely used in diesel engines) and (3) visual data acquisition system. The spray images were captured using a Photron SA3 high speed camera. The CVV was illuminating using an LED light. Figure 1 shows experimental setup of spray system. The Injector specification, Camera specification and injection setup are listed in Figure 1. The Spray experiments followed three steps to ensure accurate results: (1) the fuel injection system (fuel tank, common rail and fuel line fittings) was emptied, cleaned and dried by an air compressor for each new blend

test. (2) The fuel filter of each test was removed and replaced with a new one. After ensuring all the injection systems were cleaned and emptied, the spray testing started with a number of initial injections before the new images captured. (3) The spray test was repeated three times. The final spray characteristics were calculated by averaging the 6 plumes from the injector from all tests. Lights were installed on three of the windows and a high-speed camera on the fourth window for the purpose of spray visualisation. The inside of the vessel was painted black to ensure a good background for the images and to increase the images' contrast and enhance the visibility of the spray. The injector was mounted horizontally in the vessel so that all the spray axes are visualised through the front window. The definition of spray tip penetration is the distance between the nozzle tip and the maximum outer point of each spray.

The spray cone angle is the angle between two straight lines from the nozzle tip and the outer contour of the injected spray. The images were processed in three steps before quantifying the spray characteristics: (1) Images were read into MATLAB, then the recorded images were converted into binary images (2) An automatic threshold calculation algorithm was employed to determine the spray outline (edge) from the images. (3) Boundary pixels of each spray plume of each image were measured to quantify spray characteristics by measuring from spray contour. The flowchart of image processing is displayed in Figure 2

The fuel spray is assumed to occupy a cone with a hemisphere. The spray volume (V) was calculated as a function of spray penetration (S) and spray cone angle (θ) [12, 13]:

$$V = \left(\frac{\pi}{3}\right) S^3 \left[\tan^2(\theta) \right] \frac{1 + 2 \tan\left(\frac{\theta}{2}\right)}{\left[1 + \tan\left(\frac{\theta}{2}\right)\right]^3} \quad (1)$$

Table 2. Specifications of fuel injection system, camera specification and injection setup.

Injector specification	
Injector type	Bosch electromagnetic common rail injector (solenoid type)
Number of injector holes	6
Hole diameter	0.18 mm
Injection quantity	12 mg
Injection enclosed angle	156°
Camera specification	
Camera resolution @ frame rate	1024×1024 pixels @ 2000 fps
Injection setup	
Injection pressure	300 and 500 bar
After start of injection time (ASOI)	0.5-1.5 ms

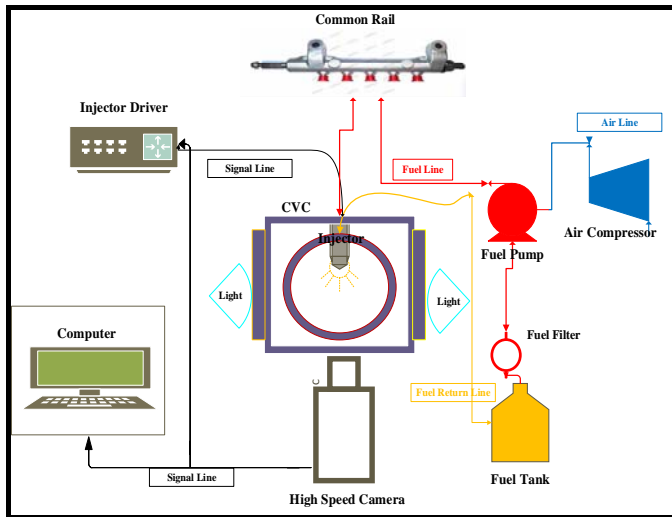


Figure 1. Schematic of fuel injection system setup and visual data acquisition system.

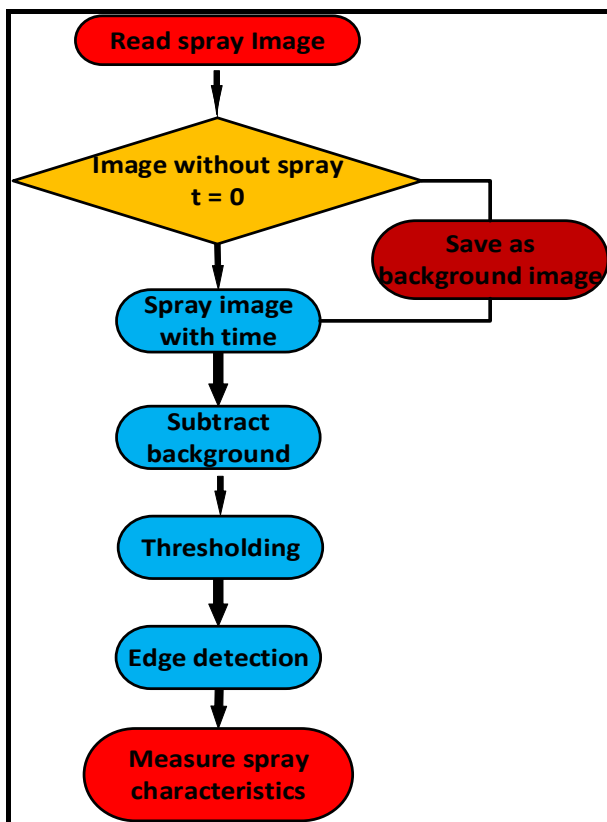


Figure 2. Flowchart of image processing.

3. Results and discussion of spray test

3.1 Spray images

Spray images are derived from the triplicate tests. Rows from top to bottom show ASOI (Figure 3 and Figure 4). The scaling of spray images or spray pattern body became bigger as a result of increased ASOI and injection pressures (IP) values. Spray images of neat diesel fuel were used as a baseline. The spray characteristics were quantified from these images.

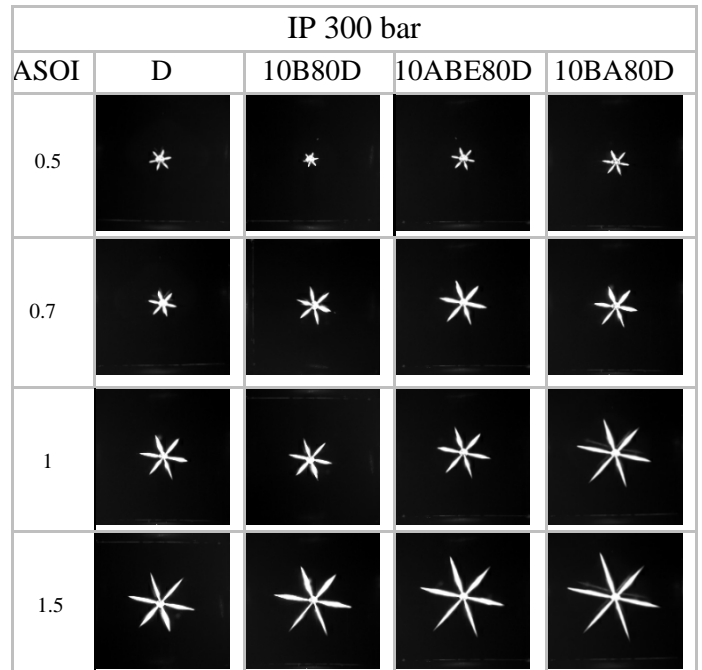


Figure 3. Spray images of test fuels at injection pressures 300 bar.

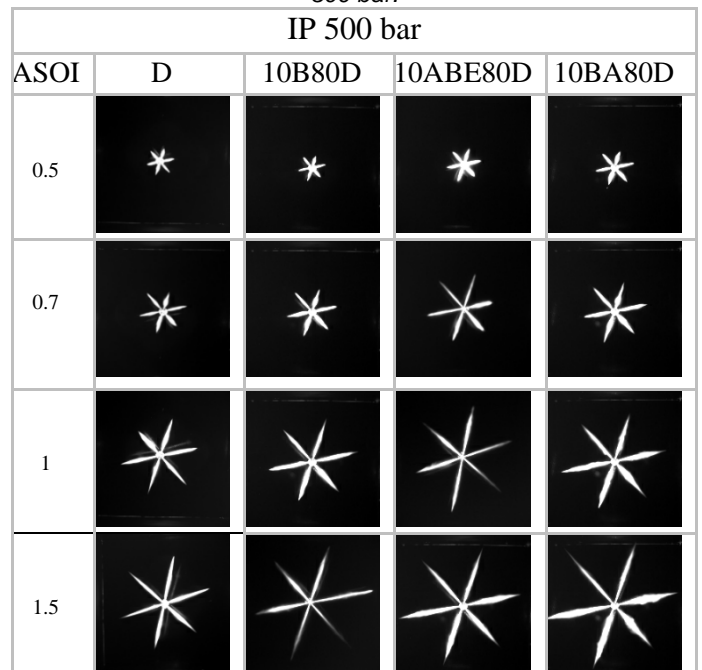


Figure 4. Spray images of test fuels at injection pressures 500 bar.

3.2 Spray tip penetration (S)

Figure 5 shows spray penetration of test blends. Alcohol-diesel blends showed increment in spray plumes area ranked from shortest to longest as: 100D, 10B, 10ABE and 10BA. Including acetone in ABE mixture and BA mixture improves the spray characteristics compared to pure butanol (B) due to its lower viscosity. A lower viscosity reduces the friction between fuel and the surface of injector nozzle hole, which causes a higher fluid velocity exiting from the injector nozzle. Fuels that have lower boiling points and higher heats of evaporation, such as alcohols (B, ABE and BA), can improve the evaporation rate. In an internal combustion engine, the process of atomization of the fuel spray is an important mechanism in which the fuel is mixed

effectively within the gas combustion chamber. Therefore, atomization and combustion rate will be increased. The high spray area (longer spray tip penetration) can enhance air-fuel mixing rate and better combustion efficiency due to the increased surface area of contact between fuel and air.

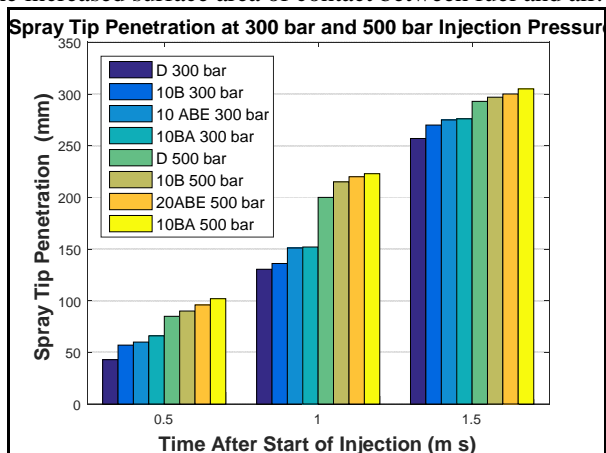


Figure 5. Spray penetration of test fuels at injection pressures 300 bar and 500 bar.

3.3 Spray cone angle (θ)

All alcohol blends showed slightly widened plumes (Figure 6). The increase in injection pressure leads to a slightly narrowed spray cone. When there is an insufficient radial momentum to overcome penetration resistance and the pressure difference across the sheet, then spray shoulders become strongly curved.

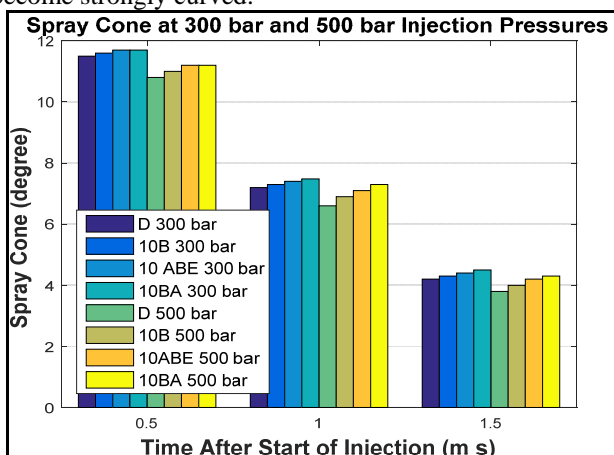


Figure 6. Spray cone angle of test fuels at injection pressures 300 bar and 500 bar.

3.4 Spray volume (V)

The spray volume of the test blends is presented for both injection pressures. The spray volume is calculated as a function of spray penetration (S) and spray cone angle (θ) under different injection conditions. The spray volume of the alcohol-diesel blends was higher than neat diesel due to their higher spray penetration length. Therefore, the contact surface area between the air and fuel would be increased, thereby resulting in increased mixing and reaction rates.

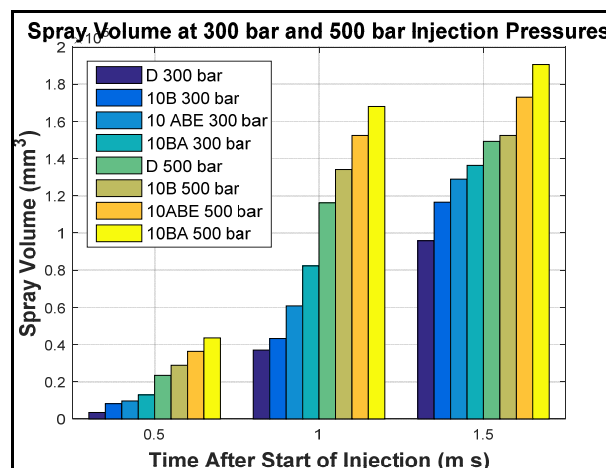


Figure 7. Spray volume of test fuels at injection pressures 300 bar and 500 bar.

4. Conclusions

High-alcohol chains of 10% B, BA and ABE and neat diesel were tested in a CVV to investigate the effect on spray characteristics. It was found that spray penetration was increased as a result of addition of any alcohol blends to diesel fuel as well as of increased injection pressure. Spray cone angle (θ) was slightly widened while it was slightly narrowed as a consequence of increased fuel injection. Spray penetration and spray volume of BA-diesel blend was higher compared to ABE-diesel and B-diesel blends. BA-diesel blends could be best blend for enhancing the spray characteristics of neat diesel, namely improved atomisation and evaporation rate compared to pure butanol (B) and ABE-diesel blends. Then, combustion behavior and engine performance of BA-diesel blend could be enhanced as a result of improved spray characteristics compared to other blend.

5. Acknowledgments

The first author would like to thank the Iraqi Government Ministry of Higher Education and Scientific Research for supporting the research. The authors are also grateful to Rishabh Choudhury for his assistance with the spray test.

6. References

- [1] Z. Zhang, S. Zhu, J. Liang, L. Tianand, G. Li, *Fuel*, 2018, 211(Supplement C): p. 95-101
- [2] H. Wu, K. Nithyanandan, J. Zhang, Y. Lin, T. Lee, C. Leeand C. Zhang, *Applied Energy*, 2015, 149: p. 367-378.
- [3] S. J. M Algayyim., A. P Wandel, T. Yusaf., *BIOFUEL*, 2018: p. 1-10.
- [4], D. F. Todd and E. P Scott, *MEASUREMENT SCIENCE and TECHNOLOGY*, 2015, 26(1): p. 012002.
- [5] S. N. Soid. and Z. A. Zainal, *Energy*, 2011, 36(2): p. 724-741.
- [6] W. Yu, W. Yang, B. Mohan, K.L.Tay and F. Zhao., *APPLIED ENERGY*, 2017, 185: p. 1372-1382.
- [7] S. J. M Algayyim., A. P Wandel, T. Yusaf. *ENERGIES*, 2018, 11(5): p. 1298.
- [8] C. Baeand J. Kim, . *PROCEEDINGS OF THE COMBUSTION INSTITUTE*, 2017, 36(3): p. 3389-3413.
- [9] H. Liu, C.Lee,M. Huo and M. Yao, *ENERGY & FUELS*, 2011, 25(4): p. 1837-1846.
- [10] H. Wu, K. Nithyanandan, T.H, Lee, C.-f.F. Lee and C. Zhang, *ENERGY & FUELS*, 2014, 28(10): p. 6380-6391.
- [11] P.C, Chen, W.-C., W.L. Roberts and T. Fang, *FUEL*, 2013, 103: p. 850-861.
- [12] W. R. d. S, Trindade., and R. G. d. Santos, *RENEW SUST ENERG REV*, 2017, 69: p. 642-651.
- [13] J. B. Heywood, *Internal combustion engine fundamentals*. 1988: McGraw-Hill New York.

Flame image velocimetry for in-flame flow field analysis in an optically accessible diesel engine

J. Yang, L. Rao, Y. Zhang, C.M. de Silva and S. Kook*

School of Mechanical and Manufacturing Engineering, The University of New South Wales, Sydney, Australia

Abstract

Flame Image Velocimetry (FIV) is an effective diagnostic method for visualising the flow structures within the flame in optical diesel engines. Through applying cross-correlation on a pair of high-speed natural luminosity images, the contrast variation in luminosity signals is tracked to derive the instantaneous flow field. Using an optimised set of FIV processing parameters, detailed information regarding the in-flame flow motion and turbulent flow structure is provided. The present study shows the FIV results obtained for a selected two-hole fuel injection case in a small-bore optical diesel engine. The flow fields based on FIV analysis indicate that the jet-wall interaction causes a radial jet flow along the piston-bowl wall. The subsequent jet-jet interaction leads to the formation of turbulent vortices in the centre of the combustion chamber. Also, the jet-swirl interaction on the up-swirl side of the jet induces counter-rotating ring vortices, which are larger and more clearly defined than other vortices.

Keywords: FIV, Diesel injection, Jet-wall interaction, Jet-jet interaction, Jet-swirl interaction

1. Introduction

The in-cylinder flow development has a significant impact on the air-fuel mixing, which is critical for the engine efficiency and emissions in diesel engines [1]. The fuel-injection-induced flow structure is complex as it is influenced by multiple factors such as jet-wall interaction [2], jet-jet interaction [3] and jet-swirl interaction [4]. To better understand the injection induced flow fields in a diesel engine, a variety of diagnostic techniques have been applied. For example, two-dimensional, time-resolved particle image velocimetry (PIV) using a high-speed laser and camera has been favoured by most recent studies [1,3,5]. From the PIV results, it was shown that the variation in jet-jet interaction alters the flow inertia and thus changes the surrounding air-entrainment characteristics [3]. It was also reported that a swirl flow could affect the spatial distribution of fuel droplets during injection at the fuel spray boundary though no significant impact on the main flow of liquid fuel jet was found [6]. However, it must be noted that, the PIV measurement is limited to a non-combusting environment. This is because the scattered light from seeding particles under the combustion environment is masked by the strong light scatter from the soot luminosity signals. Given the flow motion within the flame could directly affect mixing and combustion, this is a significant limitation.

Recently, flame image velocimetry (FIV) was introduced as an effective way to visualise the in-flame flow fields in a diesel engine [7]. The FIV tracks the contrast variations in soot luminosity signals and extracts in-flame flow fields using a cross-correlation method. Previous studies applied FIV to diesel engines, from which the vortex structures induced by the swirl flow [8] and their role in enhanced soot oxidation was found [9]. Our recent study performed the optimisation of FIV processing parameters and we demonstrated FIV's potential to analyse flow fields in a small-bore, automotive-size diesel engine [10].

This paper implements FIV in an optically accessible diesel engine wherein jet-wall, jet-jet and jet-swirl interactions

generate complex in-flame flow structures. With high-speed imaging of the diesel flames and subsequent FIV analysis, detailed information about the flow direction and the formation of turbulent vortices is presented.

2. Experiments

2.1 Engine setup and operating conditions

As shown in Figure 1, the high-speed soot luminosity imaging was conducted in a single-cylinder, small-bore, optical diesel engine. The engine specification and operating conditions are listed in Table 1. This optical diesel engine is modified from a four-cylinder 1.6-litre diesel engine with three cylinders being deactivated. As illustrated by the sample image in Fig. 1(left), the soot luminosity imaging was conducted via the optical access provided by the quartz piston window installed on the extended piston top and a 45° reflex mirror. The original 8-hole injector was modified into a two-hole configuration through laser welding such that the tailored jet-jet interaction condition was achieved. The left two adjacent holes with the separation angle of 45° also allowed long injection duration which could prolong the jet-wall

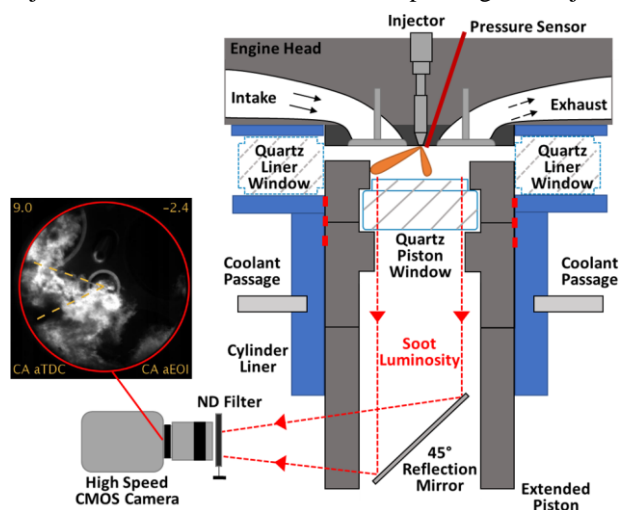


Figure 1: A schematic of the optical engine and soot luminosity imaging setup

Table 1: Engine specification and operating conditions

Displacement	395.5 cm ³
Bore size	77.2 mm
Stroke length	84.5 mm
Compression ratio	16.2
Swirl ratio	1.7
Engine speed	1200 rpm
Intake temperature	303 K
Wall (coolant) temperature	363 K
Fuel	Ultra Low Sulphur Diesel (CN 51)
Injection system	Bosch Solenoid Injector (CR12-20) Bosch Common rail (CR/V4/10-12S)
Number of holes	8 (6 blocked and 2 left open)
Jet separation angle	45°
Rail pressure	100 MPa
Injection timing	9°CA bTDC
Injection duration (signal)	548 μs
Injected fuel mass	16 mg
Firing mode	10-skip firing

interactions and subsequent jet-jet interactions.

In-cylinder pressure was measured by a piezo-electric transducer (Kistler 6056A) through the glow plug hole of engine head, with sampling frequency of 100 kHz (0.072 °CA resolution). The high-speed camera (Photron FASTCAM SA-X2) was used for soot luminosity imaging, with a pixel resolution of 512 by 512. To reduce the saturation of soot luminosity signals, the exposure time was set at 1 μs, the lens aperture was minimised at f/32, and a neutral-density filter (ND = 2.5) was used as illustrated in Fig. 1. The imaging frequency was set at 30 kHz corresponding to the temporal frame separation of 33 μs (or 0.24 °CA).

2.2 FIV processing

FIV analysis was conducted on the raw soot luminosity images using PIVLab, a Matlab-based open source code. Detailed FIV processing procedure and the optimisation of post-processing parameters are found in our previous work [10]. Hence, only a brief summary is provided here based on an example image shown in Fig. 2(left). After masking the image, signals within the red circle (i.e. piston bowl and quartz window boundary) were enhanced using the contrast limited adaptive histogram equalisation (CLAHE). The

cross-correlation algorithm was then applied to the interrogation window (i.e. sub-regions) in two consecutive frames, e.g. Frame A and Frame A+1, in which the pixel displacement due to the flame movement were tracked based on the signal contrast variation. In this process, a multi-pass Discrete Fourier Transform (DFT) cross-correlation algorithm was used in which the peak value in the correlation matrix (spatial domain) is selected to estimate the most probable displacement within the interrogation window to subpixel accuracy. This displacement is presented as a velocity vector as illustrated in Fig. 2(middle). One may argue that the current result could be affected by the off-plane flow motion outside the r-θ plane (i.e. horizontal plane). However, the flame development during the main combustion period is predominantly driven by the r-θ motion. Hence, the impact of movements in other direction (e.g. r-z, the vertical plane) is deemed insignificant. The resulting flow fields are shown in Fig. 2(right). The corresponding timing was added to each image with crank angles after top dead centre (°CA aTDC) on the left and crank angles after end of injection (°CA aEOI) on the right.

3. Results and discussion

3.1 In-cylinder condition and raw images

Figure 3 shows the in-cylinder pressure and apparent heat release rate (aHRR) traces for firing and motoring conditions. The pressure rises at about 5.5 °CA aTDC for the firing cycle, departing from the motoring pressure trace. This indicates the start of combustion. With the development of combustion, in-cylinder pressure increases to the peak of 4 MPa and then starts to decrease during the mixing-controlled combustion phase and late-cycle burn phase. The crank angle range for FIV analysis in the present study is illustrated on the pressure trace. The peak in aHRR occurs at 9 °CA aTDC, implying the premixed burn phase. The injection period is also shown in the aHRR plot.

Figure 4 shows the soot luminosity images during the combustion event, with the jet axes illustrated by two orange dashed lines. The swirl flow direction is also illustrated. From the images, it is seen that the first soot luminosity signal occurs at 5.9 °CA aTDC, which is the timing that the aHRR trace showed a sharp increase and the firing pressure exceeded the motoring pressure. Figure 4

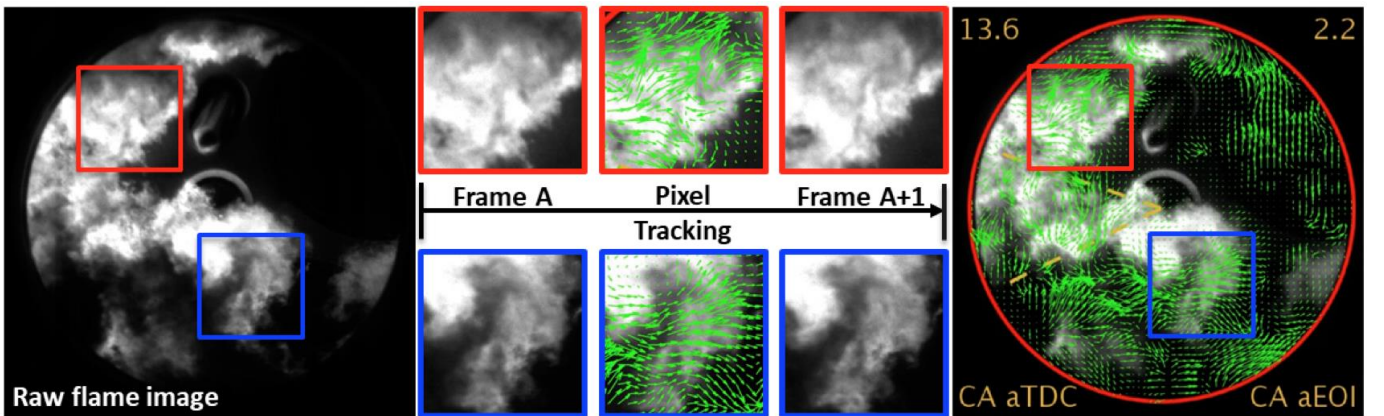


Figure 2: Image post-processing for flame image velocimetry (FIV)

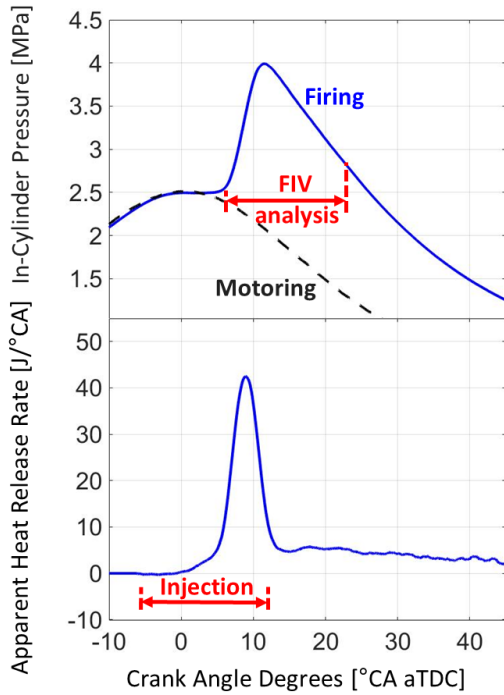


Figure 3: In-cylinder pressure and apparent heat release rate (aHRR) traces for motored and fired conditions

shows that a large amount of soot luminosity signals appears in-between the two jets, indicating high soot formation due to locally fuel-rich mixtures in the jet-jet interaction region. As the injection continued until 11.4 °CA aTDC, the jet-wall interaction pushed the flame out of the jet-jet interaction region, and thus the soot luminosity signals travel along the piston-bowl wall. The jet-wall interaction also caused the sooting flame to recoil off the wall and penetrate back towards the nozzle. The swirl flow effect is also evident in Fig. 4. The wall-jet on the down-swirl side travels faster than that on the up-swirl side, causing asymmetric signal distribution.

3.2 FIV-derived in-flame flow fields

The FIV analysis was performed to a selected crank angle range of 7.3 ~ 22.2 °CA aTDC in Fig. 4. This was because the signal development prior to this crank angle range was dominated by the premixed combustion, instead of the flow-induced mixing, and for later crank angles, the jet-jet interaction seen in the 2 o'clock direction would not occur in a real engine at this late cycle.

The derived flow fields using FIV are shown in Fig. 5. The flow vectors show that, at 7.3 °CA aTDC, the flow structure upon the jet impingement on the wall is chaotic; however, there is a clear direction of the flow along the piston-bowl wall on both up-swirl and down-swirl sides (as illustrated by two white arrows). This agrees with the observation in the soot luminosity images that two wall-jets travelling along the wall due to jet-wall interaction. At 9.0 °CA aTDC, the flow vectors indicating jet-wall interaction become clearer. This is highlighted in a magenta box on the bottom-left corner where a zoomed in image is presented. This image shows flow vectors impinging on the wall as well and the radial movement in both directions afterwards. The flow vectors along the bowl wall become more intense at 11.2 °CA aTDC and start to settle down from 13.8 °CA aTDC as the injection ended at 11.4 °CA aTDC.

At the centre of the piston bowl, flow vortices start to form from 9 °CA aTDC, which last until 19.3 °CA aTDC. As shown in the region highlighted by the blue box at 13.8 °CA aTDC, the vortices are formed in this region as the flame is directed back towards the nozzle due to jet-jet interaction. This is likely to enhance the mixing in this region, and thereby increasing soot oxidation. The vortices are also generated in the wall-jet head region. For example, as the wall-jet travels along the bowl wall, multiple vortices start to develop on the up-swirl side as shown in the region highlighted by a red box. These vortices show clockwise rotation as they are induced due to the interaction between the wall-jet and the counter-clock-wise swirl flow. By contrast, no such vortices are observed on the down-swirl side with the velocity vectors showing only the coherent

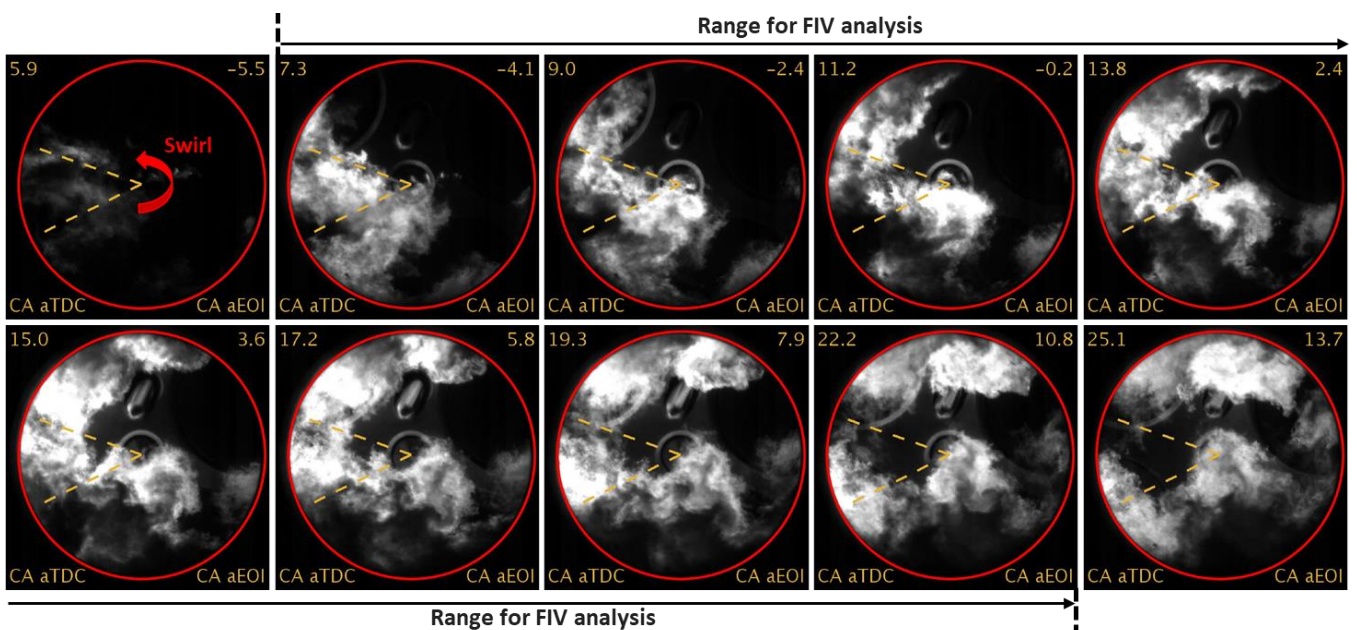


Figure 4: Raw frame images of natural soot luminosity movie during the flame development for two nozzle holes

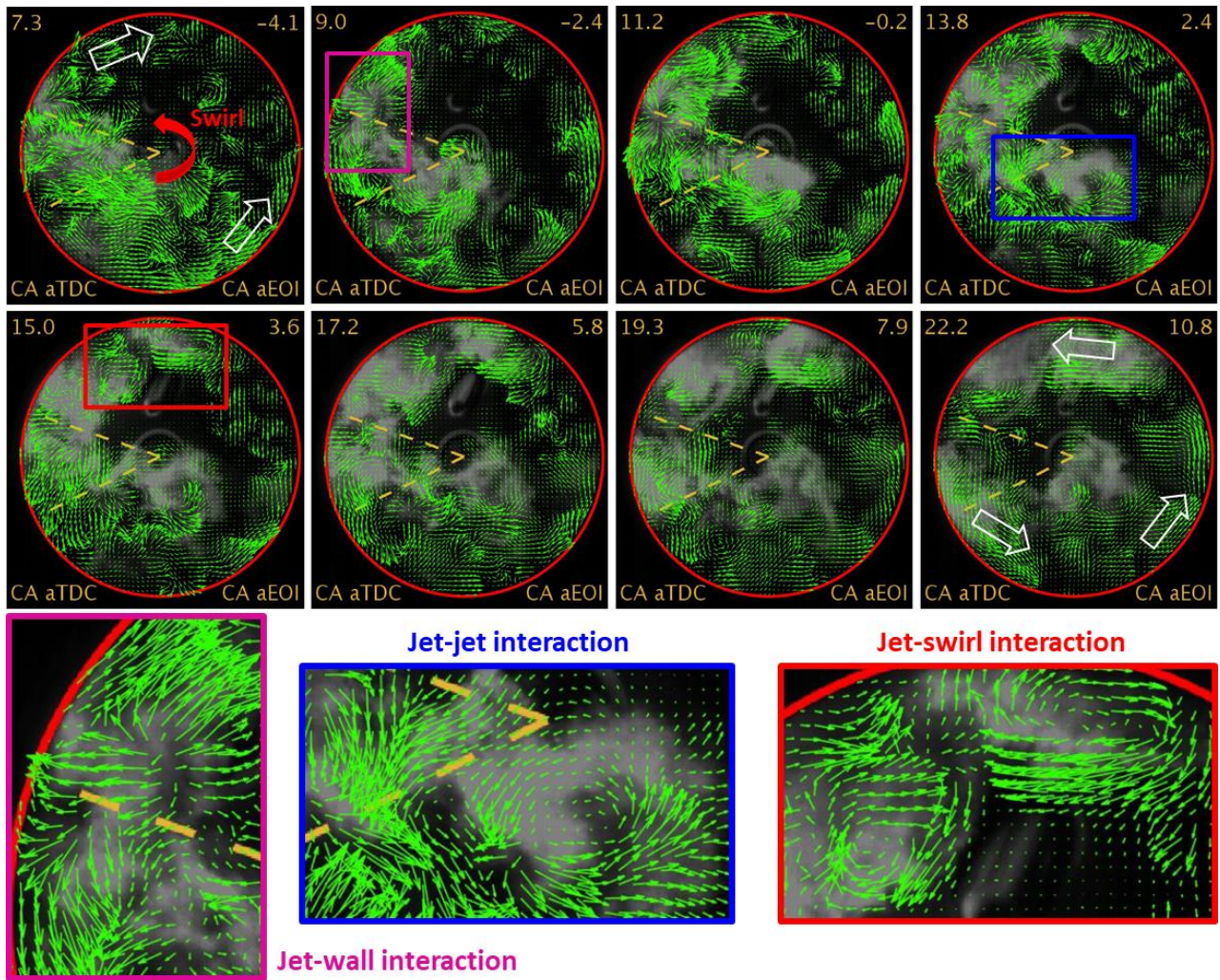


Figure 5: Flow fields within the flame under the influence of jet-wall, jet-jet and jet-swirl interactions

flow direction. These flow characteristics could explain higher mixing and lower soot measured on the up-swirl side than that on the down-swirl side [11]. At 22.2 °CA aTDC and afterwards, the flow fields are dominated by counter-clock-wise bulk flow motion, consistent with the swirling solid-body rotation. This is illustrated by white arrows.

4. Conclusions

In this study, FIV analysis has been performed in a small-bore optical diesel engine using high-speed soot luminosity movies. The FIV used in the present study successfully captured the velocity vectors indicating the jet impingement on the wall and the radial flow along the wall. The flow vortices were observed in the center of the piston bowl due to jet-jet interaction-induced flow back towards the nozzle. The jet-swirl interaction also generated vortices on the up-swirl side due to the counter-rotating wall-jet and swirl flows. On the down-swirl side, however, the vortices were not observed as the wall-jet and swirl flow travel in the same direction.

5. Acknowledgments

The experiments were performed at the UNSW Engine Research Laboratory, Sydney, Australia. We thank the funding support provided by the Australian Research Council via the LIEF scheme.

6. References

- [1] P. Stansfield, G. Wigley, T. Justham, J. Catto, G. Pitcher, *Exp. Fluids* 43 (2007) 135–146.
- [2] L.M. Pickett, J.J. López, *SAE Tech. Pap.* 2005 (2005).
- [3] L.-M. Malbec, G. Bruneaux, *SAE Int. J. Engines* 3 (2010) 107–123.
- [4] S. Kook, C. Bae, P.C. Miles, D. Choi, M. Bergin, R.D. Reitz, *SAE Tech. Pap.* 2006 (2006).
- [5] B. Petersen, P.C. Miles, *SAE Int. J. Engines* 4 (2011) 1623–1641.
- [6] J. Senda, D. Choi, M. Iwamuro, H. Fujimoto, G. Asai, *SAE Tech. Pap. Ser. 1* (2010) 1537–1553.
- [7] M. Shioji, T. Kimoto, M. Okamoto, M. Ikegami, *Trans. Japan Soc. Mech. Eng. Ser. B* 54 (1989) 2228–2235.
- [8] D.E. Winterbone, D.A. Yates, E. Clough, K.K. Rao, P. Gomes, J.H. Sun, *Proc. Inst. Mech. Eng. Part C J. Mech. Eng. Sci.* 208 (1994) 223–240.
- [9] M.J. Bergin, R.D. Reitz, S. Oh, P.C. Miles, L. Hildingsson, A. Hultqvist, *SAE Tech. Pap. Ser. 1* (2010) 776–790.
- [10] L. Rao, S. Kook, *SAE Tech. Pap.* 2019-April (2019) 1–14.
- [11] Y. Zhang, D. Kim, L. Rao, S. Kook, K.S. Kim, C.B. Kweon, *Proc. Combust. Inst.* 37 (2019) 4847–4855.

Image selection method for combustion analysis in an optical diesel engine

S. Meng, Y. Zhang and S. Kook*

School of Mechanical and Manufacturing Engineering, The University of New South Wales, NSW 2052, Australia

Abstract

Planar laser-based imaging is an effective tool to visualise the spatial development of key radicals and species inside the cylinder of a diesel engine. As there are multiple radicals and chemical species governing diesel combustion, the simultaneous imaging is required using multiple lasers and cameras. As this means a major infrastructure investment, various laser-based imaging diagnostics are often performed one at a time using a single system. Considering inherent cyclic variations in an engine, many images are obtained at each crank angle location and their ensemble average is used as a representative image for each radical and species. The ensemble-averaged images are then presented together to discuss their interactions and influence on diesel combustion. However, the averaged images show smeared out signals, which makes it hard to analyse turbulent flame structure. The present study evaluates an alternative approach in presenting various laser-based images from different engine cycles. The idea is that, for a set of images obtained from a selected radical/species and at a given crank angle, an individual image is selected based on the cross-correlation coefficients that are compared to the ensemble-averaged image. This method chooses an individual image that is the most similar with the ensemble-averaged image and thus enabling the discussion on the overall spatial distribution of radicals/species without losing structural details. Three planar laser-induced imaging diagnostics were performed in a single-cylinder optical diesel engine including planar laser induced fluorescence of hydroxyl radical (OH-PLIF), formaldehyde molecule (HCHO-PLIF) and planar laser induced soot incandescence (soot-PLII). The application of the selection method to these images showed that the OH growth out of the HCHO region near the wall is much clearer in the selected individual image than the ensemble-averaged images. The suspected PAH/soot interference in the HCHO-PLIF signals was also captured more effectively from the selected images.

Keywords: Diesel engine, Correlation coefficient, Image selection, PLIF, and PLII

1. Introduction

Laser-based imaging is the most effective and widely used technique to investigate flame development. Using laser beams tuned at specific wavelengths, intermediates species and combustion products could be excited or heated to capture fluorescence or incandescence signals. For instance, planar laser-induced fluorescence of hydroxyl radicals (OH-PLIF) can be imaged to identify high-temperature reaction zones and to analyse flame structures [1-5]. The laser-based imaging in engines poses a significant challenge due to high-pressure ambient gas conditions requiring high pulse energy, turbulent flame development within a confined space bounded by the cylinder head and moving piston, and inherent cyclic variations caused by the change in intake air pressure, fuel injection, mixture formation, and heat transfer [6]. For high-speed engine operation up to 6000 rpm (i.e. 50 fuel injections per second), the laser-based imaging in a diesel engine also requires careful synchronisation of the laser pulse, camera trigger and fuel injection timing [3, 7, 8].

To study combustion processes in sequence of time inside the cylinder of a diesel engine, laser-based imaging should be repeated for various crank angles. For each species and radicals, this imaging should also be repeated. This means laser-based images taken from different engine cycles [7, 8]. Significant efforts are made to minimise this cyclic variation in an optical diesel engine. For example, the in-cylinder pressure trace is monitored to ensure the images are taken at almost identical bulk gas conditions [2, 9]. The temperature of combustion chamber wall is fixed using a water heater/circulator, which helps minimise the variation

in heat loss. Often, a skip firing mode is used for engine operation, which implements fuel injection every a few motoring cycles to ensure the residual gases from the previous firing cycle is expelled completely [2,5,7,9]. Despite all these efforts, inherent cyclic variation associated with fluctuation in the intake air pressure, mixture distribution, turbulent flow fields is unavoidable. Time-resolved, high-speed imaging reduces the cyclic variation concern as the imaging does not need to be repeated for various crank angles [10]; however, this still needs to be repeated for various firing cycles to ensure one instantaneous movie obtained from one cycle is not biased. Similarly, the simultaneous laser-based imaging of multiple species and radicals could remove the concern on the cyclic variation among the radicals/species, but one set of images from one selected cycle cannot simply represent a given combustion condition. Therefore, multiple images should be taken either one at a time or simultaneously and the cycle-averaged (or ensemble-averaged) images should be evaluated.

When the ensemble-averaged images are used to discuss the flame structures and distribution of the measured species, a well-known challenge is smearing-out effects of the images. That is, each image pixel contains a signal in some cycles but not in other cycles, removing the fine details at the flame boundary and the pattern change within the flame. In a turbulent diesel flame, this becomes a significant limitation to discuss spatial development of radicals and species. The present study evaluates an alternative approach with a question: what if one selected individual image containing all the fine details and

* Corresponding author
E-mail address: s.kook@unsw.edu.au

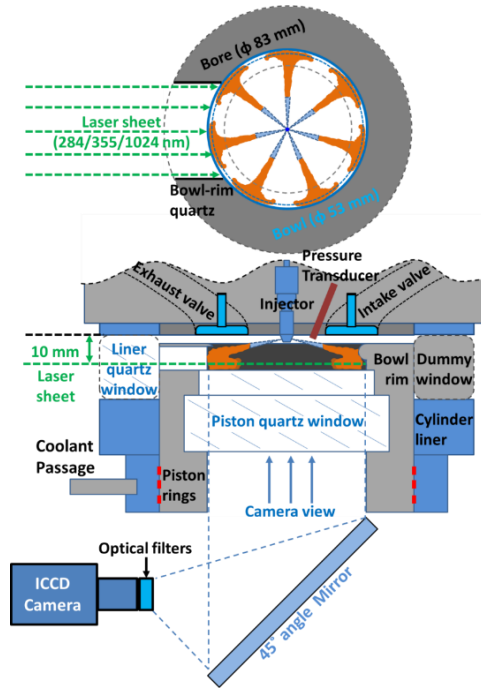


Figure 1: Illustration of the optical diesel engine and laser diagnostics setup in the bottom-view (top) and side-view (bottom) orientations

Table 1: Engine specification and operating conditions

Engine speed [rpm]	1200
Intake air temperature [°C]	27
Coolant (water) temperature [°C]	90
Common-rail pressure [MPa]	50
Fuel	Kerosene
Cetane number	40
Fuel density at 15°C [kg/m ³]	796
Lower heating value [MJ/kg]	43.4
Kinematic viscosity at 40°C [mm ² /s]	4.8
Pilot injection timing [CAD bTDC]	11
Main injection timing [CAD bTDC]	6
Pilot injection duration [ms]	0.370
Main injection signal duration [ms]	0.590
Pilot injection proportion [%]	20
Total injected fuel mass [mg/cycle]	9
Total energy input [J/injection]	~391

turbulent structures can represent a set of images taken at a selected crank angle and for a given radical/species from various engine cycles, as the ensemble-averaged image does.

2. Experiment

2.1 Optical engine and laser diagnostics

The laser-based imaging was performed in a single-cylinder optical diesel engine as illustrated in Fig. 1. The specification and selected operating conditions for the

diagnostics are listed in Table 1. The optical engine has a piston top and cylinder liner made of quartz. In addition, the piston bowl rim is also a quartz window to provide the optical path for laser beam insertion. For the present study, the laser beam elevation was fixed at 10 mm below the cylinder head. Before inserted into the piston bowl, the laser beam was converted into a 0.3-mm thick sheet covering the entire field of view of $\phi 53$ -mm piston-bowl. The laser-excited signals were recorded using an ICCD camera (Lavision Nanostar) through the optical path of the piston quartz and a 45° reflex mirror.

As noted in Fig. 1, three different laser wavelengths were used depending on the imaging diagnostics. The 284-nm laser with a pulse energy of 25 mJ at 10 Hz was used for OH-PLIF imaging using a Rhodamine-6G-filled dye laser (Sirah CobraStretch) pumped by a 532-nm beam from an Nd:YAG laser (SpectraPhysics Quanta-Ray Pro-230). An optical filter set of 300-nm band pass filter (40-nm FWHM) and two 305-nm long-pass filters was placed in front of the ICCD camera to isolate the OH-PLIF signals lying in a spectrum range of 308~320 nm. Also, the third harmonic and fundamental beam of this Nd:YAG laser were used for HCHO-PLIF and soot-PLIF, respectively. The 355-nm laser beam had a pulse energy of 160 mJ to excite HCHO and the fluorescence signals were captured using a combination of 385-nm long-pass filter, 430-nm band-pass filter (10-nm FWHM), 450-nm short-pass filter and the ICCD camera. The 1064-nm beam of the Nd:YAG laser at a pulse energy of 200 mJ was used to induce soot incandescence (soot-PLIF), which was recorded using the ICCD camera coupled with a 430-nm band-pass filter (10 nm FWHM) and a 450 nm short-pass filter.

2.2 Engine operation

Throughout the experiment, the 27°C intake air was naturally aspirated and the heated water at 90°C was circulated through the engine head, cylinder liner, and engine block to mimic a warmed-up engine condition. The fuel delivered through the common-rail injection system was a kerosene-based surrogate fuel with cetane number of 40. At a fixed common-rail pressure of 50 MPa, 20% of the total fuel mass (9 mg) was assigned to a pilot injection executed at 11°CA bTDC, while the main injection timing was set at 6°CA bTDC. A 10 skip-firing mode with 1 injection cycle followed by 9 motoring cycles was used in the present study, which was to expel residual gases from the previous firing cycle and to keep the thermal loading on the quartz windows below the burst limit. For each crank angle and species, a total of 20 injection cycles were executed for image taking. For the record of in-cylinder pressure, a piezo-electric pressure transducer (Kistler 6056A) was used.

3. Results and discussion

3.1 In-cylinder pressure and aHRR

The black lines plotted in Fig.2 (top) are the cycle-averaged in-cylinder pressure traces of each engine run of 20 firing cycles. The ensemble-averaged pressure trace of all the engine runs are plotted in red line and the corresponding apparent heat release rate (aHRR) averaged pressure trace is

shown in Fig. 2 (bottom), describing a general combustion behaviour for individual runs. The in-cylinder pressure traces indicate repeatable bulk gas conditions; however, the run-to-run variations and cyclic variations in each of these engine runs are not to be missed.

3.2 Image selection method

Figure 3 (left) shows a total of 20 OH-PLIF images taken at 9°CA aTDC, which corresponds to the peak aHRR location at which strong OH signals due to high-temperature reaction are expected. The images show overall similar structures with intense OH-PLIF near the jet-wall impingement point for each jet. The signals are clear on the left side where the laser beam was inserted. However, the significant beam attenuation caused almost no detectable

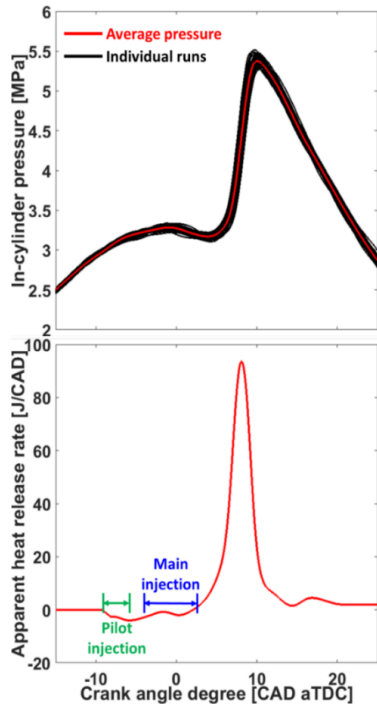


Figure 2: In-cylinder pressure and apparent heat release rate traces

signals on the right side. This pattern is also repeated on all 20 images. Upon these images, the ensemble-averaged image was produced as shown in the top right of Fig. 3. The overall OH-PLIF distribution observed from the 20 images is seen again in this average image. However, as previously mentioned, the signals are smeared out losing all the turbulent flame structures. To address this issue, a best-representing individual OH-PLIF image was selected by applying a correlation-coefficient based method [2,7]. Specifically, a two-dimensional, normalised cross-correlation coefficient ($r_{2d,xy}$) was calculated for each set of images of a given imaging timing using:

$$r_{2d,xy} = \frac{\sum_i \sum_j (x_{i,j} - \bar{x})(y_{i,j} - \bar{y})}{\sqrt{\sum_i \sum_j (x_{i,j} - \bar{x})^2 \cdot \sum_i \sum_j (y_{i,j} - \bar{y})^2}} \quad (1)$$

where x is the ensemble-averaged image count, \bar{x} is the image mean of the ensemble-averaged image count, y is an image count of an instantaneous image, \bar{y} is the image value of the instantaneous image, and i and j denote the row and column pixel, respectively. The cross-correlation coefficient represents the degree of similarity between two images; the higher the coefficient, the more the resemblance. The cross-correlation coefficient was calculated for all the images of 20 individual cycles against the ensemble-averaged image, which is plotted on the bottom-right corner of Fig. 3. The highest cross-correlation coefficient was measured at 0.8613 as highlighted in green box. The corresponding image is shown on the top-right corner of Fig. 3, which indicates high similarity to the ensemble-averaged image while keeping detailed pattern and structure in this selected individual cycle image.

3.3 Evaluation of the image selection

One question is raised whether the selected images can depict a picture of sequential development for combustion analysis, especially when the images of multiple laser diagnostics are combined to show a transition of reaction

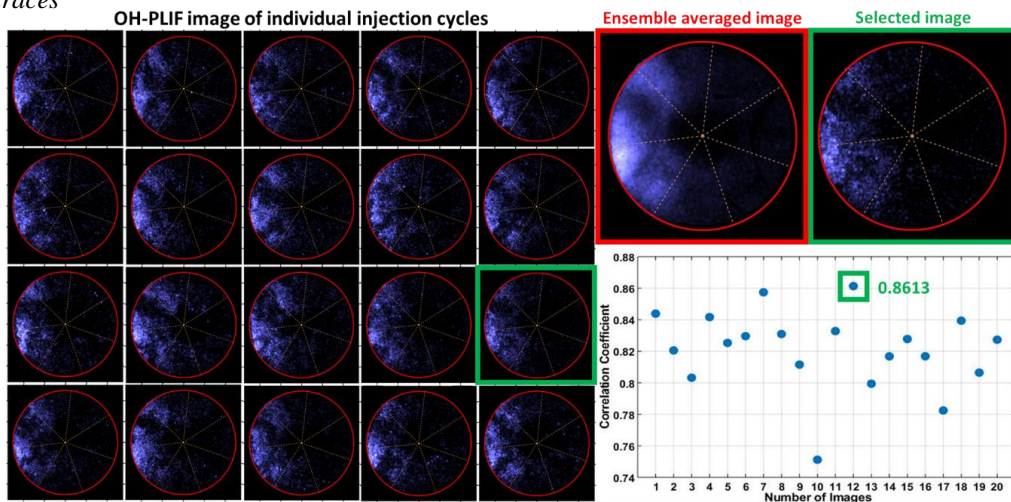


Figure 3: OH-PLIF images from 20 firing cycles (left), the ensemble averaged image of all 20 cycles and the selected instantaneous cycle image (top-right), and the correlation coefficients of all 20 firing cycles (bottom-right). The selected image with the highest correlation coefficient of 0.8613 is marked by a green box.

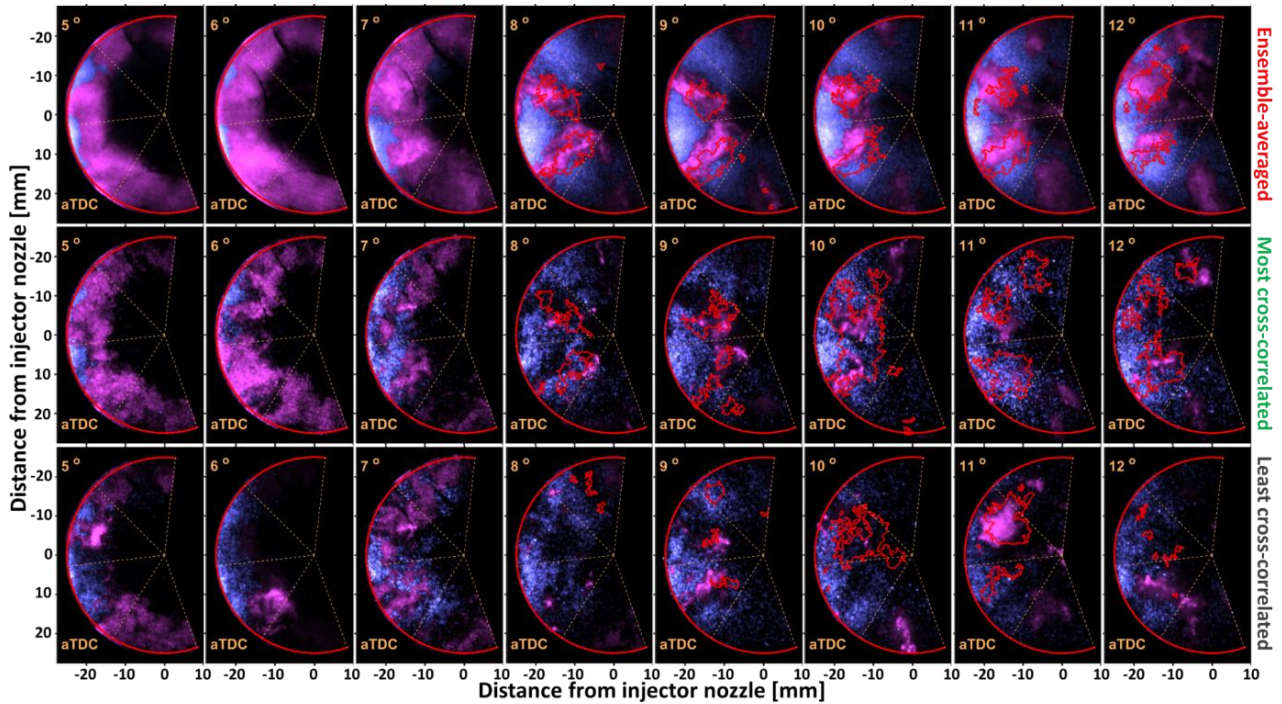


Figure 4: The combined HCHO-PLIF (purple) and OH-PLIF (blue) images with soot-PLII boundary lines (red) overlaid on the images using the ensemble averaging method (top) and the image selection method for highest (middle) and lowest (bottom) cross-correlation coefficients.

stages. Figure 4 shows the ensemble-averaged, the most correlated and the least correlated OH- and HCHO-PLIF images from 4 to 12°CA aTDC. The PLIF images were combined by false colouring OH in blue and HCHO in purple. In addition, the soot-PLII signal boundaries were overlaid using red lines.

Both ensemble-averaged and the most correlated images show the same trend that the OH-PLIF initially develops from the jet-wall impingement point and then spread through the entire HCHO-PLIF region. However, it is the selected individual images with the highest cross-correlation coefficients that show the growth of OH radicals within the HCHO region more clearly. Particularly, at 7°CA aTDC, the OH overtakes the HCHO distribution during the low- to high-temperature reaction transition occurs, which is captured better in the selected image. When HCHO-PLIF signals are found between the jet axes only (8°CA aTDC and after), it is also the selected image indicating more effectively that these are interference signals from PAH/soot through scattered pocket structures. The soot boundaries also match better with the remaining HCHO PLIF signals. In comparison, the least correlated images show poor consistency with the ensemble-averaged images and fail to capture the crucial trends observed from the best selected images.

4. Conclusion

The present study performed a cross-correlation coefficient-based selection of OH-PLIF, HCHO-PLIF and soot-PLII images obtained from many different cycles in an optical diesel engine. The most correlated PLIF and PLII images are overlaid and compared with those of the ensemble-averaged images. The ensemble-averaged and the most

correlated images showed the same overall flame development trend. However, the selected images for the highest cross-correlation coefficients exhibited the OH growth out of the HCHO region more clearly and the PAH/soot interference in the HCHO-PLIF signals were captured more effectively. Therefore, for the discussion of diesel combustion based on laser-based images, the selection of individual images could be a useful alternative method to the presentation of ensemble-averaged images.

Acknowledgement

The experiments were performed at the UNSW Engine Research Laboratory, Sydney, Australia. The funding support was provided by CCDC Army Research Laboratory and ITC-PAC.

References

- [1] S. Singh, M. P. B. Musculus, and R. D. Reitz (2009) *Combustion and Flame*, vol. 156, no. 10, pp. 1898-1908
- [2] M. K. Le, S. Kook, and E. R. Hawkes (2015) *Fuel*, vol. 140, pp. 143-155
- [3] Q. Tang, H. Liu, M. Li, M. Yao, and Z. Li (2017) *Combustion and Flame*, vol. 177
- [4] J. E. Dec and E. B. Coy (1996)
- [5] A. M. Rusly, M. K. Le, S. Kook, and E. R. Hawkes (2014) *Fuel*, vol. 125, pp. 1-14
- [6] M. Aldén, J. Bood, Z. Li, and M. Richter (2011) *Proceedings of the Combustion Institute*, vol. 33, no. 1, pp. 69-97
- [7] C. L. Genzale, R. D. Reitz, and M. P. B. Musculus (2008) SAE International
- [8] Q. Tang, H. Liu, M. Li, and M. Yao (2017) *Applied Energy*, vol. 185, pp. 708-719
- [9] M. K. Le, S. Kook, Q. N. Chan, and E. R. Hawkes, (2014) in *Proceedings of the 19th Australasian Fluid Mechanics Conference, AFMC 2014*
- [10] Z. Wang et al. (2019) *Proceedings of the Combustion Institute*, vol. 37, no. 4, pp. 4751-475

Effect of intake air e-boosting on external EGR-diluted diesel combustion

X. Liu and S. Kook*

School of Mechanical and Manufacturing Engineering, The University of New South Wales, NSW 2052, Australia

Abstract

Exhaust gas recirculation (EGR) has been used in modern diesel engines to reduce thermal NO formation through the diluted charge and lower specific heat ratio. While the reduced engine-out emissions of NO_x (NO and NO₂) is demonstrated, the use of EGR leads to decreased engine power output, simply due to decreased heat release rate. This is compensated through intake air boosting, most commonly using a supercharger, turbocharger, or both. The increased intake air pressure boosts the induced air mass and thus the in-cylinder pressure increases to generate more power, which may recover the loss caused by EGR. A drawback of this approach is increased efficiency loss as the supercharger is driven by the crank shaft. For turbochargers, a delayed activation (i.e. turbo lag) is an issue as the engine speed should be sufficiently high for the exhaust gas to drive the turbine. An alternative technology is e-boosting, i.e. a battery powered electric compressor, which is independently operated and thus is free from efficiency loss or turbo lag. This study evaluates this new approach using an in-house made e-booster in a single-cylinder automotive diesel engine. For a fixed EGR rate of 25%, which was shown to achieve significant reduction in NO_x emissions, the e-boost pressure was varied between 100 to 145 kPa (absolute). The results showed that higher intake air pressure leads to increased in-cylinder pressure and a more stretched apparent heat release rate profile over a wider crank angle range. This results in increased net indicated efficiency while further reducing engine-out NO_x emissions. Compared with the baseline condition of no EGR and no e-boosting, 140 kPa of intake air pressure was enough to recover the power loss caused by 25% EGR while achieving 75% reduction in NO_x emissions.

Keywords: Diesel combustion, exhaust gas recirculation (EGR), intake air e-boosting, indicated efficiency, NO_x.

1. Introduction

One of the most significant challenges for diesel engine developers is to reduce emissions of nitrogen oxides (NO_x) and particulate matter (PM) simultaneously without compensating efficiency/fuel consumption. While PM emissions are becoming less concerned due to the use of high-pressure common-rail injection system and diesel particulate filter (DPF), the NO_x reduction is more complex due to its trade-off characteristics with engine power and efficiency. Low temperature combustion (LTC) diesel [1] is a widely used strategy, which keeps the flame temperature low to suppress thermal NO formation. This is implemented using exhaust gas recirculation (EGR) for reduced intake air oxygen concentration. The diluted air reduces the flame temperature. The higher heat capacity of the exhaust gas also leads to decreased flame temperature. However, the reduced flame temperature means lower heat release rate and in-cylinder pressure, which results in decreased power output and lower engine efficiency [2, 3]. One immediate solution is to use aftertreatment systems such as a lean NO_x trap and urea-based selective catalytic reduction (SCR) – i.e. maintaining high power output, high NO_x engine operation but reduced tailpipe NO_x emissions. However, the efficacy of lean NO_x trap was questioned when it was a part of the recent NO_x emissions scandal. The SCR is becoming popular for its high conversion rate, which, however requires regular refill of the urea tank.

Turbochargers and superchargers are commonly used in production diesel engines to increase engine efficiency and power output while reducing fuel consumption [2, 3]. The improvement over naturally aspirated engines is made possible by boosting the intake manifold pressure higher than the atmosphere pressure. Higher intake air pressure increases the ambient-gas density within the cylinder, and hence leads to higher pressure condition during the combustion event. In addition, higher ambient density

means higher air-entrainment rate and enhanced mixing [4]. Previous studies showed that both lift-off length and ignition delay are reduced at higher intake boosting and thus reduce the pre-combustion mixing [4, 5]. Less premixed combustion also means lower combustion temperature, which can contribute to NO_x reduction. Therefore, the intake air boosting could be used to compensate the power/efficiency loss caused by EGR, resolving the efficiency-NO_x trade-off characteristics and potentially further reducing NO_x.

One major drawback of turbochargers is a turbo lag. Since the turbine shaft is driven by the exhaust gas, a certain level of engine speed is required to achieve enough exhaust gas flow rate. This is addressed using variable geometry turbochargers in which the vane angle changes to reduce the required exhaust gas flow rate at low engine speed; however, the activation of turbocharger is still not immediate. The supercharger, an air compressor driven by the crank shaft, has much faster response but its boosting level is very limited and is not decoupled with the engine speed. More importantly, the supercharger reduces the engine efficiency as it is driven by the crank shaft. An alternative technology that has recently been commercialised is e-boosting. Often called a mild hybrid system, new diesel cars come with a higher voltage (e.g. 48-V) Li-Ion battery pack in addition to the 12-V lead-acid battery to enable frequent shut on and off of the engine depending on the driving mode. An air compressor driven by an electric motor, i.e. e-booster, is also used to replace superchargers/turbochargers. Since the operation of the e-booster is independent of the engine, e-boosting achieves increased power output with no efficiency loss or turbo lag issues.

The present study evaluates the e-boosting as a promising technology to achieve NO_x reduction with no compromise

in engine power output. In a single-cylinder automotive diesel engine, high EGR rate of 25% was used to achieve significant NO_x reduction while the e-boosting level was increased until the power loss due to EGR is recovered. How the engine power output and efficiency change due to variation in e-boosting level at this high EGR rate is assessed in this study. The combustion-induced noise and engine-out emissions of NO_x, uHC, CO and smoke are also discussed.

2. Experiments

The engine performance and emissions testing were conducted in a single-cylinder common-rail diesel engine with a single-overhead cam and 16 valves. As illustrated in Fig. 1, the engine was modified from a two-litre four-cylinder production diesel engine with only one active cylinder being used for a research purpose. The single-cylinder engine has a displacement volume of 497.8 cm³ with bore and stroke of 83 and 92 mm. The geometric compression ratio of this engine is 17.7 and the swirl ratio is 1.4, as listed in Table 1. Both intake and exhaust manifolds are connected with 60-litre surge tanks to avoid pressure fluctuations associated with the single-cylinder engine operation. A high pressure common-rail and three-piston pump (Bosch CP3) was used for fuel delivery through a solenoid-type injector with a minisac nozzle tip. At this tip, seven evenly spaced 134 μm holes with 150° included angle were drilled, which were hydro-grounded with a K-factor of 1.5 and discharge coefficient of 0.86. Fuel injection parameters including injection pressure, timing, and duration are independently controlled using a universal common-rail control unit (Zenobalti ZB-9013P) based on the crank shaft-mounted rotary encoder signals (Autonics E40S8).

A piezo-electric pressure transducer integrated into a glow plug adapter (Oprand PSIGlow-A) was used to measure the in-cylinder pressure. The in-cylinder pressure was recorded for 100 successive firing cycles. The raw data was used to calculate the averaged in-cylinder pressure trace, peak pressure rise rate (peak PRR), indicated mean effective pressure (IMEP) and the coefficient of variation of IMEP (CoV of IMEP). The ensemble-averaged in-cylinder pressure trace was also used to calculate the apparent heat release (aHRR) and the combustion phasing.

The engine was connected with an Eddy Current (EC) dynamometer (FroudeHoffmann AG-30HS) for constant speed tests at 2000 rpm. Before and during the engine operation, heated water at 90°C was circulated through the cylinder head, liner and engine block using a water temperature controller/circulator (ThermalCare Aquatherm RQE0920). The measured intake air temperature of 27°C did not vary throughout the tests. For e-boosting, a conventional supercharger (Rotrex C15) was modified so that the drive shaft is connected to a 7.5-kW AC motor. At the shaft speed of 0~64,800 rpm, the measured intake air pressure was 100~145 kPa (absolute). For exhaust gas recirculation (EGR), a conventional EGR valve and pipe was used to connect the intake and exhaust manifolds. The EGR rate was evaluated based on the carbon dioxide (CO₂) concentration in the intake and exhaust gas using CO_{2intake}/

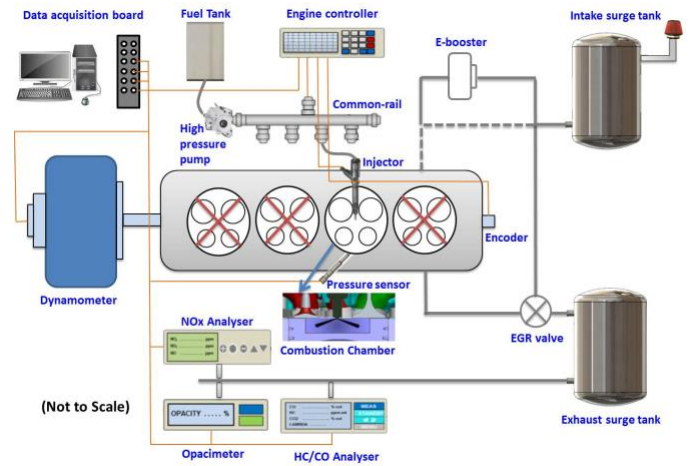


Figure 1: Schematic diagram of a single-cylinder common-rail diesel engine setup.

Table 1: Engine specification and selected operating conditions

Displacement volume [cm ³]	497.8
Bore/stroke [mm]	83/92
Compression ratio	17.7
Swirl ratio	1.4
Engine speed [rpm]	2000
Coolant temperature [°C]	90
Intake air temperature [°C]	27
Intake air pressure [kPa] (absolute)	100 – 145
EGR ratio [%]	0, 25
Common-rail pressure [MPa]	100
Fuel	Conventional Diesel
Injection timing [°CA bTDC]	8 - 3
Total injected fuel mass [mg]	19.9

CO_{2exhaust} [7]. The EGR rate was swept from 0% to 25%. The no EGR condition was used as a baseline. Higher EGR rate was also tested but unstable combustion (e.g. CoV of IMEP higher than 5%) was noticed. The common-rail pressure was fixed at 100 MPa, which achieved the highest IMEP and lowest overall engine-out emissions [8]. A conventional diesel fuel was used and the injection timing was varied between 8 and 3°CA bTDC to hold the combustion phasing constant, similar to our previous study [9]. The 19.9 mg injected fuel mass was calculated based on the measured injection rate using a Bosch tube-type injection rate meter [10]. This corresponds to about 9 bar IMEP for medium load condition in this small size diesel engine.

Five emissions were measured for various e-boosting levels. The noise emission was estimated using Shahlari et al.'s algorithm [8, 9], which converts the measured in-cylinder pressure to decibel (dB) by applying filters for the loss of noise transmission due to the engine structure and the frequency response of human hearing system. It was noted that the sampling rate was 100 kHz, which is 5-fold higher than required 20 kHz to resolve the attenuation function frequencies ranging between 0.1 and 10 kHz. The

engine-out exhaust emissions including smoke, nitrogen oxides (NO_x), and unburnt hydrocarbons (uHC) and carbon monoxide (CO) were measured using an opacimeter (Horiba MEXA-600S, ± 0.15 m⁻¹ light absorption coefficient accuracy), a chemiluminescence-type gas analyser (Ecotech 9841AS, 1% accuracy), and a non-dispersive infrared (NDIR) analyser (Horiba MEXA-584L, 1.7% accuracy), respectively.

3. Results and discussion

3.1 In-cylinder conditions

Figure 2 shows the ensemble-averaged in-cylinder pressure and apparent heat release rate (aHRR) traces for all the tested conditions of the present study. The baseline condition with no e-boosting and no EGR (grey line) shows high peak in-cylinder pressure of about 8.6 MPa with the start of combustion determined by the rise of aHRR occurring at about 4°CA aTDC. Since the injection timing was set at 8°CA bTDC, this means 12°CA of ignition delay time. In comparison, the 25% EGR condition at the same 100 kPa intake pressure (no e-boosting, black line), a significant effect of EGR is observed. The in-cylinder pressure measured at TDC shows about 600 kPa reduction as the exhaust gas with higher heat capacity replaced the fresh air. As a result, the start of combustion was retarded to 8°CA aTDC, and since the start of injection was fixed at 8°CA bTDC as of no EGR condition, the ignition delay time was increased to 16°CA. This caused increased charge premixing, which is reflected in higher peak aHRR than that of the baseline condition. However, the start of combustion (or combustion phasing in general) was retarded with the main heat release occurring later in the expansion cycle. This, together with lower TDC pressure, led to lower in-cylinder pressure despite higher peak aHRR.

At a fixed EGR rate of 25%, various intake air pressures ranging between 100 to 145 kPa were applied. For this

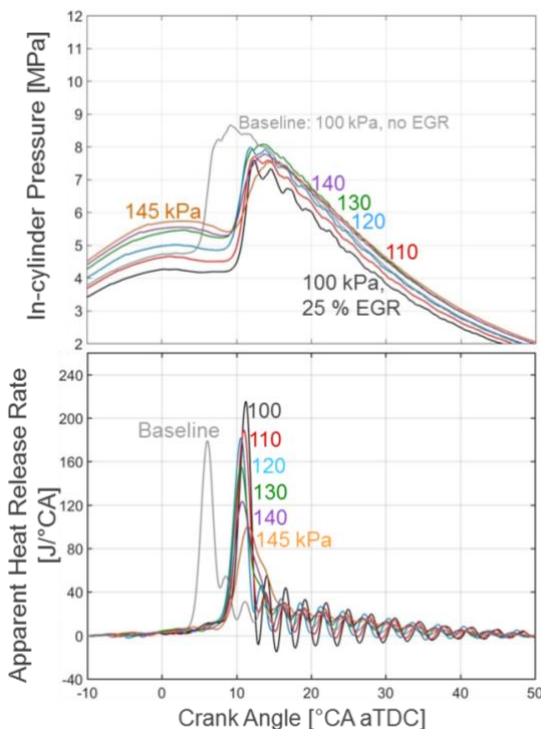


Figure 2: In-cylinder pressure and apparent heat release rate (aHRR) for various intake air pressure

variation, the CA10 (i.e. crank angle of 10% heat release) was fixed by adjusting injection timing to isolate the intake air pressure effects from the combustion phasing effect. From the figure, a clear trend is observed that higher e-boosting level leads to higher compression pressure. This was simply due to increased air mass/density, and thus a monotonic increase in the in-cylinder pressure for higher intake air pressure is observed. It is seen that only 10 kPa increase in the intake pressure could recover the TDC pressure loss caused by 25% EGR. At the highest e-boosting level, the TDC pressure reaches 5.7 MPa.

The peak in-cylinder pressure due to combustion also increases with increasing intake air pressure up to 130 kPa. However, at the intake pressure higher than 140 kPa, the peak in-cylinder pressure shows a decreasing trend. This was because the aHRR during the premixed burn phase was reduced. That is, the increased intake air pressure caused decreased ignition delay time and reduced premixing. In Fig. 2, the peak aHRR measured during the premixed burn phase showed a monotonic decrease with increasing intake air pressure. Therefore, the increasing trend observed for the peak in-cylinder pressure indicates the direct impact of increased intake air pressure; however, the decreased premixed burn could reverse the trend at much higher intake air pressure.

3.2 Power output and engine efficiency

Figure 3 shows the results of net IMEP, coefficient of variation (CoV) of IMEP, net indicated efficiency, and indicated specific fuel consumption (ISFC). The net IMEP shows a strong influence of EGR. Compared to the baseline condition achieving 920 kPa of IMEP, 25% EGR led to 125 kPa reduction in IMEP. By contrast, the increased intake air pressure through e-boosting shows almost linear increase in

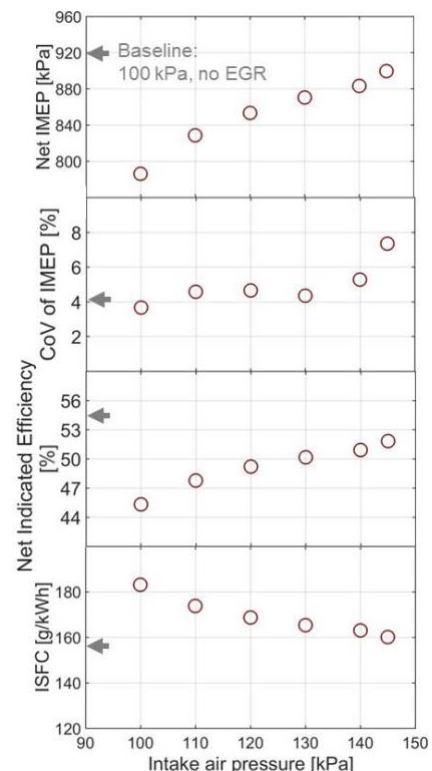


Figure 1: Power output and efficiency parameters

IMEP. This was despite the fact that the peak in-cylinder pressure was reduced at intake pressure of 140 kPa or higher. The close examination of in-cylinder pressure traces (Fig. 2) indeed suggests high in-cylinder pressure at late cycle. For example, the in-cylinder pressure at 30°CA aTDC shows the same monotonic increase with increasing intake air pressure, similar to that at TDC. It was noted when the peak aHRR was decreased at higher intake air pressure, the aHRR in fact showed a more stretched profile with lower peak value but a certain level of aHRR lasting until late crank angles throughout the mixing-controlled and late-cycle burn phases.

The further increase of intake air pressure to achieve even higher IMEP was hindered by increased CoV of IMEP. For example, 145 kPa of intake air pressure shows 7.5% CoV of IMEP, which well exceeds 5%, the fluctuation limit commonly accepted by the industry. Since the injected fuel mass was fixed, the net indicated efficiency and indicated specific fuel consumption (ISFC) show a simple reverse trend to the net IMEP. Figure 3 shows that high net indicated efficiency of 51% and low ISFC of 162 g/kWh could be achieved at 140 kPa intake air pressure. This significantly recovers the power and efficiency loss caused by 25% EGR although the baseline condition of 54% efficiency and 158 g/kWh ISFC could not be fully recovered due to unstable combustion at higher e-boosting level.

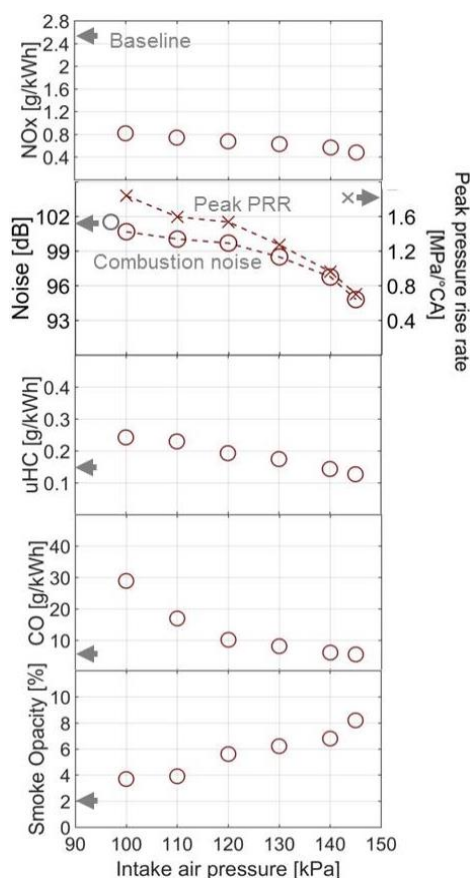


Figure 3: Emissions

3.3 Emissions

Figure 4 shows the engine-out emissions. It is observed that 25% EGR was very effective in reducing NO_x emissions. By applying e-boosting, the NO_x emissions were further reduced. This was consistent with a decreasing trend in the peak aHRR (Fig. 2), indicating lower premixed burn and lower thermal NO formation. The combustion noise shows almost no influence of EGR; however, due to decreased premixed burn, the peak pressure rise rate (PRR) decreases with increasing intake air pressure, which resulted in reduced noise. The uHC and CO emissions show a significant benefit of increased intake air pressure. The application of 25% EGR increased the uHC/CO emissions, which were fully recovered by applying high intake air pressure of 140 kPa, as shown in Fig. 4. For fixed injected mass of the present study, higher boosting means higher air mass for enhanced oxidation. However, the measured smoke opacity, which increased with the application of 25% EGR, became worse at higher intake air pressure. This was not unexpected because the premixed burn was reduced at higher intake air pressure. The typical smoke-NO_x trade-off characteristics of diesel combustion is observed again, which requires further investigation in future.

4. Conclusions

The performance and emissions variations of diesel combustion due to EGR and e-boosting has been investigated in a single-cylinder automotive diesel engine. The results show higher EGR rate of 25% could achieve significant reduction in NO_x at the expense of engine power, efficiency, uHC/CO, and smoke emissions. By applying e-boosting up to 40 kPa (or 140 kPa absolute intake air pressure), the power and efficiency loss could be significantly recovered. Due to reduced premixed burn at higher intake air pressure condition, NO_x, and noise emissions were further reduced. The increased air pressure also led to decreased uHC and CO emissions due to enhanced oxidation. However, increased smoke emission due to EGR became worse at higher intake air pressure, which requires further investigation.

Acknowledgement

The experiments were performed at the UNSW Engine Research Laboratory, Sydney, Australia. The funding support for this research was provided by the Australian Research Council via Linkage Projects scheme.

References

- [1] S. Kook, C. Bae, et. al. (2005) *SAE Technical Paper* 2005-01-3837.
- [2] N. Uchida, Y. Daisho, et. al. (1992) *SAE Technical Paper* 920117.
- [3] N. Uchida, Y. Daisho, et. al. (1993) *SAE Technical Paper* 930601.
- [4] W. F. Colban, P. C. Miles, et. al. (2007) *SAE Technical Paper* 2007-01-4063.
- [5] L. M. Pickett, D. L. Siebers, et. al. (2005) *SAE Technical Paper* 2005-01-3843.
- [6] D. L. Siebers and B. Higgins (2010) *SAE Technical Paper* 2001-01-0530.
- [7] C. Woo, S. Kook, et. al. (2015) *SAE Int. J. Fuels Lubr* **8** pp. 597–609.
- [8] C. Woo, S. Kook, et. al. (2016) *Fuel* **180**, pp. 9–19.
- [9] X. Liu, H. Goyal, et. al. (2019) *SAE Technical Paper* 2019-01-1148.
- [10] S. Padala, C. Woo, et. al. (2013) *Fuel* **109**, pp. 597–607.
- [11] A. J. Shahlari, C. Hocking, E. et. al. (2013) *SAE Int. J. Engines* **6**, pp. 541–552.
- [12] A. J. Shahlari, E. Kurtz, et. al. (2015) *Int. J. Eng Res* **16** pp. 829–850.

Initial Characterisation of a hybrid air-blast and electrostatic atomizer for spray combustion

Tushar Ahmed¹, Agisilaos Kourmatzis^{1,*}, and Assaad R. Masri¹

¹ School of Aerospace, Mechanical, and Mechatronic Engineering,
The University of Sydney, NSW 2006, Australia

Abstract

While electrostatic atomization of dielectric liquids has been extensively studied in the literature, the details of a hybrid atomization mode which combines the effects of a coaxial shearing air-flow and electrostatic charge, remain very poorly understood. This paper presents a new burner design that enables a systematic investigation of the combined effects of charge and aerodynamic forces on atomization, for improved control of droplet size, and the eventual application to spray combustion. The aerodynamic effects are studied over a range of Weber numbers, with a range of spray specific charge levels and liquid jet velocities. The findings suggest that the hybrid mode can enhance the spray angle noticeably, with an increasingly significant effect at lower aerodynamic Weber numbers. Analysis of the root mean square of velocity fluctuations at the location of highest mean velocity, indicate that the introduction of the electric charge can potentially have an influence on local mixing behaviour.

Keywords: EHD, Electrostatic atomization, Air-blast atomization

1. Introduction

Electrostatic atomization of insulating dielectric liquids (liquids having higher electrical resistivity, over $\sim 5 \times 10^8 \Omega\text{m}$) has been a technique tested for some decades [1-5] and involves the introduction of a unipolar charge to a dielectric liquid, in order to generate a repulsive force that overcomes the surface tension force. The method offers some unique advantages over conventional atomization techniques which include: i) allowing the user to control the size as well as the motion of the droplet independent to the flow boundary conditions ii) preventing the coalescence of droplets due to the presence of like charge on droplets, and iii) offering a certain degree of control over the size distribution of produced droplets [6-9].

Electrostatic atomization of dielectric liquids, commonly known as Charge Injection Atomization, is not to be confused with electrosprays, the latter of which pertain to the atomization of conducting liquids under the influence of a surface charge [10]. Electrosprays are commonly used in pesticide sprays, disinfection, generation of highly dispersed micro-particles, and thin film preparation. While the electro-spraying method is promising, use of that technique for electrically insulating liquids (such as Kerosene, Diesel, BioDiesel, and a number of synthetic fuels) necessitates the addition of conductive additives, a requirement which is not needed for charge injection systems. This makes the charge injection method of particular interest for a number of spray combustion applications.

Studies to date in this area have found that the presence of the same polarity of charge among droplets is capable of increasing the evaporation rate by improved spray plume dispersion [11] and can lower soot production by creating larger inter-particle separation [12]. Atomization of highly viscous fuels like biodiesel can also benefit from the advantages of using an electrostatic atomizer [13]. A disadvantage of this method is the limited liquid flow rate

because of the very small orifice diameters required to maintain a high charge to volume ratio. Multi-orifice atomizers can be used to ameliorate this issue, but this arrangement may result in a variable charge distribution from one jet to the next, making prediction of the global spray characteristics difficult [14]. Combination of the charge injection mode with a co-flowing air-blasting mode of atomization is therefore useful to enable an assisted mode of atomization on top of electrostatic charge, while it is also more practical for burners for lean operation.

The purpose of this study is to investigate a hybrid electrostatic and air-blast atomization technique. The first section describes the design and features of this injector and evaluates its spray current characteristics against a similar point-plane charge injection atomizer designed by [15]. Spray images for various liquid jet velocities and Weber numbers are subsequently shown along with spray angle measurements to ascertain the basic operation of the atomizer. These are then followed by a brief selection of results highlighting the potential effects of charge on the fluctuations of velocity in the centreline of the flow.

2. The Atomizer

The atomizer is a combination of a traditional co-axial air-blast component and a point-plane electrostatic atomizer as shown in Figure 1. The design features a long high voltage brass needle placed at a designated distance (L) from an electrically grounded nozzle tip. The liquid is then allowed to flow between this gap, where it acquires charge. Above a particular threshold voltage, the charge injected into the liquid will be sufficient enough to influence the atomization of the jet (resulting in a high current in the spray). The charged jet will come out from the injector and flow coaxially within the air stream, which is generated by the air-blast part of the injector. The design of the injector allows adjusting the inter-electrode gap to control the electric field between the HV electrode and the grounded nozzle. For this study, a 250 micron orifice (D) and a fixed

* Corresponding author. agisilaos.kourmatzis@sydney.edu.au

inter-electrode gap $L/D=2$ were used. Locally available Diesel was used as the dielectric fluid, the properties of which and a detailed working principle of the electrostatic stage of the atomizer can be found in [13]. The maximum applied potential ranged from 4 kV to 7 kV.

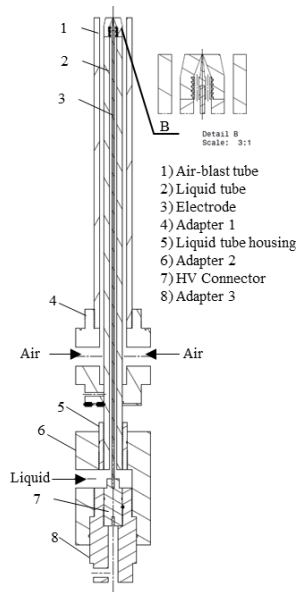


Figure 1: Schematic of the hybrid air-blast and electrostatic atomizer.

2.1 Electrical performance of the atomizer

The amount of charge injected by an electrostatic atomizer per unit time is referred to as the total current, which is a combination of leakage current (lost to ground) and spray current (carried out by the liquid into the spray). One common way of assessing the performance of an injector is by measuring its spray current, as higher spray currents are indicative of improved atomization [1]. The threshold voltage for this injector (where spray current increased significantly with voltage) at the chosen L/D was found to be -3 kV and measured by gradually increasing the applied voltage from zero to a point where the spray current starts to register on the picoammeter. A Spellman SL series high voltage supply was used to supply the high voltage and the spray current was measured using a Keithley model 6485 Picoammeter, which is capable of measuring a maximum current of 20 mA and minimum of 2 nA.

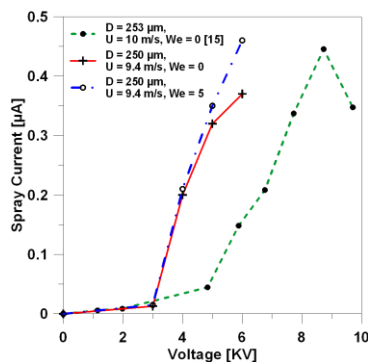


Figure 2: Spray current vs. voltage measurement for both the present atomizer and for data obtained from [15].

Figure 2 shows the spray current measured for this particular injector with and without air-blast cases, alongside data obtained from [15]. As we can see both the spray current measurements follow the same trend and are in the same order of magnitude. Differences in the precise value of spray current are to be expected [1] and are a result of using different Diesel, where previous work has shown significant differences in spray current between UK Diesel and US Diesel [15] as well as different electrode materials. The charge is also influenced by the sharpness of the electrode, however the result here confirms successful operation of the electrostatic stage with and without airblast.

3. Results and Discussion

3.1 Spray shape and spray cone angle

Qualitative images were taken using a DSLR camera having an exposure time 1/60s and exposure compensation of -3, to investigate the spray shape and spray cone angle for various applied potentials, jet velocities, and Weber numbers. Figure 3 shows the spray as a function of air velocity and charge level for a liquid jet velocity $U=12.9$ m/s. It is evident that at zero Weber number and zero applied voltage, namely 1A, a spray is not formed (dripping mode only). The gradual increase in air velocity leads to fragmentation of the liquid jet with fine droplets formed in a roughly conical shape, clearly visible in Figure 3 (1B and 1C). By implementing charge, starting from 2 to 4 in Figure 3, the spray quality increases substantially for both the Weber numbers tested. Application of charge not only helps to increase the dispersion of the spray but also generates a higher number of small droplets, that tend to concentrate around the periphery of the spray.

To examine the effect of charge more quantitatively, the spray cone angles are calculated using an in-house Matlab code which is a combination of a simple image post-processing code and width measurement code. Initially, the RGB image is converted into a grayscale image. Subsequent to this, based on the average light intensity, a threshold was applied to obtain a binary image. Finally, the spray width was calculated by finding out and applying a polynomial curve fitting on the nonzero elements for the left and right edges of the binary image. Figure 4 shows the effect of changing the applied voltage level on the spray cone angle. It is noticeable that the spray cone angle increases with increasing charge, and this happens regardless of the liquid jet velocities. The results show that the addition of charge is promising towards improving dispersion and downstream mixing even when significant aerodynamic forces are present. However, the use of charge in increasing spray cone angle is more effective in low Weber number cases, and therefore it is expected that the effect of charge diminishes at very high We numbers, though an increase in the liquid injection pressure or decrease in orifice size to increase the spray specific charge, could be implemented to avoid this issue.

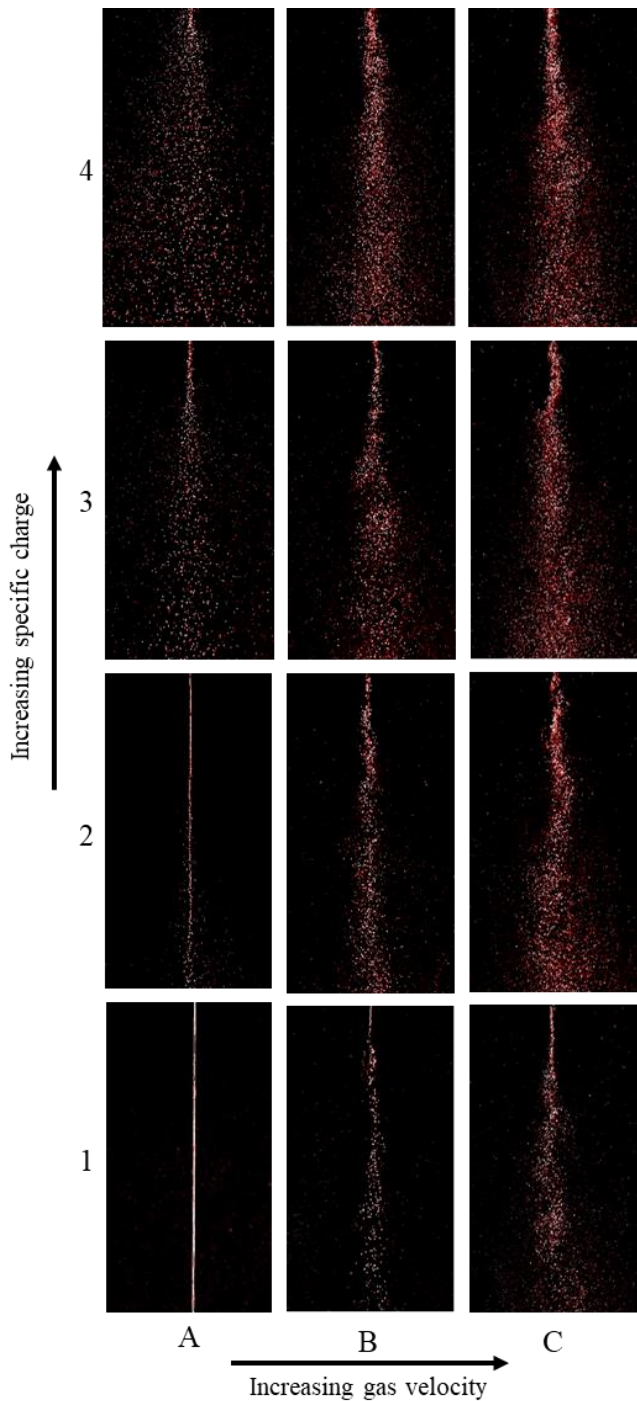
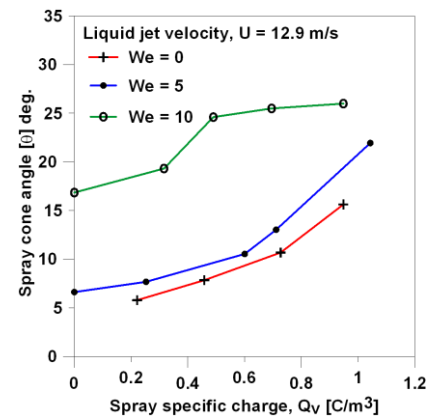


Figure 3: Global images of the spray in hybrid mode: from left to right $We=0,5,10$ and from bottom to top applied voltage= $0,-4,-5,-6$ KV. The liquid jet velocity was maintained as $U=12.9$ m/s.

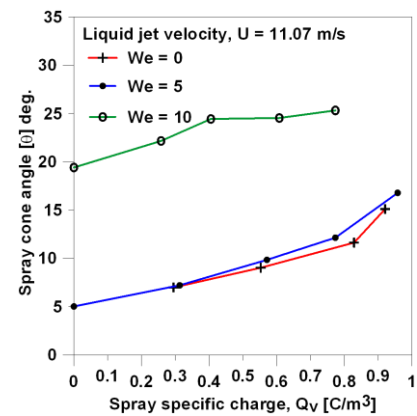
3.2 Flow field and droplet size characteristics

A commercial dual-component laser/phase Doppler anemometry system (TSI Model FSA 3500/4000) was used to measure droplet sizes and velocities. At each measurement point, 10000 samples were taken to ensure statistical convergence. Further operational and functional details along with uncertainties and errors related to this particular PDA system can be found in [16-17]. Measurements here are only presented for the case $U=12.9$

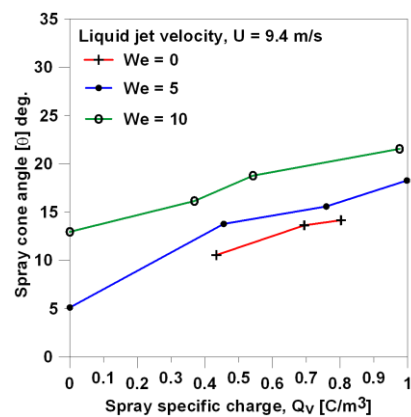
m/s and $V=7$ kV at approximately 30 mm downstream of the atomizer exit where the mean axial velocity is maximum, which is approximately in the centerline of the spray. Figure 5 shows the rms of velocity fluctuations for both axial (5A and 5B) and radial (5C and 5D) velocities at the centerline for five subranged data points. The Y-axis of Figure 5 shows rms of velocity fluctuations (axial on top row and radial on bottom row) normalized by rms fluctuations for droplets in the range of 0-10 μm , which is closely representative of gas phase [16]. The X-axis presents the mid-point of each sub-range group.



A



B



C

Figure 4: Spray cone angle plotted vs. the spray specific charge for a liquid jet velocity of 12.9, 11.07, and 9.4 m/s for three different exit Weber numbers

From Figure 5, it is visible particularly for $We=5$ that the employment of charge (right column of Fig. 5) seems to make all droplet size subranges less responsive to the gas phase. This could be indicative of the influence of the local electric field on altering the local dynamics of the droplets, though this requires further study to be fully understood. This effect seems to be more dominant with the radial fluctuating component (bottom row), and this would be in agreement with previous work which demonstrated that the

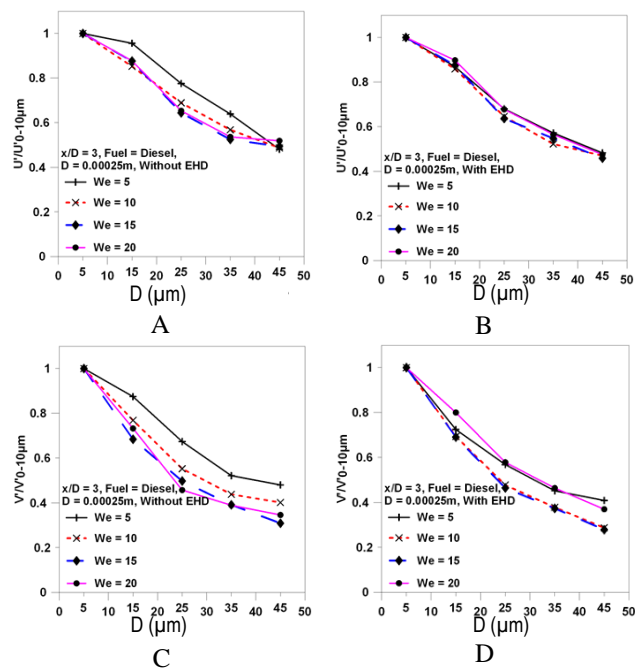


Figure 5: Local rms fluctuations of axial and radial velocities at the centerline normalized by the gas phase velocities plotted vs. the midpoint Diameter of five droplet size subranges: 0-10 μm , 10-20 μm , 20-30 μm , 30-40 μm , 40-50 μm .

radial electric field is at least an order of magnitude greater than that of the axial electric field generated by the charged droplets at the centerline [18]. The normalized rms values for both axial and radial velocities are also found more sensitive towards charge for low Weber number cases, which is also consistent with the global spray images presented.

4. Conclusions

This paper has presented a new burner geometry that enables the injection of unipolar charge into a dielectric liquid jet, which is simultaneously exposed to aerodynamic shear. Initial characterization has been presented here for Diesel, but the burner can also be operated with a range of other dielectric liquids including Kerosene and various Bio and Synthetic fuels. From the experimental results of the present study, by changing the applied voltage, the liquid jet velocity and Weber number the following conclusions are obtained.

- Under a “hybrid” (airblast + EHD) mode, the spray cone angle clearly increases by increasing specific charge over the range of studied Weber numbers and jet velocities. However, lower Weber number cases are found more sensitive to charge
- Measurements of the RMS of axial and radial components of the velocity fluctuations at the spray centerline demonstrate that EHD has the potential to effect local droplet dynamics even in the presence of a coaxial air flow.

Future work will focus on detailed measurements of the full droplet size and velocity distributions to characterize the atomizer as well as testing combustion characteristics in a piloted burner geometry.

5. Acknowledgments

The authors would like to acknowledge and thank Mr. Othman Jaber for his help during the experiment. This research is supported by the Australian Research Council.

6. References

- [1] J.S. Shrimpton, Charge Injection Systems, *Springers, Verlag Berlin Heidelberg*, 2009
- [2] J.S. Shrimpton and A.J. Yule (1998) *JASME Fluids Engineering*. **120**, pp. 580-585.
- [3] Robinson. Kelly S, Turnbull Robert J. and Kim Kyekyoon (1980) *IEEE Trans Ind Appl*. **2**, pp. 308-317.
- [4] J.S. Shrimpton and A.J. Yule (1999) *Experiments in Fluids*. **26**, pp. 460-469.
- [5] A.J. Yule, J.S. Shrimpton, A. Watkins, W. Balachandran, and D.Hu (1995) *Fuel*. **74**, pp. 1094-1103.
- [6] A.R.H. Rigit and J.S. Shrimpton, (2006) *Atomization and Sprays*. **16**, pp. 421-442.
- [7] J.S. Shrimpton and A. J. Yule (2001) *Atomization and Sprays*. **11**, pp. 365-396.
- [8] A.R.H. Rigit and J.S. Shrimpton, (2006) *Atomization and Sprays*. **16**, pp. 401-419.
- [9] J.S. Shrimpton (2005) *Ieee T Dielect*. **12(3)**, pp. 573-8.
- [10] Dimitrios C Kyritsis, Ismael Guerrero-Arias, Subir Roychoudhury, and Alessandro Gomez (2002) *Proceedings of the Combustion Institute*. **29**, pp. 965-972.
- [11] J.S. Shrimpton and Y. Laoonual (2006) *International journal for numerical methods in engineering*. **67(8)**, pp. 1063-1081.
- [12] J. Bellan and K. Harstad (1997) *Proceedings of ICLASS*.
- [13] T. Ahmed, A. Kourmatzis, P.X. Pham and A.R. Masri, (2018) *Fuel*. **231**, pp. 244-252.
- [14] A. Kourmatzis, J. Allen and J.S. Shrimpton, (2010) *Atomization and Sprays*. **20**, pp. 269-280.
- [15] Ghazi Malkawi, (2009) *Ph.D. Thesis, University of Illinois*.
- [16] A. Lowe, A. Kourmatzis and A.R. Masri, (2017) *Combustion and Flame*. **176**, pp. 511-520.
- [17] J.G. Gounder, A. Kourmatzis, and A.R. Masri, (2012) *Combust. Flame*. **159**, pp. 3372-3397.
- [18] J.S. Shrimpton, A. J. Yule, and A.P. Watkins (1996) *A3rd ECCOMAS Computational Fluid Dynamics Conference*, pp. 97-103.

Measurement of wave speeds at the liquid-air interface of an air-blast atomized biodiesel spray

A. Gutteridge, G. Singh, A. Kourmatzis*, A.R. Masri

School of Aerospace, Mechanical and Mechatronics Engineering, The University of Sydney, NSW, Australia

Abstract

The disintegration of a liquid jet into a spray by a fast gas stream is a process known as air-blast atomization and is widely used for many practical processes. The successive steps of atomization from the initial instabilities to the eventual formation of droplets remain the subject of debate. This paper demonstrates a quantitative approach in which jet instabilities can be measured from the use of two-dimensional high speed microscopic backlit imaging. It was determined through image processing that the liquid jet interface develops two stages of acceleration before jet-breakup. The accuracy of the image processing was verified and deemed suitable for calculating parameters such as the liquid jet wavelength, amplitude, and acceleration. These are useful parameters for the correlations of liquid jet breakup with downstream droplet/ligament statistics.

Keywords: Primary Atomization, Instabilities, Wave speed, Shadowgraph

1. Introduction

In atomizers, a liquid jet or sheet issues from a nozzle as a continuous body of fluid and then inter-facial instabilities, oscillations and perturbations start to develop between the gas and liquid streams. These instabilities can amplify in magnitude under favorable conditions and cause the liquid jet to disintegrate into ligaments. This process is commonly referred to as primary atomization [1].

The instabilities occurring on the surface of a liquid jet have been a subject of investigation for over a century. Earlier work utilized linear stability analysis [2] to determine key flow characteristics such as downstream droplet diameter and jet breakup length [3]. Unfortunately, these correlations are only applicable to idealized, symmetric flow conditions in which the breakup mechanisms are predominately determined by surface tension forces. In most practical applications of atomizers, these correlations are insufficient.

For the case of coaxial air blast atomizers in which the liquid jet is injected with a co-flowing annulus of air, there are several parameters that influence the atomization process [4]. As the liquid jet interface interacts with the gas phase, the combination of velocity and density gradients leads to the formation of instabilities at the liquid-gas interface. While the relative role of Kelvin-Helmholtz and Rayleigh-Taylor type instabilities is not clear, such instabilities grow and propagate as they advect downstream leading to jet disintegration. The ligaments which form from primary atomization would ultimately fragment and subsequently disperse to form a dilute spray, largely comprised of spherical droplets, downstream of the atomizer nozzle. This is one of the many modes of development for a liquid jet and is commonly seen in membrane-type breakup regimes of sprays [5].

In practice, it is often quite difficult to determine the mode of development of the liquid jet from an intact core to a polydispersed population of droplets and in most cases, it can be a combination of several types of instabilities which exist over a wide range of non-dimensional parameters. For example, the “flapping” instability [6] in which an atomizing liquid jet is destabilized over a large scale in comparison to

its nozzle diameter can be found in membrane, pulsating and super-pulsating breakup regimes [7,8]. Through previous experimental correlations [9] of various quantities such as liquid breakup length or wavelength sizes of instabilities, it is clear that a universal way of describing the primary atomization process for coaxial air blast atomizers requires further work.

This paper aims to provide measurements of the initial instabilities occurring in a biodiesel liquid jet subjected to a co-flowing high-speed airflow and to statistically determine the key characteristics of primary atomization at the near-field regime of this coaxial air blast atomizer.

2. Experimental apparatus

The coaxial air blast atomizer (SYNSBURN™) used to investigate the atomization process is illustrated in Figure 1. A 17-gauge needle (ID = 1.067 mm, OD = 1.473 mm) ejects liquid coaxially with an air blast tube (ID = 10mm) illustrated with the red and blue arrows respectively. This burner is centered within a 180 x 180 mm wind tunnel providing a homogenous wind speed of 5 m/s [11]. The fluid employed here is biodiesel which consists of a short carbon chain length saturated fatty acid ester [10] and is referred to hereon as B1. The mass flow rate of the air blast and the liquid loading of biodiesel can be changed to develop a wide range of non-dimensional parameters. The two-dimensional high speed macroscopic backlit imaging is set up as illustrated in Figure 2.

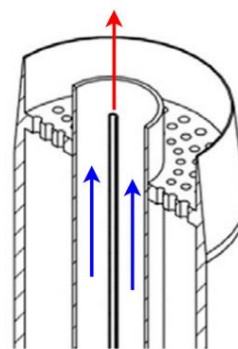


Figure 1: Diagram of atomizer (modified from [11]).

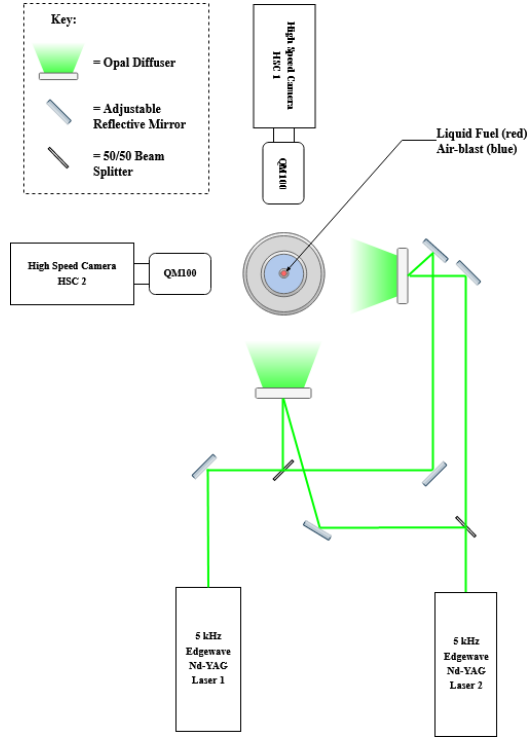


Figure 2: Top view illustration of the imaging system. Two 5 kHz lasers are split and directed to the center of two opal diffusers utilizing reflective mirrors. The diffused light provides illumination for the high speed cameras.

The imaging system consists of two 5 kHz 532nm Edgewave Nd-YAG lasers which are diffused through a series of opal glass diffusing optics that provide the illumination for a specified region in the spray. The spray characteristics are captured by two high-speed LaVision HSS6 cameras which are coupled with long-distance QM100 microscopes to provide a 3.56 mm x 3.56 mm image with a 768 x 768-pixel resolution (4.6 $\mu\text{m}/\text{pixel}$). A LaVision high-speed controller with DaVis imaging software enables 4 images to be captured. The four images consist of two angles (high-speed cameras 1 and 2, referred to hereon as HSC1 and HSC2) at two different periods, Δt , which ranges from 5 μs to 30 μs depending on the speed of the flow. For each axial location, 2000 images are recorded for each frame.

2.1 Parametric analysis

To investigate the jet instabilities developing downstream, a set of inlet parameters were chosen such that the jet breakup length would be several axial locations downstream from the nozzle exit. These parameters, as well as the associated fluid properties, are listed in Table 1.

Table 1: Flow parameters.

Property	Value
B1 Liquid Density, ρ_L (kg/m ³)	877
Air Density, ρ_G (kg/m ³)	1.2047
B1 Viscosity, μ_L (Ns/m ²)	$1.99 \cdot 10^{-3}$
Air Viscosity, μ_G (Ns/m ²)	$1.8205 \cdot 10^{-5}$
Surface Tension, σ (N/m)	0.025
Liquid Jet Exit Velocity, U_L (m/s)	0.96
Air-blast Exit Velocity, U_G (m/s)	28.85

To categorize what is occurring at the near field break up and atomization of the biodiesel, several non-dimensional parameters can be calculated. The key non-dimensional numbers [9,12] are given as:

$$Re_G = \frac{\rho_G U_G d_G}{\mu_G}, \quad Re_L = \frac{\rho_L U_L d_L}{\mu_L},$$

$$M = \frac{\rho_G U_G^2}{\rho_L U_L^2}, \quad m = \frac{\dot{m}_L}{\dot{m}_G}$$

$$We_R = \frac{\rho_G (U_G - U_L)^2 d_L}{\sigma}$$

Firstly, we have the liquid and gaseous Reynolds number, and as Table 2 illustrates the co-flowing air is a turbulent jet whereas the liquid jet is laminar. As a result, the instabilities occurring on the laminar jet are largely due to a large slip velocity between the fluid and the gas causing a shear force acting on the gas boundary layer. In addition, there is the momentum flux ratio (M) which has been shown to provide strong correlations with the break-up length of the liquid core, with a lower M generally indicating longer breakup lengths [13]. The mass flux (m) provides similar insight. Lastly, there is the aerodynamic Weber number (We_R), which is the ratio of the aerodynamic forces respective to the stabilizing surface forces acting on the liquid surface.

Table 2: Non-dimensional calculations.

Non-dimensional parameter	Value
Re_G	2812
Re_L	450
M	1.25
m	0.2
We_R	40

3. Results

3.1 Qualitative observations of near-field primary atomization

The flow conditions described in §2.1 were captured utilizing the two high-speed cameras and are depicted in Figure 3. Each frame represents one axial location which has been normalized by the co-flowing ID of 10mm (x/D). It is clear by observation of the fluid flow that there are several complex mechanisms occurring during the breakup of the liquid jet. Firstly, the jet develops helical waves at the surface which propagate downstream in both speed, and amplitude. As these waves reach a critical size, sheet thinning occurs (approximately at $x/D=0.7$) in which the jet is stretched into thin liquid sheets and ultimately results in membrane-like breakup [9]. The length of the liquid jet at that breakup location fluctuates and can significantly vary in location due to the chaotic nature of the process. As the jet breaks due to primary atomization, secondary atomization occurs in which additional break-up [14] creates large ligaments and droplets which develop interfacial instabilities (see highlighted circle in Figure 3). Ultimately, the ligaments and larger liquid objects will deform into spherical droplets further downstream, where spherical droplets can be identified by $x/D=2.0$.

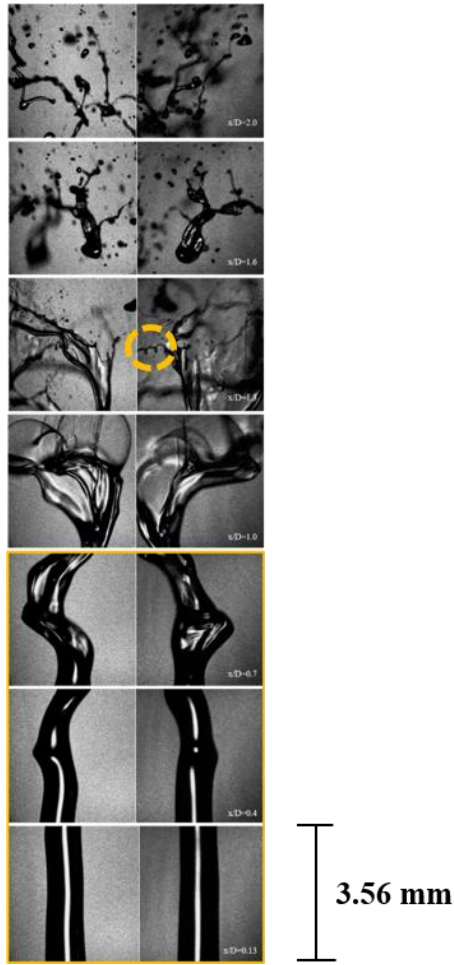


Figure 3: Instantaneous flow visualization of HSC1 (left) and HSC2 (right) of the jet breakup. The images are of different axial locations and are selected individually from different runs of the experiment.

3.2 Quantitative near field jet breakup characteristics

Data from the high-speed camera pairs are obtained through in-house image processing code written in Matlab. Firstly, the background noise of the camera is reduced by a low-pass Gaussian filter and the image is binarized utilizing a predetermined background threshold. Previous work [15,16] has demonstrated the suitability of binarization towards analysis of fragment statistics both for spherical and non-spherical objects. Here, the primary focus is on the region highlighted in the yellow box in Figure 3 in which there is a single intact jet as the focus is on wave instability analysis. As the frame reaches $x/D=1.0$, the binarization process does not lend itself to calculate the wavelength and wave speed, given that the identification of a liquid-air interface becomes increasingly difficult due to the membrane-like nature of the jet.

Once correctly binarized, the liquid jet boundary is extracted from each image. This is achieved by tracing the region boundaries of the liquid jet utilizing the bwboundaries function in MATLAB. From the jet boundary, the peaks of the waves can be identified and tracked through the time difference of laser 1 and 2 set by the high-speed controller.

Figure 4 illustrates the process. The solid wave represents the crest (circle) and boundary of a wave as it propagates downstream captured at $200\mu s$. After $5-30\mu s$ (set by the high speed controller) a second image is captured shown as the dashed boundary in Figure 4. The axial and radial location of the peak can then be recorded which provides sufficient data to determine velocity and acceleration. This is repeated for 2000 images for both high-speed cameras at a set axial location. The wave speed was measured at $x/D=0.7$ for both HSC1 and HSC2. Figure 5 illustrates that the overall average wave characteristics as indicated in the probability density function are very similar as measured from the two cameras. HSC1 peaks at a normalized wave speed of $U_z = 1.93m/s$ and respectively for HSC2 $U_z = 1.73m/s$, which is within the expected margin of error [15,16]. Measurements from both angles have a similar positive skewed distribution of velocity. This indicates that while average wave parameters such as velocity or acceleration are not dependent on the view angle of the spray, parameters such as instability wavelengths could benefit from multiple angle imaging systems.

Superimposed wave boundaries of one frame

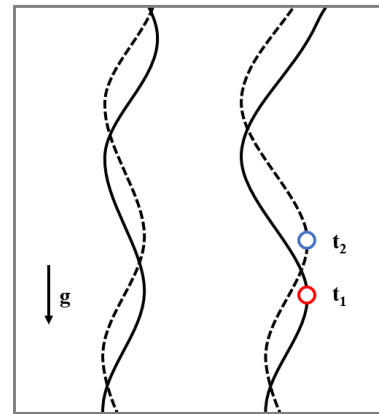


Figure 4: Liquid jet boundary development and tracking of wave crest location. The solid boundary represents the wave captured at 5 kHz and the dashed boundary is the same wave 5-30 microseconds after (adjusted by highspeed controller).

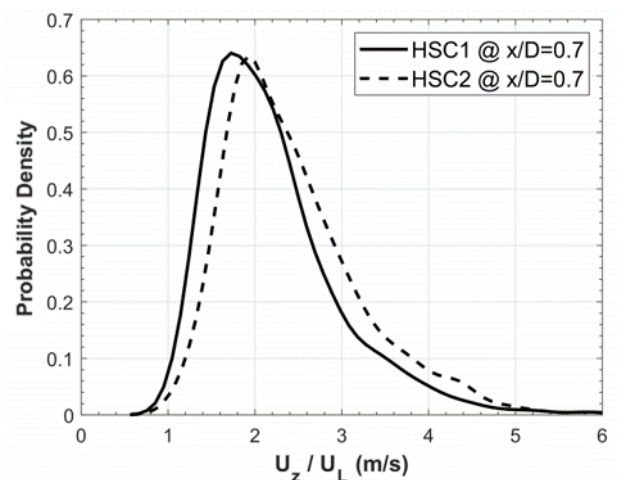


Figure 5: Probability density function of normalized wave crest velocity at $x/D=0.7$ for both high-speed cameras.

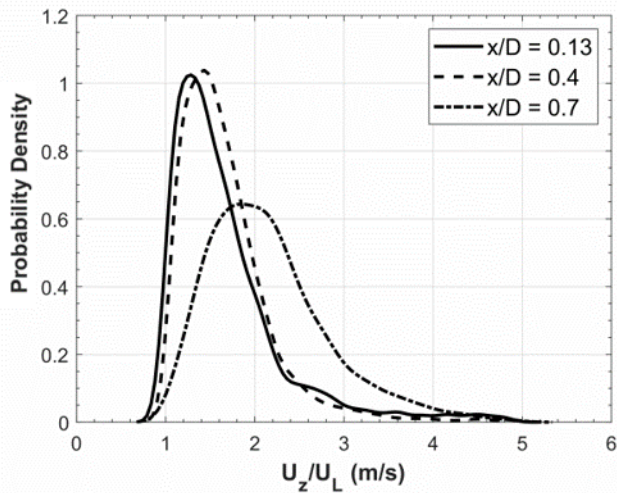


Figure 6: Probability density function of normalized wave crest velocity through primary atomization.

To determine the wave speed and comment on how it develops downstream, a similar process is used for three axial locations; $x/D = 0.13, 0.4$ and 0.7 respectively. At each location, the wave speeds were calculated for both HSC 1 and HSC 2. Figure 6 demonstrates that as the wave is progressively perturbed by the instability forming on the surface, the wave crest increases in speed. From the figure, it is clear that each location has a dominant wave speed denoted by the peak of the pdf. This peak corresponds to a normalized value of $U_z = 1.28 \text{ m/s}$, $U_z = 1.43 \text{ m/s}$ and $U_z = 1.85 \text{ m/s}$ from the first to last axial location respectively. Furthermore, the first two axial location distributions are positively skewed following a similar shape with a slight increase in normalized velocity. This illustrates that as the liquid jet exits the needle, the velocities of the waves accelerate due to the surrounding gas flow over what seems to be a narrower range that is likely less influenced by aerodynamic forces. However, once the wave crests begin to experience higher aerodynamic drag forces from the surrounding air-flow due to their change in wavelength and amplitude, they can accelerate further, and result in a broader distribution of wave speeds. This is indicated in Figure 6 at $x/D = 0.7$ where the probability density function shifts into a broader shape with a much larger characteristic peak velocity in comparison to the previous axial locations.

An analysis of the wave speed just before jet breakup was also manually conducted in which peaks were traced frame by frame to ensure the validity of the results at each axial location. It was determined that the average wave speed at approximately $x/D = 0.7$ was $U_z = 1.89 \text{ m/s}$ with a standard error of the mean as 0.01 m/s which is consistent with the characteristic peak value of the pdf at that location. Therefore, the method used in calculating wave speed can provide reasonably accurate results for the liquid jet in coaxial atomizers.

4. Conclusions

This paper provides an experimental method capable of capturing the primary atomization process for an air-blast atomizer. It utilizes two high-speed cameras coupled with long-distance microscopes to provide high-resolution data of the near field regime of the atomizer. This data can be correctly processed and analyzed to obtain accurate and statistical data of key characteristics of the liquid jet such as the wave speed and acceleration.

To the best of the authors' knowledge, this is one of very few contributions to provide quantitative statistics of wave crest speeds in the primary atomization region of a spray. The liquid jet undergoes a transition in wave speed before it becomes unstable and breaks up into ligaments and droplets. Future work will include investigation over a wider non-dimensional space.

5. References

- [1] Lefebvre, A. H., & McDonell, V. G. (2017). *Atomization and sprays*. CRC press.
- [2] Chandrasekhar, S. (2013). Hydrodynamic and Hydro-magnetic stability. *Courier Corporation*.
- [3] Rayleigh, L. (1878). On the instability of jets. *Proceedings of the London mathematical society*, 1(1), 4-13.
- [4] Marmottant, P., & Villermaux, E. (2004). On spray formation. *Journal of fluid mechanics*, 498, 73-111.
- [5] Chigier, N., & Farago, Z. (1992). Morphological classification of disintegration of round liquid jets in a coaxial air stream. *Atomization and Sprays*, 2(2).
- [6] Matas, J. P., & Cartellier, A. (2013). Flapping instability of a liquid jet. *Comptes Rendus Mécanique*, 341(1-2), 35-43.
- [7] Charalampous, G., Hadjiyiannis, C., & Hardalupas, Y. (2019). Proper orthogonal decomposition of primary breakup and spray in co-axial airblast atomizers. *Physics of Fluids*, 31(4), 043304.
- [8] Leroux, B., Delabroy, O., & Lacas, F. (2007). Experimental study of coaxial atomizers scaling. Part I: dense core zone. *Atomization and Sprays*, 17(5).
- [9] Dumouchel, C. (2008). On the experimental investigation on primary atomization of liquid streams. *Experiments in fluids*, 45(3), 371-422.
- [10] Kourmatzis, A., Pham, P. X., & Masri, A. R. (2013). Air assisted atomization and spray density characterization of ethanol and a range of biodiesels. *Fuel*, 108, 758-770.
- [11] Lowe, A., Kourmatzis, A., & Masri, A. R. (2017). Turbulent spray flames of intermediate density: Stability and near-field structure. *Combustion and Flame*, 176, 511-520.
- [12] Lasheras, J. C., Villermaux, E., & Hopfinger, E. J. (1998). Break-up and atomization of a round water jet by a high-speed annular air jet. *Journal of Fluid Mechanics*, 357, 351-379.
- [13] Villermaux, E., Rehab, H., & Hopfinger, E. J. (1994). Breakup regimes and self-sustained pulsations in coaxial jets. *Meccanica*, 29(4), 393-401.
- [14] Guildenbecher, D. R., López-Rivera, C., & Sojka, P. E. (2009). Secondary atomization. *Experiments in Fluids*, 46(3), 371.
- [15] Kourmatzis, A., Pham, P. X., & Masri, A. R. (2015). Characterization of atomization and combustion in moderately dense turbulent spray flames. *Combustion and Flame*, 162(4), 978-996.
- [16] Pham, P. X., Kourmatzis, A., & Masri, A. R. (2017). Simultaneous volume-velocity measurements in the near field of atomizing sprays. *Measurement Science and Technology*, 28(11), 115203.

Comparison of real-time NO_x emission measurements from two heavy-duty diesel engines

G M Hasan Shahariar^{1,2}, Thuy Chu-Van^{1,2}, Timothy A. Bodisco³, Mojibul Sajjad^{1,2}, Kabir Adewale Suara^{1,2}, Zoran Ristovski^{1,2} and Richard J. Brown^{1,2*}

¹ Biofuel Engine Research Facility, QUT, Brisbane, QLD 4000, Australia

² International Laboratory for Air Quality and Health, QUT, Brisbane, QLD 4000, Australia

³ School of Engineering, Deakin University, 75 Pigdons Rd, Geelong, Victoria 3216, Australia

Abstract

This study investigated the real-time NO_x emissions from a heavy-duty diesel truck and a bulk carrier ship. The test road vehicle was driven on a combination of a flat and hilly route from Brisbane to Toowoomba that covered urban, rural and motorway driving. On-board ship emissions were measured on the sea from the port of Gladstone to Newcastle. NO_x emissions from both engines were compared and analysed to understand the influence of engine parameters as well as route variables and power transmission on NO_x emissions. Results from these measurements show that truck NO_x emissions increased with the engine power and speed however a significant NO_x emission can be seen during the idling condition while producing low power. On the other hand, ship NO_x emissions followed an approximate cubic relationship as a function of engine RPM that is completely different from that of the truck.

Keywords: On-road emissions, On-board ship emissions, NO_x emissions, Air pollution.

1. Introduction

Diesel engines are widely used in on-road and marine transportation for their outstanding power generation, fuel economy, durability and high thermal efficiency [1]. Combustion of fossil fuels causes a significant amount of gaseous and particle emissions that contribute to global greenhouse emissions, air pollution, and human health risks [2], [3]. NO_x emissions contribute to smog formation, can cause various respiratory problems, heart disease, and exacerbation of asthma. Road vehicle and marine transport are historically major sources of air pollution in urban and coastal areas. Improving air quality is a primary concern for most of the countries.

The International Maritime Organization (IMO) has implemented regulations to control the shipping emissions and US Environmental Protection Agency (EPA) and the European Union are implementing regulations to control the pollutants from diesel engine emissions. In European emission standards, the emission characteristics of vehicles are performed through laboratory tests. The test is performed using a chassis-dynamometer and the vehicle is driven through a predefined test-cycle (New European Driving Cycle, NEDC). During the test cycle, the vehicle is run at different operating conditions and the exhaust emissions are sampled using different gas analysers to measure the pollutants in the exhaust stream [4], [5]. On-road vehicle driving is categorised as steady-state and transient cycles. The steady-state cycle can evaluate the vehicle engine performance and emission behavior at a specific range of operating conditions with a minimum engine speed time profile variation. Laboratory tests allow a wide range of operating conditions and repeatability. On the other hand, the transient cycle with varying speed is often carried out to obtain emission data from on-road driving [5], [6]. Some transient cycles like the worldwide harmonised light vehicles test cycle (WLTC) may be the representations of on-road measurements, however,

vehicles vary depend on types, uses, and so many other factors, also one single cycle may not represent the real road driving emissions [7]. Vehicle driving parameters such as speed, acceleration, deceleration, stopping and gear shifting are important factors for emission measurements [8]. In this case, real driving emission testing can provide more realistic data than engine test bench or chassis-dynamometer [9], [10]. Moreover, in some cases, real driving emission testing found much higher values than that of the test bench. Based on the real driving measurements on 541 diesel cars, Euro 6 vehicles emissions were on average 4.5 times higher than Euro 6 limit and Euro 5 vehicles were 4.1 times higher than the limit [11], [12]. The engine emissions are influenced by both engine internal factors such as engine operating conditions, driving parameters, exhaust after-treatment systems and external factors including ambient air and temperature. These factors cannot be completely achieved in a test bench setup. In the case of ship emissions, three major measurements methods are available, known as onboard measurements, test-bed measurements and ship plume-based measurements [13]. Testbed measurements investigate the exhaust emissions at a wide range of engine load conditions and a variety of fuel types can be used [14]. This allows a detailed understanding of emission characteristics at a wide operating range. On the other hand, ship plume-based measurements may provide insights about the emission characteristics from ship plume [15], it is not convenient due to the uncertainties and high cost. Therefore, onboard ship emission measurements are necessary for the complete investigation of realistic emission factor [13], [16]. There are very few on-board measurements which have been performed and more investigations are necessary to improve the data quality and emission factors. The major emission source for the ship is the main engines (MEs) which are used for the ship propulsion. Most of the main engines are slow speed, two-stroke marine diesel engines, using heavy fuel oil (HFO) and having a maximum

operating speed up to 300 rpm. On the other hand, the smaller auxiliary engines (AEs) are used to generate electricity especially when the ships are stationary and at berth in ports near to the locality. Therefore, emissions from auxiliary engines significantly contribute to residential areas of air pollution. Auxiliary engines are generally medium or high-speed marine diesel engines (engine speeds 500-2500 rpm) with an estimated power output 30-3000 kW [17]. In road-transport application, diesel engines are classified as light duty (power range 52.2 to 126.8 kW), medium duty (power range 126.8 to 186.4 kW) and heavy-duty (power range greater than 186.4 kW). The gross vehicle weight rating (GVWR) is, for light duty (less than 14541 kg), medium duty (14541 kg to 24608 kg) and heavy-duty (more than 24608 kg). Heavy-duty diesel vehicles tend to operate in both urban and localized areas are responsible for ambient air pollution. Moreover, shipping-related emissions are contributing to air pollution especially in coastal areas and cities. According to the study of Eyring et al., more than 70% of ship emissions have been found up to 400 km inland [18]. Therefore, a combined study is required for both types of engines to understand the emission behavior and influencing factors. The findings will contribute to updating the existing policy by considering both emission sources to maintain air quality.

The aim of the current study is to investigate the engine performance and NO_x emissions from a large bulk career ship through on-board measurement and a heavy-duty truck equipped with NO_x after-treatment system through real driving emission measurements to get insights on emission behaviour relying on engine types and applications.

2. Experimental method and setup

2.1 On-board ship emission measurements

The measurements were conducted on October and November 2015 in a bulk carrier ship on the voyage from port Gladstone to Newcastle. HFO was used as the fuel and the fuel properties were obtained from the bunker delivery receipt and laboratory analysis [13]. The specifications of the ship and engine are given in table 1. Two sampling points were created in the exhaust line after the turbocharger of the main engine. The position of the sampling points was approximately 0.2 m downstream from the turbocharger. The measuring instruments were installed on a deck in the machinery room. The first sampling point was for particle measurements, where raw hot exhaust flow was directed through a dilution system. The second sampling port was used for the gaseous exhaust measurement. The concentration of the gases including nitrogen oxides (NO_x) in the raw exhaust gas was measured using a Testo 350 XL portable emission analyser through a dilution system. The length of the exhaust sampling line was around 1.2 m and the exhaust flow rate was around 0.98-1.2 standard liter per minute (SLPM). Engine performance data such as engine power, fuel consumption, engine revolution, and exhaust gas temperature were measured by ship instrumentation. The schematic of exhaust sampling line is given in figure 1.

Table 1: The specifications of the ship and the engine.

Owner of the ship	CSL Australia
Build year	2002
Engine type	2-stroke, single acting, cross head, marine diesel engine
Output and revolution	6880 kw and 102 rpm
Number of cylinders and bore x stroke	6 and 500 x 1910 mm

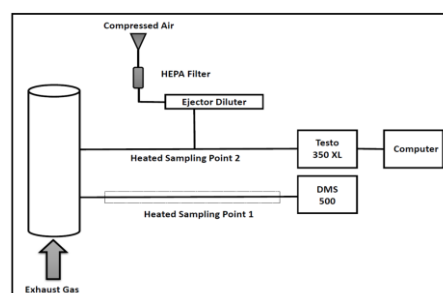


Figure 1: The schematic of the ship exhaust sampling line.

2.2 Real-time truck emission measurements

The experimental investigation was conducted on a K200 Kenworth Truck equipped with an SCR NO_x after-treatment system. The truck was driven from Brisbane to Toowoomba both in the flat and hilly route that covered city, motorway and rural route to perform the measurements. The specifications of the test vehicle and engine are given in table 2. The gaseous emissions were measured using an ECM miniPEMS system that contains NO_x, O₂, exhaust temperature, exhaust pressure sensors, OBDII and GPS. The measured data was stored to an SD card. The sensor used for the NO_x measurement was a ceramic exhaust sensor manufactured by ECM (Engine Control and Monitoring). The precision of the sensor from the manufacturer specification is ± 5 ppm (0-200 ppm), ± 20 ppm (200-1000 ppm) and ± 2.0 % (>1000 ppm). Two NO_x sensors were connected to the exhaust pipe before and after the SCR catalyst to measure the NO_x concentration in both conditions. A pressure sensor and a temperature were also connected to the exhaust pipe to obtain the exhaust pressure and temperature data. The PEMS also connected with the truck's ECU to record the engine performance data and vehicle parameters. The schematic of the exhaust line is given in figure 2.

Table 2: The specifications of the test vehicle and engine.

Test vehicle model	K200 Kenworth
Engine	Cummins ISXe5
Engine type	4-cycle, in-line, 6 cylinder, Turbocharged/charge air cooled
Compression Ratio	17.2:1
Cylinder bore and stroke	137 x 169 mm

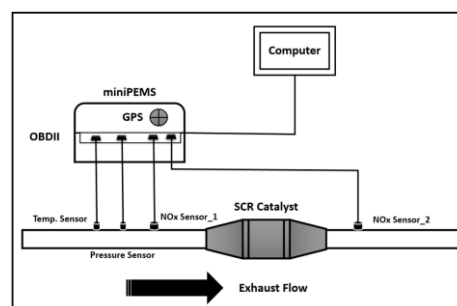


Figure 2: The schematic of the truck exhaust line.

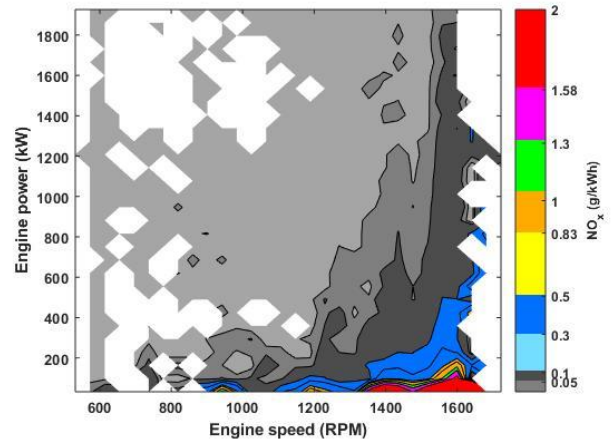
3. Results and discussion

The NO_x emissions obtained from the real-time measurement from two different types of the heavy-duty diesel engine are presented below. The truck trip covered city road, motorway, rural road; also, there was a variation in altitude (maximum height 700 m and minimum height 56 m). There was a frequent shifting of the driving parameters such as gear engagement, acceleration, deceleration, hard acceleration, cruising due to traffic condition. All these parameters have meaningful influences on vehicle performance and emissions. On the other hand, marine engine operation is comparatively stable compared to road vehicle engine.

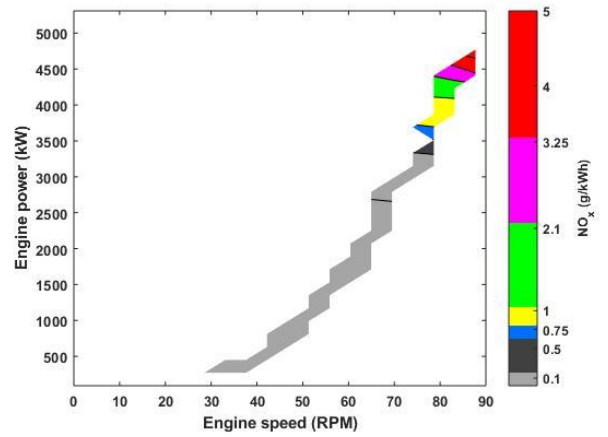
Figure 3(a) and (b) show the NO_x emissions before and after the SCR catalyst. Variation in color represents the change in NO_x quantities and white region indicates no data points. NO_x emission is high at relatively higher engine speed and low power. However, at idling condition while the engine is producing less power NO_x emission is highest. The catalyst NO_x conversion is better at all conditions excepts the idling condition. There is still high NO_x there that can be seen in figure 3(b). NO_x emission after the SCR at idling condition are limited due to low exhaust temperature. NO_x emission strongly influenced by combustion temperature, which in the case of ship the engine power correlates strongly with exhaust temperature and hence NO_x emissions (figure 3(c)). Ship NO_x data follows an approximate cubic curve related to the specialized ship application where the engine is directly mechanically coupled to the propeller with no gear box. This result is speed power relationship of form $Power \propto RPM^3$ due to the thrust co-efficient characteristics of a propeller. This is significantly in contrast to NO_x characteristics in the pre-catalyst measurements from the truck which has a gear box ((figure 3(a)).

NO_x emission with respect to engine speed rate (RPM/s) that is calculated by the equation $(\Delta RPM/\Delta t)$ is shown in figure 4 (a),(b),(c). The variation of engine speed is much higher in the truck engine than marine engine due to the wide range of driving dynamics and route variables. One thing is common in both engines that high NO_x emission can be seen at stable conditions. Truck engine repeatedly switches gears for the acceleration, deceleration, stopping due to the traffic conditions and route variables. Ship engine speed is almost stable during the whole course and NO_x emissions increases with the engine power.

(a)

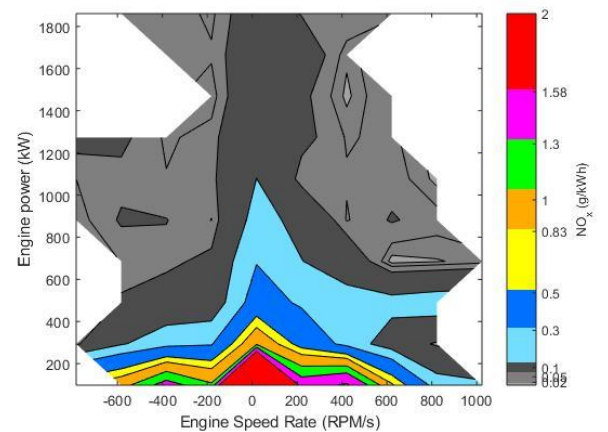
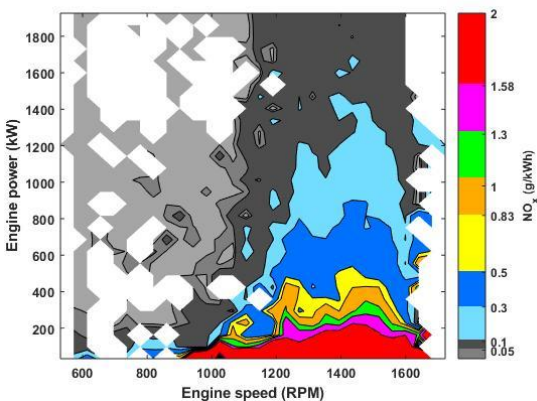


(b)

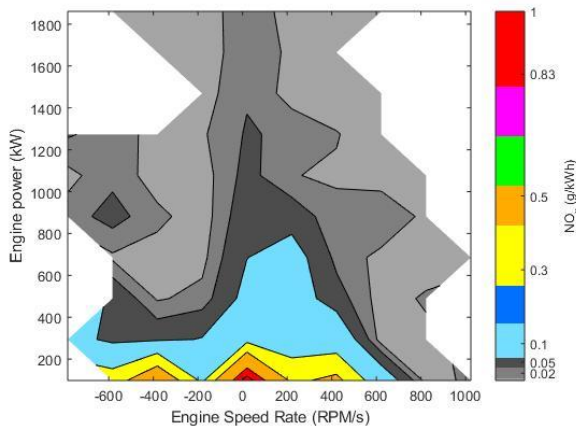


(c)

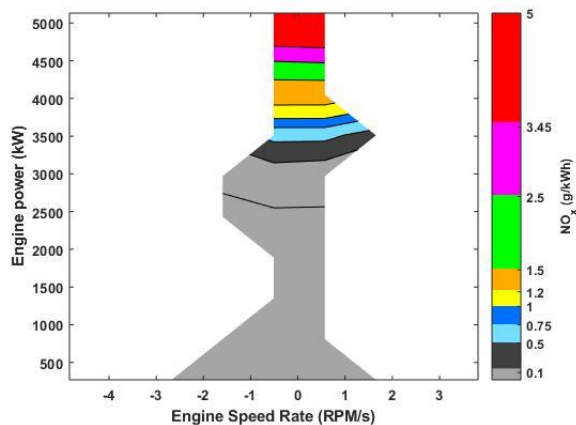
Figure 3: NO_x emission with engine speed and power (a) truck engine before SCR catalyst, (b) truck engine after SCR catalyst, (c) ship engine.



(a)



(b)



(c)

Figure 4: NO_x emission with engine speed rate (rpm/s) and power (a) truck engine before SCR catalyst, (b) truck engine after SCR catalyst, (c) ship engine.

4. Conclusion

The current study presents the real-time NO_x emission measurements of a modern heavy-duty truck and a bulk carrier ship. The truck covered urban, rural and motorway driving on both flat and hilly route and ship emission measured during the voyage on the sea. The study has shown that there is a significant difference between the NO_x emission behavior of the on-road and seagoing vehicle. The measurements also showed that on-road NO_x emissions is significantly high at idling condition. However, ship NO_x follows an approximate cubic relationship.

5. Acknowledgments

The authors gratefully acknowledge the support of Mr Wally Walker and Mr Aaron from Tytec Logistics Pty Ltd and Mr Trevor Bayley from Green Distillation Technologies for Truck emissions measurements. The ship emissions measurements has been conduct through the

support of the International Association of Maritime Universities (IAMU) and the Nippon Foundation in Japan.

6. References

- [1] R. Lee, J. Pedley, and C. Hobbs, "Fuel quality impact on heavy duty diesel emissions:-a literature review," *SAE Trans.*, pp. 1952–1970, 1998.
- [2] M. Viana *et al.*, "Impact of maritime transport emissions on coastal air quality in Europe," *Atmos. Environ.*, vol. 90, pp. 96–105, 2014.
- [3] X. Querol *et al.*, "Speciation and origin of PM10 and PM2. 5 in selected European cities," *Atmos. Environ.*, vol. 38, no. 38, pp. 6547–6555, 2004.
- [4] L. Pelkmans and P. Debal, "Comparison of on-road emissions with emissions measured on chassis dynamometer test cycles," *Transp. Res. Part D Transp. Environ.*, vol. 11, no. 4, pp. 233–241, 2006.
- [5] S. Prakash and T. A. Bodisco, "An investigation into the effect of road gradient and driving style on NO_x emissions from a diesel vehicle driven on urban roads," *Transp. Res. Part D Transp. Environ.*, vol. 72, pp. 220–231, 2019.
- [6] T. J. BARLOW, S. Latham, I. S. McCrae, and P. G. Boulter, "A reference book of driving cycles for use in the measurement of road vehicle emissions," *TRL Publ. Proj. Rep.*, 2009.
- [7] E. G. Giakoumis and A. T. Zachiotis, "Comparative evaluation of eight legislated driving schedules in terms of cycle metrics and emissions from a diesel-powered turbocharged van," *Transp. Res. Part D Transp. Environ.*, vol. 58, pp. 139–154, 2018.
- [8] M. André, R. Joumard, R. Vidon, P. Tassel, and P. Perret, "Real-world European driving cycles, for measuring pollutant emissions from high- and low-powered cars," *Atmos. Environ.*, vol. 40, no. 31, pp. 5944–5953, 2006.
- [9] V. Franco, M. Kousoulidou, M. Muntean, L. Ntziachristos, S. Hausberger, and P. Dilara, "Road vehicle emission factors development: A review," *Atmos. Environ.*, vol. 70, pp. 84–97, 2013.
- [10] T. A. Bodisco, S. M. A. Rahman, F. M. Hossain, and R. J. Brown, "On-road NO_x emissions of a modern commercial light-duty diesel vehicle using a blend of tyre oil and diesel," *Energy Reports*, vol. 5, pp. 349–356, 2019.
- [11] C. Baldino, U. Tietge, R. Muncrief, Y. Bernard, and P. Mock, "Road Tested: Comparative Overview of Real-World Versus Type-Approval NO_x and CO₂ Emissions from Diesel Cars in Europe," 2017.
- [12] B. Giechaskiel *et al.*, "Evaluation of NO_x emissions of a retrofitted Euro 5 passenger car for the Horizon prize 'Engine retrofit,'" *Environ. Res.*, vol. 166, pp. 298–309, 2018.
- [13] T. Chu-Van *et al.*, "On-board measurements of particle and gaseous emissions from a large cargo vessel at different operating conditions," *Environ. Pollut.*, vol. 237, pp. 832–841, 2018.
- [14] M. Anderson, K. Salo, Å. M. Hallquist, and E. Fridell, "Characterization of particles from a marine engine operating at low loads," *Atmos. Environ.*, 2015.
- [15] J. M. B. Loov *et al.*, "Field test of available methods to measure remotely SO_x and NO_x emissions from ships," *Atmos. Meas. Tech.*, vol. 7, no. 8, pp. 2597–2613, 2014.
- [16] H. Agrawal, Q. G. J. Malloy, W. A. Welch, J. W. Miller, and D. R. Cocker III, "In-use gaseous and particulate matter emissions from a modern ocean going container vessel," *Atmos. Environ.*, vol. 42, no. 21, pp. 5504–5510, 2008.
- [17] D. A. Cooper, "Exhaust emissions from ships at berth," *Atmos. Environ.*, 2003.
- [18] V. Eyring *et al.*, "Transport impacts on atmosphere and climate: Shipping," *Atmos. Environ.*, vol. 44, no. 37, pp. 4735–4771, 2010.

A Parametric Study on Fluidisation Characteristics and Product Yields in Bubbling Fluidised Bed Reactor

Joshua Clissold¹, Salman Jalalifar^{1,2}, Fatemeh Salehi^{1,*}, Rouzbeh Abbassi¹

¹ School of Engineering, Faculty of Science and Engineering, Macquarie University, Sydney, NSW, Australia

² Australian Maritime College, College of Sciences and Engineering, University of Tasmania, Launceston, Tasmania, Australia

Abstract

Fluidisation of sand particles and consequently their mixing with biomass particles have significant effects on bio-oil production in bubbling fluidised bed reactors (BFBR). Minimum fluidisation velocity (MFV) which is a function of particle size, is an important factor that shows the lower limit for the velocity of fluidising media in BFBR. The fluidising media is an inert gas (usually nitrogen) that carries vapour products towards the reactor outlet. Increasing the carrier gas velocity shortens the residence time and hence the secondary reactions are minimised. This maximises the production of bio-oil as a favourable product. However, increasing the nitrogen velocity is only favourable up to a certain limit, called the maximum effective velocity (MEV). If the nitrogen velocity exceeds MEV, the sand and unreacted biomass particles are thrown out of the reactor that negatively affects the bio-oil production. This study performs computational fluid dynamic (CFD) simulations for biomass fast pyrolysis process in a 2-D standard lab-scale BFBR to analyse how MEV varies as the sand particle size increases. The model is first validated by the experimental data. Then, a parametric study is conducted for the carrier gas velocities in a range of 0.3-1.1 m/s for different particle sizes, i.e. a range of 0.4-1 mm for sand particles and a range of 0.2-0.5 mm for biomass particles. The model shows the MEV changes as the particle size increases although its trend significantly differs from the MFV.

Keywords: CFD, Biomass, Bubbling fluidised Bed, Fast pyrolysis, Bio-oil.

1. Introduction

The extraction and use of fossil fuels have drastic consequences for the planet. Climate change is arguably one of humanity's biggest issues today and causes negative effects all over the Earth. There is also a limited supply of fossil fuels that cannot be replenished, once it has been extinguished. The estimated depletion time for oil is approximately 35 years, and for coal, it's 107 years [1, 2]. These reasons alone show the drastic changes towards more sustainable fuels for the future. Manufacturing and usage of bio-oil is an alternative process for replacing fossil fuels, particularly crude oil. However, biomass-derived fuel systems are still expensive and hence optimising the existing systems is essential to further maximise the economic and environmental benefits of bio-oil production. Any form of organic matters available on Earth can be classified as biomass. This includes wood, agricultural products (as well as their waste by-products), aquatic plants and algae, both terrestrial and aquatic animals, and human waste [4, 5]. Organic matters also benefit from their carbon neutrality since the carbon dioxide used to grow organic matters in the photosynthesis process, is released back into the atmosphere as they are burned. This is known as the carbon cycle. In contrast to fossil fuels, the energy provided using organic matters does not add or take away carbon from the cycle [5, 6].

Pyrolysis is one of the main thermochemical processes that convert biomass to bio-oil. It decomposes materials at moderate temperatures with a short residence time of vapours in an inert atmosphere and it is a favourable process for the production of bio-oil [6, 7]. The three main products of biomass decomposition are solid biochar, non-condensable gases, and liquid bio-oil. There are multiple

reactors that have been designed for bio-oil production using the fast pyrolysis process [5, 9-12]. Among them, bubbling fluidised bed reactor (BFBR) is the most popular design due to its straightforward applications and high production of bio-oil yield. In a typical BFBR, heat carriers that have high conductivity (i.e. sand particles) are initially packed. The feedstock is injected from the side of the reactor while an inert carrier gas (usually nitrogen) flows from the bottom of the reactor. Nitrogen plays two major roles. Firstly, it fluidises the sand particles that allows mixing of hot sand and cold virgin biomass particles and provides the required heat for thermal decomposition of biomass. Secondly, it carries the products towards the reactor outlet.

Various operating parameters that affect bio-oil percentage have been numerically studied in recent years [5, 9, 13, 14]. The results confirmed that operating temperature has a significant effect on the bio-oil production and the optimum range of temperature for the maximum production is 773–800 K. For temperatures above 800 K, the secondary crack occurs which converts condensable vapours to non-condensable gases, decreasing the bio-oil yield. Particle size is also a key influencing parameter. If the heat rate is not sufficient to penetrate the biomass core, more unreacted biomass accumulates inside the reactor since the intraparticle temperature gradient is higher for larger particles. It was also found that feedstocks with higher contents of cellulose that are preheated up to 400 K, result in a higher rate of bio-oil yield.

The previous study [5] showed higher carrier gas velocities increase bio-oil production. However, it is not still clear how the optimum velocity varies as the particle size increases. It obviously becomes more difficult to fluidise

larger sand particles [14] and hence, a minimum fluidisation velocity (MFV) is defined as a function of particle size to ensure the fluidisation occurs. On the other hand, higher carrier gas velocities shorten the residence time of condensable vapour. This reduces the possibility of the secondary crack of condensable vapours to non-condensable gases, increasing the bio-oil yield. However, there are upper limits for the carrier gas velocity. If the nitrogen velocity exceeds a certain limit, which is called maximum effective velocity (MEV), sand particles are pushed out of the reactor bed that negatively affects the mixing between sand and biomass particles. It has been demonstrated that the heat transfer between biomass and sand particles is maximised if the cold virgin biomass particles are surrounded by hot sand particles of larger size [5]. High carrier gas velocities may also cause removing small and low-density biomass particles from the reactor bed which is not desired. Hence, it is important to effectively select the carrier gas velocity to ensure that adequate time is provided for mixing between sand and biomass particles, and biomass and sand particles are not removed from the reactor.

In this study, computational analysis is performed to understand the effects of the carrier gas velocity on the product yields as the sand particle size varies. For this purpose, the fast pyrolysis process in a 2-D standard lab-scale bubbling fluidized bed reactor (BFBR) is numerically studied. The model is first validated against the experimental data and then a parametric study is performed to analyse the optimum values of the nitrogen velocity for different sand and biomass particle sizes.

2. Methodology

The simulations are performed using Ansys Fluent V18.0. A Eulerian-Granular approach is adopted for the simulations. The method is a combination of the Multi-Fluid Model (MFM) and a chemical solver for reactions/kinetics of biomass particles. A brief description of the method is given in this section.

2.1 Multi-fluid Model

The MFM treats all phases as a continuing sequence of reactions, or as an inter-penetrating continuum [5, 14]. Each phase and their exchange of mass, momentum, and heat, are analysed, as well as the chemical reactions between phases. The primary phase is considered as the gas phase, which consists of three different species; nitrogen, condensable vapour, and non-condensable gases. There are usually multiple secondary solid phases which are biomass and sand phases in this study. They consist of seven species for the biomass phase including virgin cellulose, virgin hemicellulose, virgin lignin, active cellulose, active hemicellulose, active lignin, and biochar, and one species for the sand phase. For each phase, the conservation equations for volume fractions are derived. These equations are then used to model the drag and heat correlations between phases, as well as to describe the solid phase properties in the form of granular flow. The phase volume fractions provide the linkage between the phases whereas

granular values including temperature, pressure, viscosity, etc. are obtained using the kinetic theory of granular flow (KTFG). A detailed description of the models can be found in Refs [9, 14, 17].

2.2 Chemical kinetics of a single biomass particle

The biomass fast pyrolysis process occurs in an inert atmosphere and hence it rapidly decomposes into biochar, condensable vapour, and non-condensable gases. Detailed chemistry models are still challenging due to the complexity of the chemical reactions and the lack of information on the formation of intermediate species, [4, 15]. In this study, a superimposed reaction kinetics based on multi-component multi-step reaction kinetics is adopted to simulate the biomass fast pyrolysis process [16]. As shown in Fig. 1, virgin biomass converts to active biomass which then converts to biochar, condensable vapour and non-condensable gases. In the secondary reaction, condensable vapours react to form non-condensable gases which increase as the residence time of vapours increases [16]. The biochemical structure of biomass is a function of a lignocellulosic compound;

$$\text{Biomass} = \alpha \text{ Cellulose} + \beta \text{ Hemicellulose} + \gamma \text{ Lignin} \quad (1)$$

where α , β , and γ represent initial mass fractions of the species. The reaction rate constants are then calculated using

$$k_i = A_i \exp[-Ea_i/(RT)] \quad (2)$$

where k_i is the rate constant for the reaction “i”, A_i and Ea_i are the Arrhenius constant and activation energies, respectively, R is the gas constant, and T is the temperature in Kelvin. The kinematic parameters are presented in Table 1 whereas the thermophysical properties are shown in Table 2. The chemical reactions do not include the sand phase and nitrogen as they are inert. Nitrogen is included in the gas phase and it contributes to partial pressure [5]. In the simulations, the incompressible ideal gas model equates the density of the gas phase species and granular models are adopted to obtain the viscosity of species in the solid phase.

3. Experimental Validation

The numerical simulations are first validated against the measurements conducted for a standard lab-scale BFBR [17]. A schematic configuration of the experimental test rig is shown in Fig. 2. The reactor bed temperature and nitrogen velocity are 773K and 0.36 m/s, respectively. The sand particles have a diameter of 520 μm and they are packed to a height of 5.5 cm with a volume fraction of 0.59. The biomass particles have a diameter of 400 μm . The biomass feedstock is red oak with an initial composition of $(\alpha, \beta, \gamma) = (0.41, 0.32, 0.27)$. The pre-treatment temperature of the red oak is 300 K with a feed-rate of 100 g/h. A non-slip condition is applied for the walls. Similar to the experiment, the reactor's walls have a temperature of 800 K to a height of 8 cm that mimics the external heating. The mesh has 2055 cells, leading to an acceptable level of accuracy [5].

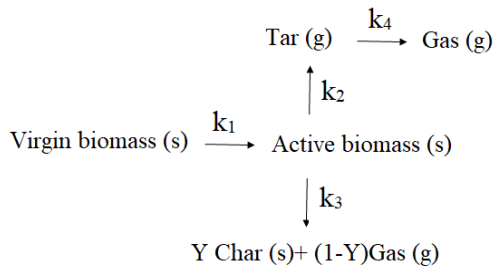


Figure 1: Chemical reaction scheme for pyrolysis of a lignocellulosic biomass

Table 1: Reaction kinetics for biomass fast pyrolysis [17].

Components	Reaction	A (s ⁻¹)	E (MJ/kmol)	Heat release, (kJ/kg)
Cellulose	k _{1c}	2.8 × 10 ¹⁹	242.4	0
	k _{2c}	3.28 × 10 ¹⁴	196.5	255
	k _{3c}	1.3 × 10 ¹⁰	150.5	-20
Hemicellulose	k _{1H}	2.1 × 10 ¹⁶	186.7	0
	k _{2H}	8.75 × 10 ¹⁵	202.4	255
	k _{3H}	2.6 × 10 ¹¹	145.7	-20
Lignin	k _{1L}	9.6 × 10 ⁸	107.6	0
	k _{2L}	1.5 × 10 ⁹	143.8	255
	k _{3L}	7.7 × 10 ⁶	111.4	-20
Tar	k ₄	4.25 × 10 ⁶	108	-42

Table 2: Thermo-physical properties of each species [17]

Species	Density ρ (kg/m ³)	Molecular weight (g/mol)	Heat Capacity C _p (K/kg K)	Dynamic viscosity μ (kg/m s)	Thermal conductivity k (W/m K)
Condensable	-	100	2500	3 × 10 ⁻⁵	2.577 × 10 ⁻²
Non-condensable	-	30	1100	3 × 10 ⁻⁵	2.577 × 10 ⁻²
N ₂	-	28	1121	3.58 × 10 ⁻⁵	5.63 × 10 ⁻²
Biomass	400	*	2300	-	0.3
Biochar	2333	12.01	1100	-	0.1
Sand	2649	60.08	800	-	0.27

* The molecular weights are 162.14, 132.11, 208.21 for cellulose, hemicellulose and lignin, respectively.

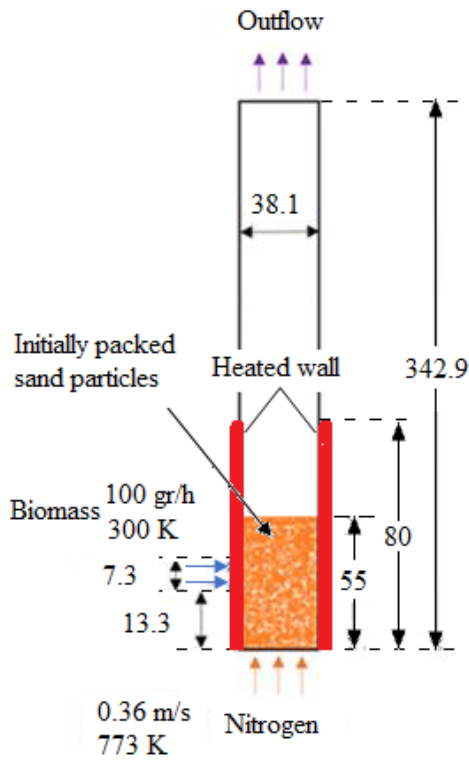


Figure 2: 2-D set up of the BFBR model for CFD analysis (all dimensions are in millimetres)

Once statistically steady-state conditions are achieved, the time-averaged yields are computed by analysing the outflux yields of each biomass by-product. The unreacted biomass is computed as a leftover percentage of the three by-products. The predicted product yields are compared with the measurements in Table 3, confirming that the predicted biochar and non-condensable gases agree well with the measurements. Although condensable vapour is slightly

under-predicted, the agreement is still satisfactory. The percentage of the observed discrepancy between the predicted and measured values are 12.8, 6.3, and 4.6 for condensable, non-condensable, and biochar, respectively.

4. Results and discussion

Simulations are performed for a wide range of particle size and carrier gas velocities to identify the optimum velocity as a function of the sand particle and biomass particle size. The range of sand particle size is 0.4-1 mm whereas biomass particles are in a range of 0.2-0.5 mm. The carrier gas velocity varies between 0.3 and 1.1 m/s. In all simulations, other operating parameters are the same as the base case given by the experiment [17]. In total, 32 simulations are performed to conduct the parametric study. The highest efficiency of the thermochemical conversions is obtained when a larger portion of the biomass is converted into products. Fast pyrolysis is the most favourable process for the production of a high-quality bio-oil and hence the optimum values for the carrier gas velocity are those that result in minimum unreacted biomass and maximum bio-oil yield.

Figure 3 presents bio-oil and unreacted biomass yields as a function of the nitrogen velocity for different sand particle sizes. The nitrogen velocity is normalised by the MFV for each particle size. Increasing the carrier gas velocity initially enhances bio-oil production and reduces unreacted biomass. However, a further increase in the nitrogen velocity has negative effects on bio-oil production while it increases the amount of unreacted biomass. A similar trend is observed for all particle sizes, confirming there is an MEV for each size. Figure 4 illustrates the variation of MFV normalised by MEV values as the sand particle size increases. The ratio between MEV and MFV decreases as

the particle size increases. With increasing the sand particle size, the MFV and MEV increase however their ratio decreases. It can be seen that initially there is a steep reduction in MEV/MFV while it becomes less sensitive as the particle size increases and a further increase from 0.8 mm to 1 mm marginally changes the ratio.

Table 1: The percentage of product yields for fast pyrolysis of red oak

Components	CV ^a	NCG ^b	BC ^c	UB ^d
Experiment [17]	71.7 ± 1.4	20.5 ± 1.3	13 ± 1.5	-
Simulation	62.5	19.2	13.6	4.7

^aCV: Condensable Vapour ^cBC: Biochar
^bNCG: Non-condensable Gases ^dUB: Unreacted Biomass

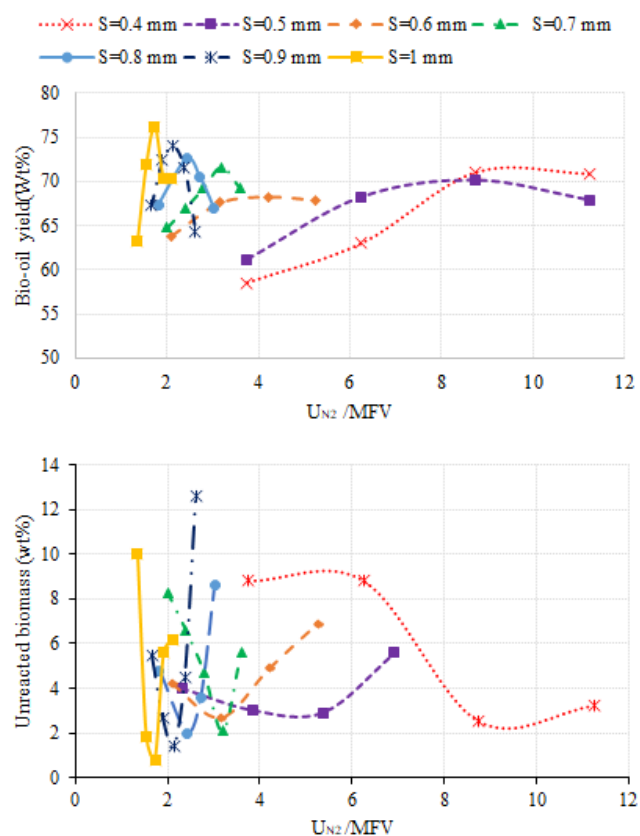


Figure 3: (a) Bio-oil yield and (b) unreacted biomass variation with carrier gas velocity

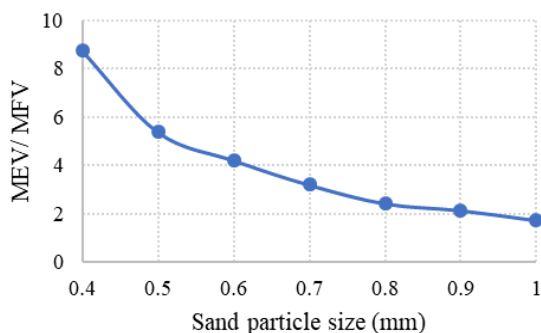


Figure 4: The ratio of MEV/MFV with respect to sand particle size

5. Conclusions

Fast pyrolysis process was numerically studied in a standard 2-D lab-scale bubbling fluidized bed reactor. The model was validated against the experimental data of red oak fast pyrolysis, demonstrating good agreement between the predicted and measured values. The effect of particle sizes (sand:0.4-1 mm, biomass: 0.2-0.5 mm), and carrier gas velocity (0.3-1.1 m/s) on the fluidisation and the product yields were analysed. The results proved that similar to the minimum fluidisation velocity, there was an upper limit velocity, called maximum effective velocity (MEV), that maximised the bio-oil yield production and led to minimum unreacted biomass. It was found that when the carrier gas velocity exceeded the MEV, sand and unreacted biomass particles were thrown out of the reactor, leading to a reduction in the bio-oil production.

6. References

- [1] T. Bruckner and I.A. Bashmakov (2014), Energy Systems. In: Climate Change: Mitigation of Climate Change. Contribution of Working Group III to the Fifth Assessment Report of the Intergovernmental Panel on Climate Change.: Cambridge University Press, Cambridge, United Kingdom and New York, NY, USA.
- [2] S. Shafiee and E. Topal (2009) When will fossil fuel reserves be diminished? Energy Policy. **37**, pp. 181-189.
- [3] Y. Isa., Makarfi and E. Ganda, Tinashe (2018) Bio-oil as a potential source of petroleum range fuels. Renewable and Sustainable Energy Reviews. **81**, pp. 69-75.
- [4] A. Demirbas (2001) Biomass resource and biomass conversion processing for fuels and chemicals. Energy Conversion and Management. **42**, pp. 1357-1378.
- [5] S. Jalalifar et al. (2018) Parametric analysis of pyrolysis process on the product yields in a bubbling fluidized bed reactor. Fuel. **234**, pp. 616-625.
- [6] N.L. Panwar, R. Kothari, and V.V. Tyagi (2012) Thermo chemical conversion of biomass – Eco friendly energy routes. Renewable and Sustainable Energy Reviews. **16(4)**, pp. 1801-1816.
- [7] J. Lee, A.K. Sarmah, and E.E. Kwon (2019). Chapter 1 - Production and Formation of Biochar. Biochar from Biomass and Waste. **1(1)**, pp. 3-18.
- [8] O. Onay, and O.M. Kockar (2003) Slow, fast and flash pyrolysis of rapeseed. Renewable Energy. **28(15)**, pp. 2417-2433.
- [9] J.S. Cardoso et al. (2018) Improved numerical approaches to predict hydrodynamics in a pilot-scale bubbling fluidized bed biomass reactor: A numerical study with experimental validation. Energy Conversion and Management. **156**, pp. 53-67.
- [10] L. Gartzten et al. (2019) Kinetic modeling and experimental validation of biomass fast pyrolysis in a conical spouted bed reactor. Chemical Engineering Journal. **373**, pp. 677-686.
- [11] H.S. Heo et al. (2010) Bio-oil production from fast pyrolysis of waste furniture sawdust in a fluidized bed. Bioresource technology. **101(1)**, pp. 91-96.
- [12] A. Oasmaa et al. (2009) Fast pyrolysis bio-oils from wood and agricultural residues. Energy & Fuels. **24(2)**, pp. 1380-1388.
- [13] Jalalifar et al., (2017) Numerical modelling of a fast pyrolysis process in a bubbling fluidized bed reactor. In: IOP Conference Series: Earth and Environmental Science. **73**, 012032.
- [14] Q. Xiong, S. Aramideh, and S.-C. Kong (2013) Modeling effects of operating conditions on biomass fast pyrolysis in bubbling fluidized bed reactors. Energy & Fuels. **27(10)**, pp. 5948-5956.
- [15] M.V.d. Velden et al. (2010) Fundamentals, kinetics and endothermicity of the biomass pyrolysis reaction. Renewable Energy. **35(1)**, pp. 232-242.
- [16] R.S. Miller, J.J.C.s. Bellan (1997) A generalized biomass pyrolysis model based on superimposed cellulose, hemicellulose and lignin kinetics. **126(1-6)**, pp. 97-137.
- [17] Q. Xue et al. (2012) Experimental validation and CFD modeling study of biomass fast pyrolysis in fluidized-bed reactors. Fuel. **97**, pp. 757-769.

LES/PDF Modelling of Turbulent Premixed Flames in the Flamelet Regime Using an MMC – Shadow Position Mixing Model

Y. Shoraka^{1,*}, S. Galindo-Lopez¹, M. J. Cleary¹, A. R. Masri¹, A. Y. Klimenko²

¹ School of Aerospace, Mechanical and Mechatronics Engineering, The University of Sydney
Sydney, NSW 2006, Australia

² School of Mechanical and Mining Engineering, The University of Queensland
Brisbane, QLD 4072, Australia

Abstract

This paper presents a shadow position mixing model developed in the Multiple Mapping Conditioning (MMC) framework for LES/PDF modelling of turbulent premixed flames. The developed model provides localness of mixing in composition space by enforcing locality in a shadow position space and uses an adjustable diffusion coefficient proportional to the turbulent propagation speed so that the flame surface in shadow position space approximates the ensemble position of the premixed flame front in physical space. In the current paper, the performance of the proposed model is assessed by a hybrid Euler/Lagrange simulation of a piloted premixed methane-air jet flame (flame F3) experimentally studied by Chen et al. [1]. The selected flame is located in the thin reaction zone regime. For this purpose, three sets of numerical simulations are performed by setting the average number of particles per LES cell to 10, 20 and 40, respectively. The reasonable agreement obtained between the simulation results and the experimental data demonstrates the capability of the developed shadow position mixing model for LES/PDF modelling of turbulent premixed flames in the flamelet regime.

Keywords: Turbulent Premixed Combustion, Multiple Mapping Conditioning, Shadow Position Mixing Model

1. Introduction

Development of less polluting and more efficient combustion devices is essential for decreasing the harmful impacts of burning fossil fuels on the environment. Notwithstanding the emergence of lean premixed combustion as a promising technology for reducing pollutant emissions and increasing the efficiency of combustion, this mode is prone to combustion instabilities. Therefore, careful investigation of physical processes that occur in premixed turbulent flames is of prime importance for the development of cleaner combustion devices [2]. Nowadays, numerical simulations are an indispensable tool for the design and analysis of combustion devices. Nevertheless, a numerical study of turbulent combustion is not a trivial task due to the existence of a wide range of time and length scales. Although Direct Numerical Simulation (DNS) can be used to resolve all the relevant scales of turbulent reacting flows, utilisation of this method requires substantial computational resources, and it is not feasible for industrial applications. To alleviate this problem, Reynolds Averaged Navier-Stokes (RANS) and Large Eddy Simulation (LES) techniques are proposed, wherein the averaged flow quantities and large-scale flow motions are resolved, respectively.

Despite the resolution of large, energy-carrying flow structures, LES of turbulent premixed combustion is still a challenging task because the chemical source terms are highly nonlinear and the molecular mixing of species happens at the subgrid scale [2, 3]. Various methodologies have been proposed for modelling turbulent premixed combustion such as geometrical flamelet approaches, e.g. level-set/G-Equation based models [4], the thickened flame [5] and flame surface density approaches [6], the statistical flamelet approach [7] and Transported Probability Density Function (TPDF) approaches [8-12]. The prominent advantage of the TPDF methods is that the nonlinear

chemical source terms appear naturally in closed form in the governing equations, and, unlike flamelet methods, are derived independent of the flame regime and can be applied to nonpremixed, partially premixed and premixed turbulent combustion. Nonetheless, the micromixing term in the PDF transport equations requires modelling [13, 14]. The essential characteristics of a micromixing model are the conservation of scalar means, accurate prediction of the scalar variances' decay rate, linearity and independence, Gaussianity in homogeneous turbulence and localness in scalar space. In this respect, various micromixing models, e.g. Interaction by Exchange with the Mean (IEM), Coalescence and Dispersion (CD), Mapping Closure (MC), Euclidean Minimum Spanning Tree (EMST), Multiple Mapping Conditioning (MMC), Shadow Position Mixing Model (SPMM) and Parameterized Scalar Profile (PSP) have been developed [13, 14].

Although the incorporation of finer computational grids should make LES less sensitive to the performance of micromixing models [13], applications of conventional micromixing models, e.g. IEM and CD, to thin premixed flames is problematic due to the potential for non-physical mixing of burnt and unburnt species across the flame front that is not resolved in LES [9]. Therefore, a micromixing model which can enforce localness relative to the flame front should be developed for these flames. MMC is a suitable framework for the development of such a model as therein, mixing is local or conditioned in a mathematically independent reference space [9, 14, 15]. In nonpremixed flames, mixture fraction is used as the reference variable for enforcing localness, and Cleary and Klimenko developed a sparse MMC based TPDF model for LES wherein one stochastic particle per 30 LES cells was sufficient for obtaining promising results in LES of nonpremixed turbulent flames [16, 17].

In premixed combustion, however, the mixture fraction cannot be used as the reference variable since burnt and unburnt gasses with similar mixture fractions and different compositions may exist in different sides of the flame front. To circumvent this problem, Straub et al. [9] developed an MMC model that conditions mixing on the reaction progress variable and coupled it with an artificially thickened flame model for LES/PDF modelling of premixed flames. Sundaram et al. [18, 19], on the other hand, developed a shadow position reference variable for modelling micromixing in the MMC framework. The proposed model is altered from the original SPMM model proposed by Pope [20] by introducing an adjustable diffusion coefficient proportional to the turbulent propagation speed. Therefore, it enforces mixing localisation in a shadow position space and makes the flame surface in shadow position space approximate the ensemble position of the flame front in physical space. In the current paper, the MMC-shadow position mixing model is implemented within the mmcFoam package [15] and is used for LES of the turbulent piloted premixed methane/air flame F3 that is experimentally studied by Chen et al. [1]. Flame F3 is primarily in the thin reaction zone regime near the flamelet region [1], and is previously studied by means of LES using the G-Equation model [4], the thickened flame approach [5], Lagrangian [8, 11] and Eulerian [10, 12] TPDF approaches and the statistical flamelet approach [7].

In the rest of this paper, at first, the LES/PDF methodology and the MMC-shadow position mixing model are briefly discussed in Section 2. Afterwards, results obtained for three LES/PDF simulations of F3 flame are presented and discussed in Section 3. Finally, conclusions are given in Section 4.

2. Methodology

The mmcFoam package utilises a hybrid Euler/Lagrange approach for LES/PDF modelling of turbulent premixed combustion. Eulerian schemes are used for numerical discretisation and temporal integration of the mass and momentum conservation equations to obtain filtered pressure, filtered velocity and turbulent diffusivity fields. In the LES simulations, the Smagorinsky model and the PISO algorithm are used for subgrid modelling and pressure-velocity coupling, respectively [15]. After that, integrated Eulerian fields are interpolated to particle locations, and Lagrangian particles are evolved using a fractional step scheme based on the traditional set of stochastic Ito equations which are complemented with additional stochastic differential equations for the shadow position reference variable.

2.1 MMC – shadow position mixing model for premixed combustion

Stochastic Ito equations used for evolution of Lagrangian particles in physical space as well as the change of their composition as the result of mixing and reaction are:

$$d\mathbf{x}^p = \left[\tilde{\mathbf{U}} + \frac{1}{\bar{\rho}} \nabla(\bar{\rho} \mathcal{D}_{eff}) \right] dt + \left(\sqrt{2\mathcal{D}_{eff}} \right) d\mathbf{w}_x^p \quad (1)$$

$$d\phi_\alpha^p = [\omega_\alpha(\boldsymbol{\Phi}^p) + \mathbb{S}(\phi_\alpha^p)] dt \quad (2)$$

In Eqs. 1 and 2, the superscript p indicates a stochastic quantity, overlines $\tilde{\cdot}$ and $\bar{\cdot}$ denote Favre and conventionally filtered quantities, \mathbf{U} represents the velocity vector, ρ is the density, \mathcal{D}_{eff} is the summation of molecular and subgrid-scale diffusivities, $d\mathbf{w}$ denotes the independent Wiener process vector and ω_α and \mathbb{S} represent chemical reactions and the molecular mixing process, respectively. The modified evolution equation of the shadow position vector is given by

$$d\xi^p = \tilde{\mathbf{U}} dt + \frac{\mathbf{x}^p - \xi^p}{\tau_\xi} + \left(\sqrt{2\mathcal{D}_\xi} \right) d\mathbf{w}_\xi^p \quad (3)$$

where τ_ξ , which is known as the flame span parameter, is a characteristic time scale that is computed dynamically in the current work as equal to the subgrid turbulent timescale, and \mathcal{D}_ξ is the diffusion coefficient of the shadow position variable. Therefore, the accurate prediction of the structure of the flame depends on the proper adjustment of \mathcal{D}_ξ . Sundaram and Klimenko [19] proposed that \mathcal{D}_ξ can be calculated as:

$$\mathcal{D}_\xi = \mathcal{D} \lambda^2 \quad (4)$$

where

$$\lambda = u_t / s_l \quad (5)$$

In Eqs. 4 and 5, \mathcal{D} is the molecular diffusivity, s_l denotes the laminar flame speed and u_t indicates a measure of the turbulent propagation speed. In the current work, λ is set as a fixed parameter equal to the ratio between the turbulent and laminar flame speeds, which are set to be equal to 3.895 m/s and 0.4 m/s, respectively. It can be observed that unlike the original shadow position mixing model developed by Pope [20], where \mathcal{D}_ξ is directly linked to the turbulent diffusivity, here \mathcal{D}_ξ is an adjustable parameter proportional to the turbulent propagation speed to make the flame surface in shadow position space approximate the ensemble position of the flame front in physical space [19]. To emulate the effects of molecular mixing on the PDF, particles are mixed toward their weighted mean using a modified CD algorithm [15], and a k-dimensional tree is used to minimise the average effective distance between all particle pairs to enforce localness. The effective distance between particle pairs is calculated as:

$$\hat{d}_{p,q}^2 = \sum_{i=1}^3 \left(\frac{d_{x_i}^{p,q}}{r_m / \sqrt{3}} \right)^2 + \sum_{j=1}^3 \left(\frac{d_{\xi_j}^{p,q}}{\xi_m / \sqrt{3}} \right)^2 \quad (6)$$

In Eq. (6), $d_{x_i}^{p,q}$ and $d_{\xi_j}^{p,q}$ indicate the distances between particle pairs in physical and shadow spaces, respectively, and r_m and ξ_m are model input parameters that represent the characteristic mixing distances in physical and shadow spaces. These parameters can be tuned such that the localness

is enforced more in one space at the expense of localness in the other one.

3. Results and Discussion

3.1 Simulation Setup

Flame F3 consists of a central jet composed of a stoichiometric methane/air mixture at room temperature with a diameter of 12 mm and the bulk velocity, U_0 , of 30 m/s corresponding to a jet Reynolds number of 24200. The centerline turbulent kinetic energy of the jet, k_0 , is equal to $3.82 \text{ m}^2/\text{s}^2$. The central jet is surrounded by a large pilot stream that flows through an array of 1165 holes whose diameter is 1 mm with the exit velocity of 84 cm/s [1]. The pilot is modelled as an annulus with a thickness of 28 mm and the bulk velocity of 1.32 m/s.

The computational domain is a cylinder with length and diameter of 15 and 10 jet diameters, respectively, wherein 1 million hexahedral computational cells are generated to achieve a grid size of 0.5 mm near the jet and pilot boundary. Zero pressure gradient boundary conditions are applied at the inlets, and fixed total pressure boundary conditions are used at the domain sides and the outflow. A separate pipe flow simulation is performed to obtain realistic boundary conditions at the inlet for the central jet. The boundary conditions for the pilot are set at the temperature of 1785 K to account for heat losses. In the Eulerian simulations, temporal integration is performed using the second-order backward scheme. For spatial discretisation of diffusive and convective terms, Gauss scheme and a TVD method are incorporated, respectively. The timestep size is obtained by using a CFL number of 0.3 in the simulations, and for calculating the chemical reaction rates, a two-step, six-species methane/air reaction mechanism is used [21].

Three sets of numerical simulations are performed to investigate the effect of the average number of Particles Per Cell (PPC) on the mixing distances in shadow position space and the accuracy of the results by setting 10, 20 and 40 PPC. In the simulations done for the current paper, localness is enforced exclusively in shadow position space, and the characteristic mixing distance in shadow space, ξ_m , is set to be equal to 0.00035 m. Particles are sorted based on their distances in shadow position space such that the existence of the adequate number of particles ensures that the mixing distance between particle pairs in shadow position space and the possibility of non-physical mixing of burnt and unburnt species in the vicinity of the flame front is minimised.

3.2 Results

Figure 1 shows the PDF distribution for the particles' mixing distance in shadow position space, $\delta\xi_{mix}$. For the sake of clarity, the abscissa is normalised by the laminar flame thickness, δ_{lf} , in this figure. The mixing distance between particle pairs in shadow position space is calculated as:

$$\delta\xi_{mix} = \sqrt{\frac{\sum_{j=1}^3 (d_{\xi_j}^{p,q})^2}{3}} \quad (7)$$

and δ_{lf} is equal to 0.175 mm [1]. Samples used for generating the PDF distributions depicted in Fig. 1 are obtained from 5 different time steps for each simulation from particles with methane mass fractions in the range of $0.001 < Y_{CH_4} < 0.0551$ to neglect particles which do not participate in chemical reactions. By integrating the area under the PDF curves illustrated in Fig. 1, it is found that the probabilities of obtaining mixing distances in shadow position that are less than the laminar flame thickness are 41%, 53% and 65% respectively for simulations performed using 10, 20 and 40 PPC. Figure 2 depicts the time-averaged and instantaneous temperature contours at 0.076 s at the mid-plane of the computational domain. It reveals that, excluding a slight difference in the flame length, the flame structure for simulations using 10, 20 and 40 PPC are quite similar.

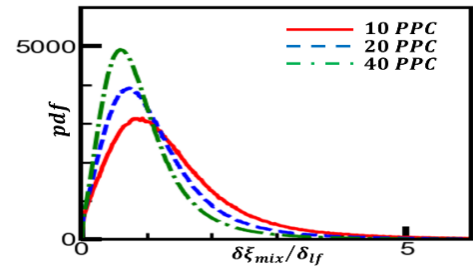


Figure 1: PDF distribution of mixing distance in shadow position space

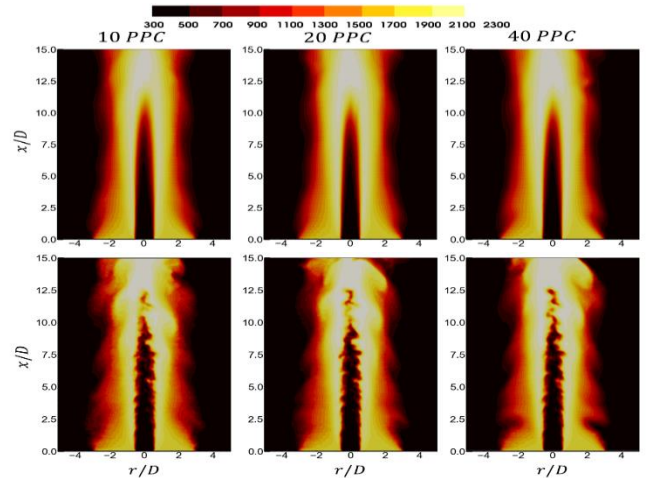


Figure 2: Time-averaged (top) and instantaneous (bottom) temperature contours at time = 0.076 s

Figure 3 shows the mean radial profiles of the normalised turbulent kinetic energy, normalized axial velocity, progress variable and species mass fractions at four different locations throughout the flame. In this figure, mean turbulent kinetic energy and mean progress variable are obtained as:

$$\langle k \rangle = \frac{\sum_{i=1}^3 \langle u_i'^2 \rangle}{2} + \langle k_{sgs} \rangle \quad (8)$$

$$\langle C \rangle = \frac{\langle T \rangle - T_u}{T_b - T_u} \quad (9)$$

where $\langle \cdot \rangle$ and k_{sgs} indicate the time averaging procedure and subgrid-scale turbulent kinetic energy, and T_u and T_b are 298 K and 2248 K, respectively [1]. From the results illustrated in Fig. 3, it is observed that the burning rate is slightly over-predicted at $x/D = 2.5$ and $x/D = 8.5$ and this results in a steeper rise in the mean radial progress variable profile and a slight over-prediction of the jet's width. Nonetheless, the predicted progress variable profiles are in good agreement with experimental data for all of the performed simulations at $x/D = 4.5$, and 6.5 in the flame region as the observable differences between the simulations' results and experimental data occurs in the co-flow region. Results obtained for the mean profiles of the turbulent kinetic energy shows substantial underprediction, which we believe to be due to excessive dissipation of the Smagorinsky model. Predicted statistics for the species mass fractions are also in a good agreement with the experimental data, and the considerable underprediction of the CO mass fraction could be the result of inaccuracies in the two-step chemical reaction mechanism. Future simulations with detailed kinetics schemes will investigate this issue in detail.

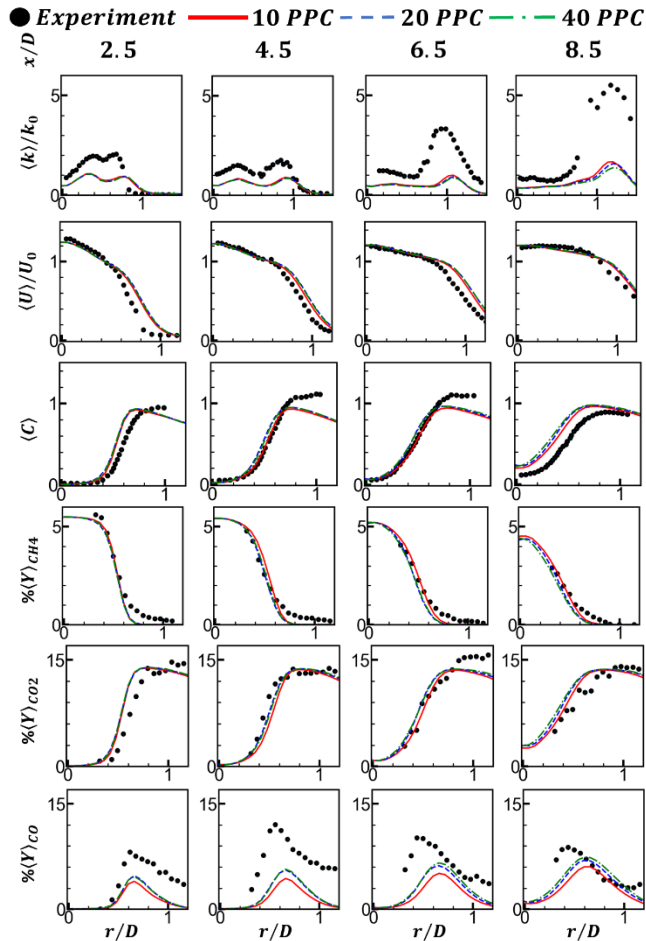


Figure 3: Mean radial profiles of the turbulent kinetic energy, axial velocity, progress variable and species mass fractions

Comparisons obtained using 10, 20 and 40 PPC indicates that the predicted mean profiles are very close to each other. Moreover, it can be observed that the flame surface in shadow position space has followed somewhat closely the ensemble of the flame front in physical space; thereby

forming a thicker front. Future simulations, especially with larger mixing distances in shadow position space, will be performed to investigate the performance of the model further.

4. Conclusions

A newly proposed shadow position mixing model developed in the Multiple Mapping Conditioning (MMC) framework has been incorporated for the LES/PDF simulation of premixed flames using a hybrid Euler/Lagrange simulation methodology. The incorporated model enforces the localness of mixing in composition space by enforcing locality in a shadow position space. The good agreement obtained between the simulation results for a piloted premixed methane-air jet flame located in the thin reaction and the experimental data has shown that the incorporated mixing model is capable of adjusting the shadow position to the ensemble position of the premixed flame front and adapting the predicted flame structure to the desired premixed flame regime.

5. Acknowledgements

This research is supported by the Australian Research Council. Numerical simulations were performed using the University of Sydney's high-performance computing cluster.

6. References

- [1] Y.-C. Chen, N. Peters, G.A. Schneemann, N. Wruck, U. Renz, M.S. Mansour, *Combustion and flame*, 107 (1996) 223-244.
- [2] N. Swaminathan, K.N.C. Bray, *Turbulent premixed flames*, Cambridge University Press, 2011.
- [3] H. Pitsch, *Annu. Rev. Fluid Mech.*, 38 (2006) 453-482.
- [4] H. Pitsch, L.D. De Lageneste, *Proceedings of the Combustion Institute*, 29 (2002) 2001-2008.
- [5] Z. Yu, H. Zhang, T. Ye, M. Zhu, *Applied Mathematics and Mechanics*, 39 (2018) 1277-1294.
- [6] G. Wang, M. Boileau, D. Veynante, K. Truffin, *Combustion and Flame*, 159 (2012) 2742-2754.
- [7] I. Langella, N. Swaminathan, *Combustion Theory and Modelling*, 20 (2016) 410-440.
- [8] H. Wang, T. Pant, P. Zhang, *Flow, Turbulence and Combustion*, 100 (2018) 147-175.
- [9] C. Straub, A. Kronenburg, O.T. Stein, G. Kuenne, J. Janicka, R.S. Barlow, D. Geyer, *Combustion and Flame*, 196 (2018) 325-336.
- [10] M.A. Picciani, E.S. Richardson, S. Navarro-Martinez, *Flow, turbulence and combustion*, 101 (2018) 1119-1136.
- [11] S.L. Yilmaz, M.B. Nik, P. Givi, P.A. Strakey, *Journal of Propulsion and Power*, 26 (2010) 84-93.
- [12] I.A. Dodoulas, S. Navarro-Martinez, *Flow, turbulence and combustion*, 90 (2013) 645-678.
- [13] D.C. Haworth, *Progress in Energy and combustion Science*, 36 (2010) 168-259.
- [14] C. Celis, L.F.F. da Silva, *Flow, Turbulence and combustion*, 94 (2015) 643-689.
- [15] S. Galindo-Lopez, F. Salehi, M.J. Cleary, A.R. Masri, G. Neuber, O.T. Stein, A. Kronenburg, A. Varna, E.R. Hawkes, B. Sundaram, *Computers & Fluids*, 172 (2018) 410-425.
- [16] M.J. Cleary, A.Y. Klimenko, *Physics of Fluids*, 23 (2011) 115102.
- [17] Y. Ge, M.J. Cleary, A.Y. Klimenko, *Proceedings of the Combustion Institute*, 34 (2013) 1325-1332.
- [18] B. Sundaram, A.Y. Klimenko, M.J. Cleary, U. Maas, *Proceedings of the Combustion Institute*, 35 (2015) 1517-1525.
- [19] B. Sundaram, A.Y. Klimenko, *Proceedings of the Combustion Institute*, 36 (2017) 1937-1945.
- [20] S.B. Pope, *Physics of Fluids*, 25 (2013) 110803.
- [21] B. Franzelli, E. Riber, L.Y.M. Gicquel, T. Poinsot, *Combustion and flame*, 159 (2012) 621-637.

Numerical Analysis of Point Source Fire on Fire-Wind Enhancement

Esmaeel Eftekharian^{1,2*}, Fatemeh Salehi², Yaping He¹, Kenny C. S. Kwok³,

¹Center for Infrastructure Engineering, School of Computing Engineering and Mathematics, Western Sydney University, Australia

²School of Engineering, Macquarie University, Australia

³School of Civil Engineering, The University of Sydney, Australia

Abstract

Fire-wind enhancement phenomenon is referred to as an increase of wind velocity through interacting with fire. Wind enhancement during bushfire attacks can significantly increase pressure load on buildings and consequently pose a threat to the structures built in bushfire prone areas. The aim of this work is to study the effects of point source fire size on fire-wind enhancement. For this purpose, the large eddy simulations (LES) are performed for different fire-wind interaction scenarios. The simulations are conducted using FireFOAM solver which is an opensource C++ computational fluid dynamic (CFD) platform. A module is implemented to the solver to extract individual fire-induced force fields generated due to the fire-wind interaction. The effects of fire source size under two different conditions are investigated, namely, constant fire intensity (fire heat release rate per unit area) and constant fire heat release rate. The results reveal that increasing the size under constant fire intensity amplifies the fire-induced negative pressure gradient and causes a stronger wind enhancement. The LES results for different fire size while the fire heat release rate is constant show that the wind enhancement does not substantially change along the fire plume centreline downstream of the fire source. However, maximum wind enhancement, being formed symmetrically at the two sides of domain centreline, significantly reduces for the larger fire source size. The results also show that in both constant fire intensity and constant heat release rate conditions, the region of wind enhancement is expanded with the increase of fire source size.

Keywords: Fire-wind enhancement, fire source size, FireFOAM, LES.

1. Introduction

Fire-wind interaction has been a focus of interest for many years due to the key role of wind in the deterioration of natural calamities and industrial accidents. Fire-wind interaction is basically a two-way coupling problem. Wind influences fire spread [1] as well as flame geometrical features such as flame length [2], flame tilt angle [3,4] and flame base drag phenomenon [5]. On the other hand, fire affects wind aerodynamic features [6]. It has been experimentally shown that when the fire flame is exposed to the free-stream wind, the wind velocity profile is considerably altered downstream of the fire source [7]. Computational fluid dynamic (CFD) approach has been applied to study the effects of fire on free-stream wind velocity, confirming fire significantly increased wind velocity at near-ground region downstream of the fire source [6,8]. Coanda-effect was taken as the reason behind the fire plume attachment to the ground immediately downstream of the fire source, whereas buoyancy force was recognised as the dominant mechanism to lift the plume further downstream of the fire source [8]. Recently, Eftekharian et al [9] employed FireFOAM solver [10] to conduct large eddy simulations (LES) for fundamental analysis of fire-wind enhancement phenomenon. It was found that when wind interacted with fire, the fire flame was tilted toward wind direction and due to the entrainment mechanism, a favourable (negative) pressure gradient was generated along the wind direction in the plume region which caused the flow acceleration and consequently the wind enhancement [9]. For a point source fire, the maximum wind enhancement occurred at the location of counter-rotating vortices forming downstream of the fire source [9]. The numerical studies have been also conducted to understand the effects of different parameters such as

upstream wind velocity, fire intensity and terrain slope on fire-wind enhancement. The LES results revealed that under constant fire intensity, increasing the free-stream wind velocity reduced fire-wind enhancement [11]. In addition, the results confirmed that the upslope terrain intensified the fire-induced negative pressure gradient, while downslope terrain mitigated its value and causes a reduction in fire-wind enhancement effects [12]. In spite of these studies, there is still gap in our understanding on the importance of fire source characteristics. In this study, we aim to shed more light on how the size of the point source fire influences the fire-wind enhancement.

2. Model Description

2.1 Numerical Model

This study uses FireFOAM solver as a CFD open source C++ tool that solves the thermos-fluid governing equations. FireFOAM is a solver derived from OpenFOAM platform designed for low Mach number fire simulations, allowing the user to customise library/solver source codes to serve a specific purpose. FireFOAM uses large eddy simulation (LES) method to treat turbulent structures and it solves the Favre filtered thermos-fluid governing equations, namely, continuity, momentum, energy, species, and state equations [10, 13, 14] as below:

$$\frac{\partial \bar{p}}{\partial t} + \frac{\partial (\bar{\rho} \tilde{u}_i)}{\partial x_i} = 0 \quad (1)$$

$$\frac{\partial (\bar{\rho} \tilde{u}_i)}{\partial t} + \frac{\partial (\bar{\rho} \tilde{u}_i \tilde{u}_j)}{\partial x_j} = -\frac{\partial \bar{p}}{\partial x_i} + \frac{\partial}{\partial x_j} \left[\bar{\rho} (v + v_t) \left(\frac{\partial \tilde{u}_i}{\partial x_j} + \frac{\partial \tilde{u}_j}{\partial x_i} - \frac{2}{3} \frac{\partial \tilde{u}_k}{\partial x_k} \delta_{ij} \right) \right] + \bar{\rho} g_i \quad (2)$$

$$\frac{\partial (\bar{\rho} \tilde{h})}{\partial t} + \frac{\partial (\bar{\rho} \tilde{u}_j \tilde{h})}{\partial x_j} = \frac{D\bar{p}}{Dt} + \frac{\partial}{\partial x_j} \left[\bar{\rho} \left(\alpha + \frac{v_t}{Pr_t} \right) \left(\frac{\partial \tilde{h}}{\partial x_j} \right) \right] + \dot{q}''' - \nabla \cdot \dot{q}_r''' \quad (3)$$

$$\frac{\partial \bar{\rho} \tilde{Y}_m}{\partial t} + \frac{\partial (\bar{\rho} \tilde{u}_j \tilde{Y}_m)}{\partial x_j} = \frac{\partial}{\partial x_j} \left[\bar{\rho} \left(D_c + \frac{\nu_t}{Pr_t} \right) \frac{\partial (\tilde{Y}_m)}{\partial x_j} \right] + \omega_m \quad (4)$$

$$\bar{p} = \bar{\rho} R \tilde{T} \quad (5)$$

where the symbols “-” and “~” specifies spatial and Favre filtering. u is velocity, p is static pressure, h is the specific enthalpy, Y_m is the mass fraction of species m , and g is gravitational acceleration. ν and ν_t donate the laminar and turbulent viscosities, respectively. D_c , α , R , Pr , and δ are laminar diffusion coefficient, thermal diffusivity, gas constant, Prandtl number, Kronecker delta, respectively, whereas ω_m is the reaction rate of species m . \dot{q}''' and \dot{q}_r'' are heat release rate per unit volume (W/m^3) from chemical reactions and the total radiation emission intensity (W/m^2) of the gas mixture, respectively. Momentum equation (Eq.2) can be written based on the components of the force acting on a fluid parcel:

$$\rho \vec{a} = \rho \frac{D\vec{u}}{Dt} = -\nabla p + \rho \vec{g} + \Phi \quad (6)$$

where a is acceleration and Φ is the viscous shear stress vector. The first, second and third terms on the right-hand side of Eq. 6 indicate the forces due to pressure gradient, gravity, and viscous effects, respectively. A module was implemented into the FireFOAM solver to extract the evolution of these individual forces. FireFOAM uses the eddy dissipation concept and the infinitely-fast chemical reactions to treat combustion modelling.

2.2. Geometrical Model

The computational domain includes a rectangular box with the dimension of 60m×18m×30m as shown in Fig. 1. The methane is injected with a constant rate from a rectangular source with a length of L that mimics the fire source located 3 m downstream of the inlet.

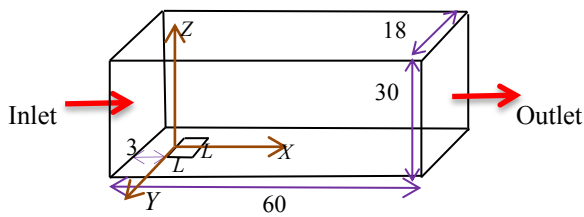


Figure 1. A schematic view of the computational domain where L shows the fire source length. All dimensions are in meter.

2.3. Boundary and simulation conditions

The inlet boundary is defined as the atmospheric boundary layer in the form of power-law profile:

$$U(Z) = U_{ref} \left(\frac{Z}{Z_{ref}} \right)^{\alpha_t} \quad (7)$$

where U_{ref} and Z_{ref} are the reference velocity (3 m/s) and the reference height (3m), respectively. α_t is the terrain coefficient which is determined according to the terrain category (here 0.16). Turbulent eddies were generated on

the mean velocity profile at the inlet using the vortex method [15]. Open boundary condition (total pressure) was used for the domain top whereas slip boundary conditions were prescribed for the domain sides. Outflow boundary condition was adopted for the domain outlet. To study the importance of the fire source size, the simulations were performed for $L=0.3$ and 0.9 m while the fire intensity defined as the heat release rate to the area was kept constant. This somehow represents a larger fire in bushfire scenarios where increasing the fire source size enhances the heat release rate. An additional case with $L=0.9$ m was considered while the initial heat release rate remains unchanged and hence the fire intensity decreased. A summary of the considered scenarios is presented in Table.1

Table 1. Simulation scenario description

Scenario number (S#)	Fire source dimension (L)	Fire heat release rate (MW)	Fire intensity (MW/m^2)
1	0.9 m	5.220	6.44
2	0.3 m	0.580	6.44
3	0.9 m	0.580	0.72

3. Validation and grid sensitivity analysis

The simulations employed a total grid number of about 4 million with a grid number of 190, 232 and 75 in X , Y and Z direction, respectively. The mesh was refined near the fire flame region to reduce the computational cost and simultaneously capture more physics of the flow field. We have performed a grid-sensitivity analysis in our previous studies [9, 12] and a similar grid size near the flame region was used in the current study.

The current study was validated against experimental data of McCaffrey [16]. McCaffrey's experiment [16] includes the injection of methane from a fire source with the same size as that used in S#2 into still air. The results shown in Fig. 2 confirm the validity of the applied numerical model. An extensive validation for cross-flow fire interaction against other experimental data [7] can be found in our previous study [9].

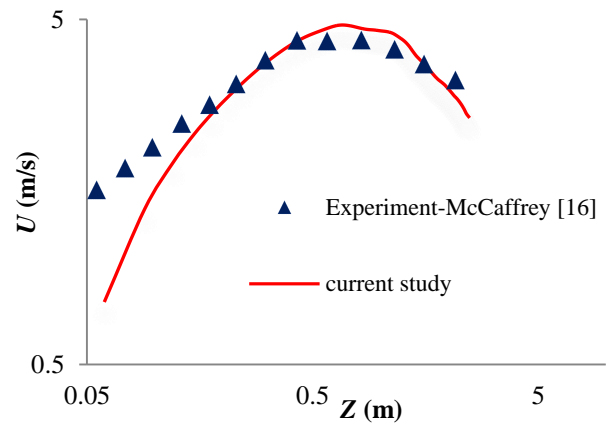


Figure 2. Comparison of fire plume centerline velocity between our numerical model and experimental data of [16].

4. Results and discussion

The simulations were performed for total flow times of 40 seconds. The transition period for the simulations was considered 20 seconds and therefore flow characteristic parameters were averaged over the last 20 s of the simulation time.

As discussed in section 2.3, three simulations were performed to analyse the effects of fire source size on fire-wind enhancement under (a) a constant fire heat release and (b) a constant fire intensity.

Figure 3 compares the planar longitudinal velocity distribution along the centerline ($Y=0$) for different simulation scenarios. The velocity was normalised by the reference velocity. Increasing the fire source size while the fire intensity is constant (S#1 and S#2) shows that the larger the fire source, the stronger the wind enhancement. This trend is expected since the larger fire source (0.9m) produces fire heat release rate nine times as much as the small fire source (0.3m). On the other hand when the fire heat release rate remains unchanged while the fire source is larger (S#2 and S#3) there is no significant variation in the wind velocity enhancement downstream of the fire along the domain centerline although the fire intensity remarkably reduced.

To shed more light on the observed behaviour, the cross-sectional distribution of normalised longitudinal wind velocity at $X=2.7$ m is presented in Fig. 4a.

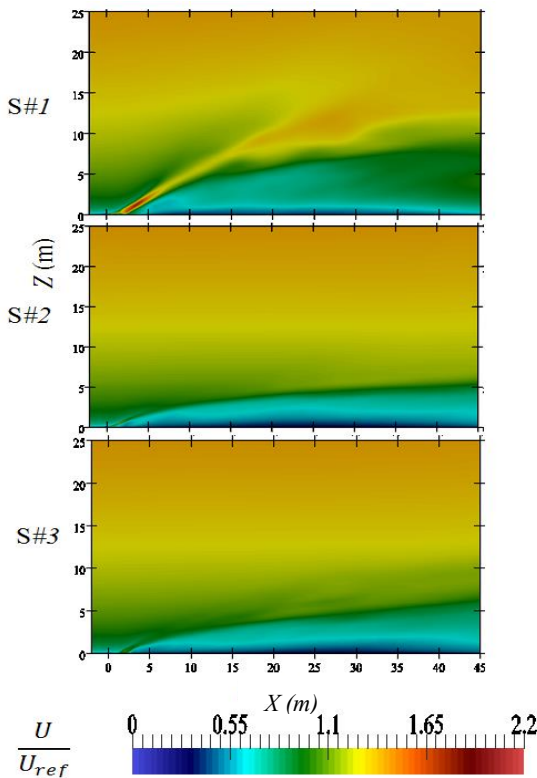


Figure 3. Comparison of planar normalized longitudinal velocity distribution along the domain centerline ($Y=0$).

Although changing the fire source size under a constant fire heat release rate marginally affects the enhanced wind along the centerline, cross-sectional distribution of wind enhancement undergoes a substantial reduction when the size of fire source increases. The observed reduction in wind enhancement can be explained using the pressure gradient distributions that reveal the mechanism causing fire-wind enhancement. The results are presented in Fig 4b. The maximum wind enhancement occurs at the location of counter-rotating vortices [9]. Under a constant fire heat release rate (S#2 and S#3), the results demonstrate the longitudinal fire-induced pressure gradients, generated in these locations, decrease as the fire source becomes larger. Consequently, the maximum wind velocity enhancement reduces with the increase of fire source size.

Comparison between S#1 and S#2 reveals that a larger fire creates stronger fire-induced pressure gradient and consequently causes more intensified wind enhancement, as observed in Fig. 4.

Considering all three scenarios indicates that the size of the fire source determines the region of wind enhancement by fire; the larger the fire source, the larger the wind enhancement region. Similar region of enhancement can be observed for the simulation scenarios in which the fire source size is similar (S#1 and S#3), though the intensity of wind enhancement is different due to the combined effects of difference in fire heat release rate and fire intensity. Self-similar solution may exist for the wind enhancement region downstream of the fire source which potentially can be the subject of future studies.

Figure 5 compares the vertical distribution of normalised longitudinal velocity for different cases at the longitudinal distances of $X=-1.8, 2.7, 3.6$ and 5.4 m. The results show that in all case, the wind enhancement initially increases

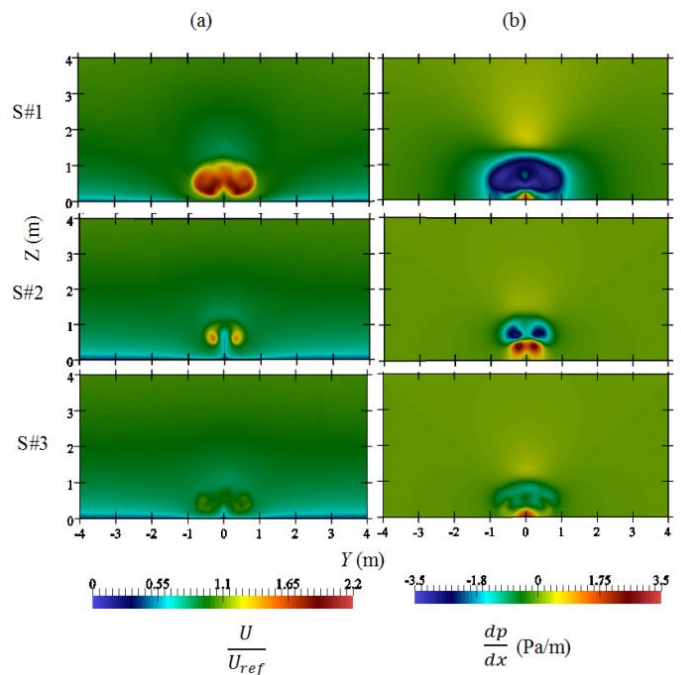


Figure.4 Cross-sectional distribution of (a) normalized velocity and (b) pressure gradient at $X=2.7$ m.

until it reaches to the maximum value immediately downstream of the fire source and then undergoes a gradual reduction further downstream of the fire source.

A similar trend is also observed in Fig. 3. Enlarging the fire source size while the heat release rate is constant does not significantly affect the wind enhancement along the centerline, which is consistent with the trend observed in Fig. 3. In contrast, under constant fire intensity, wind enhancement is considerably augmented in the larger fire source scenario along the centerline, as shown in Figs 3 and 5.

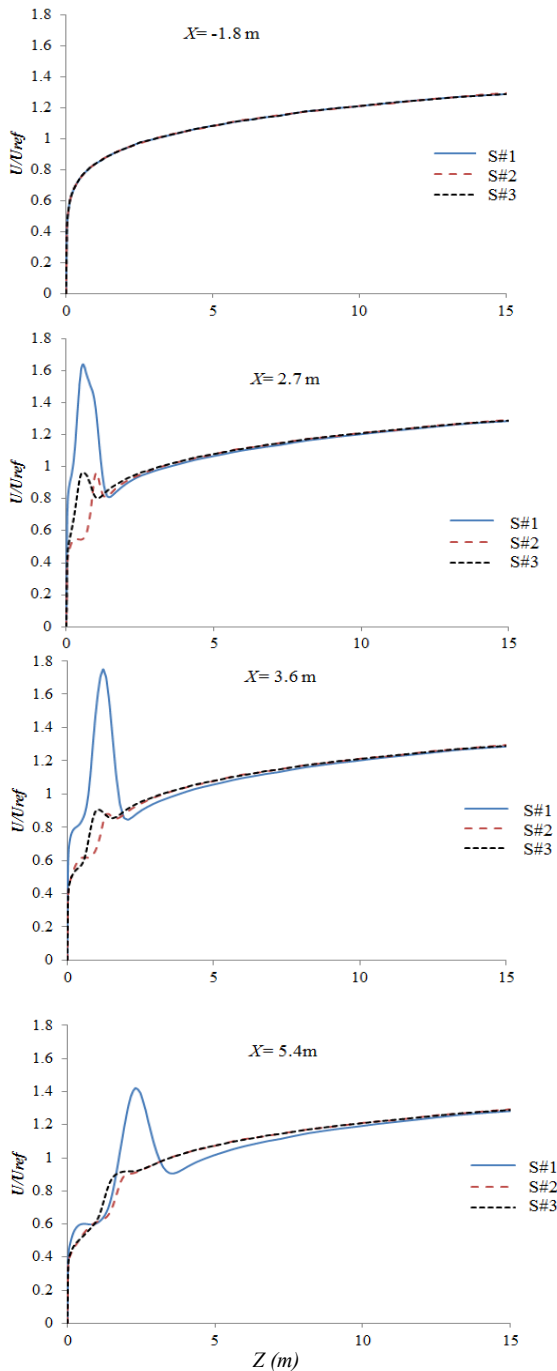


Figure.5 vertical distribution of normalised longitudinal velocity at different distances along the domain centerline ($Y=0$) for different simulation scenarios (#1, #2 and #3).

5. Acknowledgements

This project is funded by the Australian Research Council Discovery Project grant ARC DP160103248.

6. Conclusion

This study applied large eddy simulations to analyse the effects of the size of point source fire on fire-wind enhancement under both constant fire intensity and contact heat release rate. The main findings of this study can be summarized as below:

1- Under constant fire intensity, increasing of fire source size led to a significant increase in wind enhancement. This trend was mainly due to stronger fire-induced pressure force in the larger fire source scenario.

2- Under a constant fire heat release rate, with the increase of fire size, wind enhancement almost remained unchanged along the domain centerline, whereas the maximum wind enhancement, occurring symmetrically at the two sides of domain centerline, considerably reduced when fire source size increased.

3- The region where the wind was enhanced was expanded with the increase of fire source size. Moreover, the fire source size determined the shape of wind enhancement region. The results showed an almost similar wind enhancement region was associated with similar fire source sizes, though the extent to which wind was enhanced was different due to the change in the fire heat release rate.

7. References

- [1] M. Li, C. Wang, Z. Li, S. Yang, K. Fukumoto, and C. Fan, (2018), *Fuel*, **216**, pp. 390-397.
- [2] L. Hu, L. Wu, and S. Liu (2013) *Fuel*, vol. **111**, pp. 613-620,
- [3] L. Hu, S. Liu, J. L. de Ris, and L. Wu (2013) *Fuel*, **106**, pp. 730-736
- [4] F. Ferrero, M. Munoz, and J. Arnaldos, (2007) *Fuel Processing Technology*, **88**, pp.
- [5] J. Welker and C. Sliepcevich, (1966) *Fire Technology*, **2**, pp. 127-135, 1966.
- [6] Y. He, K. C. S. Kwok, G. Douglas, and I. M. Razali (2011) *Fire Safety Science* **10**, pp. 1449-1462.
- [7] T. Hirano and M. Kinoshita, (1975) *Symposium (International) on Combustion* **15**, pp. 379-387
- [8] K. Kwok, Y. He, and G. Douglas, (2012) *Proceedings of the Institution of Civil Engineers-Engineering and Computational Mechanics*, **165**, pp. 253-263.
- [9] E. Eftekharian, Y. He, K. C. S. Kwok, R. H. Ong, and J. Yuan, (2019) *International Journal of Thermal Sciences*, **141**, pp. 84-95
- [10] Y. Wang, P. Chatterjee, and J. L. de Ris, (2011) *Proceedings of the Combustion Institute*, **33**, pp. 2473-2480.
- [11] E. Eftekharian, M. Ghodrat, R. Ong, Y. He, and K. Kwok (2018), in *Australasian Fluid Mechanics Conference*, Adelaide, Australia, 10-13 Dec 2018.
- [12] E. Eftekharian et al., (2019) *Case Studies in Thermal Engineering*, **14**, No. 100467
- [13] C. J. Greenshields, *OpenFOAM Foundation Ltd* (2015), **3**.
- [14] C. J. Wang, J. X. Wen, Z. B. Chen, and S. Dembele, *International Journal of Hydrogen Energy* **39**, pp. 20560-20569
- [15] F. Mathey, D. Cokljat, J. P. Bertoglio, and E. Sergent, (2006) *Progress in Computational Fluid Dynamics*, **6**, pp. 58-67.
- [16] B. J. McCaffrey, *Center for Fire Research National Engineering Laboratory National Bureau of Standards* Washington, D.C, USA NBSIR 79-1910, 1979.

Joint OH-CH PLIF imaging in highly-sheared turbulent premixed propane flames

M.A. Kanj, M.J. Dunn, M. Juddoo, S. Steinmetz, W. Guoqing, A.R. Masri.

School of Aerospace, Mechanical and Mechatronic Engineering
The University of Sydney, NSW, 2006, Australia

Abstract

In this paper we report the structure and stability characteristics of highly-sheared turbulent premixed propane flames using joint OH-CH planar laser induced fluorescence (PLIF) imaging. The burner utilized consists of two concentric tubes for the main jet surrounded by an annular pilot. Turbulent shear is generated by passing different fractions of the fuel-air mixture through the two concentric fuel tubes. The percentage of shear is changed by either changing the velocity difference between the two fuel streams or by changing the recess distance between the concentric fuel tubes. The Bunsen-like flames length shorten, and the flame tip becomes wider downstream with shear rates between the two main jet streams. PLIF imaging of OH and CH show that the flame fragmentation rate increases with the increase in the shear rate, which explains the appearance of local extinction either in the flame sections near the pilot flame. The number of flame segments or number of breaks grows with the rise in the shear rate before settling at specific maximum value. In agreement with many previous studies of turbulent flames over many geometries, an increase in the local extinction near blow-off is observed.

1 Introduction

Highly sheared turbulent premixed flames are now receiving remain extremely difficult to model because of the possible transition in the flame structure between regimes of flamelets and possibly broadened zones which require a different modelling treatment. Earlier work on this topic by Driscoll and co-workers [1] have employed a burner that stabilises highly turbulent premixed flames of methane-air with values of u'/S_l in the range of 25 to 243. They have found that preheat zones (marked by layers of formaldehyde) may be broadened but at much higher turbulence level than originally proposed. However, reaction zones (marked by the layers of CH) remain relatively thin even at values of u'/S_l higher than 200. They have then reported a modified version of the premixed regime diagram which essentially extends the region of relevance of flamelets. The key argument is that sufficiently large turbulent diffusivity is required to force a broadening in the pre-heat zone.

Results obtained from our group using a highly sheared premixed burner support the conclusions of Driscoll et al. [1]. The burner, which is also employed here introduces by splitting the premixed fuel-air mixture into two concentric streams of different velocities. Measurements of PLIF CH-OH have shown that CH layers remain thin and comparable to the laminar flame thickness even close to breakages in the CH layers at high levels of u'/S_l . The paper also reports increasing rate of breakages in the CH layers as shear is increased and the flame shortens marking an approach to extinction.

The paper marks a continuation of the earlier work but with a different fuel, namely propane-air (we use liquid petroleum gas delivered from commercial supplier of LPG in a quality-controlled environment, which is about 90%

propane by volume). The shift to LPG is driven by the need to test fuels of higher carbon content but also with different levels of molecular diffusivity. Turbulent premixed propane/air flames have been tested by Lee et al. [2], where the flame surface properties have been explored at Lewis numbers varying between 0.98 and 1.86 with turbulence intensities normalised by the laminar flame speed varying from 1.42 to 5.71. Thus, the flame structures and thereby flame surface areas and flame pocket areas are affected by Lewis number while the flame curvature and orientation statistics are determined by the turbulence conditions. This paper presents PLIF-CH-OH imaging in LPG-air flames with an equivalence ratio of 0.85 but increasing level of shear. The next section describes the experimental set-up followed by samples images of the flame structure. Section 4 presents an in-depth analysis of the flame structure before the conclusion.

2 Experimental Setup

2.1 Burner setup

In this paper all the flames reported are stabilized on the modified piloted Sydney burner [3-5]. The propane/air mixture was split into two annular concentric tubes residing within the pilot annulus, the 'jet' with inner diameter of 2.5 mm and the 'annulus' with inner diameter, D , of 7.5 mm (0.25 mm wall thickness) as shown in *Figure 1*. In order to have a coflow with a constant speed of 15 m/sec, the burner is surrounded by a 150 mm x 150 mm wind tunnel. The jet inside the annulus can be recessed upstream from $L_r = 0$ cm to 30 cm.

The burner can generate shear induced turbulence in two different ways for a given fixed equivalence ratio, ϕ , and bulk velocity, U_b . By varying the diversion ratio, Q , the volumetric ratio of the stream flowing in the jet divided by the total mixture flow rate of both the annular and the jet tubes. The other way is by changing the recess length of the jet with respect to the annulus where if $L_r = 30$ cm the burner will act as a homogenous burner since all the

Corresponding author. Mohammed Kanj
E-mail address: mkan0694@uni.sydney.edu.au

mixture will be flowing inside the annulus.

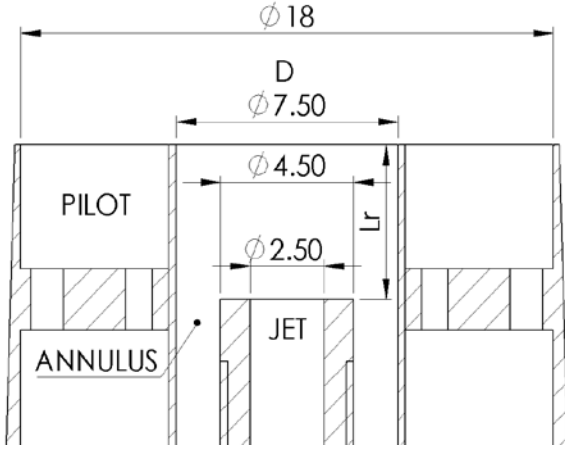


Figure 1: schematic view of the modified Sydney piloted jet burner.

At constant equivalence ratio, ϕ , the growth in the bulk velocity, U_b , and in the diversion ratio, Q , will shorten the flame length, whereas with enlarging the difference in length between the jet and the annulus tubes the flame length increases as shown in previous work [6]. A five-gas pilot (CO_2 , O_2 , C_2H_2 , N_2 and H_2) is utilized, with an unburnt gas velocity of 3.44 m/sec utilized for all cases in this study. Both the adiabatic flame temperature and the C/H ratio of the burnt pilot gases are the same as that of a stoichiometric $\text{C}_3\text{H}_8/\text{air}$ mixture with a heat release of 2.07 kW. A summary of the flame conditions explored in this paper are summarized in **Table 1**.

Table 1: Table of selected flame cases.

Flame	ϕ	U_b m/s	Q	L_f mm	U_j m/s	U_a m/s	U_j/U_a
p085_U80_Q00_Lr300	0.85	80	0	300	0	212.3	0
p085_U80_Q08_Lr035	0.85	80	0.08	35	17	194.7	0.08
p085_U80_Q30_Lr035	0.85	80	0.3	35	63.6	148.1	0.4
p085_U80_Q38_Lr035	0.85	80	0.38	35	80.6	131.5	0.6
p085_U80_Q45_Lr035	0.85	80	0.45	35	95.4	117	0.8
p105_U100_Q00_Lr300	1.05	100	0	300	0	265.2	0
p105_U100_Q08_Lr35	1.05	100	0.08	35	21.2	244.3	0.08
p105_U100_Q30_Lr35	1.05	100	0.3	35	79.6	185.8	0.4
p105_U100_Q38_Lr035	1.05	100	0.38	35	100.8	163.9	0.6
p105_U100_Q45_Lr035	1.05	100	0.45	35	119.2	146.2	0.8

2.2 Joint LIF-OH-CH

A schematic diagram of the high-speed simultaneous CH and OH PLIF imaging system used in this experiment is shown in **Figure 2**. A Sirah Credo dye laser is pumped by a 120 W Edgewave Nd:YAG laser at 532 nm containing DCM in ethanol which forms the CH PLIF system. The $P_1(4)$ line of the CH $\text{C}^2\Sigma^+-\text{X}^2\Pi(0,0)$ system is excited by doubling frequency of the 632 nm dye laser output to get a UV beam at 315.589 nm. At 10 kHz repetition rate, the UV beam pulse energy is 0.2 mJ. A UV laser bandwidth

full width half maximum of $0.25\pm 0.05 \text{ cm}^{-1}$ is obtained from excitation-emission wavelength scans over CH and OH transitions near the $P_1(4)$ CH transition. Before the CH UV beam is focused into a sheet by a 300 mm focal length UV lens, it is expanded to a height of 40 mm. A knife-scanning technique is used to measure the CH UV beam waist at the laser focus to be $210 \mu\text{m}$. A two-stage LaVision IRO image intensifier coupled to a high-speed star 6 (HSS6) camera and two sets of coupled 3-element lenses (CVI LAPQ-APMQ) with a clear aperture of 60 mm are used to collect the CH fluorescence. The CH detection system field-of-view (FOV) is 25 mm x 25 mm with a projected pixel size of $26.75 \mu\text{m}/\text{pixel}$. To minimize interference, a 300 nm long-pass filter (Semrock 300LP) coupled with a 200 ns intensifier gate was applied. For the flames selected in this work, the excitation wavelength and filter are selected in order to maximize the CH signal-to-noise ratio whilst minimizing interferences from OH.

For the OH PLIF, the $Q_1(6)$ line of the $\text{A}^2\Sigma^+-\text{X}^2\Pi(1,0)$ band at 283.011 nm is utilized. A Sirah dye laser containing Rhodamine 6G in ethanol is pumped using a 30 W Edgewave Nd:YAG laser at 532 nm. The UV beam at 283 nm with an energy of 0.1 mJ/pulse at a repetition rate of 10 kHz is generated by doubling the frequency of the dye laser output. Since the focal point of the OH laser sheet needs to be matched with the CH laser sheet, after the 300mm cylindrical focusing lens, a diverging lens is placed after the CH beams has expanded to a height of 40 mm. The OH excitation beam, which has a $180 \mu\text{m}$ waist, is overlapped with the CH UV beam at the probe volume. The OH collection system is identical to the one that is used to capture the CH fluorescence, while a $315 \pm 10 \text{ nm}$ bandpass filter is used to capture the OH fluorescence signal at 314 nm, thereby rejecting interferences from Rayleigh and other spurious scattering processes at 283 nm. To avoid cross talk of OH LIF generated by the OH laser beam onto the CH camera, the OH excitation beam is delayed relative to the CH excitation beam by 250 ns. The projected pixel size of the OH system is $26.75 \mu\text{m}/\text{pixel}$ and the FOV is 25 mm x 25 mm.

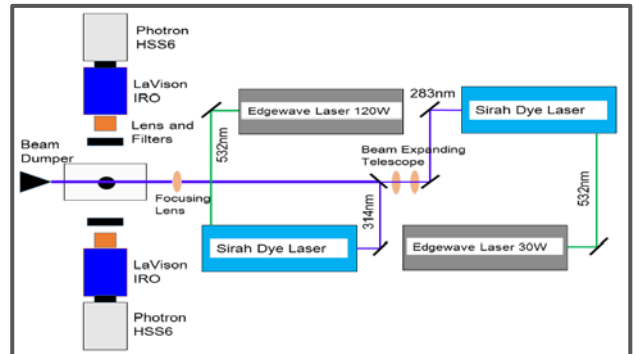


Figure 2: CH and OH LIF imaging optical layout schematic diagram

A polynomial of 3rd order is used to map the OH and CH images as per Soloff et al. [7]. Morning and afternoon image mapping process are employed for every data collection day in order to ensure a reliable overlap of the OH and CH images can be achieved. After image mapping

the background and the mean flame chemiluminescence were subtraction from each OH and CH image and a 2x2 pixel binning of the images, to reduce the amount of data to be processed and to reduce the impact of read noise on the processed image, was applied. The mean flame chemiluminescence images were obtained with the laser blocked, collected from each flame at the respective locations and conditions. A further 2x2 median filter was applied to remove the noise from each image after the correction for the beam profile inhomogeneity.

3 Instantaneous Flame Structure

Figure 3 shows a sample of OH and CH mapped images for flames of different shear levels ($Q= 0, 0.3$ and 0.45) and axial locations for recess length of 35 mm at specific equivalence ratio ($\phi=0.85$) and bulk speed ($U_b=80$ m/sec). For each case two different columns are represented with green color for CH signal and pink for OH signal as shown the color scale knowing that the results presented here are qualitative. Due to the pilot flame, the CH and OH layer are adjacent near the jet exit except for 45% shear flame which is close to blow-off. The OH broad region is anticipated in the pilot stream and further downstream because of the hot combustion products. On the other side the CH layers are known as thin layers and they provide a marker of the OH inner boundaries. The CH layer starts to break-up progressively with moving downstream due to local extinction or the transmission of local extinction occurred in previous flame locations.

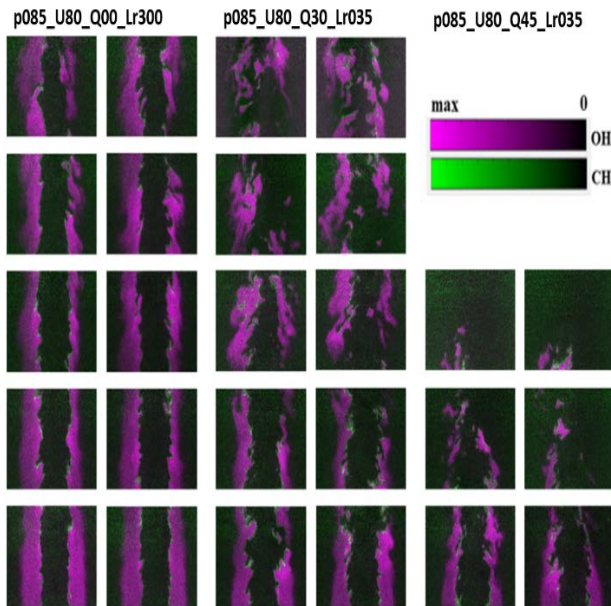


Figure 3: Temporal sequence of instantaneous 10 kHz images of joint LIF-CH-OH for flames of $\phi=0.85$, $U_b=80$ m/sec, with $Q=0, 0.3$, and 0.45 .

4 Image Analysis

4.1 Edge Tracing Methodology

A threshold must be applied to the collected images in order to draw the edges of CH and OH areas and to delineate the relevant information in each image. After the basic image processing outlined in section 3 a

thresholding method is employed. The OH and CH images have different features, therefore a different thresholding method for each image is employed to produce high quality results. A local skeletal tracing method to determine the thin CH profiles is used in this study following the method developed and outlined by Skiba et al. [8]. In **Figure 4** a sample image is used to show step-by-step the method used to obtain the CH layer and thickness.

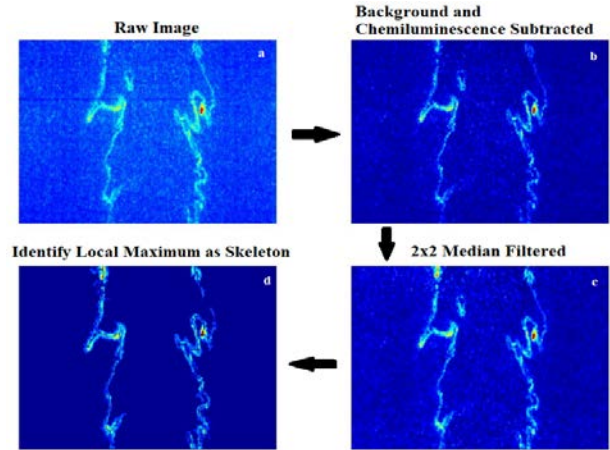


Figure 4: Sample CH image passing through the processing method applied to extract the CH skeleton. a) Raw image; b) background and chemiluminescence correction applied; c) using a 2x2 median filter; d) expressing the local maximum as skeleton.

Ohtsu et al. [9] expanded an automatic thresholding method that looks over each OH image and apply a threshold that uses Fukunaga et al. [10] analysis to peak the discriminant criterion. The OH images are binarized and the OH boundary is determined after applying the combined Ohtsu et al. [9] and Fukunaga et al. [10] methods. The OH boundary is only the inner unburned side of the flame as shown in **Figure 5**. This method cannot be used with CH images because it will produce erroneous fragments. The length of the OH and CH edges is then determined after applying the OH boundary tracing and the CH skeletal tracing.

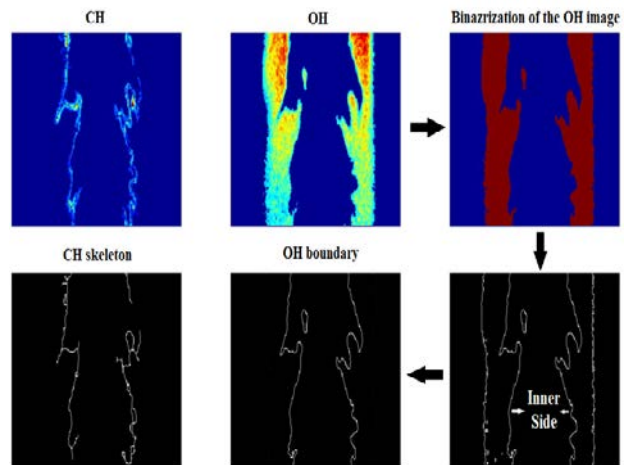


Figure 5: Reading out the OH boundary after the binarisation of the image.

4.2 Frequency of Flame Breakages

The CH Skeleton is extracted using the procedure described in Section 4.1 as well for the OH boundary using the automatic threshold method. The number of segments in the OH layer is then subtracted from that of the CH layer and as a result the number of breakages in the CH layer, N_{break} , is calculated manually as shown in **Figure 6**.

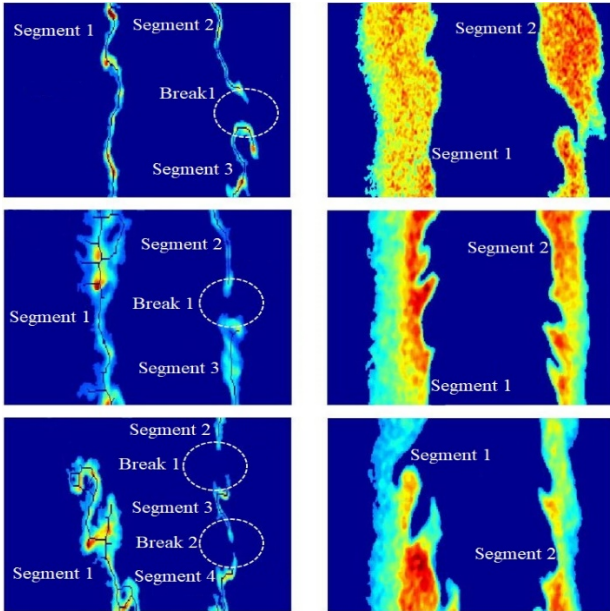


Figure 6: CH and OH images are used to show how the method works in calculating the number of breakages in each image.

The fragmentation level in the flame can be deduced from the number of breakages in the flame front which may occur either from local extinction or quenching events. The means, for 100 images per axial location, of the flame breakages (N_{break}) at different axial locations for two different equivalence ratio ($\phi=0.85$ and 1.05) flames are presented in **Figure 7**.

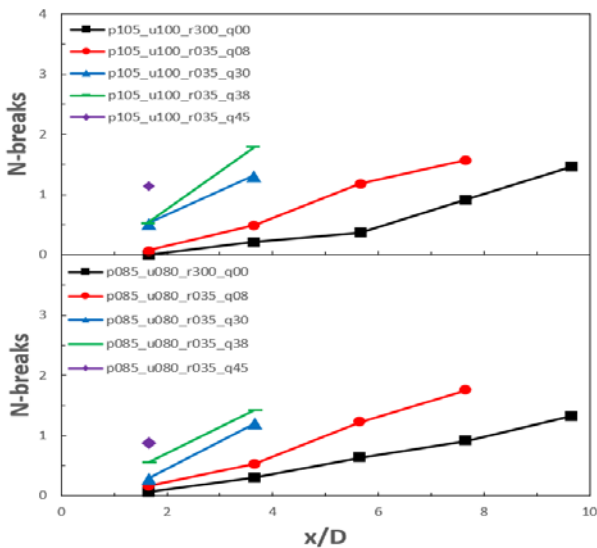


Figure 7: Mean Number of breakages, N_{break} , along the jet flame downstream.

5 Conclusions

The study of the impact of shear rate and equivalence ratio of piloted premixed flames using propane as fuel has been studied in this paper using joint imaging PLIF imaging of OH and CH. The major conclusions of this study are:

- With increasing shear rates between the two jet streams the flame length decreases, and the flame tip opens with the flame heat release zone transitioning from a conical to a cylindrical structure.
- For increasing shear rates, local extinction starts to appear in the flame at regions downstream and then with further increases in the shear rate local extinction events start to occur near the pilot flame.
- Increasing the rate of turbulent shear increases the fragmentation rates and the breakage rates with axial locations.
- In comparison to the results of methane flames [6], we can recognize a reduction in the fragmentation rates for propane flames.

6 Acknowledgment

Work at the University of Sydney was supported by the Australian Research Council.

7 References

- [1] T. M. Wabel, A. W. Skiba, J. E. Temme, J. F. Driscoll, Measurements to determine the regimes of premixed flames in extreme turbulence, *Proceedings of the Combustion Institute*, 2017, Vol.36(2), pp.1809-1816.
- [2] T. W. Lee, G. L. North, and D. A. Santavicca, Surface Properties of Turbulent Premixed Propane/Air Flames at Various Lewis Numbers, *Combustion and Flame* 93:445-456 (1993).
- [3] S. Meares, A.R. Masri, A modified piloted burner for stabilizing turbulent flames of inhomogeneous mixtures, *Combust. Flame* 161 (2014) 484-495.
- [4] S. Meares, V.N. Prasad, G. Magnotti, R.S. Barlow, A.R. Masri, Stabilization of piloted turbulent flames with inhomogeneous inlets, *Proc. Combust. Inst.* 35 (2015) 1477-1484.
- [5] R.S. Barlow, S. Meares, G. Magnotti, H. Cutcher, A.R. Masri, Local extinction and near-field structure in piloted turbulent CH₄/air jet flames with inhomogeneous inlets, *Combust. Flame* 162 (2015) 3516-3540.
- [6] W. Jin, S.A. Steinmetz, M. Juddoo, M.J. Dunn, Z. Huang, A.R. Masri, Effects of Shear Inhomogeneities on the Structure of Turbulent Premixed Flames, *11th Asia Pacific Conference on Combustion (ASPACC 2017)*, Shanghai: The Combustion Institute.
- [7] S.M. Soloff, R.J. Adrian, Z.C. Liu, Distortion compensation for generalized stereoscopic particle image velocimetry, *Meas. Sci. Tech.* 8 (1997) 1441-1454.
- [8] A.W. Skiba, T.M. Wabel, C.D. Carter, S.D. Hammack, J.E. Temme, J.F. Driscoll, Premixed flames subjected to extreme levels of turbulence part I: Flame structure and a new measured regime diagram, *Combust. Flame* 189 (2018) 407-432.
- [9] N. Ohtsu, A Threshold Selection Method from Gray-Level Histograms, *IEEE Trans. Sys., Man and Cybernetics* 9 (1979) 62-66.
- [10] K. Fukunaga, Introduction to statistical pattern recognition (2nd ed.), *Academic Press Professional, Inc. San Diego, CA, USA*, 1990.

Ignition Waves in Compartment Fire Flashover

Vasily Novozhilov *

Centre for Environmental Safety and Risk Engineering (CESARE), College of Engineering and Science, Victoria University,
Victoria, Australia

Abstract

Flashover is the most dangerous stage of compartment fire development. This is a transition from slowly growing to fully developed fire, associated with rapid growth of fire size. Primary mechanism for such transition is ignition of all available fuel in the compartment by radiation from hot smoke layer formed by the initial, slowly growing fire. Although this mechanism is well recognised, its details are difficult to investigate, both theoretically and experimentally. Existing models assume that ignition process occurs instantaneously once radiation level in the compartment reaches critical values. Close examination of rare experimental data reveals that ignition, in fact may occur in the form of wave propagating across compartment combustible load. The aim of the paper is, first to estimate the rate of such propagation from available experimental data. Secondly, it seeks to propose a model which captures essential physics of the process and can describe ignition wave propagation. Ignition front position, as a function of time is extracted from experimental data. It is found that ignition wave accelerates, at least in a particular experiment considered. Non-linear integral equation that describes propagation of such type of combustion wave is derived. Equation appears to be rather complicated and will likely require numerical methods for its analysis.

Keywords: Ignition Wave, Fire, Flashover

1. Introduction

Flashover is one of the two (along with fire ignition) major instabilities observed in compartment fires. In qualitative terms, this is a transition from slowly growing to fully developed fire. One of principal mechanisms of flashover is ignition of virgin combustible materials by radiation emitted from hot smoke layer. The latter is generated by the initial fire. More detailed view reveals that ignition of virgin material occurs in the form of wave.

The present paper discusses the basic flashover scenario which proceeds through ignition of virgin fuel. The mechanism of ignition wave initiation and propagation is discussed, along with experimental evidence of this phenomenon. The rate of propagation is extracted, for the first time, from available experimental data. The theory of the phenomenon is presented, in particular the equation that governs the spread of ignition wave is derived.

2. Description of the mechanism

2.1 Flashover

Flashover is a very rapid transition from slowly growing initial fire to fully developed fire, whose Heat Release Rate (HRR) is substantially higher. Generally, flashover is also a demarcation point between fuel-controlled and ventilation-controlled fire burning regimes. Possibility of flashover makes compartment fires especially dangerous.

Obviously, substantial increase of fire HRR requires growth in fire area. This may only be achieved via involvement (ignition) of virgin (i.e. not involved in the initial fire) combustible materials available in the compartment.

Fire area may grow by different mechanisms. First, flame may spread, as a combustion wave, igniting nearby layers of solid material. This is a conventional mechanism of flame spread over solid fuels, which is observed during slowly growing stage of fire.

Such flame spread is, however too slow to cause sudden transition in fire behavior.

An alternative mechanism which, in fact leads to flashover is an ignition of virgin materials by radiation. The latter is emitted by hot smoke layer, developed over initial fire. This mechanism, if occurs, results in a very quick involvement of virgin fuel as radiation fills the compartment rather uniformly.

The sketch of such flashover mechanism is presented in Fig. 1.

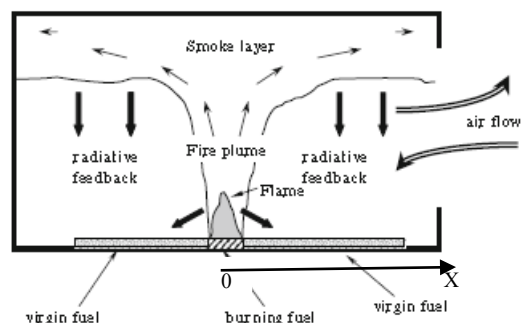


Figure 1: Flashover development via ignition of virgin materials by smoke layer radiation

Quantitatively, flashover may be correlated with radiation levels on the floor of the compartment reaching the values of the order of $15\text{-}20\text{ kW/m}^2$. Such radiation fluxes are sufficient for ignition of most solid combustible materials, initially existing at room temperature.

Another quantitative criterion for flashover is a quick rise of compartment temperature to $500\text{-}600\text{ }^\circ\text{C}$.

Finally, quite often compartment windows gets broken at this stage, and flames ejecting from windows into surrounding may be seen. This phenomenon is a visual indication of flashover.

The described flashover mechanism has been discussed in the literature. For example, Graham *et al.* [1] presented one-equation model for temperature evolution of the smoke layer (see also subsequent references to similar models in their paper). Novozhilov [2] developed more consistent approach using two-variable model where both temperatures of the smoke layer and the virgin fuel are followed.

The model [2] allows critical conditions for flashover to be predicted in terms of compartment configuration, fuel properties and HRR of initial fire. Ignition of virgin materials is considered as an instantaneous process in the model.

2.2 Ignition wave during flashover

Experimental data on flashover are rare due to necessity to create relatively well-controlled large scale fires.

Examination of available evidence reveals that ignition process during flashover occurs rapidly but not instantaneously.

Such conclusion is derived, for example, from experimental tests conducted by former Fire Research Station (FRS, UK) in the course of replicating a Stardust nightclub fire in Dublin in 1981.

FRS created an elongated compartment (similar to short tunnel) with one end closed. Number of rows of seats were installed on the floor.

Initial fire was initiated at the closed end of the compartment. As initial fire develops and forms smoke layer an ignition wave spreading through the seat rows may eventually be seen. As the wave travels magnitude of fire increases since ignited seats contribute to HRR.

Exact parameters of the experiment are not known. Basic estimation of the speed of propagation of ignition wave maybe be obtained, nevertheless from the experiment video [3].

3. Ignition wave speed from experimental data

In this section we present the result of processing the video experimental data [3].

Several successive images of high temperature soot-laden ceiling jet and ignition wave are presented in Figs 2-5. Overall time span of the process visualized in Figs. 2-5 is about 25 s.

The plot of ignition front position as a function of time is produced by considering video images in the Figs. 2-5 and making estimation of the relative distance travelled by the front over specified time intervals.



Figure 2: Ignition wave initiation. Assigned time $t=0$ s.



Figure 3: Ignition wave propagation, $t=13$ s.



Figure 4: Ignition wave propagation, $t=20$ s.



Figure 5: Ignition wave propagation, $t=21$ s.

This plot is presented in Fig. 6. Due to apparent limitation of estimation accuracy, and the absence of exact parameters of the FRS experiment, we are only interested here in the qualitative propagation velocity behavior. That is, the major question of interest is whether ignition wave accelerates, decelerates, or spreads with approximately constant speed.

Intuitively, one would expect that flashover is associated with acceleratory ignition.

This intuitive expectation is generally supported by the data in Fig. 6.

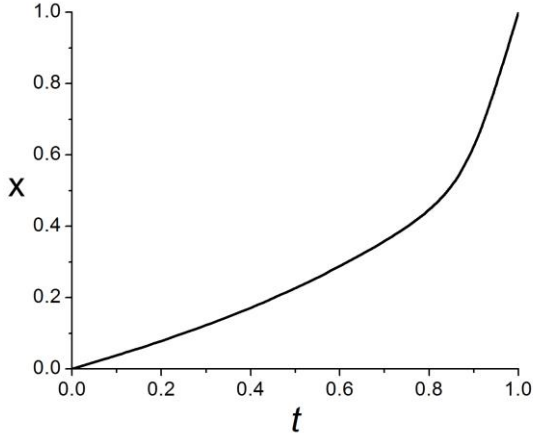


Figure 6: Estimated position of ignition front, as a function of time.

Fig. 6 is presented in non-dimensional variables where distance is normalized by the maximum visible length of the region where ignition wave propagates, and time by the overall propagation time inferred from the video.

Overall acceleration of the ignition wave is evident. The last section of the curve (from 0.9 to 1.0 in non-dimensional time) describes a very short period of time of just several seconds. Due to limited accuracy it is difficult to distinguish between the linear and non-linear curve behavior in this region. Nevertheless, the wave seems still be slightly accelerating. It is believed that acceleration would be more evident if experimental data beyond this point were available.

4. Basic theory

4.1 Condition of existence

Let us assume that initial fire is burning at steady-state rate.

In order for ignition wave to be initiated, the following condition must be met.

Radiative flux emitted by smoke, at least at the location of the initial fire source ($x = 0$, Fig. 1), must reach a level sufficient for ignition of virgin fuel.

This condition is met if $\exists t_{cr} < \infty$ such that

$$T_s(0) - T_0 = -\frac{1}{\sqrt{\lambda\rho c}} \frac{1}{\sqrt{\pi}} \int_0^{t_{cr}} \frac{\dot{q}(0,\tau)}{\sqrt{t_{cr} - \tau}} d\tau \quad (1)$$

where $T_s(0) \equiv T_s(x) \equiv T_s$ is a critical surface temperature of the material required for ignition, λ , ρ and c are thermal properties of solid combustible material, t time,

and $\dot{q}(0,\tau)$ radiative flux absorbed by the material at the location $x = 0$.

The relation (1) is a well known basic relation, which is a consequence of the heat transfer equation and relates temperature at any location within the domain with the time history of heat flux at the same location (e.g. Landau and Lifshits [4]).

Radiative heat flux at the origin of the coordinate system (Fig. 1) is given by

$$\dot{q}(0,\tau) = -\varepsilon\sigma W \int_0^\infty F(x,0) (T_g^4(x) - T_0^4) dx \quad (2)$$

Here ε is emissivity, σ Stefan-Boltzmann constant, W compartment width (i.e. dimension perpendicular to the direction of ceiling jet propagation, Fig. 2-5) and

$$F(x,0) = \frac{\cos(\theta_1)\cos(\theta_2)}{\pi r^2} \quad (3)$$

is a “kernel” of the expression for a view factor between the two infinitesimal surfaces (Ozisik [5]).

In the case considered in the present section (i.e. steady-state fire) the flux (2) does not actually depend on time, but the formula (2) is written in a general form bearing in mind its application to time-dependant flux later in the section 4.3.

Actual temperature distribution along the ceiling jet, in a steady-state fire, can be obtained from the experiments and theoretical model by Tanaka and Novozhilov [6]. Their investigation shows exponential decay of temperature downstream the ceiling jet, which also conforms with the results of other studies. Specifically [6]

$$T_g(x) = T_0 + (T_g(W/2) - T_0) \exp\left(-\frac{hP}{\dot{m}c_p} x\right) \quad (4)$$

where T_g is ceiling jet temperature, T_0 is ambient temperature, c_p gas specific heat, h heat transfer coefficient for losses to compartment walls, P part of compartment cross-sectional perimeter corresponding to locations of contact between walls and hot smoke.

Mass flow rate \dot{m} is given by

$$\dot{m} = \frac{(1 - \gamma_r)\dot{Q}}{c_p(T_g(0) - T_0)} \quad (5)$$

where \dot{Q} is fire HRR, γ_r a fraction of HRR emitted as radiation.

For a typical cellulosic material the critical temperature is $T_s \sim 873$ K. The ceiling jet temperatures at the two specific locations $T_g(0)$ and $T_g(W/2)$ may be estimated using well-known Alpert correlations [7].

Combined with the formulae (2-5), the condition (1) provides restriction on the minimum fire HRR, which is required to initiate the ignition wave.

4.2 Ignition wave driven by steady-state fire

For instructive purposes it is useful to consider ignition wave driven by steady-state fire.

If ceiling jet attains steady-state condition, radiative flux at each location on the floor of the compartment remains constant. The magnitude of the flux decreases along the floor away from fire, i.e. with increasing coordinate x . This is an experimental fact, which can also be formally derived from the model (2-5).

The basic theory of ignition of thermally thick materials may be applied. Specifically, it is well known [8] that in such a case the inverse of square root of ignition time is proportional to applied heat flux. This implies

$$t_{cr} \sim \frac{1}{\dot{Q}^2(x)} \quad (6)$$

Ignition wave propagation velocity must drop with travelling distance, at least after certain point, since at sufficiently far locations radiative flux is too weak to cause ignition (i.e. ignition time turns into infinity). This obviously contradicts experimental observations, Fig. 6.

In reality, radiation from the ceiling jet is augmented, of course, by involvement of the fuel ignited at the wave front and burning continuously behind it.

General equation describing propagation of ignition wave must take this effect into account.

4.3 Equation for ignition wave propagation

In this section we derive general equation which describes ignition wave propagation.

Let $x(t)$ be current position of ignition front. Here time is therefore, a critical (ignition) time as in the equation (1); we drop the subscript to have conventional notation for independent variable in the final equation.

Effect of virgin fuel involvement along propagation of the ignition front is described by modification of the mass flow rate as follows

$$\dot{m} = \frac{(1 - \gamma_r) [\dot{Q} + W \dot{m}_f^n Q_{comb} x(t)]}{c_p (T_g(0) - T_0)} \quad (7)$$

where \dot{m}_f^n is mass burning rate, per unit area, of the ignited fuel, Q_{comb} is heat of combustion of materials in the compartment.

Radiative flux at any location $y \geq 0$ is given by

$$q(y, \tau) = -\varepsilon \sigma W \int_0^\infty F(\xi, y) (T_g^4(x(\tau), \xi) - T_0^4) d\xi \quad (8)$$

Now the flux is indeed time-dependent, due to equation (7) which implies that the distribution $T_g(y)$ depends on the

position $x(t)$ as a parameter. The equation for flame (ignition front) spread is obtained by applying the general integral relation (1) at the position $x(t)$

$$T_s - T_0 = \frac{\varepsilon \sigma W}{\sqrt{\lambda \rho c}} \frac{1}{\sqrt{\pi}} \times \quad (9)$$

$$\times \int_0^t \int_0^\infty F(\xi, x(t)) (T_g^4(x(\tau), \xi) - T_0^4) d\xi \frac{d\tau}{\sqrt{t - \tau}}$$

Initial condition for the flame front is $x(0) = 0$.

Here the temperature distribution along the jet is given by the equation (4) with the mass flow rate substituted from equation (7), and the temperature $T_g(\dot{m}, W/2)$ adjusted for the current mass flow rate accordingly. The equation (9) is of rather complicated nature. It is a non-linear repeated integral equation. As a future work, it is planned to classify wave propagation regimes that can be obtained from this equation. In particular, we are interested in whether it admits acceleratory solutions that agree qualitatively with experimental data in Fig. 6. Another question is whether it admits solutions with constant speed of propagation, similar to many other types of waves observed in combustion systems. For example, flame spread on vertical combustible walls may theoretically occur at constant speed, although at very specific values of material parameters.

It is conjectured that equation (9) has only acceleratory solutions. An attempt will be made to prove this statement rigorously, i.e. by analytical methods. On the other hand, it is clear that in general case the equation (9) will need be solved numerically.

Validation of the model is intended using a set of reduced-scale well controlled experiments. The experiments are likely to be conducted by collaborators from the University of Fukui, Japan.

5. Conclusions

Experimental data has been processed to obtain ignition front time history plot during flashover in compartment fires. It is demonstrated that ignition wave propagates in acceleratory manner.

A non-linear integral equation describing ignition wave propagation during compartment fires is proposed.

6. References

- [1] Graham, T.L., Makhviladze, G.M. and Roberts, J.P. (1995) *Fire Saf. J.* **25**, pp. 229–259.
- [2] Novozhilov, V. (2010) *J. Eng. Math.* **67(4)**, pp. 387–400.
- [3] <http://bufvc.ac.uk/dvdfind/index.php/title/781>.
- [4] Landau, L.D. and Lifshits, E.M. (1987) *Fluid Mechanics*, 2nd ed., Oxford, Butterworth-Heinemann.
- [5] Ozisik, M.N. (1985) *Heat Transfer. A Basic Approach*, New York, McGraw Hill.
- [6] F. Tanaka and V. Novozhilov, Predicting Fire Spread in a Tunnel using Simple Theoretical Model, *Twelfth Asia-Pacific Conference on Combustion (ASPACC 2019)*, 2019.
- [7] Evans, D.D. (1995) In: *SFPE Handbook of Fire Protection Engineering* (DiNenno et al., Eds.), Quincy, National Fire Protection Association.
- [8] Panagiotou et al. (1991) *Combust Flame*, **84**, pp. 223–.

Grid Sensitivity Study for Air Blast Atomisation Using an LES-PDF form of ELSA Model

F. Abbas^{1,*}, G. Tretola², M. J. Cleary¹, S. Navarro-Martinez², A. R. Masri¹

¹School of Aerospace, Mechanical and Mechatronic Engineering, The University of Sydney, Sydney 2006, NSW, Australia

²Department of Mechanical Engineering, Imperial College, London SW7 2AZ, UK

Abstract

The Eulerian–Lagrangian Spray Atomisation (ELSA) model is employed here to study the grid sensitivity and grid convergence for air-blast atomising. The sub-grid joint probability density function (PDF) of liquid volume fraction and surface density is solved in the LES context. Different grid resolutions are used to investigate the grid sensitivity and simulated results are compared with the normalised liquid volume fraction measured in an atomizing spray using the Sydney needle spray burner. This paper focuses on reporting the effects of mesh size on the liquid jet penetration and jet decay rate. Mean axial and radial profiles of liquid volume fraction and surface density for 4 million and 8 million cells are reasonably close to each other in comparison with 1 million and 2 million cells. This indicates that grid convergence is approached.

1. Introduction

The continuous development in the field of high-performance computers is helping in having necessary computing power in order to completely resolve up-to full-scale injector level. Two dimensional direct numerical simulations (DNS) under conditions similar to those of practical injectors were done by Boeck et al. [1] and Fuster et al. [2], and three dimensional DNS studies by Desjardins et al. [3], Herrmann [4] and Menard et al. [5]. Daily use of DNS under real injector conditions is still beyond the current computing limits, so we need models to capture most of the desired information about primary zone of the atomization. In past, many approaches have been developed for this attempt but two of them such as Volume of Fluid (VoF) and Level Set (LS) have proved helpful for simulating multiphase flows. Tryggvason et al. [6] has provided a detailed review on this subject. The VoF method is available in some open source CFD software including *OpenFOAM* in the form of *interFoam*, *twoLiquidMixingFoam* and *twoPhaseEulerFoam* solvers. On the other side, LS is found only in-house research codes [7] and not linked with *OpenFoam* yet.

In an earlier paper [8], the Eulerian–Lagrangian Spray Atomisation (ELSA) model was introduced with the longer-term objective of accounting for the primary atomization of air-blasted sprays. The LES framework was employed to solve a transport equation for the joint volume-surface density sub-grid Probability Density Function (PDF) and hence account for sub-grid fluctuations of the surface density and liquid volume fraction. A key advantage of this approach lies in combining the advantages of Volume of Fluid (VoF) and Level Set (LS) methods to account for atomization while capturing realistic surface effects and preserving mass conservation. The results shown in [8] were encouraging when compared to experimental data obtained in air-blast atomising sprays of acetone fuel stabilized on the Sydney Needle burner. The objective of this paper is to extend this approach by testing the effects of grid size on the results.

In LS method liquid-gas interface is represented by a level set function (φ). Its positive value ($\varphi > 0$) indicates the liquid region and negative value ($\varphi < 0$) indicates the gas region. The interface is represented by having level set function value equal to zero ($\varphi = 0$). The main advantage of level set (LS) method is its simplicity, especially in calculating the curvature κ .

The unit normal vector \mathbf{n} and curvature κ are computed as follows

$$\mathbf{n} = \frac{\nabla\varphi}{|\nabla\varphi|} \quad (1)$$

$$\kappa = \nabla \cdot \frac{\nabla\varphi}{|\nabla\varphi|} \quad (2)$$

These interface-tracking approaches have been used successfully in many cases but still suffer from numerical limitations, which effect their accuracy. The VoF method [8, 9] behaves well in terms of mass conservation but tends to be artificially diffusive so that it smears out the sharp interface, while the LS method [10] accumulates a mass conservation error at the interface. When they are used in combination [5], both sharp interface capturing and mass conservation issues have been resolved but very high computational resources are required to simulate a full scale practical injector.

The Eulerian–Lagrangian Spray Atomisation [11] (ELSA) model is based on VoF but solves for an additional surface (area) density quantity to provide an enhanced statistical quantification of the atomising spray. In LES of turbulent sprays the liquid volume fraction and surface density fluctuate at the subgrid scale and the recently proposed approach to solve for the joint probability density function (PDF) of these quantities is emerging as an attractive closure of these terms [12]. The ELSA-PDF methods has been previously tested against DNS of a high-pressure liquid injection into quiescent air. In this work as well as in [8], the ELSA approach is validated against experimental data and the objective in this paper is to report on the grid sensitivity.

2. Methodology

The ELSA model is based on solving two equations corresponding to the *liquid volume fraction* and *surface (area) density* in an Eulerian frame. The origin of the ELSA model can be traced back to the Volume of Fluid (VoF) method [9]. This approach is suitable to simulate both dense and dilute regions of the spray and subsequently the model does not need coupling with a secondary Lagrangian scheme. The model gives directly relevant quantities for spray characterisation such as Sauter Mean Diameter (SMD) and liquid dispersion based on simple relations between surface density and volume. However, a drawback of ELSA method is that it cannot distinguish between spherical droplets and

* Corresponding author. Email: fabb9259@uni.sydney.edu.au

irregular shaped ligaments with the same volume and surface density. The method has been used mostly in the RANS [13] framework and was only recently extended to LES [12].

As volume fraction and surface density fluctuate at the small, unresolved scales, one closure approach is to solve a sub-grid PDF equation for these quantities and to couple it to the conventional filtered LES equations for mass and momentum.

The incompressible instantaneous continuity equation is

$$\frac{\partial \rho}{\partial t} + u_j \frac{\partial \rho}{\partial x_j} = 0 \quad (3)$$

where u is velocity of fluid, ρ is the single density of the fluid mixture calculated as

$$\rho = \rho_l(\phi) + \rho_g(1 - \phi) \quad (4)$$

Here ρ_l is density of liquid phase, ρ_g is density of the gas phase and ϕ is liquid volume fraction. Based on the continuity equation, the liquid volume fraction equation can be written as

$$\frac{\partial \phi}{\partial t} + u_j \frac{\partial \phi}{\partial x_j} = 0 \quad (5)$$

and the surface density equation is given by

$$\frac{\partial \Sigma}{\partial t} + \frac{\partial u_j \Sigma}{\partial x_j} = - \partial \Sigma n_i n_j \frac{\partial u_j}{\partial x_j} \quad (6)$$

where Σ is the surface density defined as interface surface area per unit volume. In LES the above equations are filtered and subgrid models are required for the subgrid correlations of velocity, volume fraction and surface area. The final closed sub-grid joint PDF transport equation for the subgrid joint probability density of liquid volume fraction and surface density, P_{sgs} is written as [12]:

$$\frac{\partial P_{sgs}}{\partial t} + \frac{\partial \bar{u}_j P_{sgs}}{\partial x_j} = \frac{\partial}{\partial x_j} \left[\mathcal{D}_{sgs} \frac{\partial P_{sgs}}{\partial x_j} \right] - \frac{\partial S_{gen} P_{sgs}}{\partial \theta_2} + \frac{\partial S_{des} P_{sgs}}{\partial \theta_2} \quad (7)$$

\bar{u}_j is filtered velocity, \mathcal{D}_{sgs} represents subgrid diffusivity, θ_2 is sample space for surface density, S_{gen} is generation of surface area due to atomisation and S_{des} is destruction of surface area due to collision and coalescence. Their modelling is described in Ref. [12].

We solve an equivalent stochastic form of Eq. (7) based on the concept of stochastic fields [12], where the discrete PDF is obtained by summation over N fields

$$P_{sgs} = \frac{1}{N} \sum_{\alpha=1}^N \delta[\theta_1 - \phi^\alpha] \delta[\theta_2 - \Sigma^\alpha] \quad (8)$$

Here ϕ^α and Σ^α are the volume fraction and surface density for stochastic field α , and θ_1 and θ_2 are the sample spaces for ϕ and Σ . Following the Ito formulation, the transport equations for each field are

$$\frac{d\phi^\alpha}{dt} + \bar{u}_j \frac{\partial \phi^\alpha}{\partial x_j} = \frac{\partial}{\partial x_j} \left[\mathcal{D}_{sgs} \frac{\partial \phi^\alpha}{\partial x_j} \right] + \sqrt{2\mathcal{D}_{sgs}} \frac{\partial \phi^\alpha}{\partial x_j} dW_j^\alpha \quad (9)$$

$$\frac{d\Sigma^\alpha}{dt} + \bar{u}_j \frac{\partial \Sigma^\alpha}{\partial x_j} = \frac{\partial}{\partial x_j} \left[\mathcal{D}_{sgs} \frac{\partial \Sigma^\alpha}{\partial x_j} \right] + \sqrt{2\mathcal{D}_{sgs}} \frac{\partial \Sigma^\alpha}{\partial x_j} dW_j^\alpha + S_{gen}^\alpha - S_{des}^\alpha \quad (10)$$

The notation dW^α is a Wiener term. Note that the stochastic fields are discontinuous in time but differentiable in space (which is a point of difference with stochastic particle solutions of the PDF). Statistical quantities are obtained from the fields, for example the first moment is obtained as

$$\bar{\phi} = \frac{1}{N} \sum_{\alpha=1}^N \phi^\alpha \quad (11)$$

3. Numerical Set Up

The model is compared to experimental data from the Sydney Needle Spray Burner [14] which issues dense liquid (acetone) from a needle surrounded by an air-blast stream. The diameter of the liquid jet is 670microns and that of the air blast stream is 10mm. A single case is selected here for comparison with data and this Case 2 (N-AS2) which corresponds to a liquid loading of 75g/min. Further details about this case are shown in Table 1. This case is named with reference N=Needle, A=Acetone, S for non-reacting sprays.

Table 1: Boundary conditions for test case [14]. Re_g and Re_l refer to the Reynolds numbers of the air and liquid, respectively, U_g and U_l are the gas and liquid velocities, and We is the jet exit Weber number based on bulk gas velocity.

Cases	N-AS2(Case 2)
U_g (m/s)	36
Re_g	21800
U_l (m/s)	4.3
We	45
Re_l	7300
F/A (by mass)	0.36

The computational domain is a three-dimensional cylinder that is 50mm in the axial direction and 5mm in the radial direction. In the simulations the turbulent intensity at the liquid inlet plane is 5% of the bulk velocity and the turbulent length scale is 10% of the nozzle diameter. A Klein digital filter [15] is used to produce a realistic turbulent spectrum at the inflow. Four different mesh resolutions are selected for this study. Total number of cells, number of cells in liquid jet diameter, minimum and maximum aspect ratios are provided in Table 2. Aspect ratio is minimum along the axial centre of the jet and increases in radial directions. Maximum aspect ratio value given in Table 2 belongs to the outer locations of air jet region.

Table 2: Mesh details for four different resolutions.

Resolution (in millions)	Number of cells in liquid jet	Minimum aspect ratio	Maximum aspect ratio
1M	1000*15*15	1.05	11.00
2M	1200*21*21	1.26	10.20
4M	1500*25*25	1.17	10.50
8M	1800*32*32	1.26	9.97

4. Results and Discussion

Predicted and experimental mean liquid fraction along the centre of jet for Case 2 are represented in Figure 1. In this study, we have analysed the effect of mesh resolution on jet penetration and jet decay rate. Only measured mean liquid area fraction values are available till now, measured mean liquid volume fraction values will be provided at a later stage. Predicted values for liquid jet penetration and jet decay rates for all the mesh resolutions are overall in good agreement

with the experimental data. However, as we increase the mesh resolution, the jet penetration slightly increases, and jet decay rate considerably decreases. When we compare the results for different mesh resolutions, 4M and 8M results are reasonably close in comparison with 1M and 2M resolutions.

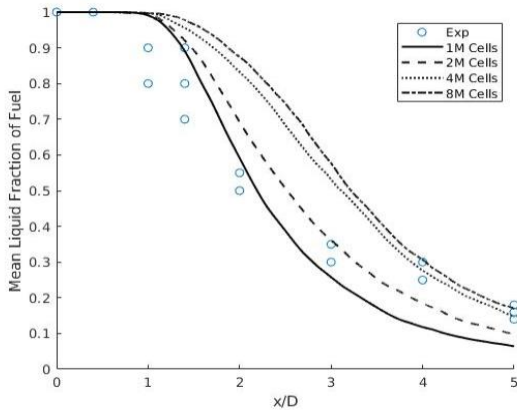


Figure 1: Axial profiles of mean liquid fraction and sensitivity to mesh resolution are represented here. Symbols refer to measured mean liquid area fraction while lines represent the calculated mean liquid volume fraction.

Figures 2&3 provides the comparison of radial profiles of mean liquid volume fraction at $x/D=1$ and $x/D=2$ respectively. At $x/D=1$ all the mesh resolutions give the similar values. For $x/D=2$ location 4M and 8M profiles are closer with each other but different with 1M and 2M mesh resolutions. The variations in peak values of mean liquid volume fraction are higher as we move from 1M to 2M and 4M resolutions and reduces considerably when we change mesh resolution from 4M to 8M.

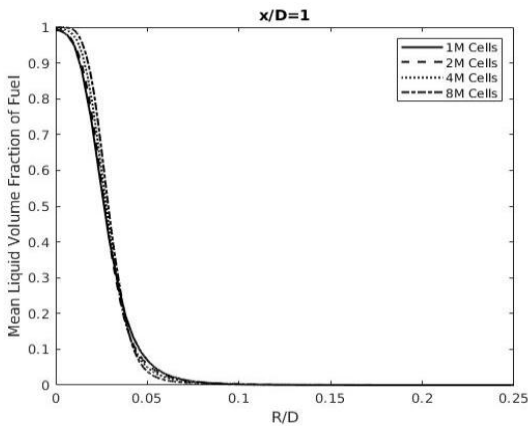


Figure 2: Radial profiles of mean liquid volume fraction at $x/D=1$ representing sensitivity to mesh resolution.

Simulated pattern of jet penetration and decay rate is represented in Figure 4. Jet penetration is almost similar, but decay rate and pattern are different for all mesh resolutions. When the mesh resolution increased from 1M to 2M and 4M, we get the longer jet penetration and less decay rate but for 8M cells jet penetration and decay rate pattern is similar to 4M cells confirming the reach of grid convergence.

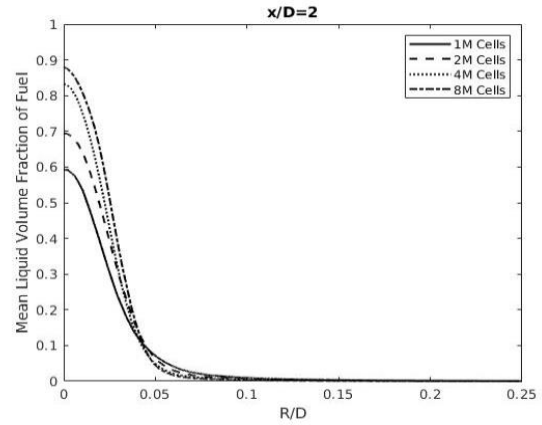


Figure 3: Radial profiles of mean liquid volume fraction at $x/D=2$ representing sensitivity to mesh resolution.

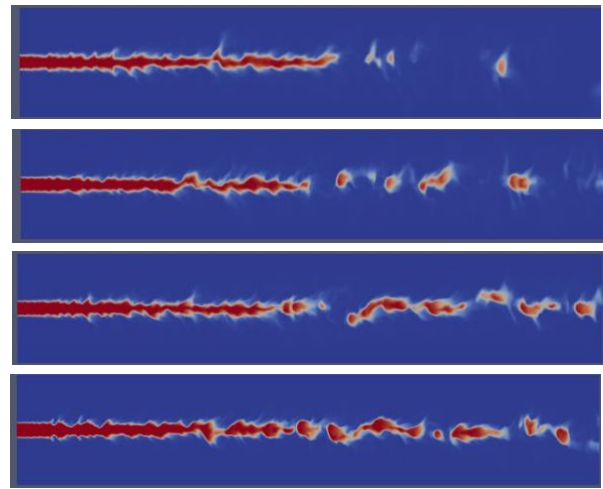


Figure 4: Liquid jet penetration and decay for 1M, 2M, 4M and 8M mesh resolutions in order from top to bottom

Axial profiles for normalised mean surface density are shown in Figure 5. The peak value change considerably for 1M to 2M and 4M mesh resolutions but this difference is very small for 4M and 8M cells cases. Results for different mesh resolutions shows the similar behaviour like mean liquid fraction profiles. Values for 4M and 8M cells are comparably close in comparison to values for 1M and 2M cells.

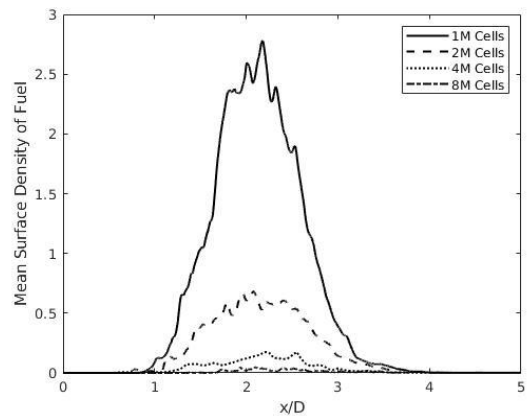


Figure 5: Axial profiles of mean surface density and sensitivity to mesh resolution

Figures 6 & 7 represent the radial profiles for normalised mean surface density for $x/D=1$ and $x/D=2$ locations respectively. At $x/D=1$ location, the peak value of the radial profile changes with mesh resolution. This difference is higher for lower resolution cases in comparison with high resolution meshes. For 4M and 8M cases, these profiles are very close giving a good indication of reach of grid sensitivity. At $x/D=2$ location, change in the peak value of the radial profile for different mesh resolutions is similar to that of at $x/D=1$ but the peak value for 4M and 8M cases are almost the same.

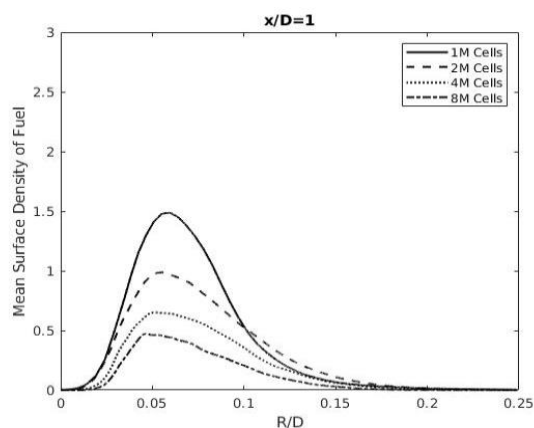


Figure 6: Radial profiles of mean surface density at $x/D=1$ representing sensitivity to mesh resolution

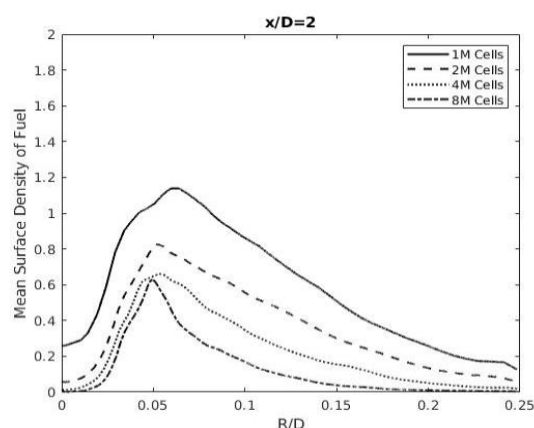


Figure 7: Radial profiles of mean surface density at $x/D=2$ representing sensitivity to mesh resolution.

5. Conclusions

This LES-PDF solution of ELSA formulation is applied to an air-blast experimental atomisation case for the first time. Mean, axial plots of liquid volume fraction show good qualitative agreement with experimental data. Mesh resolution affects the jet penetration very slightly, but also changes the decay rate very considerably. Radial profiles for mean liquid volume fraction and normalised mean surface density at different radial locations for four different mesh resolutions show that the results for 4M and 8M cells are comparable with each other and largely different to that of 1M and 2M cells resolutions. Future work will explore the grid sensitivity convergence for comparatively higher Weber number cases.

6. Acknowledgements

This work is supported by the Australian Research Council. The authors acknowledge the University of Sydney HPC service at The University of Sydney for providing computational resources used for these simulations.

7. References

- [1] T. Boeck, J. Li, E. López-Pagés, P. Yecko, S. Zaleski, Ligament formation in sheared liquid–gas layers, *Theor. Comp. Fluid. Dyn.* 21 (2007) 59-76.
- [2] D. Fuster, A. Bagué, T. Boeck, L. Le Moyne, A. Leboissetier, S. Popinet, P. Ray, R. Scardovelli, S. Zaleski, Simulation of primary atomization with an octree adaptive mesh refinement and VOF method, *Int. J. Multiphase Flow* 35 (2009) 550-565.
- [3] O. Desjardins, V. Moureau, H. Pitsch, An accurate conservative level set/ghost fluid method for simulating turbulent atomization, *J. Comput. Phys.* 227 (2008) 8395-8416.
- [4] M. Herrmann, Detailed numerical simulations of the primary breakup of turbulent liquid jets, *Proc. 21st Annual Conf. ILASS-Americas, 2008*, (2008).
- [5] T. Ménard, S. Tanguy, A. Berlemont, Coupling level set/VOF/ghost fluid methods: Validation and application to 3D simulation of the primary breakup of a liquid jet, *Int. J. Multiphase Flow* 33 (2007) 510-524.
- [6] G. Tryggvason, R. Scardovelli, S. Zaleski, *Direct numerical simulations of gas–liquid multiphase flows*, Cambridge University Press 2011.
- [7] T. Pringuey, R.S. Cant, Robust Conservative Level Set Method for 3D Mixed-Element Meshes—Application to LES of Primary Liquid-Sheet Breakup, *Commun. Comput. Phys.* 16 (2014) 403-439.
- [8] F. Abbas, G. Tretola, M. J. Cleary, S. Navarro-Martinez A. R. Masri, On the use of LES-PDF form of the Eulerian–Lagrangian Spray Atomisation (ELSA) model to simulate air blast atomisation, 12th Asia-Pacific Conference on Combustion,, Fukuoka International Congress Center, Fukuoka, Japan, 2019.
- [9] C.W. Hirt, B.D. Nichols, Volume of fluid (VOF) method for the dynamics of free boundaries, *J. Comput. Phys.* 39 (1981) 201-225.
- [10] M. Sussman, P. Smereka, S. Osher, A level set approach for computing solutions to incompressible two-phase flow, *J. Comput. Phys.* 114 (1994) 146-159.
- [11] A. Burluka, R. Borghi, Development of a Eulerian model for the “atomization” of a liquid jet, *Atomization Sprays* 11 (2001).
- [12] S. Navarro-Martinez, Large eddy simulation of spray atomization with a probability density function method, *Int. J. Multiphase Flow* 63 (2014) 11-22.
- [13] N. Beheshti, A.A. Burluka, M. Fairweather, Assessment of Σ -Y liq model predictions for air-assisted atomisation, *Theor. Comp. Fluid. Dyn.* 21 (2007) 381-397.
- [14] A. Lowe, A. Kourmatzis, A.R. Masri, Turbulent spray flames of intermediate density: Stability and near-field structure, *Combust. Flame* 176 (2017) 511-520.
- [15] M. Klein, A. Sadiki, J. Janicka, A digital filter based generation of inflow data for spatially developing direct numerical or large eddy simulations, *J. Comput. Phys.* 186 (2003) 652-665.

Particle-intense MMC-LES simulations of mixed-mode turbulent piloted jet flame

S. Aldawsari¹, S. Galindo-Lopez, M.J. Cleary and A.R. Masri

The University of Sydney, School of Aerospace, Mechanical and Mechatronic Engineering,
NSW, 2006, Australia

Abstract

The Lagrangian multiple mapping conditioning model coupled with large eddy simulation (MMC-LES) is applied to compute the structure of a turbulent piloted jet flame with compositionally inhomogeneous inlet. The calculations are compared with detailed measurements. Our current version of sparse-Lagrangian MMC-LES employs only a mixture-fraction-based approach that is suitable for non-premixed combustion. Increasing the number density of particles drives a gradual transition to an intensive MMC-LES to enable the computation of mixed-mode combustion in this flame. This intensification is applied in upstream regions where mixed-mode combustion dominates and is relaxed further downstream as the jet flame transitions to a non-premixed flame structure. The computed results for intensive and adaptive cases converge and the simulation results for the adaptive case show good agreement with experimental data.

Keywords: Turbulent flames; Partially premixed; MMC-LES.

1. Introduction

In recent times premixed combustion has been favoured for power generation, internal combustion engines and other propulsion systems for its ability to conform to progressively stricter regulations for toxic pollutant emissions. However, in practice, perfect premixing may be impossible to achieve and, such mixing imperfections may change combustion stability compared to non-premixed designs. Mixed-mode combustion systems, containing both premixed and non-premixed regions, are a pragmatic solution aimed at achieving low emissions and stability over a wide range of engine operating conditions [1]. Non-premixed and premixed combustion research have developed largely as separate branches and many combustion models and laboratory experimental flames have been developed with one of the two combustion modes in mind. An exception is the probability density function (PDF) model [2] which is derived independent of the flame mode. However, in its conventional form, the PDF approach is the most computationally costly of the available turbulent combustion models and application to engineering scale systems is limited. To enable the development of reliable numerical tools that span all combustion domains, the University of Sydney's piloted burner with compositionally inhomogeneous inlets [3] has been developed as a platform for validating models with mixed-mode capability. The burner consists of concentric pipes carrying fuel and air. The central one may be recessed to different retraction lengths resulting in different levels of mixing and inhomogeneity at the burner exit plane. In the configuration investigated in the present work, fuel issues from the central pipe and air flows in the outer one and the recess distance is set so that the mean mixture fraction at the outer edge of the mixing pipe is close to stoichiometric while richer mixtures exist towards the axis. The ensuing flame has a mixed-mode structure near the burner exit plane that transitions to a non-premixed mode downstream.

A number of turbulent models have been tested using the Sydney inhomogeneous burner. These include LES with various forms of the flamelet model [4, 5], a hybrid method combining the filtered density function (FDF) approach with flamelet tabulation [6] and full finite-rate chemistry [7], the multi-environment RANS-PDF method [8], and the sparse MMC-LES method [9] whose further development is presented here.

Sparse MMC-LES [10] is a FDF method that incorporates concepts from the conditional moment closure (CMC) [11] and flamelet models to close the molecular mixing term and achieve high accuracy at lower computational cost than FDF methods with conventional mixing models. This is done by mixing locally in a reference space that correlates with the composition space while being mathematically independent of it. The LES filtered mixture fraction is a suitable reference variable for non-premixed flames and alternatives such as a reaction progress variable [12] or shadow position [13] can be used for premixed flames. By ensuring that mixing is compositionally local, the requirement for localness in physical space can be relaxed and this enables the use of a sparse distribution of notional particles to solve the FDF stochastic transport equations. In sparse simulations there are fewer particles than LES grid cells and the opposite (conventional) situation where there are more particles than LES grid cells is referred to as intensive simulations. Galindo et al. [9] applied sparse MMC-LES with a mixture fraction reference variable to the aforementioned Sydney burner for a homogeneous non-premixed case (i.e. zero recess distance) and an inhomogeneous case. Agreement with the experimental data was good for the homogeneous inlet case but, for the inhomogeneous case, the model did not accurately capture the premixed flame structure close to the pilot and this leads to accumulated errors in the non-premixed region downstream. Current research is developing sparse MMC-LES with two reference variables representing reaction

progress and mixture fraction to capture the premixed and non-premixed flame structures, respectively [12]. While steady progress is being made on this complex two reference variable sparse MMC-LES model, the present paper explores a conceptually simple, MMC-LES model that relies on using a larger number of particles in regions where mixed-mode combustion is present. This selective intensification (referred to hereon as adaptive) is expected to result in localness in physical space in those regions and hence facilitating the computation of premixed as well as non-premixed flames. This is combined with a sparse particle distribution and mixing localness in reference mixture fraction space in region where the non-premixed mode dominates. In a previous contribution describing this approach (referred to there as “hybrid” but here called “adaptive”), MMC-LES [14] explored numerical convergence with increasing stochastic number of particles. The present paper focuses on a comparison of the adaptive version of this model where intensification is selective and applied only to region where mixed-mode combustion prevails.

2. Methodology

2.1 The model

MMC-LES is a combination of Eulerian and Lagrangian methods. Filtered equations for continuity, momentum, pressure and reference mixture fraction are simulated in an Eulerian fashion using a standard Smagorinsky subgrid model [15]. The reactive scalars are simulated in a stochastic Lagrangian frame to represent the FDF. Particle pairs are mixed linearly and over a finite time step according to

$$\phi_\alpha^p(t + \Delta t) = \phi_\alpha^p(t) + \gamma \left(\bar{\phi}_\alpha^{p,q}(t) - \phi_\alpha^p(t) \right) \quad (1)$$

$$\phi_\alpha^q(t + \Delta t) = \phi_\alpha^q(t) + \gamma \left(\bar{\phi}_\alpha^{p,q}(t) - \phi_\alpha^q(t) \right) \quad (2)$$

where γ is the mixing extent based on Lagrangian mixing time scale τ . Here we use the anisotropic (a-ISO) time scale model [16] and $\bar{\phi}_\alpha^{p,q}$ is the weighted mean of the mixing particles. Mixing pairs are selected to have controlled localness in both physical space, x , and a reference mixture fraction space, f , which is given by the filtered Eulerian mixture fraction field. The degree of localness in f and x is specified by the characteristic model parameters f_m and r_m , respectively. In this calculation, $f_m = 0.03$ and this is based on what has been found through studying the partially premixed methane-air flames [17] and r_m is obtained by

$$r_m = C_m \left(\frac{df}{dn} \frac{\Delta_L^3}{r_c^{2-D_f} D_f f_m} \right) \quad (3)$$

where $C_m = 0.5$ is a constant, the fractal dimension $D_f = 2.36$, Δ_L is the nominal spatial distance between Lagrangian particles and r_c is the inner cut off scale given by the grid size. df/dn is the reference mixture fraction gradient normal to the stoichiometric contour. The selection

of particle pairs, p and q , is based on an algorithm which approximately minimises the effective square distance

$$\hat{d}_{p,q}^2 = \sum_{i=1}^3 \left(\sqrt{3} \frac{d_{x_i}^{p,q}}{r_m} \right)^2 + \left(\frac{d_f^{p,q}}{f_m} \right)^2 \quad (4)$$

where $d_{x_i}^{p,q}$ is the distance between the particles in spatial coordinate i and $d_f^{p,q}$ is the distance between particles in reference mixture fraction space. With fixed f_m and intensification of the particle distribution, Eq. (4) leads to smaller r_m , and subsequently smaller $d_f^{p,q}$.

2.2 Numerical and test case setup

Adaptive MMC-LES predictions are compared to experimental data for the Sydney piloted jet burner [3]. Here we focus on a single, mixed-mode flame case with a bulk jet velocity of 80 m/s and the inner fuel pipe recess distance is 75 mm. The internal diameters of the inner and outer pipes carrying the fuel and air stream are 4.00mm and 7.5 mm, respectively. The jet Reynolds number is 37500.

The MMC-LES model has been implemented in a solver called mmcFoam [18] that is compatible with the opensource OpenFOAM code [19]. The computational domain consists of a 3D cylindrical mesh that extends for 32 jet diameters in the axial direction and 6 jet diameters in the radial direction. The LES computational domain has 1.7 million cells with the smallest cells on the centerline being 0.246 mm x 0.246 mm x 0.29 mm. More than 80% of turbulent kinetic energy is resolved. An additional supermesh is used to control the number of stochastic particles. A uniformly distributed supermesh is used for both an intensive case 4L/1E (4 Lagrangian particles per 1 Eulerian cell) and a sparse case 1L/27E (1 Lagrangian particles per 27 Eulerian cells). A non-uniform supermesh is used for adaptive case. Between the burner exit plane and $x/D = 1$ (where $D=7.5$ mm) each supermesh cell contains eight LES cells. The supermesh then expands gradually with downstream distance until $x/D = 30$ where each supermesh cell contains 400 LES cells. The stochastic particle number control algorithm [18] nominally maintains the particle density at 80 particles per supermesh cell. In this way the number of stochastic particles per LES (Eulerian) cell decreases from an intensive distribution of 10 particles per LES cell (10L/1E) near the burner exit plane to one particle for every 5 LES cells (1L/5E) downstream as shown in Figure 1. Our numerical convergence investigation [14] demonstrated that the predictions with this adaptive stochastic particle distribution are very close to those with a fully intensive MMC-LES simulation. The computational cost for adaptive case is approximately three times cheaper than intensive case.

The boundary conditions for mixture fraction and velocity at the jet exit plane are obtained using separate turbulent pipe flow simulations. The employed chemical mechanism is DRM-22[20] which includes 22 species and 104 reactions.

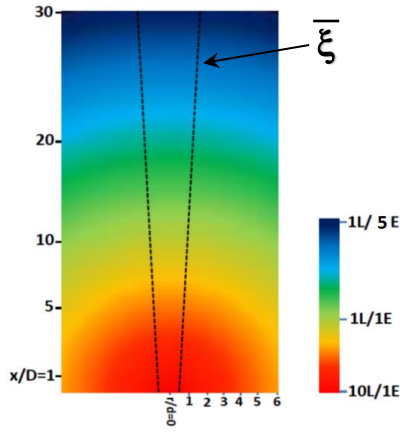


Figure 1: The distribution for the number of particles along the domain for adaptive case. Dash lines represent the average stoichiometric mixture fraction.

3. Results and discussion

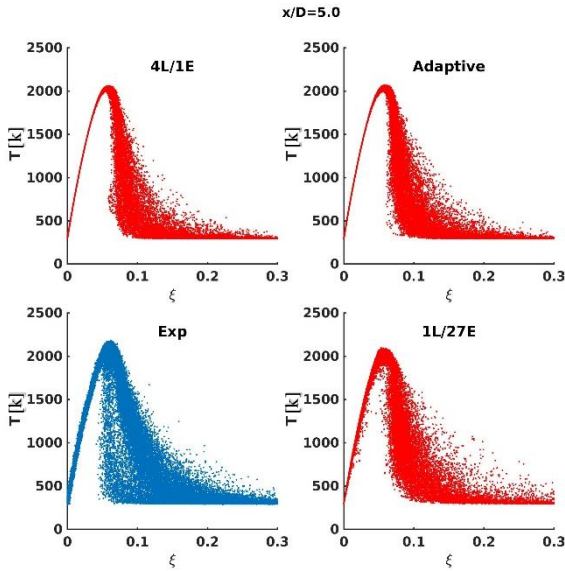


Figure 2: Scatter plots of temperature versus mixture fraction for 4L/1E, adaptive and 1L/27E cases at $x/d=5.0$.

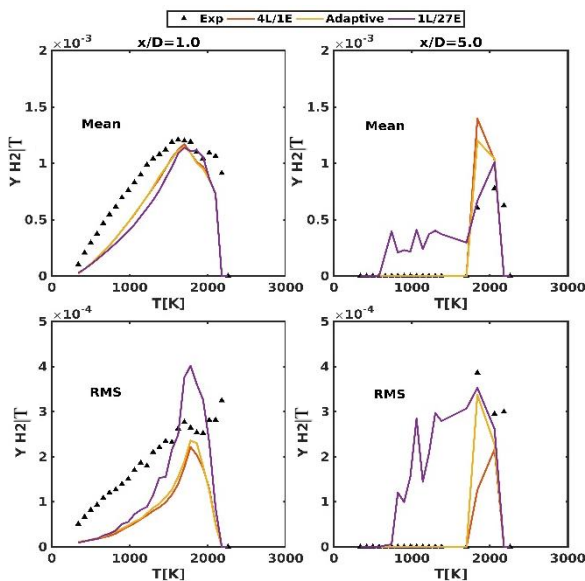


Figure 3: Conditional mean and rms of H_2 for 4L/1E, adaptive and 1L/27E cases at $x/D=1.0$ and $x/d=5.0$.

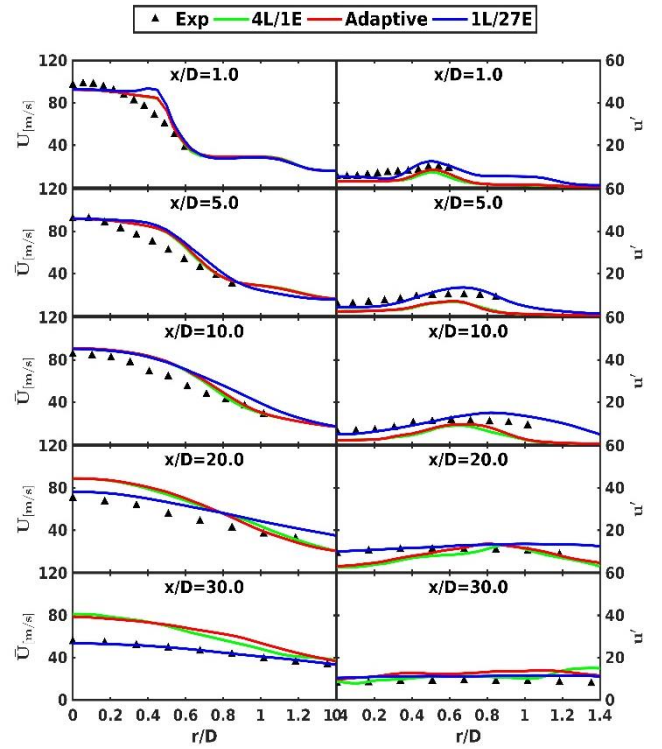


Figure 4: Radial profiles of mean and rms of axial velocity for all cases at different axial locations.

Figure 2 shows scatter plots of temperature versus mixture fraction at $x/D=5.0$. The first row shows scatter plots for intensive (4L/1E) and adaptive cases and the second row shows for experimental data and sparse (1L/27E) case. The computed results of scatter plots for all cases are similar and show good agreement with experimental data. The model results accurately capture the premixed structure with a near-vertical increase in temperature in the stoichiometric region of mixture fraction space.

Figure 3 shows means and rms profiles of the mass fraction of H_2 conditioned on temperature at $x/D=1$ and $x/D=5$. The numerical results were calculated using fluid samples in a mixture fraction interval of $0.04 < \xi < 0.06$. The premixed structure of flame is analysed for intensive, adaptive and sparse particle numbers and compared with experimental data. The conditional mean profiles for all cases at $x/D=1$ are similar but the results for the conditional rms reveal significant difference between the sparse case (1L/27E) and the intensive (4L/1E) and adaptive cases. Note that the adaptive case has an intensive distribution corresponding to 10L/1E at this location. The 4L/1E and adaptive predictions have minimal differences. The simulation results show slightly under prediction for the conditional mean and rms at $x/D=1$ in comparison with the experimental data. At $x/D=5$ the differences between the fully sparse case and, adaptive and intensive are evident for mean and rms profiles, with the sparse case exhibiting higher values for mean and rms for temperatures between 800K and 1800K. For this axial position, in general, the 4/1E and adaptive simulations show good agreement with the experiments.

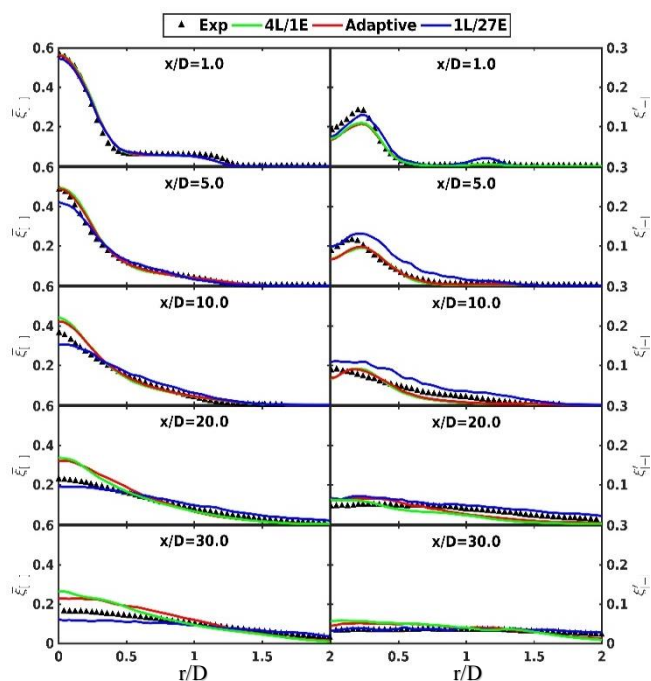


Figure 5: Radial profiles of mean and rms of mixture fraction for all cases at different axial locations.

Figure 4 shows radial profiles of mean and rms of axial velocity for intensive case, adaptive case, sparse case and experimental data at different axial locations. The computed results for intensive and adaptive cases are numerically converged. The results for both cases show good agreement with the experiment at the jet centreline up to $x/d=10.0$ with some over prediction at the interface of the jet and pilot. This could be due to slow transition from premixed flame structure to non-premixed structure as shown [14] and the premixed flame in this region tends to protect the jet velocity from decay. This lower decay at upstream locations results in an over prediction of the jet centreline velocity at downstream locations. The computed rms values of axial velocity are under predicted at most axial locations. This under prediction of results could be coming from jet inflow boundary condition. Figure 5 shows radial profiles of unconditional mean and unconditional rms of mixture fraction for all computed cases and experiment data at different axial locations. The computed unconditional mean and unconditional rms of mixture fraction are in excellent agreement with the experiment at upstream locations. At $x/D=10$ the simulation results appear to be slightly over predicted for mean profile near jet centreline and trend remains same further downstream. The reasons behind these slight variations are lower RMS velocity and slow decay of the mean velocity.

4. Conclusions

A turbulent piloted flame with a compositionally inhomogeneous inlet is simulated using the adaptive-Lagrangian MMC-LES. It is found that in the regions of the flame where mixed-mode combustion prevails, intensive and adaptive results are numerically converged. The computational cost for adaptive case is cheaper than the intensive case by a factor of about three. Additionally,

simulation results for adaptive case generally show good agreement with experimental data. However, the computed results for sparse case are inconsistent with the intensive and adaptive cases for conditional and unconditional quantities at all locations.

5. Acknowledgments

This research is supported by the Australian Research Council. The authors acknowledge the Sydney Informatics Hub and the University of Sydney's high performance computing cluster Artemis for providing the high performance computing resources that have contributed to the research results reported within this paper.

6. References

- [1] D. Rosenberg, P. Allison, J. Driscoll, Method to Measure Flame Index in a Partially-Premixed Gas Turbine Combustor, 51st AIAA Aerospace Sciences Meeting including the New Horizons Forum and Aerospace Exposition, American Institute of Aeronautics and Astronautics 2013.
- [2] S.B. Pope, PDF methods for turbulent reactive flows, Progress in Energy and Combustion Science 11 (1985) 119-192.
- [3] S. Meares, A.R. Masri, A modified piloted burner for stabilizing turbulent flames of inhomogeneous mixtures, Combustion and Flame 161 (2014) 484-495.
- [4] K. Kleinheinz, T. Kubis, P. Trisjono, M. Bode, H. Pitsch, Computational study of flame characteristics of a turbulent piloted jet burner with inhomogeneous inlets, Proceedings of the Combustion Institute 36 (2017) 1747-1757.
- [5] B.A. Perry, M.E. Mueller, A.R. Masri, A two mixture fraction flamelet model for large eddy simulation of turbulent flames with inhomogeneous inlets, Proceedings of the Combustion Institute 36 (2017) 1767-1775.
- [6] M. Rieth, J.-Y. Chen, S. Menon, A.M.J.C. Kempf, Flame, A hybrid flamelet finite-rate chemistry approach for efficient LES with a transported FDF, 199 (2019) 183-193.
- [7] H. Wang, P. Zhang, A unified view of pilot stabilized turbulent jet flames for model assessment across different combustion regimes, Proceedings of the Combustion Institute 36 (2017) 1693-1703.
- [8] N. Kim, Y.J.C. Kim, Flame, Multi-environment probability density function approach for turbulent partially-premixed methane/air flame with inhomogeneous inlets, 182 (2017) 190-205.
- [9] S. Galindo, F. Salehi, M.J. Cleary, A.R. Masri, MMC-LES simulations of turbulent piloted flames with varying levels of inlet inhomogeneity, Proceedings of the Combustion Institute 36 (2017) 1759-1766.
- [10] M.J. Cleary, A.Y. Klimenko, A detailed quantitative analysis of sparse-Lagrangian filtered density function simulations in constant and variable density reacting jet flows, Physics of Fluids 23 (2011) 115102.
- [11] A.Y. Klimenko, R.W. Bilger, Conditional moment closure for turbulent combustion, Progress in energy and combustion science 25 (1999) 595-687.
- [12] C. Straub, A. Kronenburg, O.T. Stein, R.S. Barlow, D. Geyer, Modeling stratified flames with and without shear using multiple mapping conditioning, Proceedings of the Combustion Institute 37 (2019) 2317-2324.
- [13] B. Sundaram, A.Y. Klimenko, A PDF approach to thin premixed flamelets using multiple mapping conditioning, Proceedings of the Combustion Institute 36 (2017) 1937-1945.
- [14] S. Aldawsari, S. Galindo-Lopez, M.J. Cleary and A.R. Masri, An analysis of sensitivity to mixing distance in MMC-LES of a mixed-mode turbulent piloted jet flame, 12th Asia Pacific Conference on Combustion The Combustion Institute (2019).
- [15] J. Smagorinsky, GENERAL CIRCULATION EXPERIMENTS WITH THE PRIMITIVE EQUATIONS, Monthly Weather Review 91 (1963) 99-164.
- [16] S. Vo, O.T. Stein, A. Kronenburg, M.J. Cleary, Assessment of mixing time scales for a sparse particle method, Combustion and Flame 179 (2017) 280-299.
- [17] Y. Ge, M. Cleary, A.J.P.o.t.C.I. Klimenko, A comparative study of Sandia flame series (D-F) using sparse-Lagrangian MMC modelling, 34 (2013) 1325-1332.
- [18] S. Galindo-Lopez, F. Salehi, M.J. Cleary, A.R. Masri, G. Neuber, O.T. Stein, A. Kronenburg, A. Varna, E.R. Hawkes, B. Sundaram, A.Y. Klimenko, Y. Ge, A stochastic multiple mapping conditioning computational model in OpenFOAM for turbulent combustion, Computers & Fluids 172 (2018) 410-425.
- [19] H.G. Weller, G. Tabor, H. Jasak, C. Fureby, A tensorial approach to computational continuum mechanics using object-oriented techniques, Computers in physics 12 (1998) 620-631.
- [20] A.K.a.M. Frenklach, DRM22, <http://www.me.berkeley.edu/drm/>.

CFD modelling of DC arc plasma system for application in cleaner chemical production

Jyothikrishna Perambadur¹, Alexander Klimenko², Pradeep Shukla³, Victor Rudolph¹

¹School of Chemical Engineering Technology, The University of Queensland, Brisbane, Australia

²School of Mech and mining, The University of Queensland, Brisbane, Australia

³Queensland Alliance of Environmental Health Sciences, The University of Queensland, Brisbane, Australia

Abstract

Near-atmospheric thermal plasma systems in chemical processing usually make use of the tail flame of the arc column. Many plasma-based waste destruction and metal processing technologies have been developed, though there are very few that use the plasma for synthesis reactions. This is, in part, impaired by usually extreme conditions and difficulties in modelling these reactions. The modeling of arc discharge in thermal plasma requires a combination of mutually related fluid dynamics and electromagnetic phenomena, which dictate the size and stability of the arc column. We start with a simplified tip and cup based geometry, neglecting swirl, which is often used in practice to stabilize the arc. To this end, we present a steady-state fluid model of plasma torch in OpenFOAM (CFD package), in which the plasma fluid equations along with electric and magnetic potential equations are solved in LTE (Local thermodynamic equilibrium). The simulations were carried out with various currents and different inlet plasma gas flow rates. The model illustrates the influence of inlet gas velocities and how it drags the arc column to downstream of the plasma torch showing the dominance of fluid force over the Lorentz forces within the plasma system. The current model neglects high level of turbulence generated by swirl and the accompanying reabsorption of radiant energy commonly present in commercial systems.

Keywords: tail flame, arc discharge, Lorentz force, etc.

1. Introduction

Thermal plasma is used as a heat source in many industrial processes, including plasma spraying, plasma welding and nano particle synthesis. Features that make the thermal plasma an efficient heat source are high heat flux, high quenching rates and low processing times. The basic configuration (see Fig 1) that can produce thermal plasma consists of anode, cathode, and plasma containing chamber. The electric arc is generated between the cathode and anode when these two are connected to high power DC [1]. The electric arc heats the gas in the plasma chamber and creates thermal plasma. Gases which are most often used to generate plasma, are argon, hydrogen, helium, and nitrogen.

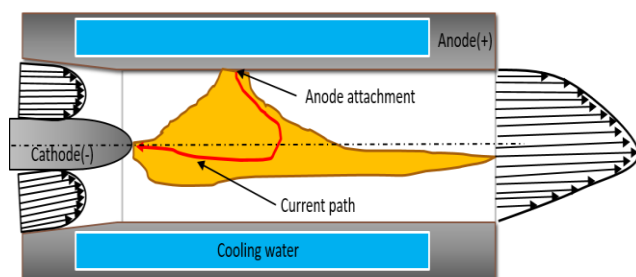


Figure 1 Idealized representation of the flow inside a DC non-transferred plasma torch..

Understanding the arc – plasma interactions has been the main topic interest over the last two decades. The arc dynamic is the result of the balance between the drag force caused by the incoming fluid and Lorentz force due to the electromagnetic nature of arc. The length of arc inside the torch may be correlated with the magnitude of voltage fluctuations. Three different modes of arc operation are observed based on these voltage fluctuations namely, steady mode, take over mode and restrike mode [1], steady mode of operation is characterized by arc attachment to a fixed

position on the anode. In this mode, the voltage fluctuations are very small. This mode of operation is not preferred due to rapid erosion of anode material. In takeover mode, the arc movement and voltage fluctuations follow a quasi-periodic pattern. As the arc attachment point moves over the anode, it distributes the heat uniformly over the anode surface and in a generally predictable way. Restrike mode is characterized by a highly unstable, relatively unpredictable movement of the arc. The voltage fluctuations are large and chaotic.

Thermal plasma modeling involves solving the conservation for mass, momentum, and energy along with the electromagnetic equations. The modeling of plasma flow is challenging due to complicated factors associated with unsteady effects caused by arc root fluctuation, non-local thermodynamic equilibrium near the electrodes or cold wall and 3-D flow effects due to arc local reattachment of the arc at the anode surface. Many two-dimensional axis-symmetric LTE models have been developed in the literature. Although these 2D models are inadequate for modeling of processes in the real plasma, they qualitatively provide temperature and velocity profiles at the outlet and assist in creating a basis for subsequent 3D-plasma jet modeling [1][2].

The 2D models tend to predict higher temperatures and velocities at the torch outlet compared to experimental findings. In 2D, because of assumed axis symmetry, the arc attachment is around the whole circumference rather than at a point. This affects the gas temperature, hence the velocity and consequently the arc attachment position which is further downstream relative to experiment. The first three-dimensional steady-state simulations were carried out by Li and Chen [2]. Their work shows that the arc attachment is a constricted spot in the azimuthal direction and work observes peculiarities in 3D flow patterns in non-transferred plasma torches. They predict the axial position of arc attachment by solving conservation equations, and by using Steinbeck's

* Corresponding author. Email: a.klimenko@uq.edu.au

minimum principle (also known as minimum entropy production applied to thermal plasma) to locate the position of the arc root. In 2002, Gonzales et al [1] used commercial software Fluent to perform steady-state simulations of arc attachment. They specified a fixed attachment using high temperature and high electric conductivity, but failed to get a convergent solution with this approach. They specified a constant electrical conductivity near the anode to get a steady-state solution. In another study of [4], the arc position was also set arbitrarily by specifying a current density profile over the anode.

A few transient simulations have been reported for non-transferred plasma torches [2-4]. Park et al. [4] used a rotating magnetic field to spin the arc radially inside the torch, but did not find the axial position that results from the imbalance between the drag and magnetic forces. A model, which uses the non-standard boundary conditions able to capture the displacement of the anode attachment spot is developed in ref[3]. This effect arises from interactions of cold flow with the plasma. They demonstrated arc reattachment by specifying the maximum electric field, as a controlling parameter. The reattachment process is achieved by specifying that the arc column connect to the anode when the electric field reaches its maximal value. The reattachment frequency is controlled by the magnitude of the maximal electric field. Trelles et al [5] used an artificially high electric conductivity near the anode to simulate the arc reattachment which is followed in this work. The assumption of artificial conductivity is only suitable for the cases where the torch is operating in steady and takeover modes. To simulate the re-strike mode, it is necessary to formulate a non-equilibrium model to capture effects of the arc root fluctuations. Although LTE models are simpler in terms of implementation and computation cost, their inability to describe non-equilibrium effects, limit their usefulness in thermal plasma processes.

The work presented here seeks to show the effect of different inflow conditions on the axial position of arc attachment in non-transferred arc plasma torch. We use steady state OpenFOAM CFD model and assume LTE.

2. Mathematical Model

2.1 Governing fluid Equations

Thermal plasma generated inside the non-transferred plasma torch is assumed to be optically thin, electrically neutral, laminar, and in local thermodynamic equilibrium (LTE) state. Based on these conditions, the coupled interactions between arc current and plasma flow are described in the frame work of magneto hydrodynamic equations.

The arc current field is obtained from the current continuity equation, along with the Ohm's law, which results in an elliptic equation for electric potential (ϕ).

$$\nabla \cdot (\sigma \nabla \phi) = \nabla \cdot (\sigma \mathbf{v} \times \mathbf{B}), \quad 1$$

where \mathbf{v} and σ are the plasma velocity and electric conductivity respectively. Here, the magnetic field (\mathbf{B}) is the self-induced magnetic field (B_s) by the arc current itself. The B_s is calculated using magnetic vector potential A from

$B_s = \nabla \times A$, where the magnetic vector potential is found from the Ampere's law as follows:

$$\nabla^2 A = -\mu_0 j \quad 2$$

Where $\mu_0 = 4\pi \times 10^{-7} \text{ TmA}^{-1}$.

The steady state equations for the transports of mass, momentum, and energy of plasma flow are described by the conservation laws. The equations are presented below.

Conservation of mass

$$\nabla \cdot (\rho \mathbf{v}) = 0 \quad 3$$

Conservation of Mass-averaged momentum

$$\nabla \cdot (\rho \mathbf{v} \mathbf{v}) = j \times \mathbf{B} - \nabla p + \nabla \cdot \boldsymbol{\tau} \quad 4$$

Conservation of Energy

$$\nabla \cdot (\rho \mathbf{v} h) = j \cdot (\mathbf{E} + \mathbf{v} \times \mathbf{B}) - \dot{R} + \nabla \cdot \left(\kappa \nabla T + \frac{5}{2} \frac{k_B}{e} j \cdot \nabla T \right) \quad 5$$

Where ρ , p , $\boldsymbol{\tau}$, h , and T are the density, pressure, stress tensor, enthalpy, and temperature, respectively. The term \dot{R} represents the radiation losses.

The thermodynamic and transport properties of argon are taken from the literature [6]. The OpenFOAM CFD fluid code is modified to include the required terms (Lorentz force ($j \times B$), joule heating ($j \cdot (\mathbf{E} + \mathbf{v} \times \mathbf{B})$) and electron enthalpy flux ($\frac{5}{2} \frac{k_B}{e} j \cdot \nabla T$)) in the momentum and energy equations along with electromagnetic relations.

2.2 Boundary conditions

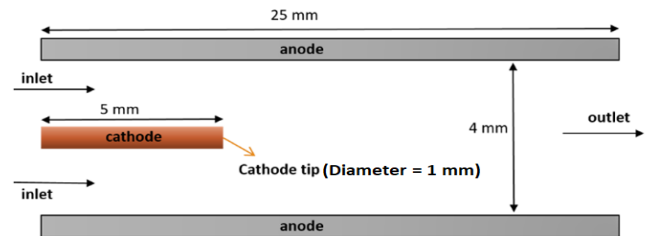


Figure 2 Sectional view of cylindrical geometry ($0 - \pi$ plane).

As seen in figure 2, the boundary of the computational domain is divided into five different parts to allow specification of the boundary conditions. Table 1 shows the boundary conditions used for different variables (for LTE); these boundary conditions are fairly typical in simulations of arc plasma torches [2]. We use non-uniform meshing inside the flow domain. Total number of cells is 913206. The meshing is refined near the electrodes to capture the effects due to large temperature and velocity gradients. To test the mesh independence, we also carried out the simulation with fine mesh having 1112324 cells.

In Table 1, the pressure at the outlet is equal to 101.3 kPa and u_i the imposed velocity profile is the profile of a fully developed laminar flow through an annulus. The cathode temperature, which is approximated by a Gaussian profile along the x-axis varying from 500 K at the inlet to 3000 K at the cathode tip. The convective heat transfer coefficient (h_w) at the anode wall is equal to $10^5 \text{ W m}^2 \text{ K}^{-1}$ (approximates the convective heat transfer due to turbulent flow in a pipe [2]). The anode cooling water temperature (T_w) is 500 K. The

imposed current density (J_{cath}) over the cathode tip is defined as

$$J_{cath} = J_{cath0} \left(\exp\left(-\left(\frac{r}{R_c}\right)^{n_c}\right) \right)$$

where r is the radial distance from the torch axis, and J_{cath0} , R_c and n_c are parameters that specify the shape of the current density profiles for integration over the cathode tip surface, equal to specified input current [2]. The values of these parameters for 310 A, $J_{cath0} = 5 \times 10^5 \text{ A/m}^2$, $R_c = 0.5 \text{ mm}$, $n_c = 4$.

Table 1 Boundary conditions

	p	v	T	ϕ	A
Inlet	$\frac{\partial p}{\partial n} = 0$	U_i	500K	$\frac{\partial \phi}{\partial n} = 0$	$\frac{\partial A}{\partial n} = 0$
Cathode tip	$\frac{\partial p}{\partial n} = 0$	0	3500 K	$\frac{\partial \phi}{\partial n} = \frac{J_{cath}}{\sigma}$	$\frac{\partial A}{\partial n} = 0$
Cathode	$\frac{\partial p}{\partial n} = 0$	0	500 - 3500K	$\frac{\partial \phi}{\partial n} = 0$	$\frac{\partial A}{\partial n} = 0$
Anode	$\frac{\partial p}{\partial n} = 0$	0	$\kappa \frac{\partial T}{\partial n} = h_w(T - T_w)$	0	$\frac{\partial A}{\partial n} = 0$
Outlet	101.3 kPa	$\frac{\partial U}{\partial n} = 0$	$\frac{\partial T}{\partial n} = 0$	$\frac{\partial \phi}{\partial n} = 0$	0

3. Results

3.1 Model comparison

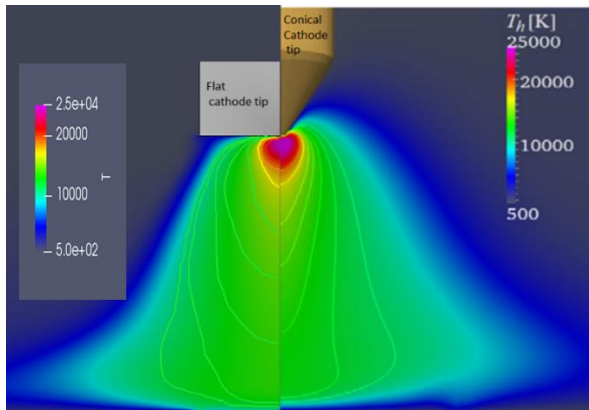


Figure 3 temperature iso-contours (10, 12, 14, 16, 18, 20, 22 and 24K kK) inside the free burning arc; present work(left) and Trelles(right)

As a test our model, we consider a similar case presented in Trelles[7]. Trelles developed non-equilibrium model to study the pattern formation on anode surface inside the free-burning arc. Free burning arc case mainly observed in plasma welding and plasma cutting, where cathode in the shape of the rod directly facing plane anode surface. The operating conditions are $I = 200 \text{ A}$. Their work considers the conical cathode tip, whereas in our case is flat cathode tip. The temperature distribution between cathode and anode

compared with Trelles. Figure 3(right) shows the temperature distribution inside the conical cathode tip and Fig 2(left) shows the temperature distribution from the present work. The major differences near the anode due to usage of flat cathode tip, restrict the radial convection of heat, results more constricted temperature distribution relative to conical cathode tip.

3.2 Results for plasma torch

The results of the 3D plasma torch operating with different inlet conditions are provided here. The ignition is achieved by imposing a high electric conductivity column between the cathode tip and a pre specified anode position next to the cathode tip. This approach is commonly used in reattachment models to introduce new attachments in the torch. The radial profile of electric conductivity given below.

$$\sigma_b = \sigma_{b0} \exp(-\beta_b (r_b/R_b)^{n_b})$$

where r_b is the radius of cylindrical channel used for reattachment process[2]. Values of parameters used in present study are $R_b = 0.5 \text{ mm}$, $\beta_b = 6$, $n_b = 4$ and $\sigma_{b0} = 10^4 \text{ S m}^{-1}$. The axial position of cylindrical channel is 5.5 mm from the inlet. The circumferential position arbitrarily chosen and fixed at zero degrees.

Table 2 Operating conditions for simulated cases

No.	Input current(I)	Input velocity(U_a)
1	310A	0.8
2	310A	4
3	310A	5.1

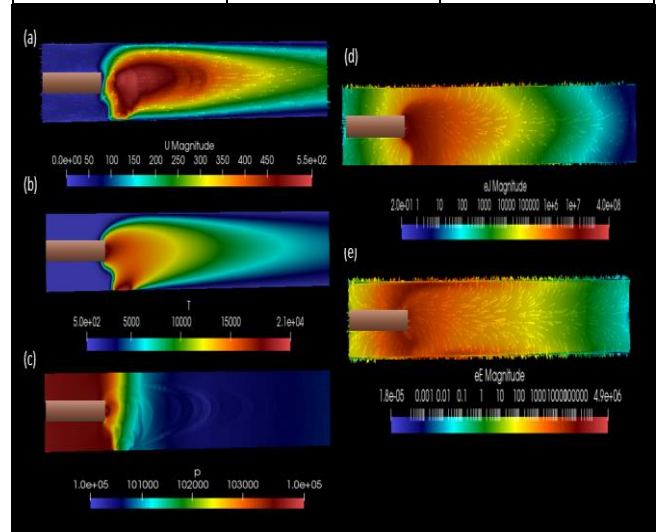


Figure 4 a) velocity, b) temperature, c) pressure, d) current density and e) electric field distribution in $0 - \pi$ plane,

The input operating conditions for simulated steady state cases are presented in Table 2. Before starting simulation, the ignition column is inserted at anode surface right next to the cathode tip. The different cases are simulated and steady state results reported. Figure 4 shows the velocity, temperature, pressure, current density and electric field distribution inside the plasma torch for case 2. The high acceleration of plasma is observed near the arc attachment on the cathode tip and anode attachment position. The higher velocities arise from rapid expansion of gas and the Lorentz force effect. The pressure is maximal at the cathode tip and equal to 3.87 kPa (gauge pressure). The initial arc column is

seen to be dragged downstream (Figure 4b) until it finds a position where the fluid drag force is balanced by the Lorentz force. Figure 4d shows the current density distribution inside the plasma torch. The electric field is observed to be higher near the arc column fringes (Figure 4e). Electric field profiles are qualitatively similar to that of literature[6].

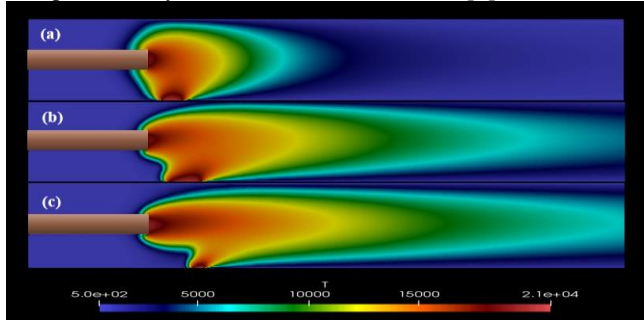


Figure 5 Temperature distribution inside plasma torch for the case 1-3 ($0 - \pi$ plane)

Table 3 : Electric power and length of arc ($I = 310A$)

U_a (m/s)	Power (kW)	Length of arc
0.8	3.8	2.28
4	9.0	3.92
5.1	10.8	4.71

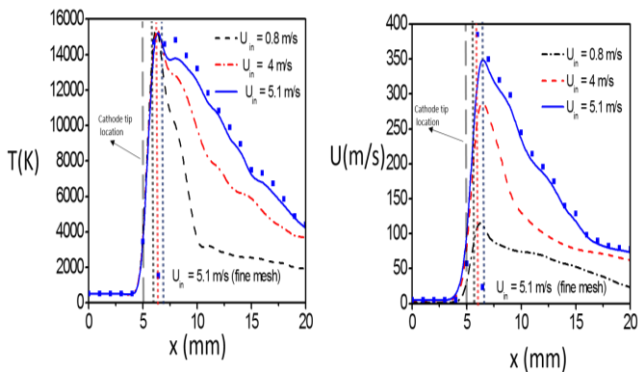


Figure 6 Radially averaged axial temperature and velocity profiles in plasma torch for cases 1,2 and 3. Vertical dotted lines corresponds to anode attachment position

We also analyzed the effect of inlet gas velocity on arc dynamics inside the plasma torch. The temperature contours [8] for these cases are shown in Figure 5. At the low inlet velocity of 0.8 m/s, the arc column displacement is very low due to strong electromagnetic force. As the inlet velocity increases to 4 m/s, the column moves downstream due to increase in the fluid drag. Further increase in inlet velocity to 5.1 m/s, the arc column is dragged further downstream from the previous location. The corresponding power consumption and length of arc are reported in Table 3. Length of arc defined as the length of curve that connects the maximum temperatures between cathode tip to anode attachment position. This clearly shows that the increase in the input velocities arc attachment moves further downstream of the torch with constant input current ($I = 310A$). Higher gas inlet velocities increase the length of arc,

thereby increasing the power consumption in the plasma torch. Figure 6 shows the radially averaged axial temperature and velocity profiles. The maximal temperature nearly constant for these three cases and observed to be near the cathode tip. Higher inlet velocities increase the amount gas exposed to the arc. The rapid expansion of the gas increases the magnitude of maximal velocity in the system. The higher arc lengths correspond to spreading out the temperature and velocity profiles.

4. Conclusions

Numerical simulations using OpenFOAM were performed to study the arc inside an argon plasma torch based on the solution of conservative equations of mass, momentum and energy along with electric and magnetic potential equations. The average voltage drop and maximum temperature are good agreement with different LTE models of plasma torch. As the inlet velocity increases, the arc is dragged downstream of the torch. This is also evident from the voltage drop, which is proportional to length of arc in plasma torch. The steady fluid model is applicable for steady arc mode where fluctuations are very small. Takeover mode operation requires a time-dependent model to capture unsteady effects caused by arc root fluctuations. The present work considers only dissociation reactions of argon at high temperature by assuming a chemical equilibrium. In our future work, the model will include kinetics of methane at high temperatures to optimize the torch design for synthesis of acetylene.

5. Acknowledgments

We are thankful to Australian Research Council and Synergen Met for supporting this project.

6. References

- [1] J. J. Gonzalez, P. Freton, and A. Gleizes, *Journal of Physics D: Applied Physics*, pp. 3181--3191, 2002.
- [2] J. P. Trelles, E. Pfender, and J. V. R. Heberlein, *Journal of Physics D: Applied Physics*, no. 18, pp. 5635-5648, 2007.
- [3] C. Baudry, A. Vardelle, and G. Mariaux, *High Temp Mat Proc*, vol. 9, no. 1, pp. 1-15, 2005.
- [4] J. M. Park, K. S. Kim, T. H. Hwang, and S. H. Hong, *IEEE Transactions on Plasma Science*, vol. 32, no. 2, pp. 479-487, 2004.
- [5] J. P. Trelles, E. Pfender, and J. Heberlein, *Plasma Chemistry and Plasma Processing*, vol. 26, no. 6, pp. 557-575, 2006.
- [6] J. P. Trelles, J. V. R. Heberlein, and E. Pfender, *Journal of Physics D: Applied Physics*, vol. 40, no. 19, pp. 5937-5952, 2007.
- [7] J. P. Trelles, *Plasma Sources Science and Technology*, vol. 22, no. 2, 2013.
- [8] L. He-Ping and Chen Xi, *Chinese Physics*, vol. 11, no. 1, pp. 44-49, 2002.

Numerical study of the flame structure and swirling motion of small-scale fire whirls

Xiang Fang¹ Anthony C.Y. Yuen², Guan H. Yeoh², and Sherman C.P. Cheung^{1,*}

¹ School of Engineering, RMIT University, Melbourne, Victoria 3083, Australia

² School of Mechanical and Manufacturing Engineering, University of New South Wales, Sydney, NSW 2052, Australia

Abstract

The fire whirl, which is a whirlwind and made up of flame and ash. The consensus is that with the intensified heat release rate, the fire whirl could cause significant destruction and fire risk to the firefighters or residents nearby the fire front line, especially in the tall building. Over the past years, lots of experiments were designed to study fire whirl. Nevertheless, the mechanisms involved in fire whirls combustion process are not evident. This paper presents two small-scale fire whirl models predicted by the large eddy simulation (LES) framework. For the very first time, predicted fire whirl flame and swirling flame structure are validated against the experimental measurements.

Keywords: Fire whirl, LES, vortex core.

1. Introduction

Fire whirl is a unique fire phenomenon which is made up of the swirling flame and re-burned ash [1, 2]. It can occur in mass forest or bushfires; or intense fires in large building void or atrium structures. Diverse from normal buoyant fires, the fire whirl has a luminous spindle shape inside the flame structure (also referred as ‘vortex core’) [3] which is initiated under certain ventilation conditions and upward movement of the heated gases. Due to the circular motion within the core, turbulent intensity, air entrainment and the mixing between air and fuel are significantly enhanced. As a result, previous studies have proven that the burning rate of fire whirl could be several times higher than the normal pool fire [4]. The flame structure of fire whirls, in general, is more concentrated and elongated along the vertical axis. Several reduced- and full-scale experiments have been carried out [5–10] investigating the combustion behaviour of fire whirl at each development stages and the mechanism of its radiant heat in igniting the surrounding combustibles.

Early experimental studies utilised two facilities, the rotating cylindrical screen and the stationary walls, to investigate the strength of vorticity within the fire whirls. In recent years, the reduced-scale fire whirl experiments were carried out to correlate the burning rate, flame structure with the ventilation conditions. [11] demonstrated that the size of the vent could be the key factor to dictate the onset of the fire whirl surrounded by stationary walls. Furthermore, Lei et al. [12] reported that the flame structure of the fire whirl is subject to the imposed circulation induced by a rotating cylindrical screen. Nevertheless, limited by the measuring instrumentations, the detailed flow characteristics (i.e. particularly at the vicinity of the flame surface and thin boundary layer above the fuel surface) and its impact on the fire whirl formation are not clearly understood.

On the other hand, Matsuyama et al. [3] employed Fire Dynamics Simulator (FDS) which utilised LES turbulent model to investigate the fire whirl flow and combustion characteristics. More recently, we proposed a [13] liquid fuel model considering radiation and convection heat feedback to model the resultant fire heat release rate and

validated our numerical predictions against the small-scale fire whirl measured by Chow and Han [10]. Unfortunately, without detailed velocity measurements, velocity predictions could only provide a qualitative analysis on the fire whirl swirling motion. A thorough validation study on both temperature and velocity field of the fire whirl is still outstanding in literature. To fill this knowledge gap, this paper presents a numerical study attempting to validate the transient temperature and velocity field predictions against two reduced-scale fire whirl experiments by Hartl and Smit using two-half cylinders model [9] and by Chow and Han using a vertical shaft model [11].

2. Mathematical formulation

In this paper, the reacting flow is represented by the governing equations of mass, momentum, energy and scalar properties [13]. The LES turbulent model was applied in this fire whirl simulation, because it has the capability to link up the temporal and fluctuating features of turbulence to fire phenomena [14]. Based on the LES framework, the generic form of the governing equations can be expressed as:

$$\frac{\partial(\bar{\rho}\tilde{\phi})}{\partial t} + \frac{\partial(\bar{\rho}\tilde{u}_i\tilde{\phi})}{\partial x_i} = \frac{\partial}{\partial x_i} \left(\Gamma_\phi \frac{\partial \tilde{\phi}}{\partial x_i} \right) + \tilde{S}_\phi$$

where ρ is the density, ϕ is the field dependent variable, Γ_ϕ and S_ϕ are the diffusion coefficient and source term, respectively. Table 1 summarises the expressions of the field variables, diffusion coefficients and the source terms for each governing equation.

	$\tilde{\phi}$	Γ_ϕ	\tilde{S}_ϕ
Mass	1	0	0
Momentum	\tilde{u}_i	μ	$-\frac{\partial \bar{p}}{\partial x_i} - \frac{\partial \tau_{ij}}{\partial x_i} - \frac{2}{3}\mu \frac{\partial \tilde{u}_i}{\partial x_i} \delta_{ij}$
Energy	\tilde{h}_s	λ	$-\frac{\partial}{\partial x_j} \left(\frac{\mu_{sGS} C_p}{Pr_{sGS}} \frac{\partial \tilde{T}}{\partial x_j} \right) + \frac{\partial \bar{p}}{\partial t} + \tilde{u}_j \frac{\partial \bar{p}}{\partial x_j}$

* Corresponding author. Email: chipok.cheung@rmit.edu.au

Mixture Fraction	\bar{f}	$\frac{k}{c_p} + \frac{\mu_t}{\sigma_t}$	0
Soot	Y_{soot}	$\frac{\mu_t}{\sigma_{soot}}$	$\frac{dM}{dt}$
	b_{nuc}^*	$\frac{\mu_t}{\sigma_{soot}}$	$\frac{1}{N_{norm}} \frac{dN}{dt}$

Table 1: Field-dependent variable, diffusion coefficient, and source terms of the generalised transport equation

In table 1, turbulent viscosity μ was modelled using the LES turbulence model. The LES turbulence model can filter small length eddies, the filtered eddies length is determined by the computational grid size. Large eddies are directly resolved while eddies which smaller than the filter length are predicted as the subgrid viscosity by the subgrid-scale (SGS) turbulence model. In this paper, the Smagorinsky model is adopted to resolve the SGS eddies while a modelling constant (Smagorinsky constant) of 0.1 has been employed [15]. For the reaction system, the mixture fraction model assumed that the thermochemical state of the combustion reaction can be governed by the mixture fraction \bar{f} . The k and C_p are the laminar thermal conductivity of the mixture and the mixture specific heat, respectively. The Prandtl number (i.e. σ_t) is taken 0.7 [16]. While the soot formation is solved by the Moss soot model which includes two semi-empirical equations.

3. Experimental configuration and numerical setup

3.1 Experimental arrangements

Numerical simulations were carried out referring to the two reduced-scale experiments conducted by Chow and Han[11] and Hartl and Smits[9] were simulated in this study.

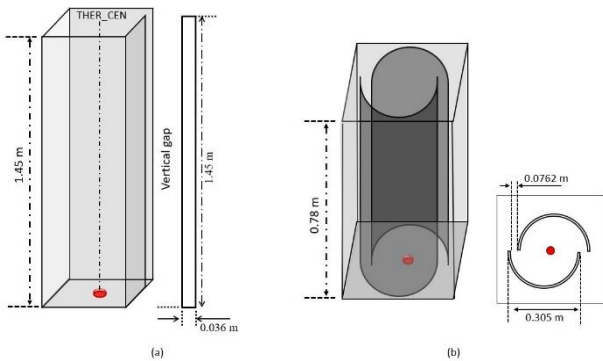


Figure 1: Schematic sketch of the three-dimensional view of (a) fully-opened vertical shaft model and (b) two-half cylinders model

Fig 1 depicts the schematic view of the vertical shaft model (a) and two-half cylinders model (b). In the vertical shaft model, a liquid fuel pool with an area of 39 cm² was placed at the centre of the model. A single ventilation gap of 3.6 cm width was opened at only one side for the onset of fire whirl. A thermocouple tree was placed at the centre of the model along the centreline of the fire whirl. For the two-half cylinders model, a pressure gas burner with the diameter of 38.1mm was centred inside the two staggered half plexiglass

cylinders. For the velocity measurements, the SPIV system which uses two imagers CMOS cameras were utilised to measure whirl circulation and inflow velocity nearing the fuel bed. As the positions of the fire whirl flame were significant unsteady, velocity images which the velocity profile fit to the Burgers vortex assumption, were collected for time-averaging.

3.2 Computational domain and boundary conditions

The general computational grid size can be determined through the characteristic length analysis based on the fire size [17]. Through characteristic length analysis, three non-uniform structured mesh system (e.g. 0.015m, 0.01m, 0.008m) can be utilized in small scale fire simulation which heat release rate is lower than 10 kw. However, as fire whirls induce tremendous swirling motion nearing fuel inlet, A 0.005m refinement structured mesh was adopted to discretise the computational domain for the vertical shaft model. Fig. 2(a) shows the mesh distribution of the computational domain for the vertical shaft model. The physical size of the computational domain is of 0.5m x 0.4m x 1.45m which consists of an extension region of 0.15m x 0.05m to minimise the end effect of boundary conditions for realistic representation of air entrainment through the vertical gap. The computational grid consists of a total 3,200,000 nodes. For the two-half-cylinders model, a hybrid mesh (i.e. structured and un-structured tetrahedra) is adopted as shown in Fig.2 (b). The structure mesh was placed at the centre of the model 0.05m x 0.05m x 0.89m where the size of each grid is of 0.001m x 0.001m x 0.001m to ensure sufficient mesh resolution to resolve the fire whirl flame. For the other part of the other domains, a total number of 11,535,000 tetrahedra cells were adopted.

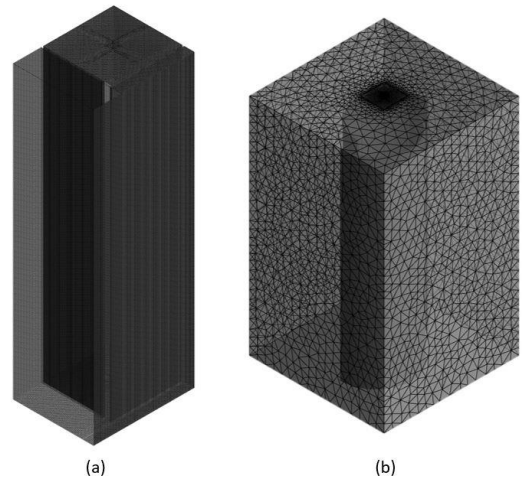


Figure 2: Mesh resolution for the vertical shaft model (a) and two-half cylinder model (b).

4. Results and discussions

4.1 Time-averaged centerline flame temperature

In the vertical shaft experiment, bare-wire K type thermocouple tree was utilised for temperature measurement. However, due to the lake of thermal shielding,

the measured temperature could not truly reflect the flow temperature. To remedy this error, Wen et al. [18] proposed a correction method to revise the temperature reading base on the thermo-equilibrium assumption:

$$\dot{q}_{conv_ther} == \dot{q}_{rad_ther}$$

$$h_{s,conv}(T_{g,corr} - T_{ther}) = \epsilon_{ther}(\sigma T_{ther}^4 - \dot{q}_r)$$

In general, the numerical predictions were satisfactorily against the corrected experimental readings. The main trend of the centerline temperature distribution was clearly presented, as shown in Fig 3. While the predicted temperature is slightly over-predicted at 0.2 m to 0.4m. The following reasons could cause these errors. Firstly, the equilibrium chemistry model is adopted for handling the combustion process. Furthermore, this model could over-predict heat release at the fuel-rich region and fuel limited region. Secondly, as the limitation of the computational resources, the predicted combustion process only has two intermediate species (carbon monoxide and hydrogen), other pollutants were considered fully oxidised in the simulation. Thirdly, the fire whirl is not exactly developed at the centre of the vertical shift, thermocouples at the centre could post error reading.

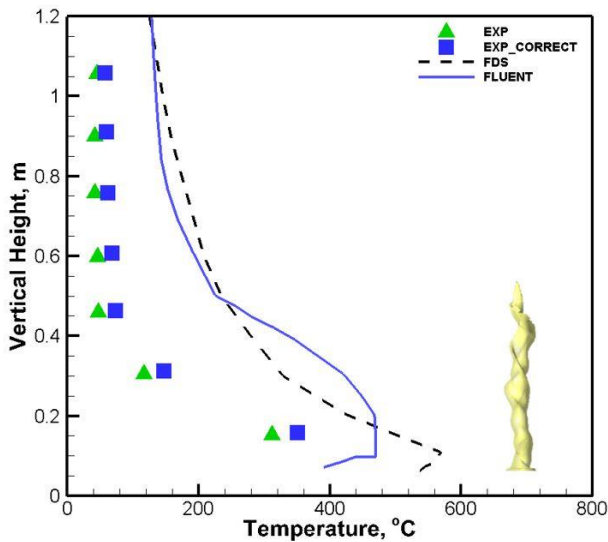


Figure 3: Axial, tangential, and radial time-averaged velocity comparisons between numerical and experiment of the two-half cylinders model.

4.1 Time-averaged velocity profile

Hartl and Smits [9] utilised the SPIV system to measure the velocity profile of a small-scale pressure burner fire whirl. The predicted velocities were time-averaged after the fire whirl was fully developed for an approximately 20 seconds after the fire whirl is fully developed at least 40 seconds. Fig. 4 shows the comparison of measured and predicted time-averaged velocity components along a horizontal line at the centre of fire whirl of 0.08 m above the fire bed. The predicted vertical velocity peak value and angular velocity peak are excellently compared with the measurement. While the distance between two angular velocity peaks is slightly under-predicted. This is indicating that the intensity of the swirl motion is slightly over-predicted by the numerical

scheme. This also evidences in the slightly over-predicted radial velocity in the comparison. This because the equilibrium chemistry model over-estimate the heat release inside the fire whirl vortex core (fuel-rich region) which over-estimates the density contrast between the fire whirl core and surrounding air leading to the stronger turbulence suppression. According to Lei et al., the flame elongation and swirling core formation are closely related to the turbulence suppression. Stronger suppression could encourage higher swirling flame structure exhibiting higher radial velocity in the predicted results

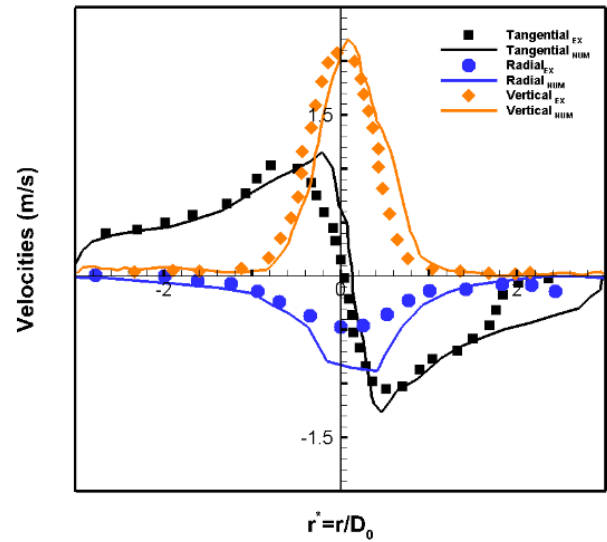


Figure 4: Axial, tangential, and radial time-averaged velocity comparisons between numerical and experiment of the two-half cylinders model.

5. Conclusions

In this article, numerical simulations have been performed on two reduced-scale fire whirl experiments using the LES turbulent model and mixture fraction combustion model with equilibrium chemistry assumption. While numerical predictions were compared reasonably well with experimental data, our predictions show that the equilibrium chemistry model could slightly over-estimate the heat release at the bottom of fire whirls. This discrepancy could also incur prediction error for the density difference between the vortex core and sounding air leading the over-prediction of radial velocity. In general, the predicted temperature trend along the vertical axis, vertical velocity, and angular velocity are in excellent agreement with the measurements. Overall, this paper presents a complete numerical scheme to capture flame temperature and the swirling flame structure of a fire whirl which is thoroughly validated against the experimental measurements.

6. Acknowledgments

The financial support provided by the Australian Research Council Industrial Training Transformation Centre (IC170100032) is gratefully acknowledged.

7. References

- [1] Emmons, H.W. and S.-J. Ying, *The fire whirl*. Symposium (International) on Combustion, 1967. **11**(1): p. 475-488.
- [2] Justesen, P., *A numerical study of oscillating flow around a circular cylinder*. Journal of Fluid Mechanics, 1991. **222**: p. 157-196.
- [3] Matsuyama, K., Tanaka, F., Ishikawa, N., Tanaka, S., Ohmiya, Y. and Hayashi, Y., *Experimental And Numerical Studies On Fire Whirls*, in *AOFSST 6*, 2004.
- [4] Lei, J., N. Liu, and R. Tu, *Flame height of turbulent fire whirls: A model study by concept of turbulence suppression*. Proceedings of the Combustion Institute, 2017. **36**(2): p. 3131-3138.
- [5] Chow, W.K., Z. He, and Y. Gao, *Internal Fire Whirls in a Vertical Shaft*. Journal of Fire Sciences, 2010. **29**(1): p. 71-92.
- [6] Hayashi, Y., Kuwana, K. Dobashi, R., *Influence of Vortex Structure on Fire Whirl Behavior*. Fire Safety Science, 2011. **10**: p. 671-679.
- [7] Huo, Y., W.K. Chow, and Y. Gao, *Internal Fire Whirls Induced by Pool Fire in a Vertical Shaft*. 2011(38921): p. T20034-T20034-6.
- [8] Chow, W.K., *A study on relationship between burning rate and flame height of internal fire whirls in a vertical shaft model*. Journal of Fire Sciences, 2013. **32**(1): p. 72-83.
- [9] Hartl, K.A. and A.J. Smits, *Scaling of a small scale burner fire whirl*. Combustion and Flame, 2016. **163**: p. 202-208.
- [10] Lei, J., et al., *Experimental investigation on flame patterns of buoyant diffusion flame in a large range of imposed circulations*. Proceedings of the Combustion Institute, 2017. **36**(2): p. 3149-3156.
- [11] Chow, W.K. and S.S. Han, *Experimental Investigation on Onsetting Internal Fire Whirls in a Vertical Shaft*. Journal of Fire Sciences, 2009. **27**(6): p. 529-543.
- [12] Lei, J., et al., *Temperature, velocity and air entrainment of fire whirl plume: A comprehensive experimental investigation*. Combustion and Flame, 2015. **162**(3): p. 745-758.
- [13] Yuen, A.C.Y., et al., *Numerical study of the development and angular speed of a small-scale fire whirl*. Journal of Computational Science, 2018. **27**: p. 21-34.
- [14] Yuen, A.C.Y., et al., *On the influences of key modelling constants of large eddy simulations for large-scale compartment fires predictions*. International Journal of Computational Fluid Dynamics, 2017. **31**(6-8): p. 324-337.
- [15] Smagorinsky, J., *GENERAL CIRCULATION EXPERIMENTS WITH THE PRIMITIVE EQUATIONS*. Monthly Weather Review, 1963. **91**(3): p. 99-164.
- [16] Cheung, S.C.P., et al., *Flickering Behavior of Turbulent Buoyant Fires Using Large-Eddy Simulation*. Numerical Heat Transfer, Part A: Applications, 2007. **52**(8): p. 679-712.
- [17] Yuen, A.C.Y., et al., *Study of three LES subgrid-scale turbulence models for predictions of heat and mass transfer in large-scale compartment fires*. Numerical Heat Transfer, Part A: Applications, 2016. **69**(11): p. 1223-1241.
- [18] Wen, J.X., L.Y. Huang, and J. Roberts, *The effect of microscopic and global radiative heat exchange on the field predictions of compartment fires*. Fire Safety Journal, 2001. **36**(3): p. 205-223.

Effect of inlet manifold water injection on diesel engine performance and emissions

Sujit Kafle, Andrew P. Wandel and Saddam Al-Lwayzy
School of Mechanical and Electrical Engineering
University of Southern Queensland, Australia

Abstract

Water in vapour form was injected into the intake manifold of a diesel engine to increase the relative humidity of the charge in an effort to reduce emissions. The test engine was operated under ambient conditions at various engine speeds with and without the use of a humidifier and the engine performance and emission parameters were measured. The relative humidity of the charge decreased with increasing engine speed because the humidifier produced a constant rate of water vapour. This increase caused a slight decrease in the engine power and torque, but there was a significant reduction in Nitrogen Oxides (NO_x) emissions.

Keywords: Diesel, Water Injection, Relative Humidity, Engine Performance, Emissions, NO_x

1. Introduction

Emissions from engines cause respiratory problems in the human population, bring negative impacts on plants and vegetation and are the primary cause of the greenhouse effect, ozone depletion, and acid rain [1, 2].

Among many of the in-cylinder control techniques, Exhaust Gas Recirculation (EGR) is common technology used to reduce emissions [3]. Recirculating a portion of engine's exhaust gases dilutes the reactants, which increases the ignition delay and reduces the exhaust gas temperature. Though this technique reduces the percentage of NO_x emissions by a significant amount, the amount of soot emissions also increases significantly.

Another in-cylinder technique is the Water-Injection (WI) system, either into the engine inlet or in emulsion with the fuel. A WI system reduces the local combustion temperature and thus reduces the NO_x production rate and lowers soot and particulate contents in the exhaust [3]. Heat is absorbed by water in the form of latent heat and sensible heat, which in turn reduces the temperature in the combustion chamber [1].

Water-in-diesel emulsion is more efficient than water injection in terms of performance characteristics and emission characteristics, as water is directly injected into the combustion zone. Water-in-diesel emulsion has longer ignition delay, lower NO_x and soot emissions and higher brake thermal efficiency at all loads and speeds when compared to water injection [4]. However, the preparation and distribution of the emulsified fuel is more complex making the system challenging to implement commercially. With regards to water injection, it is a simple-to-implement system to reduce emissions without any modifications to the engine, although an additional water tank and filling system is required.

Most in-cylinder techniques do not simultaneously reduce NO_x and smoke emissions and the combination of these techniques incur additional costs including initial investment, maintenance and energy consumption [4]. Therefore, a simple technique needs to be developed to

reduce the emissions. A WI system is tested in this paper to determine if it reduces NO_x emissions without significantly affecting the performance of the engine.

2. Methodology

In this project, a single-cylinder, 4-stroke, vertical, air-cooled Yanmar L48N diesel engine was used (Figure 1). The engine has a bore of 70 mm, stroke of 57 mm with displacement 219 cc. The 2D schematic diagram (Figure 2) provides a clear picture of the experimental set up.

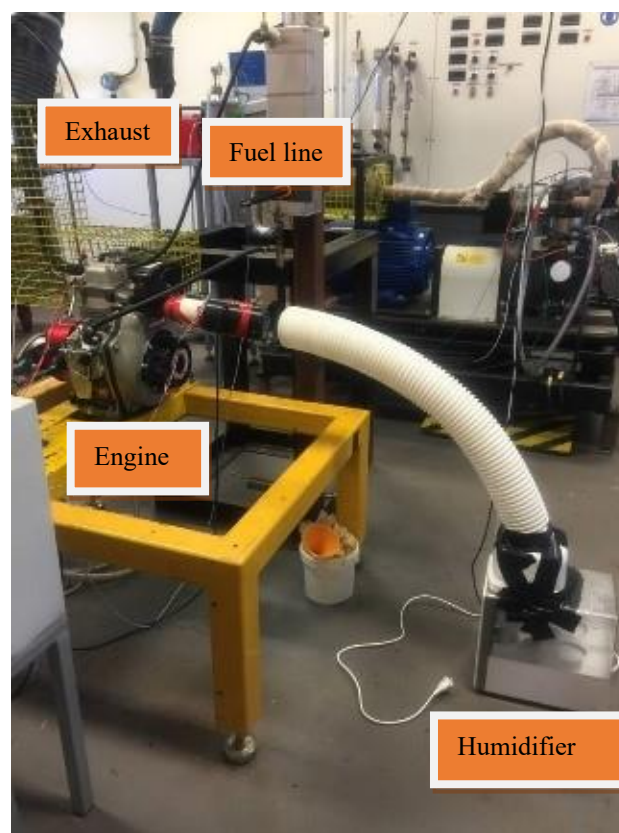


Figure 1: Experimental set up with the use of the humidifier (The humidifier is on the floor with a white connecting hose towards the engine air inlet. The engine is seated on a yellow metal frame)

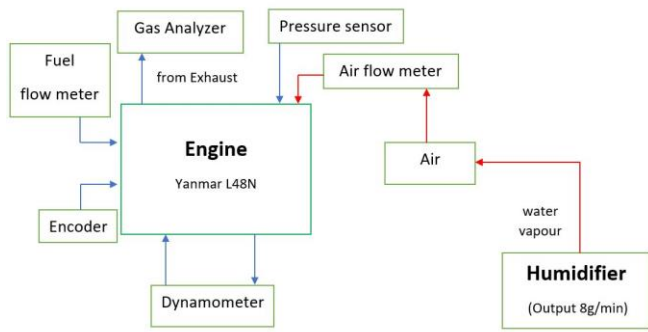


Figure 2: 2D schematic diagram of the experimental setup

The engine was first operated at normal operating conditions (in this case, 40% Relative Humidity, 25°C temperature) at different engine speeds. Water vapour from a humidifier with a water output of 8 g/min was introduced to the intake manifold of the engine and the change in the relative humidity was observed. Engine power, torque, pressure and emissions at the two levels of relative humidity were measured and comparisons were made. The engine timings were not altered when adding the humidity to the intake manifold, so any changes in engine performance and emissions are purely due to the change in humidity of the charge.

The water output of the humidifier was calibrated for a range of liquid water temperatures in the supply tank. The supply to the intake manifold was carefully sealed to ensure that the full output of 8g/min was added to the charge entering the engine.

The engine speed range was selected based on the engine performance curves. Table 1 shows the change in relative humidity (RH) with the use of the humidifier at the chosen engine speeds. The RH with the humidifier was calculated based on the increased specific humidity due to the calibrated supply from the humidifier. Although this was greater than 100% at room conditions, there was insufficient time for water to condense in the engine prior to the compression stroke increasing the saturation pressure above the partial pressure of water vapour. Because the volume flow rate of air increases with increasing engine speed, the fixed increase in specific humidity has a smaller effect on the RH at higher engine speeds.

Table 1: Change in relative humidity (RH) before and after the use of humidifier at nominal tested engine speeds

Engine Speed (RPM)	RH (Normal)	RH (with humidifier)
2600 ± 10	40%	169%
3000 ± 10	40%	143%
3600 ± 10	40%	123%
3800 ± 10	40%	120%

3. Random and Systematic Error

The engine speed during the experiment was reduced manually from 3800 RPM to 2600 RPM with the use of water-load and this created scatter in the speed range from the optimum value. This random error in the experiment

was reduced by recording measurements within a speed range with acceptable tolerance.

Likewise, the effect of temperature on the strain gauge of the torque arm was not considered. As the load was varied, the change in temperature caused deviation in the absolute values of the engine torque by +3.2 Nm at all engine speeds.

4. Results and Analysis

The results from the experiment for the test engine have been compared based on the engine speed. The error bars for all results were so small that they are not noticeable in the plots.

4.1 Pressure Traces

The in-cylinder pressure values from the pressure sensor were extracted from the computer system for all tests. The results are calculated from the average of 50 cycles.

Figure 3 shows the pressure trace at 40% RH for each engine speed. The desirable operation of peak pressure after TDC is maintained for all engine speeds. As expected, the timing of the peak pressure is advanced with increasing engine speed due to reduced time to complete combustion; this is allied with a reduction in the peak pressure. The fastest speed's pressure is close to the motored pressure, being significantly lower than for other engine speeds during the power stroke. This demonstrates that this engine speed is at the upper limit of operation for this engine.

In comparing the effects of humidity (Figures 4-7), the only significant effect on pressure is close to the slightly-increased peak pressure. This indicates that the additional humidity does not affect the evaporation and mixing of the fuel, nor the ignition delay. The additional humidity, does however, affect the reaction rates of the combustion.

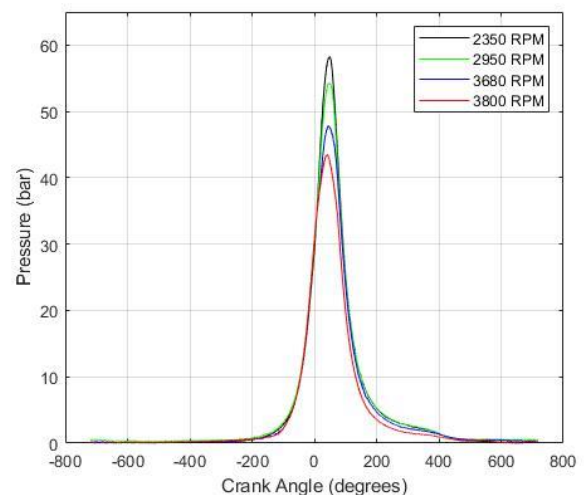


Figure 3: Pressure trace at 40% RH at different engine speeds

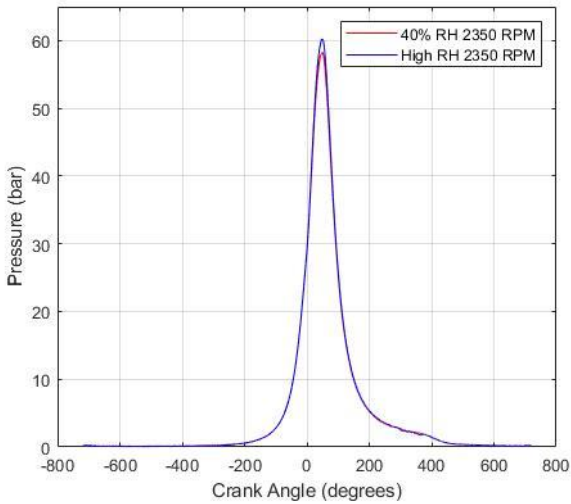


Figure 4: Pressure trace for 40% RH and High RH at 2350 RPM

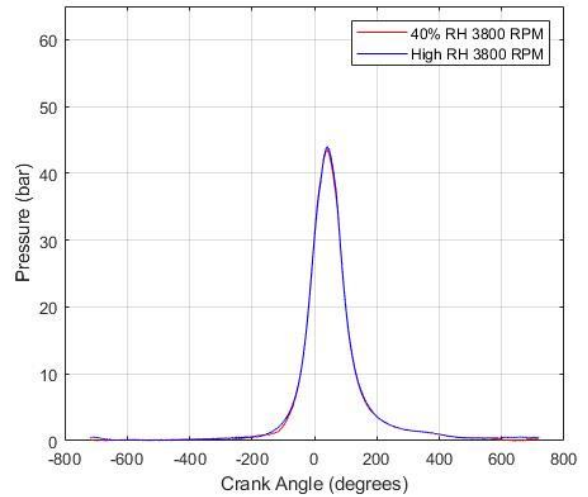


Figure 7: Pressure trace for 40% RH and High RH at 3800 RPM

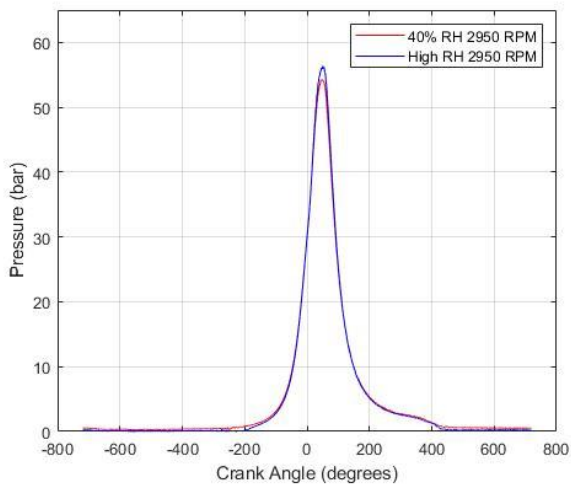


Figure 5: Pressure trace for 40% RH and High RH at 2950 RPM

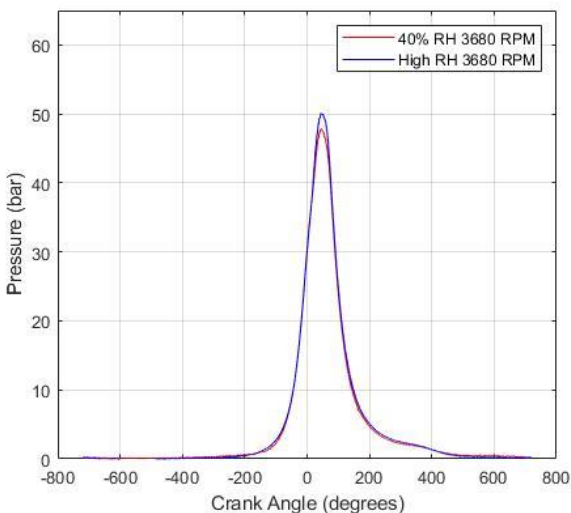


Figure 6: Pressure trace for 40% RH and High RH at 3680 RPM

4.2 Engine Performance

Figures 8 and 9 present the variation of engine power and torque for all tests. The trend of torque decreasing with increasing engine speed is apparent from the results shown in Figure 3, while 3600 RPM provides the most power for both humidity levels. Unsurprisingly, both values at 3800 RPM are significantly lower.

The increased humidity slightly increased both power and torque, as expected from pressure traces (a small increase in the vicinity of the peak pressure).

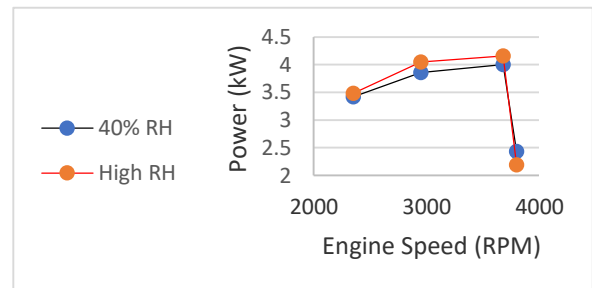


Figure 8: Power versus Engine Speed at different levels of humidity

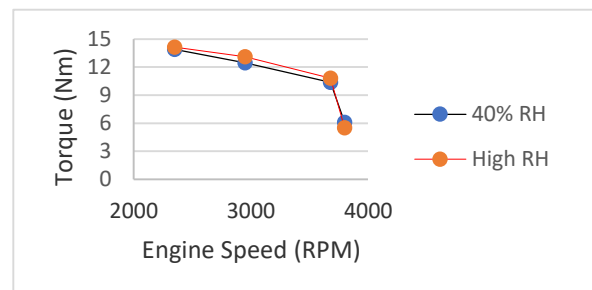


Figure 9: Torque versus Engine Speed at different levels of humidity

4.3 Emissions

Figures 10-12 represent the variation of emissions for all tests. The hydrocarbons (HC) and CO both increased by significant amounts due to the increase in humidity, with the effect of increasing with decreasing engine speed, commensurate with the variation of RH with engine speed. It is apparent that the additional water in the combustion zone has impeded the carbon reaction pathways to some extent by altering the equilibrium of the hydrogen chemistry by converting oxygen radicals into OH.

The NO_x emissions were, however, significantly improved for the intermediate speeds (Figure 12). This is predominantly through the higher concentrations of OH and lower concentrations of O interfering with the nitrogen reaction pathways.

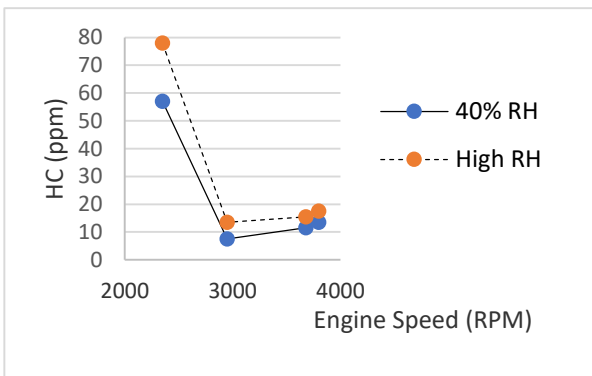


Figure 10: Hydrocarbon (HC) versus Engine Speed at different levels of humidity

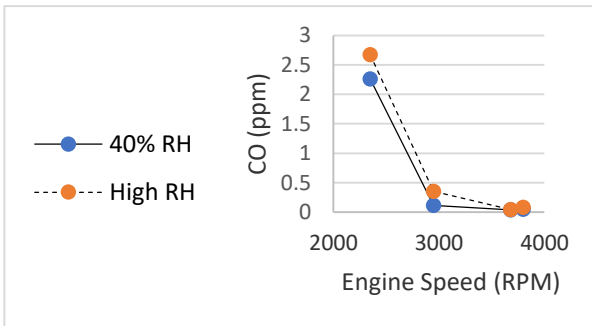


Figure 11: Carbon Monoxide (CO) versus Engine Speed at different levels of humidity

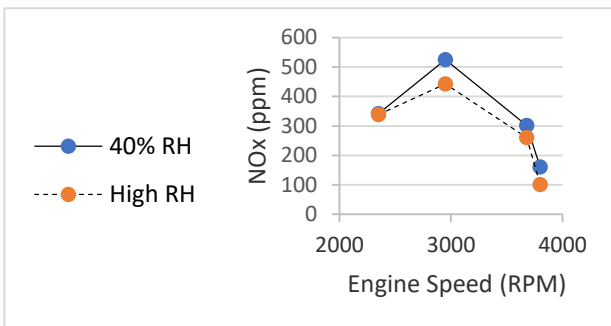


Figure 12: NO_x versus Engine Speed at different levels of humidity

Overall, water injection has made significant reductions in NO_x emissions with minor negative changes in HC and CO emissions. The additional water harvests oxygen radicals into OH, impeding both the carbon and nitrogen reaction pathways.

5. Conclusion

The water injection method has attracted attention for its potential to reduce NO_x emissions without significant changes in soot emissions, engine performance and fuel economy. Experiments were conducted, injecting water in the inlet manifold to increase the humidity of the charge. The increasing humidity slightly improved engine performance without significantly affecting the timing of the reactions. It also changed the equilibrium of the chemical reaction pathways, introducing more hydrogen into the system, which bonds with oxygen more aggressively than carbon or nitrogen. As a consequence, both carbon and nitrogen were impeded from completing oxidation, which had the desirable effect of reducing NO_x emissions while having the undesirable effect of increasing HC and CO emissions. This work provides a potential alternative for reducing NO_x emissions without significantly affecting the engine operation.

6. Acknowledgement

The authors would like to thank Mr. Brian Lenske, for his assistance in conducting the experiments.

7. References

- [1] D. Hountalas, G. Mavropoulos and T. Zannis (2007) SAE Technical Paper 2007-01-0120.
- [2] K.A. Subramanian (2011) *Energy Conversion and Management* **52**, pp. 849-857.
- [3] X. Tauzia, A. Maiboom, & S.R. Shah (2010) *Energy* **35**, pp. 3628-3639.
- [4] A. Lif and K. Holmberg (2006) *Advances in Colloid and Interface Science* **123-126**, pp. 231-239.

PRESENTATION ONLY

Numerical Investigation of Tandem Cavity Configurations with Supersonic Ethylene Combustion

Sarah Mecklem, Will Landsberg, Ananthanarayanan Veeraragavan
Centre for Hypersonics, The University of Queensland, QLD, 4072, AUSTRALIA
s.mecklem@uq.edu.au

ABSTRACT

Combustion of ethylene was numerically investigated for a 2D axisymmetric scramjet geometry consisting of a diffuser, isolator, and combustor with zero, one or two cavity flame holders in a tandem configuration. One tandem configuration positioned the second cavity in a region of local shock impingement resulting from the leading cavity. The other configuration located the second cavity further downstream. Eilmer4 with local time stepping was used to solve the reacting flow domain using a 23 species skeletal ethylene combustion mechanism. Combustion efficiency increased >4% with the use of tandem cavities, over a single cavity. The shock impinged cavity provided more rapid combustion and less pressure losses indicating earlier combustion with downstream cavities to be beneficial to overall performance.

Algebraic Flame Surface Density Model Development using Gene-Expression Programming

M.C. Ma, M. Talei, and R.D. Sandberg
Department of Mechanical Engineering
University of Melbourne, Victoria 3000, Australia
manm2@student.unimelb.edu.au

ABSTRACT

Algebraic Flame Surface Density (FSD) models for Large-Eddy Simulation (LES) are developed using Gene-Expression Programming (GEP), a machine learning approach which generates functional forms in a stochastic iterative process. This preliminary study applies this approach to a DNS dataset of a turbulent premixed methane-air jet flame. A number of models are produced and compared with the existing models from the literature by examining the predictions of the total flame surface area, correlation coefficients and conditionally averaged FSD across the flame brush for different filter sizes. The performance of the GEP developed models are found to be comparable or better than the existing models, showing the potential of the GEP approach for developing algebraic FSD models.

An Experimental and Numerical Analysis of Hydrogen Oxidation in a Flow Reactor

Zhewen Lu, Yi Yang, Joshua Lacey and Michael J. Brear

Department of Mechanical Engineering, The University of Melbourne, VIC, Australia
yi.yang@unimelb.edu.au

ABSTRACT

This paper reports some new experimental and simulation results on the oxidation of hydrogen near its second explosion limit in a flow reactor. The experiment is conducted at 950 K and 1.5-4 bar where the oxidation shows a negative dependence on pressure. The concentrations of H₂, O₂ and H₂O are measured along the reactor and are simulated using existing kinetic models. Discrepancies are observed between the experiment and the models, which cannot be explained by the issues associated with reaction initialization that are typical of flow reactor simulation. Sensitivity analysis of rate controlling reactions also shows significant differences among the models studied. This indicates that, despite hydrogen being the most studied of all fuels, the kinetic models of hydrogen oxidation require further development

An Update on the Rate Constant of $\text{H} + \text{O}_2 (+\text{M}) \rightarrow \text{HO}_2 (+\text{M})$, $\text{M} = \text{N}_2$ using $\text{H}_2/\text{O}_2/\text{NO}_x$ Reaction in a Flow Reactor

Zhewen Lu, Yi Yang, Joshua Lacey and Michael J. Brear

Department of Mechanical Engineering, The University of Melbourne, VIC, Australia
yi.yang@unimelb.edu.au

ABSTRACT

The reaction of $\text{H} + \text{O}_2 (+\text{M}) = \text{HO}_2 (+\text{M})$ is one of the most important reactions in hydrogen oxidation. This work determines the rate constant of this reaction (R2) by doping the slow oxidation of hydrogen with nitric oxide (NO) and measuring the resulting, quasi steady state concentration of NO_2 . The investigation is conducted in a turbulent flow reactor at 10 bar, 900 K – 1000 K, equivalence ratio of 0.035 – 0.038, total reaction time of 0.28 s, and for NO addition from 0 to 1300 ppm. An updated Arrhenius equation is proposed for the reaction at the low-pressure limit, $k_{2,0}^{\text{N}_2} = 1.431 \times 10^{14} \exp(+5604/RT)$, for 700 K – 1000 K by combining results from this work and the literature

Fast Pyrolysis of Lignin at Low Temperatures: An In-depth Understanding of the Char Structural Changes

Yee Wen Chua, Yun Yu and Hongwei Wu

Discipline of Chemical Engineering, Western Australian School of Mines: Minerals, Energy and Chemical Engineering, Curtin University, GPO Box U1987, Perth WA 6845, AUSTRALIA

yun.yu@curtin.edu.au; h.wu@curtin.edu.au

Lignin is one of the major components in lignocellulosic biomass and regarded as the largest renewable source of aromatic polymers. Compared to those of other major components in biomass, valorization of lignin is more challenging because of lignin having heterogeneous structures with different interunit linkages. Fast pyrolysis is a promising thermochemical technology for converting lignocellulosic biomass into fuels and chemicals. During fast pyrolysis, lignin can be converted to liquid (bio-oil), solid (biochar) and gas, and the products derived from lignin pyrolysis have important roles in the chemical properties of bio-oil.

It is known that biomass pyrolysis proceeds with the formation of a molten intermediate liquid phase, as an important phenomenon of biomass pyrolysis. Those intermediates are important precursors of volatiles thus determining the formation and properties of volatiles during pyrolysis. Some recent works have been carried out to improve the understanding of liquid intermediates from lignin pyrolysis. However, there have been no studies so far to characterise the structural changes of the low- and high-molecular-weight portions of lignin during pyrolysis. Therefore, this study employs solvent extraction [i.e., tetrahydrofuran (THF)] to separate the lignin and its char products from lignin pyrolysis into the THF-soluble (low molecular weight) and THF-insoluble (high molecular weight) portions. The structural changes of the THF-soluble portion and the whole char are then characterised by a series of techniques to provide an in-depth understanding of the char structural changes during lignin pyrolysis mechanism at low temperatures of 100–300 °C.

Our results show that the low temperature pyrolysis of lignin mainly proceeds with the pyrolysis of the low-molecular-weight portion (i.e., the THF-soluble portion) via decomposition reactions into volatiles and polymerization reactions into the high-molecular-weight portion (i.e., the THF-insoluble portion). The decomposition of the THF-soluble portion starts at ~150 °C, mainly due to the loss of the hydroxyl groups as well as the alkyl aliphatic chains. Significant decomposition of the THF-soluble portion occurs at ~175 °C, mainly because of the cleavage of weak ether bonds linked with β -carbon or γ -carbon, resulting in demethoxylation and release of some phenolic monomers or oligomers. Significant polymerization reactions start at ~175 °C, leading to the increase of the THF-insoluble portion from ~31% in the raw lignin to ~67% in the char produced at 250 °C. Majority of the functional groups such as hydroxyl, methoxyl, aliphatic and carbonyl/carboxyl gradually decrease with increasing pyrolysis temperature, resulting in the formation of more condensed char as evidenced by the decreased H/C atomic ratio (i.e., 0.78 at 300 °C) and the increased aromaticity (i.e., ~91% at 300 °C) from NMR analysis.

"PRESENTATION ONLY"

Investigation of flammability factor in CNG jets using LES

Mohammad Reza Yosri *, Joshua S Lacey, Mohsen Talei, Robert L Gordon, and Michael J Brear

Department of Mechanical Engineering, The University of Melbourne, Parkville 3010, Australia

Myosri@student.unimelb.edu.au

ABSTRACT

In this paper, injection of methane from a prototype outward opening injector into a quiescent, non-reacting, constant volume chamber (CVC) is modelled by using large-eddy simulation (LES). A range of thermodynamic conditions that are relevant to direct injection, spark ignition (DISI), compressed natural gas (CNG) engines is considered by varying the CVC and fuel rail temperature (298 K and 360 K) and CVC pressure (0.4, 1 and 3 bar). The results are validated against high-speed schlieren imaging. The internal geometry and motion of the injection hardware is simulated and the probability of finding a flammable mixture is determined. Results show that the most flammable region is formed at the edge of the jet, and this region is mainly affected by the recirculation zone and mixing regions. The location of the most flammable zone changes based on the CVC pressure. For PCVC=3 bar, the most flammable region is around the recirculation zone whereas for PCVC=1 bar, the far-mixing region affects the location of the most flammable region. It is observed that increasing the chamber temperature slightly changes the size of the flammable region.

Chemistry reduction of hydrogen-methane mixtures with a focus on the laminar flame speed

Jen Zen Ho, Mohsen Talei, Robert Gordon and Michael J Brear

Department of Mechanical Engineering, The University of Melbourne, VIC 3010,
AUSTRALIA

jenh@student.unimelb.edu.au

ABSTRACT

A modified Directed Relation Graph with Error Propagation and Sensitivity Analysis (DRGEPSA) is applied to reduce the AramcoMech 1.3 mechanism for combustion of hydrogen-methane mixtures. As opposed to reduction based on errors in homogeneous zero-dimensional (0D) reactors, this modified DRGEPSA technique considers the error in the laminar flame speed, s_L in one-dimensional (1D) freely propagating flames (FPFs). This results in a 25 species, 126 reaction, reduced mechanism that tracks its parent mechanism over 0-90% hydrogen on a volume basis in the mixture under atmospheric conditions. This reduced mechanism is compared to another reduced mechanism based on AramcoMech 2.0 obtained using a similar technique but the error is based on the autoignition delay time, τ . It is found that using a modified DRGEPSA with the error based on s_L can obtain a reduced mechanism that has less mean deviation in s_L from its parent mechanism compared to reductions based on the error in τ .

Sound generation by turbulent premixed flames with reduced chemistry

Davy Brouzet¹, **Mohsen Talei**¹, **Michael J. Brear**¹ and **Bénédicte Cuenot**²

¹ Department of Mechanical Engineering, The University of Melbourne, Victoria,
AUSTRALIA

² CERFACS, 42 Avenue Gaspard Coriolis, Toulouse Cedex 1 31057, FRANCE
brouzetd@student.unimelb.edu.au

ABSTRACT

Direct numerical simulations (DNSs) of a turbulent premixed flame are conducted using two different reduced chemical mechanisms to assess the impact of chemistry modelling on direct combustion noise. A semi-global, 2-step mechanism and a skeletal mechanism featuring 38 reactions are used. It is shown that the acoustic spectra differ in the higher frequency range $1 < St < 5$. The instantaneous flame front and flow statistics downstream of the flame, as well as the heat release rate, are shown to be significantly different between the two cases. Future work will include a more complete analysis of the impact of chemistry and turbulence/flame interaction on the sound generated to assess which of these features, or others, contribute to the differences in the observed spectra.

Preliminary Observations of Turbulent Flames in a Confined and Pressurised Jet in Hot and Vitiated Coflow Burner

M.J. Evans ¹, P.R. Medwell ¹ and Q.N. Chan ²

¹ School of Mechanical Engineering, The University of Adelaide, S.A. 5005,
AUSTRALIA

² School of Mechanical and Manufacturing Engineering, The University of New South
Wales, N.S.W. 2052, AUSTRALIA
m.evans@adelaide.edu.au

ABSTRACT

The effects of elevated pressures on combustion in hot, low oxygen environments, such as moderate or intense low oxygen dilution (MILD) combustion, are currently not well understood. To meet this gap in understanding, a confined-and-pressurised jet-in-hot-coflow (CP-JHC) burner has been developed to facilitate optical diagnostics of turbulent flames in hot and vitiated coflows for studies of flame stabilisation, structure and soot formation at elevated pressures. The CP-JHC burner has been designed for steady operation at 10 bar(g) with internal temperatures of up to 1975 K with a water-cooled, central jet issuing into a hot oxidant stream produced by a non-premixed burner. This paper describes the CP-JHC burner and peripheral systems, and presents a selection of results from commissioning and initial testing. Temperature measurements of the hot coflow with heat inputs of 9–17 kW are used to estimate the enthalpy deficit of the stream, with thermal efficiency increasing with increasing heat input, and decreasing with increasing pressure. Preliminary mean and instantaneous images of turbulent natural gas/H₂ and C₂H₄ flames, with and without chemiluminescence filters, are discussed in context of ignition pathways and soot formation at elevated pressures to highlight the need for future studies in this newly developed burner.

Multiple injections of iso-octane and *n*-heptane: Part I

S. Xing^{1,*}, G. Zhai¹, A. Srna¹, H. Mo^{1,2}, P.R. Medwell³, S. Kook¹, G.H. Yeoh¹ and Q.N. Chan^{1,*}

¹School of Mechanical and Manufacturing Engineering, UNSW Sydney, NSW 2052, Australia

²School of Mechanical Engineering, Guangxi University, China

³School of Mechanical Engineering, The University of Adelaide, SA 5000, Australia
sensen.xing@unsw.edu.au, qing.chan@unsw.edu.au

ABSTRACT

This work investigated the ignition and combustion interaction processes between two consecutive jets of iso-octane and *n*-heptane inside a quiescent steady environment with ambient density of 22.8 kg/m³, O₂ concentration of 21 vol.% and varied ambient temperature to account for the difference in ignition delays of the fuels. Three injection schedules were tested, including a pilot-main injection, in addition to a single injection with comparatively short and long injection durations as reference cases. High-speed schlieren imaging, pressure trace measurements and photodiode signal revealed that for both fuels, the high-temperature ignition of the second injection occurred after penetrating into the high-temperature combustion products from the first, with observed correlations between their associated heat release profiles with their differences in mixing time prior to ignition. Under the test conditions of this work, relative to the single injection reference cases, the interactions between the consecutive injections led to reduced ignition delay time of the second injection.

Multiple injections of iso-octane and *n*-heptane: Part II

H. Mo^{1, 2,*}, S. Xing¹, G. Zhai¹, A. Srna¹, P.R. Medwell³, S. Kook¹, G.H. Yeoh¹ and Q.N. Chan^{1,*}

¹School of Mechanical and Manufacturing Engineering, UNSW Sydney, NSW 2052, Australia

²School of Mechanical Engineering, Guangxi University, China

³School of Mechanical Engineering, The University of Adelaide, SA 5000, Australia
haijun.mo@unsw.edu.au, qing.chan@unsw.edu.au

ABSTRACT

Iso-octane and *n*-heptane were injected into a quiescent environment with ambient gas density of 22.8 kg/m³ and 21 vol.% O₂ concentration, following a pilot-main injection duration schedule of 2.6/0.2 dwell/6.5 ms. High-speed schlieren imaging was used to visualize the spray-vapor penetration trends and the progression of ignition events. Non-reacting jet models and Closed-Homogeneous Reactor (CHR) simulations were used to provide additional insights. The schlieren images show that a shorter dwell time provides a longer period for the second injection to mix with the products of the first injection until the high-temperature ignition occurs. The relevance of the prolonged mixing is highlighted by the simulation results, which suggest that the local temperature increase and the reactive intermediates from the pre-ignition reactions of the pilot injection considerably affect the ignition characteristics of the main injection.

High-order accurate hybrid LES/PDF simulations of an experimental H₂/N₂ lifted jet flame

Harshad D. Ranadive^{1,*}, Armin Wehrfritz¹ and Evatt R. Hawkes^{1,2}

¹ School of Mechanical and Manufacturing Engineering, University of New South Wales

² School of Photovoltaic and Renewable Energy Engineering, University of New South Wales

A high-order accurate hybrid large-eddy simulation/probability density function (LES/PDF) solver is applied to simulate an experimental lifted H₂/N₂ jet flame in hot vitiated coflow. Artificial fluid properties are employed to compute the sub-grid scale stress, heat flux and species mass flux in the LES. The joint PDF of the transported composition variables is solved with the aid of a Lagrangian Monte-Carlo simulation. A tightly coupled weak second-order accurate time integration scheme has been implemented to integrate the stochastic governing equations. Spatially second order schemes are employed for interpolation and mean estimation algorithms which establish the data transfer across the hybrid solvers. The simulation results of the lifted flame show reasonable predictions as compared to the experimental measurements. A detailed comparison of the statistics at different axial locations is presented for various scalar fields. The flame lift-off height, which is extremely challenging to predict accurately due to its high sensitivity to coflow temperature, is under-predicted in the current simulation. Overall the results show the capability of the LES/PDF model employing the hybrid Eulerian-Lagrangian solution methodology to simulate a challenging lifted turbulent flame.

***A-priori* evaluation of low-dimensional manifold combustion models under diesel engine conditions**

Deepak Dalakoti ^{1,*}, Armin Wehrfritz ¹, Bruno Savard ² and Evatt Hawkes ^{1,3}

¹School of Mechanical and Manufacturing Engineering, The University of New South Wales, NSW, Australia

²Department of Mechanical Engineering, University of Ottawa, Ottawa, Canada

³School of Photovoltaic and Renewable Energy Engineering, The University of New South Wales, NSW, Australia

ABSTRACT

The dataset from a recent DNS of a spatially developing turbulent jet flame in diesel engine conditions was used to *a-priori* evaluate low-dimensional manifold (LDM) combustion models. Three canonical configurations, namely zero-dimensional (0D) homogeneous reactors, one-dimensional (1D) unstrained premixed flames and a two-dimensional (2D) laminar flame were considered for chemistry tabulation. The reaction rate of progress variable was used to estimate the performance of the canonical configurations for representing the DNS data. Results indicate that the 0D homogeneous reactors cannot even qualitatively reproduce the DNS reaction rate. The 1D and 2D flames have a conditional flame structure qualitatively similar to the DNS. A quantitative evaluation reveals that the 0D homogeneous reactors incur the highest error in approximating the DNS reaction rate. The 2D laminar flame has the lowest error, marginally better than 1D premixed flames. This observation indicates the importance of diffusion processes in the turbulent flame. A new definition of progress variable is tested and is shown to be better than the conventional definition used in literature. These results indicate the importance of a prudent choice of progress variable and the canonical configuration for accurate combustion modelling.

OH-PLIF Imaging of a Low Emission Reverse-Cross Flow Combustor

Shreshtha K. Gupta^{1,3*}, Santanu Pramanik², Vaibhav K. Arghode¹, R. V. Ravikrishna² and Robert L. Gordon³

¹Department of Aerospace Engineering, Indian Institute of Technology Kanpur, India.

²Department of Mechanical Engineering, Indian Institute of Science Bengaluru, India.

³Department of Mechanical Engineering, University of Melbourne, Victoria, Australia.
shreshthakum@student.unimelb.edu.au

ABSTRACT

Reverse-cross-flow (RCF) chamber where air and exhaust is at same side and the fuel is crossly injected w.r.t air is investigated having high injection velocities (~50-100 m/s). Sufficient exhaust gas recirculation and controlled mixing has been demonstrated to result in low pollutant emissions (NO_x/CO~10/10 PPM) and stable combustion (pressure fluctuations < 0.02 %). Here, we demonstrated the reaction zone characteristics of RCF with variation in the fuel jet momentum. Fuel injection diameters of 1 mm, 1.5 mm and 2 mm were used to vary the fuel jet momentum, so that, the fuel to air-jet momentum flux ratio varies from 5.15, 1.02 and 0.32 respectively (at global fuel-to-air ratio 0.8). Other parameters were kept the same. The reaction zone is characterized by imaging the distribution of the OH radical using planar laser-induced fluorescence (PLIF) at the mid-plane where the fuel, air, and exit ports are located. The flame front and its transient behaviour are identified using the gradient of the instantaneous OH signal. The reaction zone is observed to be located at the periphery of the air jet, possibly due to the mixing of reactants and hot burned products in the shear layer. The air jet/PLIF signal is found to be deflected more with an increase in fuel-to-air jet momentum.

Experimental and numerical study of ammonia oxidation and pyrolysis in a Jet Stirred Flow Reactor. Evaluation of wall surface reactions effects

P. Sabia ^{1*}, M. V. Manna ^{1,2}, R. Ragucci ¹, M. de Joannon ¹

¹ Istituto di Ricerche sulla Combustione - C.N.R., Napoli – Italy

² Università degli Studi di Napoli, Federico II, Napoli – Italy
sabia@irc.cnr.it

ABSTRACT

The aim of this work is to present an experimental and numerical study of ammonia oxidation and pyrolysis in a Jet Stirred Flow Reactor. Tests were performed for mixtures with different equivalence ratios and several bath gases as a function of the mixture inlet temperature. In order to evaluate the potential impact of heterogeneous effects, further tests were performed adding water vapor to passivate the reactor surface. Experimental results were compared with numerical simulations using different kinetics mechanisms available in literature. Experimental results ammonia oxidation occurs through three different kinetics regimes: low, intermediate and high temperatures. NO_x and H₂ concentration profiles are very similar for low and intermediate temperatures but exhibit a strong dependence on the equivalence ratio for high temperatures. Surface effects are restricted to the NO_x profiles in the intermediate temperature regime and do not affect the O₂ and H₂ concentrations. Pyrolysis tests have shown that ammonia decomposes at inlet temperature higher than 1100 K. In pyrolytic conditions, the heterogeneous reactions affect the ammonia reactivity, by enhancing its decomposition. None of the used kinetic models could accurately reproduce the experimental data in the considered operating conditions. The main differences among mechanisms is the description of the low-intermediate temperatures reaction pathways. Peculiar attention should be paid to ammonia pyrolysis chemistry.

Classification of MILD and autoignitive ethylene flames diluted with N₂, O₂ and CO₂

Jordan A. C. Kildare*, Michael J. Evans, Alfonso Chinnici, Paul R. Medwell
School of Mechanical Engineering, The University of Adelaide
a1720995@student.adelaide.edu.au

ABSTRACT

The moderate or intense low oxygen dilution (MILD) combustion regime has been the topic of interest for various studies, particularly in an attempt to classify the flames that are observed. Flameless and autoignitive flames share many of the same characteristics with MILD combustion, pushing work towards the characterisation of this type of combustion with more rigid guidelines. Through dilution of ethylene with N₂, H₂O, and CO₂, classification of MILD and autoignitive regimes has been examined in this work on the basis of activation energy and inlet temperature. Using numerical batch reactors, the effect of the diluent on the classification of combustion under two different definitions is made, finding that the nature of diluent has little effect on the boundary between the two for a fixed oxygen fraction and inlet temperature. It is also found that a dual stage ignition process is consistent with the MILD regime. Classification of MILD combustion based on equivalent activation energy remains a consistent approach across the different diluents in determining the boundaries between autoignitive and MILD regimes when compared with previous definitions.

Numerical Modelling of Mild Combustion at Elevated Pressures

Douglas B. Proud*, Michael J. Evans, Paul R. Medwell, Florian Vandenbussche
School of Mechanical Engineering, The University of Adelaide, Australia
douglas.proud@adelaide.edu.au

ABSTRACT

Moderate or intense low-oxygen dilution (mild) combustion has been identified as a promising method for the reduction of emissions and increase in performance for a range of practical devices. Mild combustion at elevated pressures is of particular interest, due to the potential of implementing the technology in gas turbines to achieve NO_x reductions. One of the challenges regarding the numerical modelling of mild combustion is the fact that the regime is characterised by a near-unity Damköhler number, meaning that the effects of both turbulence and finite-rate chemistry must be captured in detail. A promising model for describing this turbulence-chemistry interaction is the eddy dissipation concept (EDC); however, previous investigations have been limited to the case of atmospheric pressure. This study focuses on extending a form of the EDC model which has been optimised for the mild regime, to simulate combustion at pressures of up to 10 bar(a), with some experimental results at pressure included for comparison. The experimental work was performed using a confined and pressurised jet in hot coflow (CP-JHC) combustor, and a brief description of this apparatus is provided. The comparisons—although only qualitative in nature—indicate that the model predicts the lift-off height well at a pressure of 5 bar(a), although the lack of a soot model places limitations on the simulation results. The modelling indicates a reduction in both temperature and flame length as pressure is increased, which are attributed to a decrease in turbulence intensity and jet velocity, respectively.

“PRESENTATION ONLY”

Influence of steam dilution on flame structure and soot formation of hot, diluted ethylene flames

A. Chinnici, M.J Evans

School of Mechanical Engineering, The University of Adelaide, S.A. 5005,
AUSTRALIA

alfonso.chinnici@adelaide.edu.au

ABSTRACT

Flames in hot, low oxygen environments exist in a variety of practical applications. These conditions result in significant mixing between fuel and combustion products, such as water vapour, or diluents included for emissions control. The chemical and physical effects of water vapour as a diluent are investigated in a series of ethylene flames in a jet in hot coflow burner to determine the effects on temperature and soot fields. The combined analyses of photographs, non-linear excitation regime two-line atomic fluorescence (NTLAF) of indium, planar laser-induced incandescence (LII) and one-dimensional opposed-flow flame simulations demonstrate the dominance of the chemistry, driven by the hot and diluted oxidant, in soot reduction. Although photographs appear to suggest that both highly vitiated, and highly diluted flames have global effect on the flames, detailed measurements reveal significantly different trends in their soot and temperature fields. The chemical contribution of water vapour as a reactant, as a third-body in ethylene decomposition and a source of H and OH in the rich mixture is further described, and trends subsequently identified, in the context of formation of polycyclic aromatic hydrocarbons and soot reduction.

“PRESENTATION ONLY”
Hybrid solar-combustion processes of renewable fuels

A. Chinnici, G.J. Nathan, B.B. Dally

School of Mechanical Engineering, The University of Adelaide, S.A. 5005,
AUSTRALIA

alfonso.chinnici@adelaide.edu.au

ABSTRACT

This study presents the first investigation of the influence of solar-to-fuel energy input ratio (S/F) on performance and stability characteristics of hybrid processes of solar and MILD combustion of H_2 . A laboratory-scale MILD Hybrid Solar Receiver Combustor was operated at 8-kW_{th} capacity under MILD combustion and in the mixed-mode (MILD plus solar energy simultaneously). An 18-kW_e three-lamp metal halide solar simulator and the combustion of pure hydrogen were used as energy sources. The global combustion performance and stability limits for each mode of operation are reported for different levels of heat extraction and S/F values in the range 5-25%. It was found that similar thermal performance can be achieved for both modes across a wide range of conditions, together with steady operation in response to transients, indicating for the first time that MILD combustion can be used to efficiently compensate for variability in the solar resource. Steady solar-MILD operations retain similar features of conventional MILD processes (nearly-zero emissions, thermal field uniformity) even at relatively high S/F ratio. The global combustion characteristics, performance and stability limits are found to correlate with S/F in the mixed mode, while the operability region for which steady MILD processes can occur was found to increase significantly by adding high-flux concentrated solar radiation to the combustion process and by increasing S/F .

Experimental Investigation of Soot Evolution in Turbulent Non-premixed Bluff-body Ethylene/Nitrogen Flames

A. Rowhani, Z. W. Sun, P. R. Medwell, G. J. Nathan, and B. B. Dally

Centre for Energy Technology, School of Mechanical Engineering,
The University of Adelaide, S.A. 5005, AUSTRALIA
amir.rowhani@adelaide.edu.au

ABSTRACT

Soot evolution and its correlation with the residence time have been experimentally investigated in a series of turbulent bluff-body flames. Laser-induced incandescence (LII) was employed to measure soot volume fraction (SVF), and Particle Image Velocimetry (PIV) was used to measure the flow field. The flame volume for each case was estimated from the luminosity images. The flames were stabilised on three axisymmetric bluff-body burners with different bluff-body diameters (38, 50, and 64 mm) but are otherwise identical in dimensions. A mixture of ethylene/nitrogen (4:1 by volume) issued from a 4.6 mm central round jet to the surrounding co-flowing air at a bulk Reynolds number of 15,000. The annular air velocity was kept at 20 m/s constant for all cases. The highest soot volume fraction was found in the recirculation zone within the outer vortex, adjacent to the co-flowing air for all three cases. The total mean SVF almost doubled, from 140 ppb to 250 ppb when using the 64 mm burner as compared to the 38 mm burner. A small amount of soot was observed in the neck zone and appeared to have been transported from the recirculation zone. The SVF in the jet region decreased with increasing the bluff-body diameter, which is found to be related to the decrease in the estimated total volume of the flame by almost 9%.

An Experimental Study of Laminar Flame Speed of Partially Dissociated NH₃ and Air Mixtures

Herry Lesmana^a, Mingming Zhu^{a*}, Zhezi Zhang^a, Jian Gao^b, Junzhi Wu^{a,c}, Dongke Zhang^{a,b}

^aCentre for Energy (M473), The University of Western Australia, 35 Stirling Highway, Crawley, WA 6009, Australia

^bKey Laboratory of Biofuels, Qingdao Institute of Bioenergy and Bioprocess Technology, Chinese Academy of Sciences, Qingdao, 266101, China

^cShanxi Institute of Energy, Jinzhong, Shanxi Province, 030600, China

ABSTRACT

This paper presents an experimental study of the laminar flame speed of partially dissociated NH₃ in air over the equivalence ratio of 0.9 to 1.2. The experiments were carried out using a vertical tube flame propagation apparatus under ambient temperature and pressure conditions. The ignition and flame propagation processes were recorded using a CCD camera and analysed to obtain the laminar flame speed. The degree of NH₃ dissociation varied from 0 to 10% (0 to 7.5 %v/v H₂ in the fuel mixture with a fixed H₂/N₂ ratio of 3). It was shown that a higher degree of NH₃ dissociation led to a larger initial flame kernel size upon ignition due to the presence of H₂. Regardless of equivalence ratio, the laminar flame speed increased with increasing the degree of NH₃ dissociation. By increasing the NH₃ dissociation from 0% to 10%, the maximum laminar flame speed was increased from 7.83 to 9.76 cm.s⁻¹ at the equivalence ratio of 1.10.

Computational Fluid Dynamics Modelling of Rotating Detonation Engines

Ian J. Shaw, Michael J. Evans, Rey C. Chin, and Paul R. Medwell
School of Mechanical Engineering, The University of Adelaide, S.A. 5005,
AUSTRALIA

ian.j.shaw@student.adelaide.edu.au

ABSTRACT

Rotating detonation engines (RDEs) use a continuously propagating detonation contained within an annulus to generate thrust. Although some of the geometric constraints are known, many have not yet been identified. It has been shown that larger channel widths result in greater thrust due to greater fuel consumption. Since more fuel must be consumed to generate the increased thrust, T , there may also be a variance in specific impulse, I_{sp} . It has also been found sufficiently increased channel widths result in a slowing of the detonation propagation velocity, V_D . A numerical study is presented of RDE models with varying channel widths using three dimensional modeling and large eddy simulation of a premixed H_2 /air detonative reaction. V_D , T , and I_{sp} have been computed, and second order polynomial functions have been fitted to the data, although the functions have not been verified.